


2014-11-24

Amphiphilic Degradable Polymer/Hydroxyapatite Composites as Smart Bone Tissue Engineering Scaffolds: A Dissertation

Artem B. Kutikov
University of Massachusetts Medical School

Let us know how access to this document benefits you.

Follow this and additional works at: https://escholarship.umassmed.edu/gsbs_diss

 Part of the [Biomaterials Commons](#), [Cell Biology Commons](#), [Molecular, Cellular, and Tissue Engineering Commons](#), [Musculoskeletal System Commons](#), and the [Orthopedics Commons](#)

Repository Citation

Kutikov AB. (2014). Amphiphilic Degradable Polymer/Hydroxyapatite Composites as Smart Bone Tissue Engineering Scaffolds: A Dissertation. GSBS Dissertations and Theses. <https://doi.org/10.13028/M2X889>. Retrieved from https://escholarship.umassmed.edu/gsbs_diss/755

This material is brought to you by eScholarship@UMassChan. It has been accepted for inclusion in GSBS Dissertations and Theses by an authorized administrator of eScholarship@UMassChan. For more information, please contact Lisa.Palmer@umassmed.edu.

AMPHIPHILIC DEGRADABLE POLYMER/HYDROXYAPATITE COMPOSITES
AS SMART BONE TISSUE ENGINEERING SCAFFOLDS

A Dissertation Presented

By

Artem Boris Kutikov

Submitted to the Faculty of the
University of Massachusetts Graduate School of Biomedical Sciences, Worcester
in partial fulfillment of the requirements for the degree of

DOCTOR OF PHILOSOPHY

NOVEMBER 24th, 2014

CELL BIOLOGY

AMPHIPHILIC DEGRADABLE POLYMER/HYDROXYAPATITE COMPOSITES
AS SMART BONE TISSUE ENGINEERING SCAFFOLDS

A Dissertation Presented
By

Artem Boris Kutikov

The signatures of the Dissertation Defense Committee signify completion and approval as to style and content of the Dissertation

Jie Song, Ph.D., Thesis Advisor

David Ayers, M.D., Member of Committee

Jaime Rivera, Ph.D., Member of Committee

Gang Han, Ph.D., Member of Committee

George Pins, Ph.D., Member of Committee

The signature of the Chair of the Committee signifies that the written dissertation meets the requirements of the Dissertation Committee

Paul Odgren, Ph.D., Chair of Committee

The signature of the Dean of the Graduate School of Biomedical Sciences signifies that the student has met all graduation requirements of the school.

Anthony Carruthers, Ph.D.,
Dean of the Graduate School of Biomedical Sciences

Cell Biology

November 24th, 2014

DEDICATION

I dedicate this dissertation to my grandfather, Leonid Shursky (1935 – 2012). You have instilled in me a passion for lifelong learning. I hope I made you proud.

ACKNOWLEDGMENTS

I would like to express my deepest appreciation to Dr. Jie Song for being my mentor. I first met Jie during my junior year at Worcester Polytechnic Institute. Desperate to do something productive with my summer, I agreed to a volunteer position in her lab. At that point in time, I had no idea how this one experience would have such a profound impact on my life. While anyone could say that their project was not possible without the help of their advisor, prior to working with Jie I never even considered pursuing a PhD. However, Jie's infectious excitement for science, her unwavering confidence in my abilities (especially when my own confidence may have been lacking), and the collegial atmosphere she fostered in her lab made me want to stay on board and see what we can discover. Jie has taught me how to truly be a multidisciplinary and fearless scientist, taking any approach necessary to solve a problem. Over the course of this journey, she has treated me as a colleague by allowing me to pursue my own ideas and passions while always offering advice and guidance. Thank you Jie, I will be always grateful for you putting your trust in me and helping me grow as a scientist.

I would also like to thank all of the current and former members of the Song lab who have directly contributed to my work, helped me learn new techniques, or simply provided great conversation and friendship. First, I would like to thank Dr. Tera Filion Potts, who was my mentor during my undergraduate days in the lab and has been a friend ever since. Thank you for always going out of your way who to help with experiments, provide me with general graduate

school advice, and being the “go to” for any cell biology question. Thank you to the Dr. Jianwen Xu for teaching me chemistry and polymer science. I will continue to strive to emulate your high scientific standards and attention to detail in my research. This project would not be possible without your guidance. And last but not least, an immense thank you to my friend Jordan Skelly. Jordan is a truly skilled scientist, engineer, and surgeon, going above and beyond any description of her “laboratory technician” position. While I cannot begin to list all that Jordan has contributed to my PhD in this short acknowledgments section, at a minimum none of the *in vivo* work would have been possible without her help. Thank you for taking on the difficult task of teaching me how to perform all the animal procedures and putting up with my incessant questions. Also thank you for caring for all the animals, performing all the x-rays and scans, and teaching me how to analyze the micro-CT data. And thank you for being there to proofread my writing, provide encouragement, and just being a great friend. It should also be noted that Jordan performed all of the rat mandibular defect histology imaging and microCT analysis presented for in the ongoing work section.

I would like to thank all of the undergraduates that I had the privilege of mentoring. I have truly learned as much from you as you did from me. I would specifically like to thank Anvesh Gurijala who pioneered the rapid prototyping work. I would like to thank Kevin Reyer who was integral to the shape memory studies and helped fabricate filaments for the rapid prototyping. I would also like

to thank Wendy Du, who performed the cell seeding optimization work presented in the ongoing work section.

I would also like to thank everyone else that helped contribute to the work in this thesis. I would like to specifically thank Dr. Stephen McCarthy and Dr. Evanthia Fylaktou from the University of Massachusetts Lowell for making the filaments for rapid prototyping. I would like to thank Dr. Hang Cui for patiently teaching me cell culture and molecular biology techniques. I would also like to thank Dr. Greg Hendricks and Dr. Lara Strittmatter in the microscopy core for your help with the scanning electron microscopy.

Also thank you to my thesis advisory committee Dr. Jaime Rivera, Dr. Paul Odgren, Dr. Gang Han, and Dr. David Ayers. Your advice and guidance was greatly appreciated.

Last but not least, I would like to thank my friends and family. Thank you for giving me the drive and support I needed to succeed. None of this would have been possible without you.

Thank you all.

ABSTRACT

Over 600,000 bone-grafting operations are performed each year in the United States. The majority of the bone used for these surgeries comes from autografts that are limited in quantity or allografts with high failure rates. Current synthetic bone grafting materials have poor mechanical properties, handling characteristics, and bioactivity. The goal of this dissertation was to develop a clinically translatable bone tissue engineering scaffold with improved handling characteristics, bioactivity, and smart delivery modalities. We hypothesized that this could be achieved through the rational selection of Food and Drug Administration (FDA) approved materials that blend favorably with hydroxyapatite (HA), the principle mineral component in bone. This dissertation describes the development of smart bone tissue engineering scaffolds composed of the biodegradable amphiphilic polymer poly(D,L-lactic acid-co-ethylene glycol-co-D,L-lactic acid) (PELA) and HA. Electrospun nanofibrous HA-PELA scaffolds exhibited improved handling characteristics and bioactivity over conventional HA-poly(D,L-lactic acid) composites. Electrospun HA-PELA was hydrophilic, elastic, stiffened upon hydration, and supported the attachment and osteogenic differentiation of rat bone marrow stromal cells (MSCs). These *in vitro* properties translated into robust bone formation *in vivo* using a critical-size femoral defect model in rats. Spiral-wrapped HA-PELA scaffolds, loaded with MSCs or a low-dose of recombinant human bone morphogenetic protein-2, templated bone formation along the defect. As an alternate approach, PELA and HA-PELA were

rapid prototyped into three-dimensional (3-D) macroporous scaffolds using a consumer-grade 3-D printer. These 3-D scaffolds have differential cell adhesion characteristics, swell and stiffen upon hydration, and exhibit hydration-induced self-fixation in a simulated confined defect. HA-PELA also exhibits thermal shape memory behavior, enabling the minimally invasive delivery and rapid (>3 sec) shape recovery of 3-D scaffolds at physiologically safe temperatures (~ 50°C). Overall, this dissertation demonstrates how the rational selection of FDA-approved materials with synergistic interactions results in smart biomaterials with high potential for clinical translation.

TABLE OF CONTENTS

DEDICATION	III
ACKNOWLEDGMENTS.....	IV
ABSTRACT	VII
TABLE OF CONTENTS	IX
LIST OF TABLES.....	XIII
LIST OF FIGURES	XIV
LIST OF THIRD PARTY COPYRIGHTED MATERIAL.....	XVIII
LIST OF SYMBOLS, ABBREVIATIONS OR NOMENCLATURE	XIX
CHAPTER I: INTRODUCTION.....	1
1. INTRODUCTION	2
2. OVERVIEW OF SCAFFOLD-BASED TISSUE ENGINEERING	5
3. RATIONAL DESIGN OF ORGANIC-INORGANIC COMPOSITE SCAFFOLDS FOR BONE TISSUE ENGINEERING	27
5. OVERVIEW OF DISSERTATION CONTENT	37
CHAPTER II: AN AMPHIPHILIC DEGRADABLE POLYMER/HYDROXYAPATITE COMPOSITE WITH ENHANCED HANDLING CHARACTERISTICS PROMOTES OSTEOGENIC GENE EXPRESSION IN BONE MARROW STROMAL CELLS.....	41
PREFACE	42

ABSTRACT	43
1. INTRODUCTION	44
2. MATERIALS AND METHODS.....	48
3. RESULTS	56
4. DISCUSSION.....	93
5. CONCLUSIONS.....	105
ACKNOWLEDGMENTS.....	106
CHAPTER III: SPIRAL-WRAPPED ELECTROSPUN AMPHIPHILIC POLYMER- HYDROXYAPATITE SCAFFOLD FOR TEMPLATED REPAIR OF LONG BONE DEFECTS IN RATS.....	107
PREFACE	108
ABSTRACT	109
1. INTRODUCTION	110
2. MATERIALS AND METHODS.....	116
3. RESULTS	125
4. DISCUSSION.....	155
5. CONCLUSIONS.....	161
ACKNOWLEDGEMENTS.....	161
CHAPTER IV: RAPID PROTOTYPING AMPHIPHILIC POLYMER/HYDROXYAPATITE COMPOSITE SCAFFOLDS WITH HYDRATION-INDUCED SELF-FIXATION BEHAVIOR.....	163
PREFACE	164

ABSTRACT	165
1. INTRODUCTION	167
2. MATERIALS AND METHODS.....	171
3. RESULTS	183
4. DISCUSSION.....	207
5. CONCLUSIONS.....	218
6. ACKNOWLEDGMENTS	219
CHAPTER V: SHAPE-MEMORY PERFORMANCE OF THERMOPLASTIC AMPHIPHILIC TRIBLOCK COPOLYMER POLY(D,L-LACTIC ACID-CO- ETHYLENE GLYCOL-CO-D,L-LACTIC ACID) (PELA)/HYDROXYAPATITE COMPOSITES.....	220
PREFACE	221
ABSTRACT	222
1. INTRODUCTION	223
2. MATERIALS AND METHODS.....	227
3. RESULTS AND DISCUSSION.....	234
4. CONCLUSIONS.....	256
5. ACKNOWLEDGMENTS	257
CHAPTER V: DISCUSSION AND PERSPECTIVES.....	258
1. SUMMARY OF THESIS WORK.....	259
2. FUTURE DIRECTIONS.....	265
3. CONCLUDING REMARKS.....	273

REFERENCES	275
APPENDIX I: ONGOING WORK WITH 3-D HA-PELA SCAFFOLDS	326
APPENDIX II: STEM CELL LABELING USING POLYETHYLENIMINE CONJUGATED (ALPHA-NAYBF₄:TM³⁺)/CAF₂ UPCONVERSION NANOPARTICLES.....	353
PREFACE	354
ABSTRACT	355
1. INTRODUCTION	356
2. MATERIALS AND METHODS	358
3. RESULTS	363
4. DISCUSSION	367
5. CONCLUSIONS.....	369
ACKNOWLEDGEMENTS	370
REFERENCES	377
APPENDIX II: PUBLICATIONS COMPLETED DURING GRADUATE EDUCATION	380

LIST OF TABLES

Table 4.1. Molecular weight distribution during the processing of PELA and HA-PELA.	187
Table 5.1. Shape memory properties of HA-PELA films with varying HA contents determined from strain-controlled cyclic thermal mechanical testing.	247

LIST OF FIGURES

Figure 1.1. Chemical structures of commonly used synthetic polymers in tissue engineering.....	9
Figure 1.2. Schematic of an electrospinning process.....	16
Figure 1.3. Schematic of rapid prototyping a femoral head with fused deposition modeling.....	21
Figure 1.4. The hierarchical structure of bone.....	30
Figure 2.1. Synthetic schemes for PELA and PLA.	57
Figure 2.2. Stability of HA suspension in PELA vs. PLA after 1 week.....	60
Figure 2.3. Microstructural and compositional properties of electrospun HA-PELA and HA-PLA composite scaffolds.....	63
Figure 2.4. von Kossa-stained electrospun HA-PELA composites.....	65
Figure 2.5. Tensile stress-strain curves of HA-PELA and HA-PLA composites. .	68
Figure 2.6. Hydration-dependent surface property changes of HA-PELA and HA-PLA.....	71
Figure 2.7. Mechanical property changes of electrospun PELA and PLA composite scaffolds upon hydration	74
Figure 2.8. Crystallization behavior of PELA scaffolds upon hydration. (a) DSC curves of electrospun PELA scaffolds with or without hydration history	77
Figure 2.9. ^1H NMR of PELA and PELA degradation products	80
Figure 2.10. Hydrolytic degradation of scaffolds in PBS	82

Figure 2.11. rMSC attachment and early proliferation on electrospun PELA, HA-PELA, and HA-PLA scaffolds	85
Figure 2.12. Effect of scaffold composition on the lineage commitment of rMSCs in un-stimulated culture	88
Figure 2.13. Effect of scaffold composition on the osteogenic differentiation of rMSCs under induced differentiation culture conditions	91
Figure 2.14. Depiction of a proposed structural rearrangement of the PELA block copolymer chains within HA-PELA composites upon hydration.	98
Figure 3.1. Schematic of the spiral-wrapping of HA-PELA scaffolds for implantation into a rat femoral segmental defect.....	114
Figure 3.2. Viability of rMSCs adhered to flat and spiral-wrapped HA-PELA scaffolds over time.	126
Figure 3.3. rhBMP-2 release and bioactivity.....	129
Figure 3.4. Spiral-wrapping and surgical implantation of HA-PELA scaffolds and post-op radiographical follow-ups of the site of implantation.....	132
Figure 3.5. Histological analysis of cellular infiltration and bone formation within/around the scaffold-filled defect at 12 weeks post-op	136
Figure 3.6. Hematoxylin and eosin staining of vital/scavenger organs (heart, liver, kidney, lung, spleen and pancreas).....	138
Figure 3.7. Two-dimensional bone mineral density color maps of the scaffold-filled defect over time	141
Figure 3.8. <i>In vivo</i> μ -CT monitoring of the scaffold-filled defects over time.....	144

Figure 3.9. Torsional testing of 12-week explants as a function of treatment. ..	147
Figure 3.10. Lentiviral GFP labeling of rMSCs	150
Figure 3.11. Fluorescence microscopy of GFP-labeled rMSCs adhered to HA- PELA scaffolds before and after implantation	153
Figure 4.1. Depiction of the preparation of PELA and HA-PELA 3-D scaffolds by rapid prototyping.....	174
Figure 4.2. Images of the CAD model and the rapid prototyped scaffolds.	184
Figure 4.3 Swelling behavior of HA-PELA and PELA scaffolds	190
Figure 4.4. Compressive moduli of dry and hydrated PELA and HA-PELA scaffolds	193
Figure 4.5. Hydration-induced self-fixation test	196
Figure 4.6. CCK-8 cell viability assay of NIH3T3 attachment and proliferation on HA-PELA and PELA scaffolds.....	199
Figure 4.7. rMSC attachment and osteogenic differentiation on HA-PELA scaffolds	202
Figure 4.8. PELA/HA-PELA biphasic scaffold	205
Figure 4.9. Number of PubMed citations of rapid prototyping and electrospinning publications since 2001	216
Figure 5.1. Scanning electron micrographs of the bottom surface and cross- sections of solvent-cast PELA films with 0-20 wt% of HA.	235
Figure 5.2. Elastic moduli of PELA films with 0-20 wt% of HA	238

Figure 5.3. Temperature-dependent storage moduli of PELA films with 0-20 wt% of HA.....	241
Figure 5.4. Shape memory behavior determined by strain-controlled and stress-controlled cyclic thermal mechanical testing of PELA films with 0-20 wt% of HA.....	245
Figure 5.5. Reprogrammable shape memory of HA-PELA films (20 wt% HA) ..	251
Figure 5.6. Shape memory properties of a rapid prototyped macroporous cylindrical HA-PELA (25 wt% HA) scaffold.....	254
Figure 6.1. CAD models of rat femoral defect sized scaffolds with increasing line spacing.	271

LIST OF THIRD PARTY COPYRIGHTED MATERIAL

Figure Number	Publisher
Figure 1.4	The American Association for the Advancement of Science

LIST OF SYMBOLS, ABBREVIATIONS or NOMENCLATURE

2-D – two-dimensional

3-D – three-dimensional

ALP – alkaline phosphatase

BMP – bone morphogenetic protein

CAD – computer aided design

CCK-8 – cell counting kit-8

μ -CT – micro-computed tomography

DMA – dynamic mechanical analysis

DSC – dynamic scanning calorimetry

ECM – extracellular matrix

FDM – fused deposition modeling

GFP – green fluorescent protein

GPC – gel permeation chromatography

HA – hydroxyapatite

H&E – hematoxylin and eosin

MSC – bone marrow stromal cell

NMR – nuclear magnetic resonance

PCL – poly(ϵ -caprolactone)

PDI - polydispersity

PEG – poly(ethylene glycol)

PELA – poly(D,L-lactic acid-co-ethylene glycol-co-D,L-lactic acid)

PGA – poly(glycolic acid)
PLA – poly(lactic acid)
PLGA – poly(lactic-*co*-glycolic acid)
 R_f – strain fixing ratio
 R_r – strain recovery ratio
SEM – scanning electron microscopy
SMP – shape memory polymer
 T_g – glass transition temperature
TGA – thermogravimetric analysis
 T_m – melting temperature
TRAP – tartrate-resistant acid phosphatase
UV - ultraviolet

CHAPTER I: INTRODUCTION

1. Introduction

While bone has remarkable healing capacity, large fractures or defects cannot heal without intervention. This results in over 600,000 bone-grafting operations each year in the United States alone, and this number is expected to increase with the aging population.[1] The first autologous bone graft was performed by Dr. Fred Albee in 1915.[2] Since then, autograft bone has become the gold standard because it does not illicit an adverse immune response, maintains mechanical integrity, allows for cell binding, supplies mesenchymal stem cells, and contains endogenous growth factors.[3] Autologous bone is usually harvested from the patient's iliac crest, resulting in long-term functional impairment and pain which persists for at least two years in 15-39% of patients.[4,5] Since a second operation for bone harvest is necessary, complications arise such as risk of infection, limited bone quantity, and compromised bone quality. Furthermore, rigid allograft bone is difficult to shape and fit into defects, particularly cranio-maxillofacial defects with complex geometries.[6,7] Autografting procedures are also associated with increased operating time, length of hospital stay, and blood transfusions.[8] Even with these drawbacks, autograft bone is used in 60% of grafting procedures.[9]

When an autograft is not possible, the most common alternative is to use donor bone, referred to as an allograft. This bone is heavily processed to prevent disease transmission and rejection. However this processing removes progenitor cells [10] and disrupts mechanical properties [11], osteoblast-graft interactions

[12], and growth factor stability.[13] As a consequence, allografts often fail to integrate with host bone and remodel, resulting in 10-year failure rates as high as 60%.[14]

The discovery of osteoinductive factors in bone matrix by Marshall Urist in 1965 [15] and the subsequent cloning of bone morphogenetic proteins (BMPs) by Wozney *et al.* in 1988 [16] has led to the widespread use of recombinant human bone morphogenetic protein-2 (rhBMP-2) and rhBMP-7 in bone grafting procedures. These readily available but costly synthetic bone grafts are typically composed of a collagen sponge carrier and the growth factor (rhBMP-2 or rhBMP-7). While these growth factor loaded synthetic bone graft substitutes are as effective as autografts for some indications, particularly non-weight bearing ones,[17] they require loading doses of rhBMP-2 as high as 4.9 mg or 12.7 mg per graft,[18] compared to ~5 µg/kilogram BMP-2 in natural bone.[19] Documented complications from such supra-physiologic doses rhBMP-2 include ectopic bone formation, inflammation, sexual dysfunction, and potentially cancer.[20,21] The need for such a high dose is a result of the burst release profile of rhBMP from the collagen carrier (e.g. 100% released *in vitro* after 2 days [22]). By contrast, although endogenous BMP-2 is expressed most highly early during fracture healing in mice (~1 day), it's expression is sustained during the 21-day healing cascade.[23] Furthermore, the poor handling and mechanical properties of the collagen sponge results in difficulty in inserting and retaining the graft at the defect site.[24] Other attempts to improve the handling characteristics

and bioactivity of synthetic carriers include mixing collagen with calcium phosphate minerals and forming simple gels, foams, pastes, or granules.[25] These materials tend to soften upon hydration and some composites are too brittle due to poor structural integration between components, making their stable fixation with the defect site difficult to achieve. Taken together, current synthetic bone grafts fail to recapitulate the biology of native bone and their physical properties do not support convenient clinical uses. Thus there remains a critical need for translatable bone grafting materials with improved handling characteristics and safer, more effective clinical outcomes.

The field of tissue engineering combines cell biology, materials science, and engineering to develop strategies to regenerate damaged tissues and organs. This is often accomplished by using biodegradable scaffolds that deliver cells/therapeutics, template tissue formation, and ultimately regenerate the tissue of interest [26,27]. An ideal scaffold should be one that can recapitulate the key mechanical and biological features of the tissue of interest while possessing handling characteristics that facilitate cell and/or therapeutic loading and surgical delivery. With regards to bone repair, tissue engineering approaches have the potential to overcome the limitations of autograft and allograft bone.[28–31] This dissertation will describe the development of a biodegradable amphiphilic organic-inorganic composite biomaterial for bone tissue engineering applications. Overall, I will demonstrate how rational selection and integration of FDA-approved components with synergistic interactions results in the development of

“smart” tissue engineering scaffolds with novel handling characteristics and effective biological performance.

2. Overview of scaffold-based tissue engineering

The history of tissue engineering has been previously reviewed [32,33] and will be highlighted briefly. The remainder of this section will discuss the common fabrication strategies and biodegradable polymers used to construct tissue engineering scaffolds.

2.1. Historical perspective

As described by Charles A. Vacanti, M.D.,[32] one of the pioneers in the field of tissue engineering, the idea of *de novo* construction of new tissues and organs can be traced as far back as Genesis I:1 “So the Lord, cast a deep sleep on the man, and while he was asleep, he took out one of his ribs and closed up its place with flesh. The Lord then built the rib that he had taken from the man into a woman.”[34] However, from ancient Egyptians constructing the first wooden toe replacement[35] to the 1980’s, materials for medical applications were limited to prosthetics that could provide mechanical or structural support and bioinert implants intended to resist significant adverse immune responses. The first attempt at what is now described as “tissue engineering” was credited to W.T. Green, M.D., who in 1977 cultured rabbit chondrocytes on a decalcified bone scaffold in an attempt to repair articular cartilage.[36] Dr. Green implanted the constructs into full-thickness rabbit articular cartilage defects in the knee and

observed some cartilage-like tissue formation after 10 days. Even in this early experiment, the importance of appropriate materials selection was apparent because Dr. Green reported that chondrocytes cultured on collagen sponges rather than on decalcified bone failed to induce cartilage repair. In 1981, John Burke, M.D. and colleagues described the application of a porous collagen/chondroitin-sulfate sponge covered with a Silastic® (silicone) membrane for treating burn wounds.[37] Fibroblasts and blood vessels from the wound bed grew into this “artificial skin” scaffold and remodeled the scaffold into a neodermis that could be covered with additional skin grafts.

Joseph P. Vacanti, M.D., first presented the tissue engineering concept as it is recognized today during the 1988 meeting of the New England Surgical Society.[38] In his lecture, Dr. Vacanti described his work with Robert Langer, Sc.D., where they combined cell suspensions isolated from various organs with fibrous synthetic polymeric scaffolds and implanted the constructs into animals. They originally termed this approach as “chimeric morphogenesis”.[39] A subsequent review of the emerging field now called Tissue Engineering, published in Science in 1993 by Langer & Vacanti, has been widely cited as a pioneering article that galvanized the field.[27] Dr. Charles A. Vacanti garnered widespread media attention by growing a human ear-shaped cartilage-like tissue on the back of a nude mouse dubbed the “Vacanti mouse”.[40] While this experiment demonstrated the potential of tissue engineering, true restoration of functional tissue and clinical translation to widespread use remains a challenge.

Just a few of the issues that remain include cell sourcing, immunogenicity, scalability, the vascularization of large constructs, and regulatory and business considerations. The development of appropriate scaffolds to template the tissue formation is one approach to overcome some of these challenges and advance of the field of tissue engineering.

The simplest definition of a tissue engineering scaffold is a structure that provides temporary mechanical support and shape to a growing or regenerating tissue *in vitro* or *in vivo*. [41] These scaffolds can be composed of synthetic or natural materials, or their combinations, and fabricated through a variety of techniques, some of which will be described in this thesis. While early tissue engineering scaffolds relied on simple single-component materials as structural/mechanical support, next-generation “smart” scaffolds aim to guide cell fate, respond to cell signals by degrading or releasing growth factors, and enable novel delivery modalities such as shape-memory, self-fixation, or change form (liquid to gel) at the implantation site. [41,42]

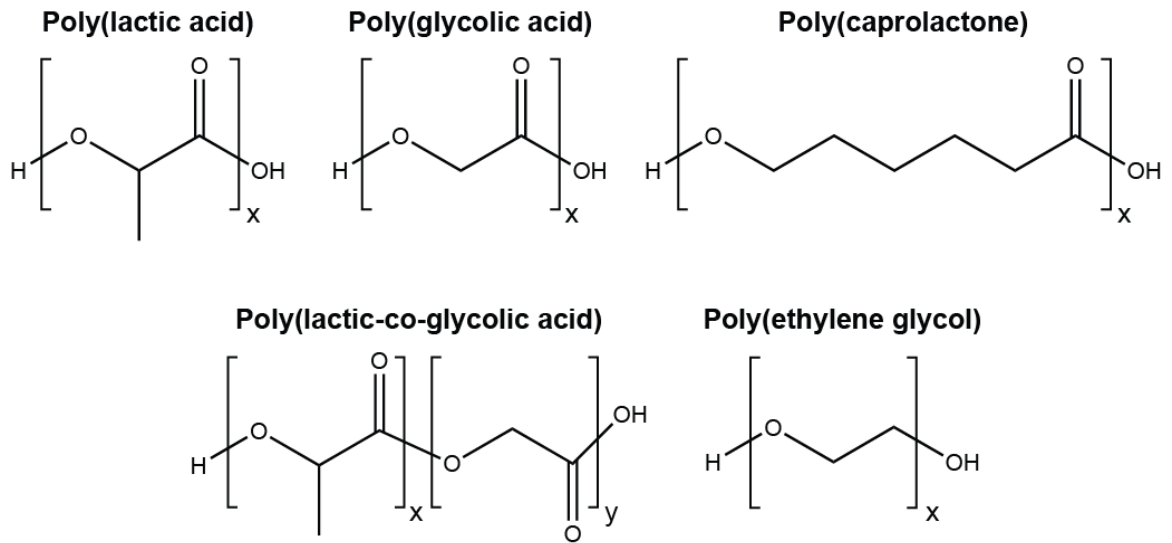
2.2. Polymers for tissue engineering scaffolds

Both natural and synthetic polymers have been used as tissue engineering scaffolds. Natural polymers such as collagen, gelatin (denatured collagen) and fibrin are part of the natural extracellular matrix (ECM) or secreted during the wound healing process. While natural materials such as collagen and fibrin are in clinical use, their batch-to-batch variability in isolation/purification, weak mechanical properties, poorly controlled degradation, cost, processing

difficulties, and immunogenicity present challenges.[43] Synthetic polymers, if properly designed, can be fabricated reproducibly in large scales, exhibit improved mechanical properties and predictable degradation behaviors, and are amenable to a variety of chemical functionalization or physical modifications to introduce bioactivity. The Food and Drug Administration (FDA) has approved many products comprised of synthetic polymers with acceptable biocompatibility. Chemical structures of the building blocks of FDA-approved degradable synthetic polymers described in this thesis are shown in Figure 1.1.

Figure 1.1. Chemical structures of commonly used synthetic polymers in tissue engineering.

Figure 1.1



2.3.1 Biodegradable polymers

The most widely used FDA-approved degradable polymers are the hydrophobic polyesters poly(lactic acid) (PLA), poly(glycolic acid) (PGA), poly(lactic-co-glycol acid) (PLGA), or poly(ϵ -caprolactone) (PCL). These materials are most commonly found in surgical products such as resorbable sutures, meshes, or orthopedic fixation devices.[44]

PLA is composed of chiral lactide building blocks that can be polymerized in an enantiomerically pure L form (PLLA) or a racemic D/L form (PDLLA).[45] PLLA is semi-crystalline and PDLLA is amorphous, resulting in vastly different mechanical properties and degradation rates. PLLA is a rigid polymer with a glass transition temperature (T_g) of 60-65 °C, melting point (T_m) of ~175 °C, and a tensile modulus of 2.7 GPa. [46] PDLLA is a weaker material (1.9 GPa tensile modulus) and has a T_g of 55-60 °C.[47] PLLA and PDLLA are thermoplastics that can be fabricated into scaffolds with a variety of architectures including dense and nanoporous films by solvent-casting and electrospinning, respectively, as well as dense filaments and macroporous 3-D scaffolds by extrusion and fused deposition modeling techniques. However, relatively high temperatures are required to melt and process PLLA (> 175 °C) and PDLLA (~>130 °C).

PLA degrades by hydrolysis of the ester bonds into lactic acid, which is a natural metabolic byproduct and may be cleared by the body as carbon dioxide and water.[44] The accumulation of lactic acid released from degrading PLA and the resulting pH drop in the vicinity of the implant can cause an inflammatory

immune response and bone resorption.[48,49] PLLA takes over 2 years to degrade, and full degradation of PLLA crystallites can take over 5 years,[49] while PDLLA degrades in ~1 yr.[44]

PGA is a highly crystalline polymer, resulting in its insolubility in most organic solvents and high stiffness (12.8 GPa tensile modulus).[47] It has a high melting point (225 °C) and is typically processed by injection molding/extrusion. PGA degrades by hydrolysis in 6-12 months, depending on its molecular weight, into glycolic acid which can be cleared by the body.[44] The degradation behavior and high-strength fiber forming ability of PGA led to its use as the first biodegradable synthetic suture material (Dexon®).[44] However its use has been relatively limited in tissue engineering due to its low solubility, limited high-temperature processing options, and high stiffness. Co-polymers of PLA and PGA, called PLGA, overcome the processing difficulties (solubility) and excessive stiffness of PGA. By varying the ratio of PLA to PGA, the degradation rate can vary from 1-2 months (50/50 ratio) to 6 months (85/15 ratio).[44] The tunable degradation rates, ease of processing, and established medical uses of PLA and PLGA have led to their wide incorporation in tissue engineering scaffolds.

The use of PCL has generally been restricted to slow degrading drug delivery devices and sutures, but more recently its application has been extended to tissue engineering applications, as reviewed by Woodruff and Hutmacher.[50] PCL is a semi-crystalline polymer that is generally weaker than

PLA (400 MPa tensile modulus)[46] and degrades by hydrolysis into caproic acid. It has a T_g of ~ -60 °C and a T_m of ~ 60 °C. The thermoplastic nature and relatively low melting point of PCL enables its facile processing into a variety of scaffold architectures by techniques such as electrospinning and rapid prototyping. PCL can be degraded by bacterial enzymes but its *in vivo* degradation modality in humans and animals is limited to hydrolysis.[50] Since PCL is more hydrophobic than PLA,[51] it has a slower degradation rate, with minimal degradation reported even after 2 years *in vivo* (initial $M_w = 66,000$ Da).[50,52]

2.3.2 Poly(ethylene glycol)

Poly(ethylene glycol) (PEG) is a hydrophilic polyether that is clinically used in formulating pharmaceuticals, such as for increasing the circulation time of protein therapeutics.[53] This increased circulation time is a result of the low-fouling nature of PEG as it is known to resist protein adhesion through the entropic penalty of releasing bound water from the hydrophilic PEG surface by approaching proteins.[54] While PEG is non-degradable, PEG chains shorter than 30-50 kDa are readily cleared through the kidneys.[53,55] Unmodified PEG is not suitable for tissue engineering applications requiring tissue integration because it is non-cell adhesive, non-degradable, and water-soluble. With the addition of bioactive molecules or fillers, however, cross-linked PEG hydrogels have been widely studied for tissue engineering.[56] PEG can also be copolymerized with water-stable and degradable hydrophobic blocks, such as PLA or PCL. Low molecular weight amphiphilic polymers composed of

biodegradable hydrophobic blocks and PEG can form nanoparticles that have been used to encapsulate hydrophobic drugs or proteins with extended circulation time.[57–59] High molecular weight (>100 kD) amphiphilic PEG-based polymers can form membranes or gels that are stable in aqueous environments and have been used as degradable anti-adhesion tissue barriers for surgery.[60–64] PEG-based copolymers have also been used for tissue engineering scaffolds as reviewed by Tessmar & Göpferich.[65]

2.3. Fabrication techniques for tissue engineering scaffolds

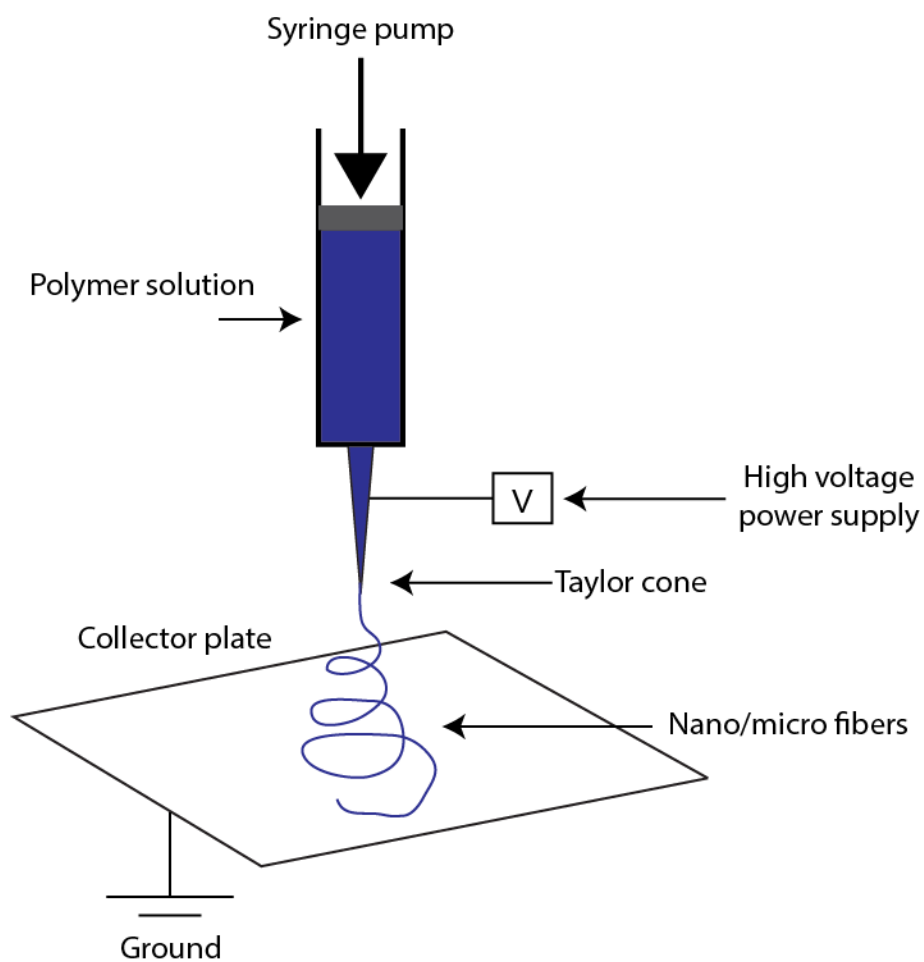
Interconnected porous structures are desired for tissue engineering because they enable cellular/tissue ingrowth, nutrient transport, and waste diffusion. For example, pore sizes of ~100 μm are required for bone and capillary ingrowth *in vivo*, with pore sizes of 300-400 μm resulting in the most bone ingrowth.[66] The high surface area of porous scaffolds also increases the capacity for the binding and release of growth factors and other therapeutics that could be used to replicate the biochemical environment of the tissue of interest. A variety of manufacturing approaches are available for tuning the architecture and porosity of scaffolds including solvent casting/particulate leeching,[67,68] gas foaming,[69] thermally induced phase separation,[70] self-assembly,[71] electrospinning,[72] and rapid prototyping.[73] Each of these approaches has its unique advantages and disadvantages, as has been reviewed previously.[74,75] Here I will describe the two manufacturing approaches used in this dissertation work, electrospinning and rapid prototyping.

2.3.1 Electrospinning

Electrospinning is a method to form nanoscale polymer fibers by ejecting a polymer melt or polymer dissolved in solvent through a syringe under high voltage. Electrostatic forces cause the polymer at the tip of the syringe to form a conical structure called a Taylor cone. As the charge buildup overcomes the surface tension of the polymer solution, the solution forms a thin jet emanating from the Taylor cone. Whipping and bending of the jet under the electric field stretches it into a nano-sized fiber while the solvent is evaporated. The resulting charged fiber is collected onto a grounded surface.[76] The size and morphology of the fibers can be tuned by varying the electrospinning parameters such as solvent, voltage, and collector distance. While the first patent for electrospinning polymeric solutions dates back to 1930,[77] it did not garner widespread attention until the 1990s, principally driven by research from the Reneker group that described the electrospinning of over 20 types of polymers including DNA.[78] Facile modification of the electrospinning apparatus has been employed to create specialized structures such as aligned fibers,[79] core-shell fibers,[80] and tubular constructs [81]. A schematic of the electrospinning process is shown in Figure 1.2.

Figure 1.2. Schematic of an electrospinning process.

Figure 1.2



The native ECM that cells create, grow on, and remodel is composed of hierarchically organized structures of which nanofibrous proteins are the basic building blocks. The ECM provides structure to the tissue and guides cell fate and function through a combination of physical and soluble signals.[82]

Electrospinning is a scaffold fabrication technique well suited for creating ECM-mimetic nanofibrous materials. The research groups of Frank Ko [83] and Gary Bowlin [84,85] performed the early work adopting electrospinning to tissue engineering in 2001-2002. The high surface area of electrospun nanofibrous materials has been shown to adhere greater numbers of cells than flat counterparts.[86] Electrospun materials also effectively retain and release growth factors, such as the sustained release of BMP-2 with >80% retention after 7 days [87]. Modification of the fiber size and alignment can direct stem cell growth and differentiation *in vitro*. [86] When tested *in vivo*, Cao et al. found that nanofibrous PCL scaffolds resulted in a less fibrous encapsulation than flat PCL films, with a 37 μm thick fibrous capsule over the film versus an 8 μm thick capsule over electrospun fibers.[88] The nanofibrous scaffold morphology may also result in improved bone healing. Woo et al. demonstrated that nanofibrous PLLA scaffolds supported more bone formation in rat calvarial defects than solvent-cast PLLA scaffolds.[89] Cai et al. found that nanofibrous PLLA membranes resulted in greater bone formation than collagen membranes in rabbit tibial defects.[90]

Electrospinning typically produces thin two-dimensional (2-D) fiber mats with high bulk porosity but pore sizes (1 – 10 μm) that are too small for the

infiltration of cells.[91] This results in difficulty in applying electrospun scaffolds to large 3-D defects and poor cellular/tissue ingrowth across the depth of electrospun materials. One approach to create 3-D constructs from electrospun membranes is to wrap [92,93] or stack [94] the membranes into 3-D configurations, however, this alone does not solve the porosity issue. The electrospinning setup can be modified to create porous 3-D constructs. Blakeney *et al.* used a grounded spherical dish with an array of metal rods as the collector.[95] This produced 3-D “cotton ball-like” scaffolds that improved cell infiltration. Yokoyama *et al.* formed 3-D sponge-like nanofibrous scaffolds by electrospinning into tertiary-butyl alcohol.[96] Kim *et al.* used a femtosecond laser to introduce pores into similar electrospun sponges, increasing the pore size from 5-10 μm to 190-380 μm .[97] Baker *et al.* increased the porosity of electrospun scaffolds by co-electrospinning sacrificial water-soluble fibers.[98] Using this method, they were able to increase cell infiltration, where cells grew mainly on the surface of the scaffolds without sacrificial fibers but fully colonized the thickness of the scaffolds bearing 60% sacrificial fibers.

2.3.2 Rapid prototyping

Rapid prototyping or solid freeform fabrication refers to a variety of techniques that produce solid structures based on computer aided design (CAD) models. Initially, rapid prototyping was used in the medical field to make custom titanium bone implants and anatomical models for guiding surgical procedures.[99] For tissue engineering applications, rapid prototyping has a

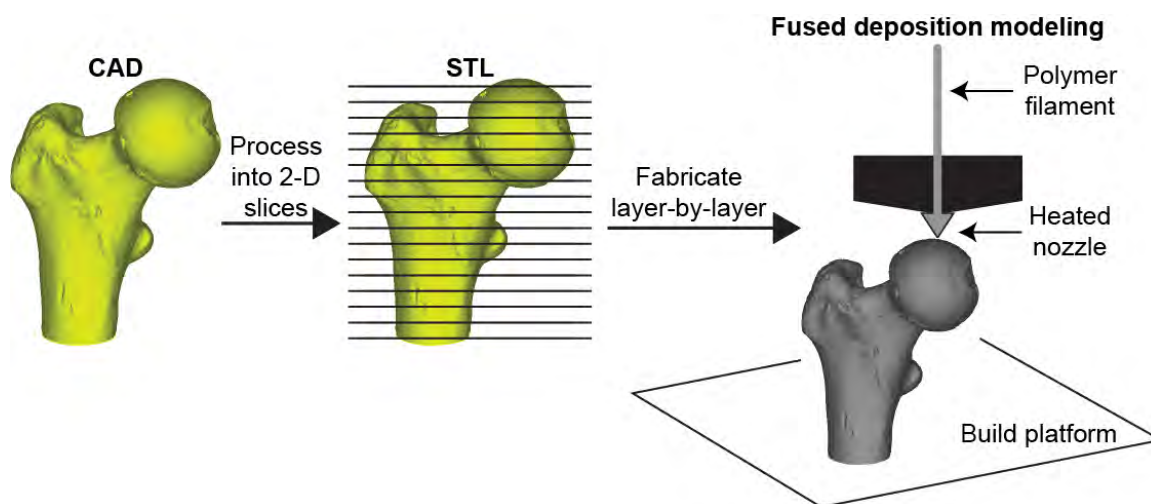
distinct advantage over indirect scaffold fabrication techniques such as solvent casting-particulate leeching and freeze-drying because it allows for the ability to precisely and reproducibly control porosity and macroscopic shape.[73,99]

Advanced rapid prototyping approaches can also incorporate multiple materials, cells/biologics, and a combination of nano, micro, and macro-scale features in a single scaffold.

Rapid prototyping techniques begin with a 3-D CAD model that has either been designed *de novo* or based on anatomical data from computed tomography (CT) scans. The CAD model is processed by software that converts the model into a collection of surface triangular patches and saves the model as an STL file.[75] In order to generate instructions for the rapid prototyping apparatus, the STL file is sliced into stacked 2-D cross-sections. The apparatus fabricates these cross-sections layer-by-layer, reproducing the final 3-D structure. Common rapid prototyping methods include stereolithography, selective laser sintering, 3-D printing, and fused deposition modeling. A schematic of the rapid prototyping process using fused deposition modeling is shown in Figure 1.3.

Figure 1.3. Schematic of rapid prototyping a femoral head with fused deposition modeling.

Figure 1.3



Stereolithography

Stereolithography was the first commercially available rapid prototyping technique, developed by 3D Systems in 1986.[100] Stereolithography is based on polymerizing photocurable liquid resins. The stereolithography apparatus uses an ultraviolet laser or projects an ultraviolet pixel pattern to harden the resin in areas defined by the STL file, and then the platform moves down to allow polymerization of the following layer. Stereolithography allows for the fabrication of complex structures with a resolution in the sub-micron scale.[101] This precise geometric control enables the fabrication of scaffolds with high surface areas and interconnected porosity by using mathematical modeling techniques such as triply periodic minimal surfaces.[102] Stereolithography is amenable to both synthetic biodegradable polymers[103] and natural materials[104], but only if they can be modified with photoreactive groups for photo-curing. Since stereolithography is a low-temperature process performed in solution, live cells can be added, enabling the direct encapsulation of cells within the scaffold.[105] However, technical challenges with such a cell encapsulation approach include inhomogeneous cell distribution due to settling, cytotoxicity imposed by the photoinitiators, and potential cellular damage by the ultraviolet light.[100] Other disadvantages of stereolithography include the expensive machinery required, the inability to print overhanging features without a support, additional post-processing to complete crosslinking, and the limited number of biocompatible stereolithography resins.[100]

Selective laser sintering

Selective laser sintering is similar in principle to stereolithography but the resin bath is replaced with a polymer powder. A high-energy laser melts the polymer powder to form a solid structure layer-by-layer. Selective laser sintering has been used for the fabrication of high-strength polymer and polymer/ceramic composite scaffolds.[75] Because the un-melted powder provides a support structure to the printed construct, complex shapes with overhangs can be produced without a support material. However, the resolution of this technique is governed by the powder morphology and heat transfer characteristics, resulting in lower dimensional accuracy (45 – 100 μm) than selective laser sintering.[106] It can also be difficult to remove trapped powder from the pores of the final scaffold.[106] The expensive machinery, high temperatures required, and the limited selection of suitable powderized polymers further limit the applications of selective laser sintering in tissue engineering.[50]

3-D printing

The term “3-D printing” is commonly used to refer to rapid prototyping in general, however the specific technique of 3-D printing involves rapid prototyping with an ink-jet based system. 3-D printing was first described by Sachs, Cima, and Cornie in 1990.[107] Their design involved depositing a stream of binder (colloidal silica) droplets from a piezoelectric inkjet nozzle onto a powder bed (aluminum oxide). As with other rapid prototyping methods, the 3-D part is built by binding the powder layer-by-layer. The powder bed allows for the printing of

overhangs without support material. This approach is more cost effective than the laser-based approaches, although it typically requires customized instrumentation. 3-D printing has been applied to tissue engineering because it does not require elevated temperatures and is amenable to a wide selection of binder and powder materials. 3-D printing has been used to fabricate scaffolds composed of natural polymers including collagen,[108] biodegradable synthetic polymers, and polymer/mineral composites.[106] However, the resolution of 3-D printing is limited by binder and powder interactions, particularly wettability and solvent evaporation, which result in a resolution of 350 μm – 500 μm .[106] The number of suitable powdered polymers and binders and the difficulty in removing unbound powder are additional limitations of 3-D printing. Rather than binding powder, ink-jet-based 3-D printers have been loaded with live cells mixed in hydrogels and used to directly print cell-laden constructs.[109] This is a promising technique for manufacturing whole engineered tissues and organs but complications such as low cell viability, inadequate cell densities, and poor nutrient diffusion within such 3-D printed cell-laden scaffolds remain.

Fused deposition modeling

Fused deposition modeling (FDM) is a simple and inexpensive rapid prototyping approach that has been widely used in the hobbyist community (RepRap) and commercialized into consumer-grade “3-D printers” by companies such as MakerBot®. Akin to a hot glue gun, a polymer filament is extruded through a heated nozzle and deposited onto a build platform. The platform

moves to allow construction of the model layer-by-layer, with the heated plastic from the layer being deposited fusing at its contact points with the previous layer. Advantages of FDM are its accessibility, the ability to print small overhangs without support material, and the lack of post-processing steps (no need for powder removal/cross-linking). The resolution is most limited by the size of the printing nozzle and extrusion characteristics of the polymer, resulting in a line width typically approaching 250 μm . [110]

Disadvantages of FDM include the requirement for thermoplastic polymers and the high temperature processing that is unsuitable for the direct deposition of growth factors or cells along with the polymer. Customized FDM-based methods have aimed to overcome these disadvantages. Instead of extruding melted polymer, 3-D fiber deposition uses a pneumatic-driven syringe to deposit viscous solutions. This technique has been used to fabricate scaffolds composed of biodegradable polymers and polymer/bioglass composites with line widths as low as 75 μm . [111] Live cells in hydrogel solutions can also be loaded into the syringe barrel and extruded into 3-D scaffolds using this method. [112]

2.3.3 Combinations of electrospinning and rapid prototyping

As described previously, electrospinning results in nanofibrous scaffolds with high surface areas but limited porosity and thickness. Rapid prototyping techniques create 3-D scaffolds with high macroporosity and unlimited thickness but the line resolution is unsuitable for fabricating nanoscale features. As recently reviewed by Dalton *et al.*, electrospinning and rapid prototyping are converging to

incorporate the advantages of each technique into one scaffold.[113] For example, nanofibers can be electrospun between layers of a rapid prototyped macroporous scaffold. This results in increased cell retention upon cell seeding onto the scaffold.[114] Alternatively, electrospinning apparatus have been modified to allow direct deposition of electrospun fibers in defined configurations. One solution is to electrospin a polymer solution into a moving grounded bath collector. This results in 3-D scaffolds with high surface roughness.[115] In another modification, melt electrospun fibers were directly deposited in controlled configurations, forming rapid prototyped materials with 20 μm fiber resolution.[116] However, these techniques are still in the proof-of-concept phase and have not yet entered widespread use in the tissue engineering community.

3. Rational design of organic-inorganic composite scaffolds for bone tissue engineering

3.1. Requirements for a bone scaffold

The requirements for an ideal bone tissue engineering scaffold vary depending on the application but there are some common clinical translation and biological factors. From a translational standpoint, the biomaterial should be simple to produce, ideally made of building blocks used in FDA-approved products, scalable, versatile in its processing, simple to store and transport, cost effective, easy to use (i.e. drug/cell loading, molding, delivery, and fixation), and ideally cell-free.[25] From a biological standpoint the material should be

biocompatible, support bone ingrowth (osteoconductive), recruit and guide the osteogenic differentiation of progenitor cells (osteoinductive), and bio-resorbable in a time-scale coincident with healing (3-6 months for bone[117]).[24] To facilitate FDA-approval, it is beneficial if these bioactivity characteristics derive from the intrinsic properties of the material (hydrophobicity/hydrophilicity, stiffness, morphology) rather than from exogenous additives.[118] These requirements could potentially be met by designing synthetic materials that mimic the key structural components of natural bone while imparting novel “smart” functionalities.

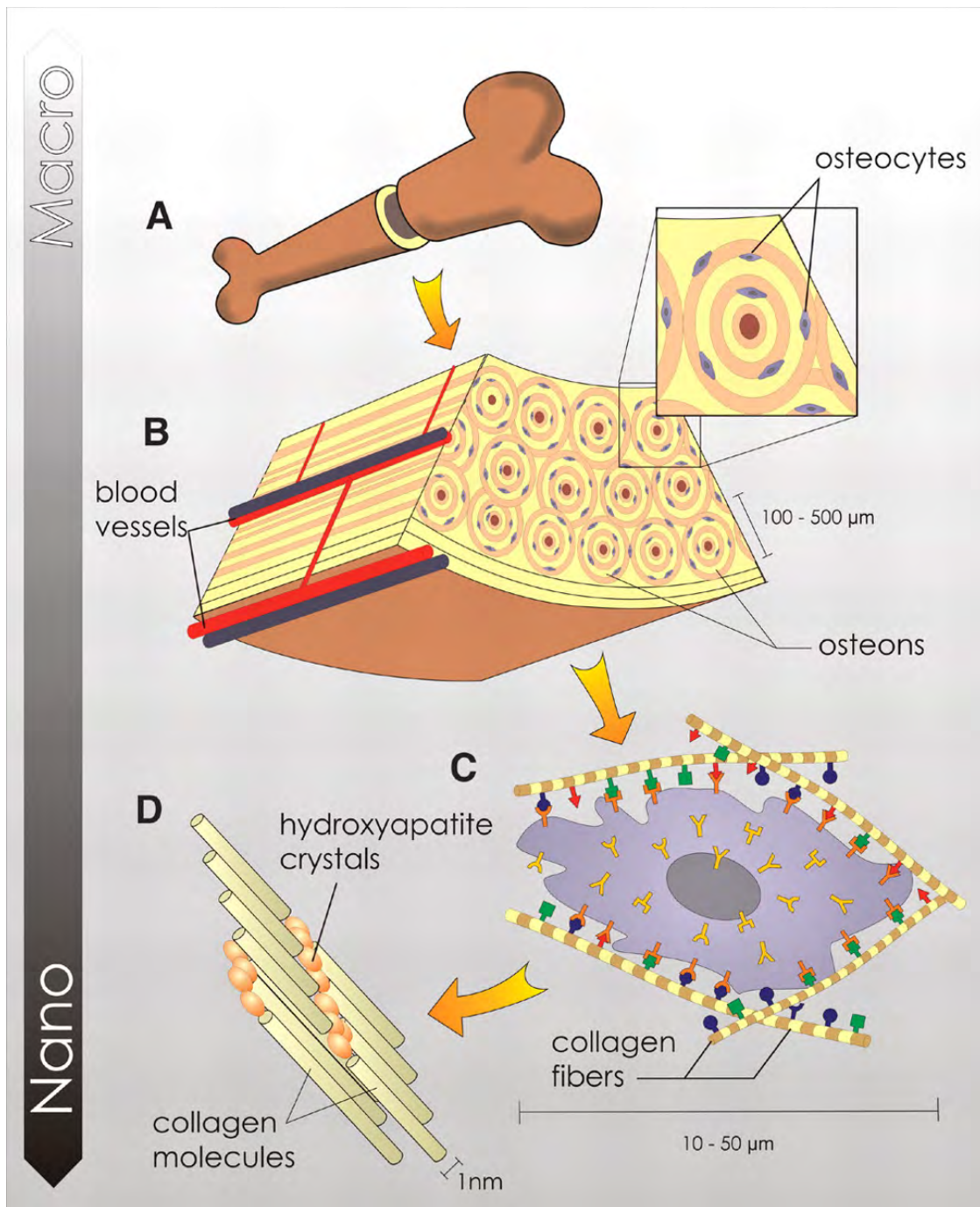
3.2. The structure and cellular composition of native bone

Bone is a complex tissue that is hierarchically organized from macroscopic into micro and nanoscopic scales.[119–121] A simplified schematic of bone’s hierarchical structure is shown in Figure 1.4. Macroscopically, bone is composed of compact cortical bone and spongy trabecular bone. Most bones are covered in periosteum, a thin highly vascularized fibrous tissue that is a source of progenitor cells and blood vessels for bone. The inner cavity of bone contains a similar fibrous tissue called the endosteum, which is also a source of progenitor cells and more differentiated bone cells. At the microscopic scale, bone is composed of sheets called lamellae. In compact bone, these lamellae are further cylindrically organized into osteons. The osteons have Haversian canals in the center, through which blood vessels provide nutrients. Transverse canals called Volkmann’s canals link the Haversian canals together. Residing in the bone are

cells called osteocytes which sense mechanical forces and guide bone turnover.[122] They can communicate to each other through a network of channels called canaliculi.[121] Osteoblasts, derived from bone marrow stromal cells (MSCs) or other progenitors (e.g. periosteal cells) are the cells that secrete osteoid and mineralize the osteoid into bone. The osteoblasts secrete signaling molecules that stimulate bone-resorbing cells called osteoclasts. Osteoclasts are multinucleated cells derived from monocytes. The coordinated remodeling activity of osteoblasts and osteoclasts is critical for skeletal injury repair and the maintenance of healthy bone tissue.[121]

Figure 1.4. The hierarchical structure of bone. From: Stevens MS, George JH. Exploring and Engineering the Cell Surface Interfance. Science (310) 2005;5751:1135-1138. Reprinted with permission from AAAS.

Figure 1.4



On the nano-scale, bone is a composite predominantly of type-I collagen and nanocrystalline hydroxyapatite ($\text{Ca}_{10}(\text{PO}_4)_6(\text{OH})_2$; HA) (50-70% dry weight, with varying degrees of carbonation and substitution by halides). Collagen provides a tough and elastic structure that is reinforced by the HA. The excellent structural integration of HA with the collagen template is critical for cortical bone's robust compressive strength (78-151 MPa), young's modulus (6-13 GPa), and fracture toughness ($2-12 \text{ MPa m}^{1/2}$). [123] Apart from mechanical reinforcement, the HA component of bone is also an important bioactive component of the ECM. HA supports bone growth (osteoconductive) and can induce the recruitment and differentiation of bone progenitor cells (osteoinductive). This bioactivity is a result of a combination of HA's physical properties including its dynamic surface that can sequester and release proteins, [124,125] the release of calcium and phosphate ions driving osteogenic differentiation of stem cell cells, [126] and mechanical cues. While replicating the complex hierarchical structure of bone is yet to be achieved, mimicking the nanoscale organic/inorganic composition of bone has been a widely used strategy in the design of bone tissue engineering scaffolds. One way this can be accomplished is by blending synthetic polymers (organic component) with HA or other osteoconductive minerals (inorganic component).

3.3. Synthetic organic-inorganic composites

Synthetic HA is clinically used in bone cements, [127] hip prosthesis coatings, [128] and for middle ear reconstruction. [129] However, the brittle

mechanical properties of HA results in poor handling characteristics and make it unsuitable for load-bearing applications. A rational strategy to overcome the brittleness and poor handling characteristics of HA while exploiting its bioactivity has been to blend HA with synthetic biodegradable polymers. These polymer-HA composite biomaterials can then be fashioned into tissue engineering scaffolds by a variety of approaches including electrospinning and rapid prototyping. The addition of HA to biodegradable polymers has been shown to improve cell attachment,[130] osteogenic differentiation of stem cells,[131,132] growth factor/drug binding and release,[133,134] and expedite bone healing *in vivo*. [135] HA and other calcium phosphates can also buffer the acid byproducts of polymer degradation, potentially mitigating adverse immune responses.[136,137] In such polymer-HA composites, adequate HA dispersion and interfacial adhesion between the HA and polymer is critical.

Poor dispersion and interfacial adhesion of HA in polymer blends results in HA aggregation and mechanical failure sites at the polymer-HA interface. This leads to deterioration of the mechanical and handling properties of the resulting composite scaffold.[138–140] Most FDA-approved biodegradable polymers, including PLA and PCL, are hydrophobic and blend poorly with the hydrophilic HA mineral. This hydrophobic-hydrophilic mismatch yields scaffolds with compromised mechanical properties and bioactivity, particularly when incorporated with high HA contents (>10 wt.%). Poor adhesion between the polymer and mineral phase is apparent when casting simple films, as described

by Kim *et al.*[141] Loading 30 wt.% calcium phosphate/PCL films under tension results in failure points at the mineral/polymer interface. Poor HA adhesion and dispersion results in further compromised performance of porous scaffolds. Jeong *et al.* used electrospinning to produce a nanofibrous composite of PLLA and 20 wt.% HA.[142] This combination resulted in a brittle material with an ultimate tensile strength of 0.262 MPa and young's modulus of 4.771 MPa. Poor dispersion of HA can also result in HA aggregates when rapid prototyping 3-D scaffolds. Rodriguez *et al.* fabricated HA-PCL composite scaffolds by fused deposition modeling.[143] Micro-computed tomography (μ -CT) reconstruction of the scaffolds showed large HA aggregates and a non-uniform distribution throughout the scaffold.

Aggregation of HA can also result in inconsistent biological properties because adhered cells are not uniformly exposed to HA. MC3T3 pre-osteoblast cells seeded on the nanofibrous composite of PLLA and 20 wt.% HA maintained viability and proliferated for 21 days, with a trend showing improved viability on the HA composites albeit with no difference at increasing HA contents.[142] D'Angelo *et al.* electrospun composites of 1-8 wt.% calcium-deficient HA and PLLA. [131] They found that the HA promoted a dose-dependent increase in osteogenic gene expression in bone marrow stromal cells, induced pluripotent stem cells, and embryonic stem cells when cultured in basal medium. However, the impact of HA was negated when the cells were cultured in osteogenic

medium. Furthermore, even at 8 wt.% HA there was a wide variation in fiber diameters and the storage modulus decreased 9-fold.

The addition of surfactants and the surface modification of HA have been used to improve the interfacial adhesion of HA with hydrophobic polymers. These approaches have demonstrated some success but also introduced ill-defined consequences on *in vivo* safety and performance. Kim *et al.* used a surfactant to disperse HA and electrospin PDLLA composites with up to 20 wt.% HA.[144] This composition increased alkaline phosphatase (ALP) activity over scaffolds without HA. However, no mechanical testing was performed. Hydroxyl groups on the HA surface are amenable to covalent coupling. Silane coupling reagents have been studied to covalently modify the reactive HA surface,[145] however, the biocompatibility of these approaches and the toxicity of leaching silane coatings is unclear.[146] Qui *et al.* modified HA with L-lactic acid and then used the modified HA as initiators to polymerize PLA.[147] The surface modification significantly increased the ultimate stress and elongation at break of PLLA composites with 15 wt.% HA. Wang *et al.* grafted PCL to the surface of HA to improve HA blending in porous PCL scaffolds.[148] The grafted HA particles resulted in significantly increased compressive modulus and compressive strength of the scaffolds, but no biological assessment was performed.

Designing biomaterials with intrinsic HA bonding capacity is an alternative strategy to improve HA dispersion and adhesion in bone tissue engineering scaffolds. Using a combinatorial phage display strategy, HA-binding

oligopeptides bearing hydroxylated residues every 3 amino acids, mimicking the periodic presence of hydroxyproline in type I collagen, was discovered.[149] Similarly, hydrophilic poly(hydroxyethyl methacrylate) (pHEMA) hydrogels are efficient templates for HA mineralization.[150–152] Cross-linked pHEMA hydrogels with 50 wt.% HA withstand compressive strains of >80% and 450 MPa compressive loads.[153] Blending HA with PEG has shown similar results.[130] This improvement in mechanical properties can be attributed to the favorable adhesion of HA, a hydrophilic mineral, with hydrophilic residues in the polymers.[138] The pHEMA-HA composites also demonstrated useful handling characteristics (press-fitting), sustained release of bioactive proteins and antibiotics,[133,154,155] and the ability to expedite healing of critical-size bone defects in rats with an exceptionally low dose of osteogenic growth factor.[135,154] However, hydrophilic polymers including pHEMA need to be crosslinked to achieve aqueous stability and mechanical integrity. Cross-linked polymers cannot be dissolved or melted for processing into diverse scaffold architectures. Therefore, the pHEMA-HA composites need to be cross-linked in specifically designed molds to achieve the desired shape. Such an approach is not practical for fabricating tissue engineering scaffolds where the desired shape and size often change case by case based on specific patients and defects. Additionally, like PEG, pHEMA is not biodegradable, thus the implant would not be absorbed. Overcoming these disadvantages of cross-linked hydrophilic polymers while maintaining favorable HA interactions could yield bone tissue

engineering scaffolds with improved processing/handling properties and bioactivity.

5. Overview of dissertation content

The overall hypothesis of this dissertation is that clinically translatable and smart bone tissue engineering scaffolds bearing useful handling characteristics and improved bioactivity can be designed through the rational selection and assembly of FDA-approved biocompatible building blocks. Specifically, this dissertation describes the development of bone tissue engineering scaffolds composed of a thermoplastic amphiphilic tri-block copolymer of PLA-PEG-PLA (PELA) and HA. In the HA-PELA composites, hydrophilic PEG blocks bind and disperse the bioactive HA, while the PLA blocks provide biodegradability and aqueous stability without cross-linking. The amphiphilic nature of PELA enables unique handling and surgical delivery characteristics including super-hydrophilicity for loading therapeutics, hydration-induced stiffening, and shape memory. The versatility of the HA-PELA platform has been demonstrated by fabricating the composite into scaffolds by electrospinning and rapid prototyping approaches. The bioactivity of these scaffolds was examined by evaluating the scaffold-bone marrow stromal cell (MSC) interactions *in vitro*, and by guiding the healing of critical-size bone defects in rats.

Chapter II describes the development and *in vitro* characterization of electrospun HA-PELA scaffolds. This chapter tests the hypothesis that the incorporation of a hydrophilic PEG block in PLA will result in a HA-polymer

composite with improved processing properties, handling characteristics and bioactivity than unmodified HA-PLA. Indeed, HA-PELA composites were electrospun with minimal settling of HA, resulting in more uniform scaffolds than HA-PLA. HA-PELA demonstrated improved mechanical properties (storage modulus, hydration-induced modulus increase, elasticity), hydrophilicity, and aqueous stability than HA-PLA. Furthermore, MSCs cultured on the HA-PELA composites exhibited higher levels of osteogenic gene expression than MSCs cultured on HA-PLA.

Chapter III describes the performance of spiral-wrapped electrospun HA-PELA scaffolds in guiding the healing of critical-size femoral segmental defects in rats. We show that MSC-seeded HA-PELA can template bone formation in the defect and that a low-dose of rhBMP-2 results in almost complete bridging of the defects by 12 weeks. Furthermore, we track the survival of transplanted MSCs by labeling them with green fluorescent protein (GFP) and show that they survive up to 7 days *in vivo*, albeit at decreased viability over time. This spiral-wrapped scaffold strategy can be used to study how combinations of exogenous cells and growth factors impact healing and for evaluating the performance of other electrospun bone tissue engineering materials *in vivo*.

Chapter IV describes the rapid prototyping of HA-PELA into macroporous scaffolds using an unmodified consumer-grade 3-D printer. An *in vitro* pull-out test was designed to quantify hydration-induced fixation of the scaffolds in a simulated confined defect. We show that PELA and HA-PELA scaffolds swell and

stiffen upon equilibration in water, resulting in their self-fixation in the simulated defect. This feature could potentially be used for the facile implantation and stabilization of bone tissue engineering scaffolds, reducing the reliance on the use of fixation devices and preventing bone resorption resulting from inadequate graft fixation. To demonstrate the potential utility of this material platform in guided bone regeneration applications, we demonstrate the differential cell attachment on the low-fouling PELA and more cell-adhesive HA-PELA and demonstrated the fabrication of biphasic PELA/HA-PELA scaffolds by rapid-prototyping. The ability of the 3-D HA-PELA scaffolds to support the attachment and osteogenic differentiation of MSCs was also demonstrated.

Shape memory materials could enable the minimally invasive delivery and stable fixation of tissue engineering scaffolds, enabling a complementary delivery strategy to the hydration-induced self-fixation behavior described in Chapter IV. Chapter V describes the thermal responsive shape memory properties of HA-PELA as function of HA content around physiological temperatures. HA incorporation increases the stiffness of PELA films but does not impact shape memory properties below 10 wt.% HA. At 20 wt. % HA, the shape recovery of PELA is slowed but overall shape memory behavior is still maintained. Furthermore, the thermoplastic nature of HA-PELA enables the re-programming of the permanent shape. Finally, we show that the shape memory performance is retained in rapid prototyped macroporous HA-PELA scaffolds.

Chapter VI will discuss conclusions of this thesis, future directions, and the translational potential of this work.

**CHAPTER II: An amphiphilic degradable polymer/hydroxyapatite composite
with enhanced handling characteristics promotes osteogenic gene
expression in bone marrow stromal cells.**

Preface

This chapter has been adapted from:

Kutikov AB, Song J. "An amphiphilic degradable polymer/hydroxyapatite composite with enhanced handling characteristics promotes osteogenic gene expression in bone marrow stromal cells" *Acta Biomaterialia* 2013; 9(9):8354-8364.

The experiments in this work were designed by Dr. Jie Song and Artem Kutikov and performed by Artem Kutikov.

Abstract

Electrospun polymer/HA composites combining biodegradability with osteoconductivity are attractive for skeletal tissue engineering applications. However, most biodegradable polymers such as PLA are hydrophobic and do not blend with adequate interfacial adhesion with HA, compromising the structural homogeneity, mechanical integrity, and biological performance of the composite. To overcome this challenge, we combined a hydrophilic PEG block with PDLLA to improve the adhesion of the degradable polymer with HA. The amphiphilic triblock copolymer PLA-PEG-PLA (PELA) improved the stability of HA suspension at 25 wt.% HA content, which was readily electrospun into HA-PELA composite scaffolds with uniform fiber dimensions. HA-PELA was highly extensible (failure strain >200% vs. <40% for HA-PLA), superhydrophilic ($\sim 0^\circ$ water contact angle vs. $>100^\circ$ for HA-PLA), and exhibited an 8-fold storage modulus increase upon hydration (unlike deterioration for HA-PLA), owing to the favorable interaction between HA and PEG. HA-PELA also better promoted osteochondral lineage commitment of bone marrow stromal cells in unstimulated culture and supported far more potent osteogenic gene induction than HA-PLA. We demonstrate that the chemical incorporation of PEG is an effective strategy to improve the performance of degradable polymer/HA composites for bone tissue engineering applications.

1. Introduction

Synthetic polymeric, ceramic, or polymer-ceramic composite scaffolds, when engineered with proper physical, chemical, and biomechanical cues, can play an important role in directing cellular fate / functions in scaffold-assisted regeneration of bone, cartilage, tendon, or their respective interfaces.[156–160] An ideal scaffold would recapitulate some key structural and biological properties of the extracellular matrices of the tissues of interest while exhibiting unique features important for its clinical translation such as scalability and ease of use.[25,26,82,161] Achieving this delicate balance requires thoughtful selection and integration of biomaterial building blocks, which remains a fundamental challenge in the design of synthetic tissue scaffolds.

Bone is a structural composite mainly of type-I collagen and calcium phosphate minerals (50-70% dry weight), of which nanocrystalline HA is the main component, that is hierarchically organized from nanoscopic to macroscopic length scales.[119,162] HA is an osteoconductive bioceramic that has been shown to support bone cell attachment, growth factor binding and release, and expedite healing of bone defects *in vivo*. [130,133,135] Due to its high stiffness and brittleness, however, HA alone is not well suited for broad orthopedic applications beyond use as a non-weight-bearing bone void filler. Consequently, HA has been incorporated with synthetic polymers as 2-D or 3-D dense or porous composite scaffolds using a wide range of fabrication techniques including, but not limited to, electrospinning, phase separation, injection molding,

and 3-D prototyping.[140,163–166] The integration of these discrete structural components can be accomplished by either direct mixing/blending or by subjecting the polymer scaffolds to HA-mineralization,[167,168] where interfacial adhesion/affinity between HA and the polymeric component is the key to achieving structural and mechanical integrity of the final composite.[138,141] In the case of fabricating HA-polymer composite scaffolds by electrospinning - a process that uses electrical charge to form non-woven fibrous meshes with fiber dimensions in the nano to micro scale[72,78,87] - additional considerations for the stability and electrospinnability of the polymer-HA solution also need to be taken into account.

PLA is one of the most widely used biodegradable polymers in synthetic tissue scaffolds. It is readily electrospinnable, and its *in vitro* and *in vivo* degradation profiles are well established. The intrinsic hydrophobicity of PLA, however, results in its poor mixing and adhesion with hydrophilic HA[169], making it difficult to electrospin HA-PLA composites with uniform fiber structures and adequate mechanical properties.[138,147,148,170] HA-PLA composites often exhibit inferior handling properties (e.g. brittleness) and inconsistent biological performance. For instance, the addition of even low contents of HA (~ 6 wt.%) results in the deterioration of the tensile modulus and impact strength of poly(L-lactic acid) (PLLA) films.[171] Scanning electron microscopy (SEM) examination of composite membranes following tensile loading reveals failure at the polymer-ceramic interface.[141] The addition of HA to PLA has led to minor

improvements in cell adhesion and proliferation.[142,144,171] The effects of HA-PLA composites on stem cell differentiation reported in the literature have been mixed, with some researchers concluding that HA promotes osteogenesis[131] or chondrogenesis[172], and others observing little impact of HA addition on differentiation.[173] We hypothesized that strengthening the interfacial adhesion between HA and PLA-based polymers could produce composite materials with greater consistency in structural, mechanical and biological performance.

Previous attempts to strengthen the interfacial adhesion between HA and PLA include the addition of amphiphilic surfactants, or modifying HA with surface-grafted polymers to improve interactions with the hydrophobic polyesters.[131,144,147,171,174,175] Such approaches, however, often introduce additives with ill-defined biological consequences. An alternative approach is to chemical integration of non-anionic structural motifs exhibiting adequate bonding affinity to HA (into the degradable polymer). Our group and others have demonstrated favorable blending of HA with hydrophilic polymers such as pHEMA and PEG.[130,151,153] In these hydrophilic composites, HA reinforces the mechanical properties of the polymers. A freeze-dried pHEMA-HA composite containing 50% HA withstood >80% compressive strains and 450 MPa loads without exhibiting brittle fractures,[153] while PEG-HA composites containing 15% HA withstand strains of ~2000% without breaking.[130] These remarkable mechanical properties are a result of strong interfacial adhesion between HA and the hydrophilic polymers.[151] In addition, the osteoconductivity

of HA has endowed the otherwise bioinert pHEMA hydrogel with the ability to enrich endogenous bioactive factors *in vivo*, promoting the healing of critical-size femoral defects in rats.[135] Unfortunately, hydrophilic pHEMA and PEG themselves lack biodegradability and are not stable in aqueous environments without chemical crosslinking, making underivatized pHEMA or PEG unsuitable for fabricating degradable HA-polymer composites by electrospinning.

Here we report the design and characterization of an electrospun, biodegradable amphiphilic polymer/hydroxyapatite composite based on tri-block copolymer PDLLA-PEG-PDLLA (PELA). Although PELAs of different molecular weights or block compositions (e.g. diblock or triblock copolymer) have been previously developed, they were intended for drug delivery applications,[176–178] modulating the physical properties of PLA blends,[179,180] or reducing non-specific protein adsorption on PLA-based tissue scaffolds.[62] The rational design of PELA to improve the interfacial binding with HA and optimize the physical and biological performance of degradable polymer-HA composite scaffolds for bone tissue engineering applications has not been previously explored. This design combines the degradability and aqueous stability of the PLA block with the HA-binding capability of the PEG block and the electrospinnability of both. We hypothesized that the addition of a hydrophilic PEG block to PLA could facilitate HA binding to the polymer, resulting in improved handling characteristics and more consistent biological activity. We tested this hypothesis by comparing the impact of HA incorporation on the performance of

electrospun PELA and PLA with similar molecular weights and polydispersity. We examined their structural integration (fiber morphology, HA distribution), surface properties (water contact angle), tensile elasticity and storage modulus, *in vitro* degradation, and impact on the attachment, proliferation, lineage commitment and differentiation of bone marrow stromal cells.

2. Materials and Methods

2.1. Materials

3,6-Dimethyl-1,4-dioxane-2,5-dione (D,L-lactide) was purchased from Sigma-Aldrich (St. Louis, MO) and purified by recrystallization twice in anhydrous toluene and dried under vacuum prior to use. PEG (BioUltra, 20,000 Dalton) was purchased from Fluka (Switzerland). Polycrystalline HA powder was purchased from Alfa Aesar (Ward Hill, MA). All other solvents and reagents were purchased from Sigma-Aldrich (St. Louis, MO) and used as received.

2.2. Polymer synthesis and characterization

PELA tri-block copolymer was synthesized by melt ring-opening polymerization. Briefly, PEG (20,000 Dalton, 4 g, 0.2 mmol) was heated to 100 °C in a Schlenk flask and stirred under vacuum for 1 h to remove residual water. The melt was cooled to room temperature before Sn(II) 2-ethylhexanoate (~95%, 24.18 mg, 0.06 mmol) in anhydrous toluene was introduced by syringe. The toluene was removed by heating the mixture under vacuum at 100 °C for 15 min. The mixture was cooled to room temperature before D,L-lactide (17.295 g, 0.12

mol) was added under argon purge. The melt polymerization proceeded at 130 °C for 5 h under argon. PLA was synthesized in the same manner with anhydrous ethylene glycol (99.8%, 0.87mg, 0.1407 mol) as the initiator. Briefly, D,L-lactide (15 g, 0.1038 mol) was added to the ethylene glycol in a Schlenk flask and heated to 130 °C. Sn(II) 2-ethylhexanoate (21 mg, 0.05 mmol) was introduced by syringe and the melt polymerization proceeded for 5 h. The crude PELA and PLA were dissolved in chloroform, purified by precipitation in methanol, and dried under vacuum.

The molecular weights and polydispersity of PELA and PLA were determined by gel-permeation chromatography on a Varian Prostar HPLC system equipped with two 5-mm PLGel MiniMIX-D columns (Agilent, Santa Clara, CA) and a PL-ELS2100 evaporative light scattering detector (Polymer Laboratories, UK). Tetrahydrofuran was used as an eluent at 0.3 mL h⁻¹ at room temperature. Molecular weight and polydispersity calculations were calibrated with EasiVial polystyrene standards (Agilent, Santa Clara, CA).

¹H NMR spectra were recorded on a Varian Mercury 400 MHz spectrometer at 298K using CDCl₃ containing tetramethylsilane as the solvent. ¹H NMR (400 MHz, CDCl₃) for PELA: δ 5.19 (m, 1126H), 3.65 (m, 1816H), 1.5 (m, 3921H) ppm.

2.3. Electrospinning

HA-PELA and HA-PLA composite scaffolds with 0 and 25 wt.% HA were prepared by electrospinning. HA powder was sonicated in 5 mL 1:4 (v/v)

dimethylformamide/chloroform for 30 min to break up aggregates before PELA or PLA (1.25g, 25% w/v) was added. The mixture was stirred overnight at room temperature and loaded into a 5 mL syringe. A high-voltage power supply (Gamma High Voltage Research, Ormond Beach, FL) delivered a voltage of 12 kV between a 22G ejection needle and an aluminum collection plate set 15 cm away. The polymer solution was fed through the needle at rate of 1.7 mL h^{-1} with a syringe pump (Orion Sage M361, Thermo Scientific, Billerica, MA), and the fibers were collected on the aluminum collector plate. The electrospinning proceeded for 2 h, with the collecting plate rotated by 90° every 15 min to ensure the homogeneity of the fibrous scaffold. The scaffolds (0.1 - 0.2 mm final thickness) were dried in a vacuum oven for 48 h to remove any residual solvent and stored in a desiccator prior to use.

2.4. Differential scanning calorimetry (DSC)

Thermal transitions of PELA and PLA were determined by conventional DSC and modulated DSC (MDSC) on a Q200 MDSC (TA Instruments, New Castle, DE). For DSC experiments, specimens ($\sim 6 \text{ mg}$) were scanned twice from $-90 \text{ }^\circ\text{C}$ to $150 \text{ }^\circ\text{C}$ ($20 \text{ }^\circ\text{C min}^{-1}$). A constant nitrogen flow of 50 mL min^{-1} was applied. Temperature was calibrated with indium, gallium, and tin standards. T_g was defined as the midpoint of the inflection tangent from the second heating curve. MDSC was used to further analyze endothermic transitions in electrospun PELA. Samples (3.6 mg) were held isothermal at $-40 \text{ }^\circ\text{C}$ for 15 min and then

heated at $2\text{ }^{\circ}\text{C min}^{-1}$ to $110\text{ }^{\circ}\text{C}$ with a 60 s temperature modulation period and an amplitude of $0.318\text{ }^{\circ}\text{C}$, as described elsewhere.[181]

2.5. Scanning electron microscopy (SEM)

As-spun and vacuum-dried scaffolds were sputter coated with Au ($\sim 4\text{ nm}$ thick) and imaged on a Quanta 200 FEG MKII SEM (FEI Inc., Hillsboro, OR) under high vacuum at 5 kV. Fiber diameter was quantified from the SEM micrographs by measuring 100 random fibers, from micrographs of five different areas, with ImageJ software (National Institutes of Health).

2.6. Thermogravimetric analysis (TGA)

TGA was used to determine the actual percentage of HA in the as-spun and vacuum-dried scaffolds. The samples were heated at a rate of $20\text{ }^{\circ}\text{C min}^{-1}$ from room temperature to $500\text{ }^{\circ}\text{C}$ and the mass changes were recorded on a TGA Q50 (TA Instruments, New Castle, DE). HA powder was used as a control.

2.7. Ultimate tensile strain and ultimate tensile stress

HA-PELA and HA-PLA scaffolds were strained to failure in order to evaluate the effect of PEG on the extensibility and strength of the HA composites. Tensile tests were carried out according to ASTM D882-97. Scaffolds (13 mm wide, 75 mm long and 0.1-0.14 mm thick) were ramped to failure on a MTS Bionix 370 testing system equipped with a 500 N load cell. A 25 mm initial grip separation and 250 mm min^{-1} grip separation rate were applied.

Ultimate tensile strain and stress were recorded at the peak of the stress-strain curve.

2.8. Water contact angle measurements

The wettability of the scaffolds was examined by the sessile drop technique. Droplets of deionized water (5 μL) were deposited onto as-spun and vacuum-dried scaffolds or scaffolds freeze-dried following 24 h equilibration in 37 $^{\circ}\text{C}$ deionized water. The water contact angle was recorded using a CAM 200 goniometer (KSV Instruments, Finland). The droplet was imaged at 30 s and the average contact angle from the left and right side of the drop was recorded. Five randomly selected areas per scaffold were used for each water contact angle measurement.

2.9. Dynamic mechanical analysis (DMA)

The tensile storage moduli of dry and hydrated (deionized water) scaffolds ($n=3$) were determined on a Q800 DMA (TA Instruments, New Castle, DE). Specimens (5.3 \times 20 mm) were cut with a parallel blade cutter and loaded onto a film tension fixture with a grip separation of 10 mm. Dry and hydrated samples were preloaded with a 0.001 N and 0.05 N force, respectively. Samples were equilibrated at 37 $^{\circ}\text{C}$ and held isothermally for 10 min prior to initiating 0.02% strain at a frequency 1 Hz and the tensile storage moduli were recorded. The 0.02% strain chosen falls within the linear viscoelastic region of the scaffolds.

2.10. In vitro hydrolytic degradation

In vitro hydrolytic degradation of PELA, HA-PELA and HA-PLA was determined by monitoring the mass loss of the scaffolds upon incubation in $\text{Ca}^{2+}/\text{Mg}^{2+}$ -free phosphate-buffered saline (PBS) (pH 7.4) at 37 °C. As-spun scaffolds were cut into 20 mm × 20 mm squares (n=3 for each time point), weighed on an analytical balance (XS105, Mettler Toledo, Columbus, OH), and placed in conical tubes containing 20 mL of PBS, and incubated at 37 °C for up to 12 weeks. At each time point, three specimens were removed, washed three times with deionized water, and lyophilized. The mass of each retrieved and dried specimen was recorded.

2.11. Rat bone marrow stromal cells (rMSCs) isolation

The rMSCs were isolated from the long bones of a 4 week old male Charles River SASCO SD rat according to the procedure approved by the University of Massachusetts Medical School Institutional Animal Care and Use Committee and described previously.[153] Briefly, whole bone marrow was flushed from the marrow canal of a dearticulated rat femur with minimal essential medium (α MEM without ascorbic acid, Life Technologies, Grand Island, NY). After lysing red blood cells with sterile water, the cells were centrifuged, resuspended in α MEM (without ascorbic acid) containing 20% FBS, 1% penicillin-streptomycin, and 2% L-glutamine, passed through a sterile strainer, and cultured in the same medium. Non-adherent cells were aspirated 4 days

after initial plating and the remaining adherent cells were cultured to 70% confluence before being trypsinized and seeded onto various scaffolds.

2.12. Attachment and proliferation of rMSCs on scaffolds

MTT cell viability assay (Roche, Indianapolis, IN) was performed to quantify cell attachment and early proliferation on the electrospun scaffolds. Scaffolds (n=3 per time point) were cut into 6.35 mm diameter circles using a hole punch, sterilized under UV for 1 h each side, and equilibrated in MSC expansion medium (α MEM without ascorbic acid, 20% FBS, 2% L-Glutamine, 1% penicillin-streptomycin) at 37 °C overnight. Passage 1 rMSCs ($15,625 \text{ cells cm}^{-2}$) were seeded on the scaffolds placed in ultra-low-attachment 96-well plates (Corning Inc., Corning, NY) and cultured in expansion medium for 24 or 96 h. The MTT assay was performed according to manufacturer's instructions. Absorbance of the MTT product was read on a Multiskan FC microplate photometer (Thermo Scientific, Billerica, MA) at 570 nm with a 690 nm background correction.

2.13. Spontaneous lineage commitment of rMSCs on scaffolds

rMSCs were cultured on the scaffolds in expansion medium to determine the effect of scaffold composition on their un-stimulated lineage commitment. Scaffolds were sterilized under UV for 1 h each side and equilibrated in MSC expansion medium at 37 °C overnight. The scaffolds were placed in ultra-low-attachment 24-well plates (Corning Inc., Corning, NY) and seeded with passage

1 rMSCs ($50,000 \text{ cells cm}^{-2}$). Following 7 and 14 days in culture, total RNA from the MSCs adhered on the scaffolds and those from rMSCs prior to seeding on scaffolds (time 0 control) was isolated using TRIzol (Invitrogen, Carlsbad, CA) and purified by Direct-Zol miniprep (Zymo Research, Irvine, CA). RNA was reverse transcribed into cDNA with SuperScript III Reverse Transcriptase (Invitrogen, Carlsbad, CA) according to manufacturer's instructions on a GeneAmp 2700 PCR system (Applied Biosystems, Foster City, CA). Quantitative polymerase chain reaction (qPCR) was performed on an Applied Biosystems 7500 fast real-time PCR system with TaqMan Gene Expression Master Mix (Applied Biosystems, Foster City, CA) and inventoried TaqMan probes for SOX9, osteocalcin, PPARG and housekeeping gene GAPDH. All reactions were performed in triplicate and gene expression was quantified using the delta-delta Ct method. Expression of each gene of interest at each time point was normalized using GAPDH and plotted as expression relative to that of rMSCs at time 0.

2.14. Osteogenic differentiation of rMSCs on scaffolds

PELA, HA-PELA and HA-PLA scaffolds were sterilized and seeded with Passage 1 rMSCs ($50,000 \text{ cells cm}^{-2}$) as described above. The rMSCs were allowed to attach to the scaffolds for 24 h before the medium was replaced with osteogenic medium (MSC expansion medium supplemented with 10 nM dexamethasone, 20 mM β -glycerol phosphate, 50 μ M L-ascorbic acid 2-phosphate). The scaffolds were cultured in the osteogenic medium for 14 days

with medium changes every 3-4 days. Total RNA was isolated, purified, and reverse transcribed to cDNA as described above. qPCR was performed with TaqMan Gene Expression Master Mix (Applied Biosystems, Foster City, CA) and inventoried TaqMan probes for Runx2, osteopontin, osteocalcin, and housekeeping gene glyceraldehyde-3-phosphate dehydrogenase (GAPDH) (Applied Biosystems, Foster City, CA). All reactions were performed in triplicate and gene expression was quantified using the delta-delta Ct method. Expression of each gene of interest at each time point was normalized using GAPDH and plotted as expression relative to that of undifferentiated rMSCs at time 0.

2.15 Statistical analysis

All data are presented as mean \pm standard deviation. Statistical significance was determined by one-way ANOVA with Tukey post-hoc testing. Differences were considered significant when $p < 0.05$.

3. Results

3.1 Synthesis of PELA and PLA

PELA and PLA control were synthesized with similar molecular weights (116,298 and 126,139 Dalton, respectively) and polydispersity ($PDI = 1.44$) by melt ring-opening polymerization of cyclic D,L-lactide, using PEG and ethylene glycol as initiators, respectively, under the catalysis of Sn(II) 2-ethylhexanoate (Figure 2.1). DSC analyses revealed glass transitions at 17.73 and 44.77 °C for PELA and PLA, respectively.

Figure 2.1. Synthetic schemes for PELA (1) and PLA (2). $x= 454$, $n= 608$, $m= 750$.

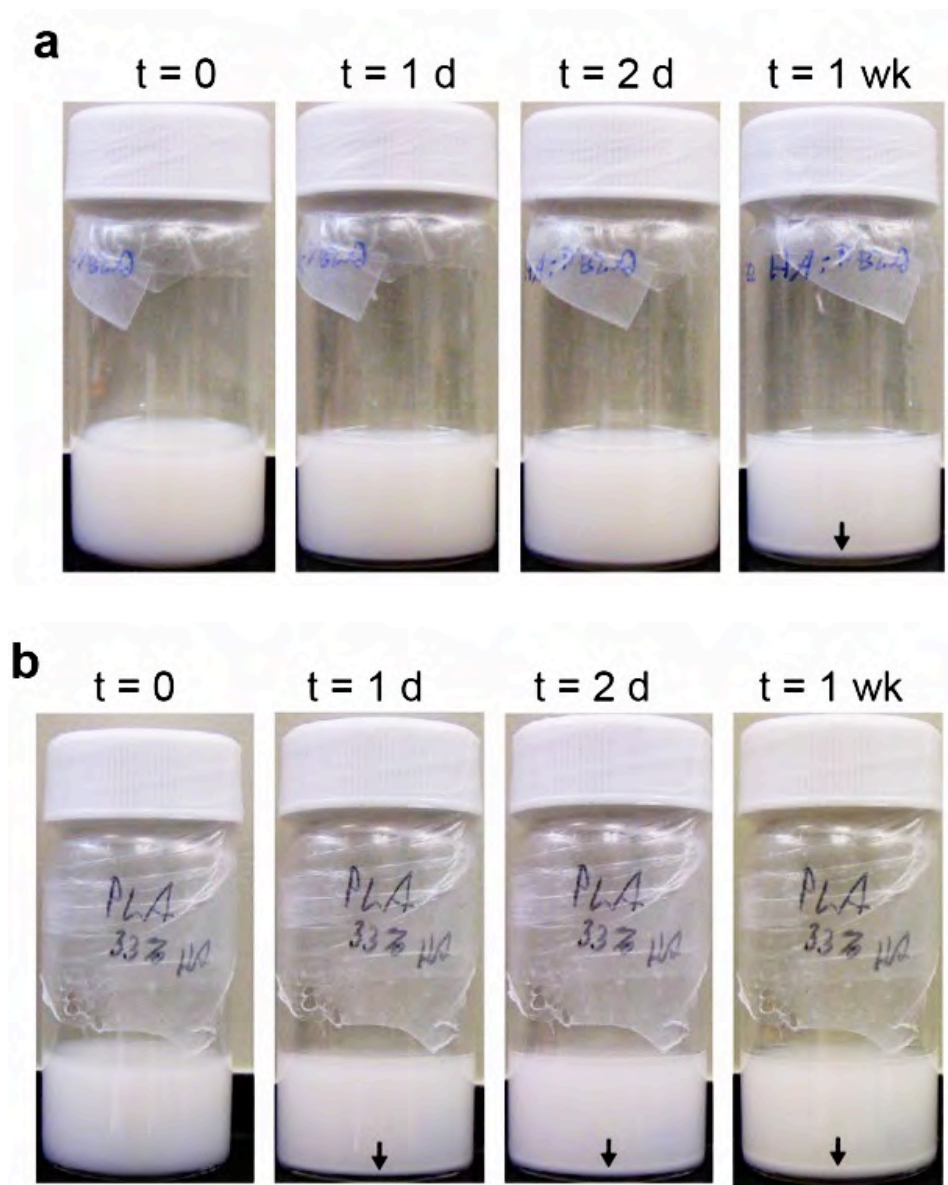
3.2 Electrospinning HA-PELA and HA-PLA composites

The improved bonding affinity of HA with the amphiphilic PELA over PLA was manifested by the significantly more stable HA-PELA suspension in 1:4 (v/v) dimethylformamide/chloroform. No obvious settling of HA from the HA-PELA suspension (at HA content as high as 33 wt.% relative to polymer weight) was detected upon storage at ambient conditions for days whereas the HA settled from the HA-PLA suspension by 24 h (Fig. 2.2). The HA-PELA suspension could be readily electrospun without noticeable blockage of the needle tip by aggregated HA as was often observed during the electrospinning of HA-PLA. HA-PELA and HA-PLA composite scaffolds (average thickness of 0.1 - 0.2 mm) with 0 and 25 wt.% HA were obtained after 2 h electrospinning and dried in a vacuum oven.

Figure 2.2. Stability of HA suspension in PELA vs. PLA after 1 week.

(A) HA (33 wt.%) in a 1:4 dimethylformamide/chloroform solution of PELA (25% w/v). (B) HA (33 wt.%) in a 1:4 dimethylformamide/chloroform solution of PLA (25% w/v). Visible settling/aggregation of HA to the bottom of the HA-PLA suspension was observed as early as day 1 (arrows) while the HA remained well-dispersed in HA-PELA suspension for days.

Figure 2.2



3.3 Microstructural and compositional analyses of electrospun HA-PELA vs. HA-PLA composites

SEM and subsequent image analysis was used to quantify the fiber uniformity of the electrospun scaffolds. While the mean diameter of the HA-PLA fibers more than doubled over that of PLA, there was no significant increase in fiber diameter of HA-PELA over that of PELA (Fig. 2.3a and b). The HA-PELA composites also exhibited a narrower distribution of fiber dimensions and fewer defects than HA-PLA.

TGA of the electrospun PELA revealed a transition at approximately 83% weight loss, which closely correlated with the weight percentage of PLA in the PELA scaffolds (Fig. 2.3c). The PLA blocks, with a lower decomposition temperature (onset ~ 297 °C) than PEG (onset ~ 340 °C), were decomposed first. This stepwise decomposition feature, however, was not observed in the HA-PELA composite, suggesting an insulating effect of HA incorporation. The HA that remained after complete PELA thermal decomposition (>400 °C) matched precisely with the weight percentage of HA in the electrospinning solution (25%). By contrast, the actual HA content in the electrospun HA-PLA composite as determined by TGA was 28.4%, $>3\%$ higher than that of the HA-PLA suspension prior to electrospinning. Homogeneous HA distribution within the HA-PELA fibrous matrix was further confirmed by von Kossa staining for calcium[182] where intense positive von Kossa stain was detected uniformly within all fibers (Fig. 2.4).

Figure 2.3. Microstructural and compositional properties of electrospun HA-PELA and HA-PLA composite scaffolds. a) SEM micrographs of electrospun scaffolds. Scale bars = 50 μm . b) Fiber diameters (n=100, mean \pm standard deviation) of electrospun scaffolds as determined from SEM micrographs using ImageJ. * $p < 0.05$ (One-way ANOVA with Tukey post-hoc). c) TGA plots of electrospun scaffolds and HA powder control.

Figure 2.3

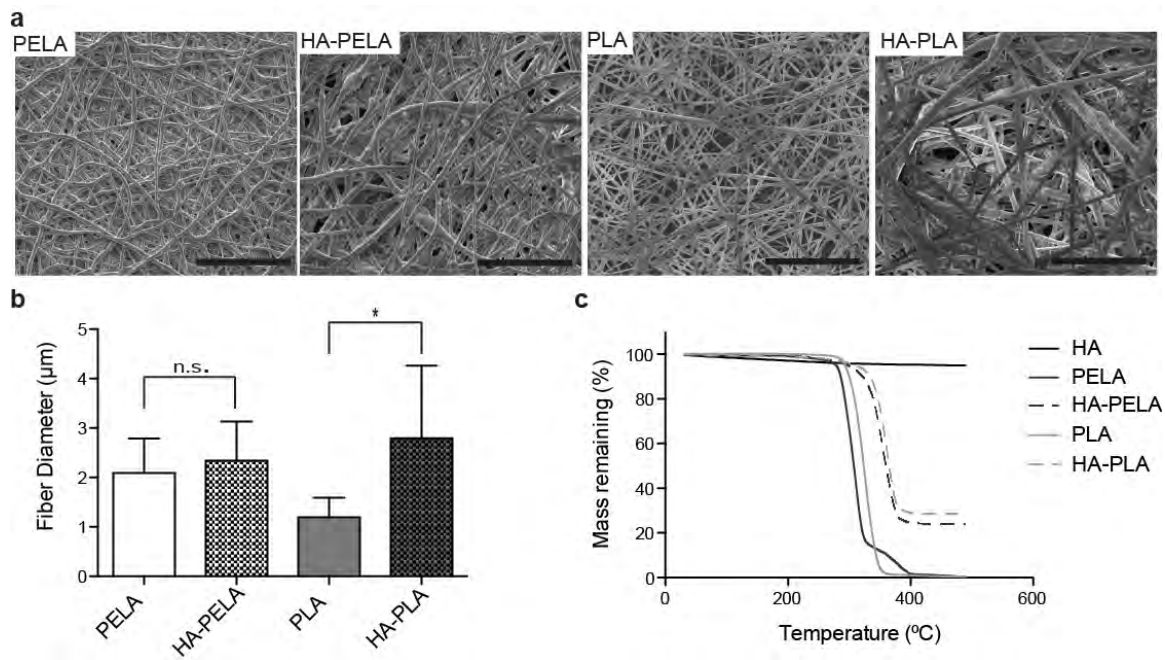
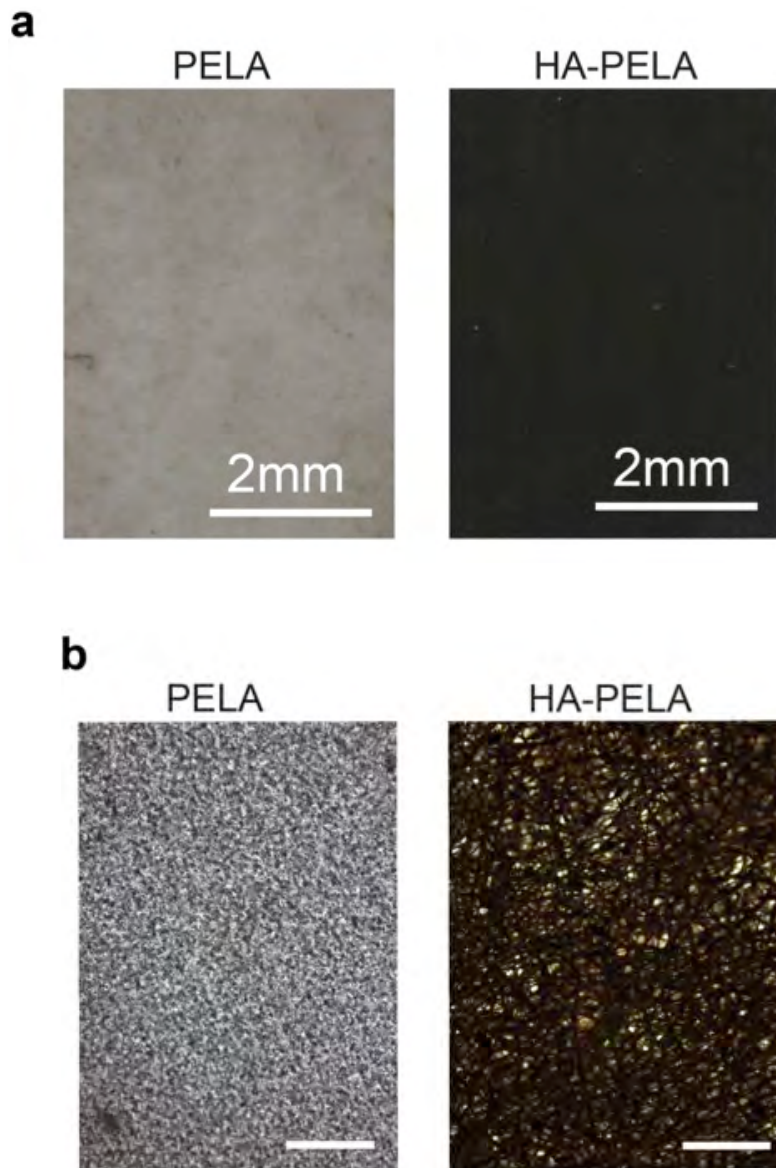


Figure 2.4. von Kossa-stained electrospun HA-PELA composites. Photographs (a) and bright-field microscopy images (b; 10× objective, scale bar: 100 μm).

Figure 2.4

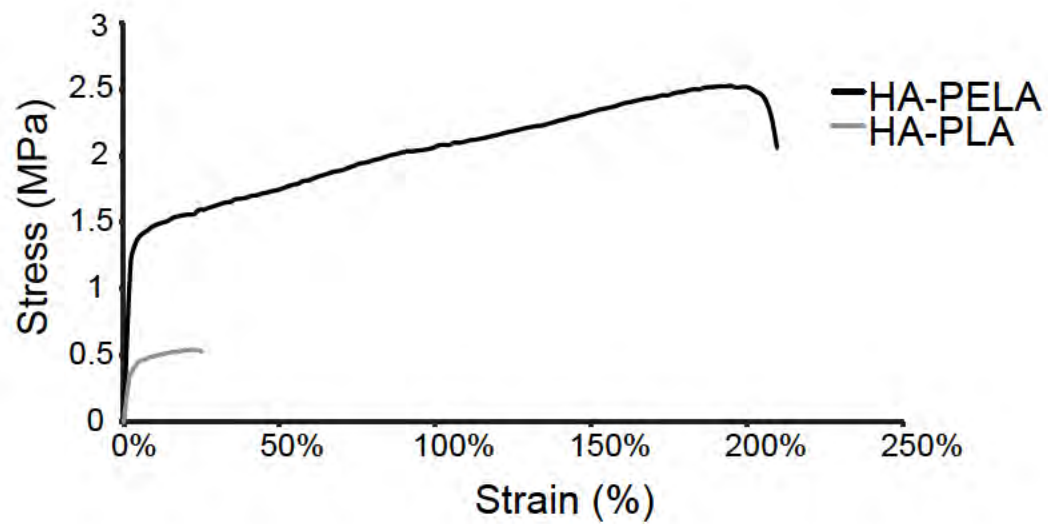


3.4 Tensile compliance of electrospun HA-PELA vs. HA-PLA composites

Tensile testing was performed to assess the extensibility and in turn the interfacial HA-polymer adhesion in the electrospun scaffolds. Electrospun HA-PELA was highly extensible, achieving ultimate tensile strains of over 200% (Fig. 2.5). By contrast, the HA-PLA was characterized with failure strains below 40%. HA-PELA also exhibited a failure stress of 2.5 MPa, 5-fold that of the HA-PLA.

Figure 2.5. Tensile stress-strain curves of HA-PELA and HA-PLA composites.

Figure 2.5

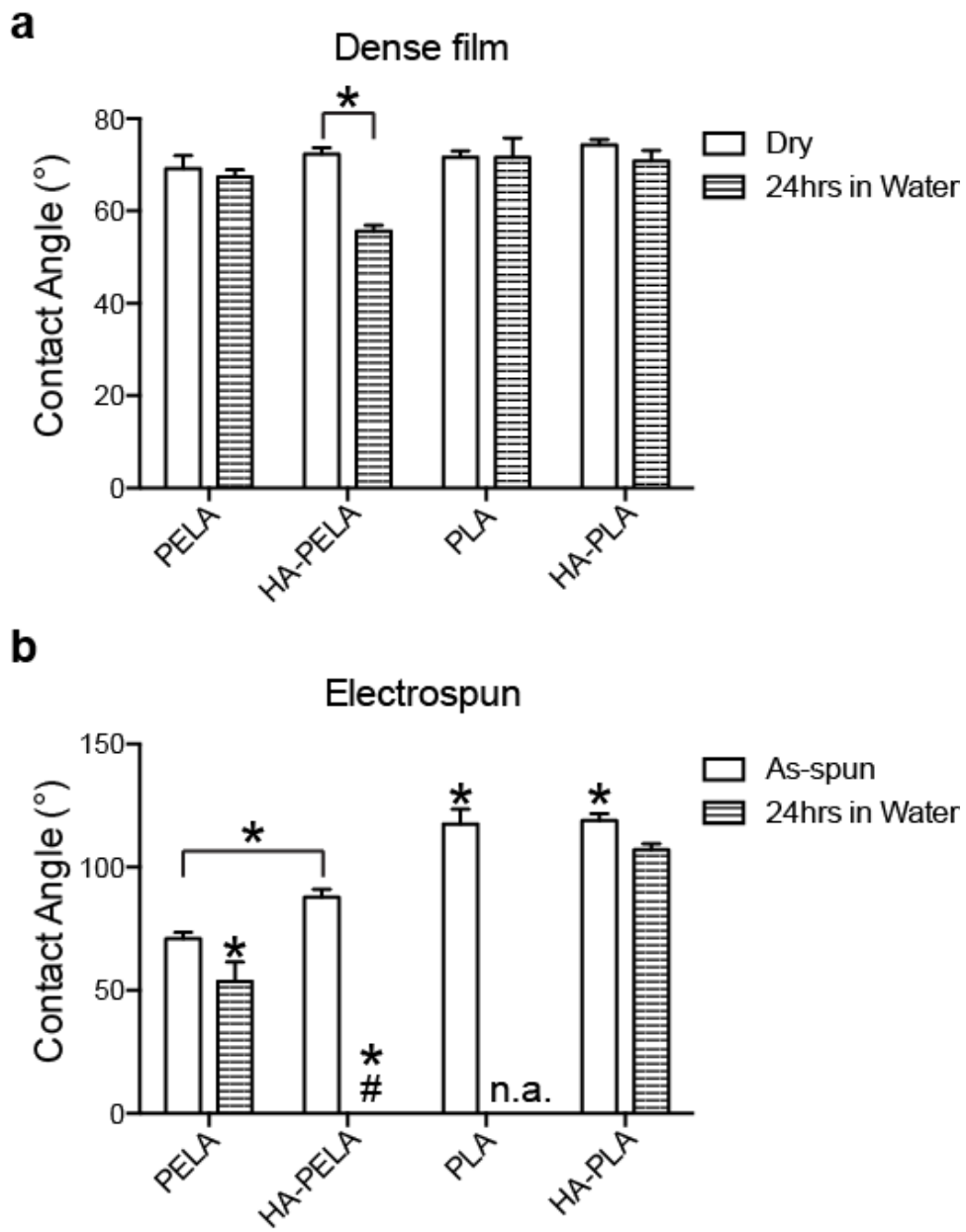


3.5 Hydration-dependent surface properties of HA-PELA vs. HA-PLA composites

The hydrophilic PEG block in PELA significantly reduced the water contact angle (increased the wettability) of the scaffolds when compared to PLA. The contact angle of HA-PELA dense films decreased by 17° following hydration (Fig. 2.6a). For electrospun scaffolds, HA incorporation slightly increased the water contact angle of the PELA but exerted no significant effect on the wettability of PLA (Fig. 2.6b). To capture the polymer chain arrangements at the fully hydrated state, scaffolds were equilibrated in water at 37°C for 24 h, and then freeze-dried before performing water contact angle measurements. The prior hydration significantly reduced the water contact angle of PELA from 71° to 54° and that of HA-PELA from $>85^{\circ}$ to 0° , revealing superhydrophilicity of the latter upon water equilibration. By contrast, water equilibration only reduced the contact angle on the HA-PLA scaffolds by 11° (Fig. 2.6b).

Figure 2.6. Hydration-dependent surface property changes of HA-PELA and HA-PLA. (a) Water contact angle of dry and lyophilized films following water equilibration (n=5). (b) Water contact angle of as-spun and lyophilized electrospun scaffolds following water equilibration (n=5). #, water fully absorbed ($\sim 0^\circ$). n.a., no contact angle obtained due to scaffold shrinkage. * $p < 0.05$ (One-way ANOVA with Tukey post-hoc).

Figure 2.6

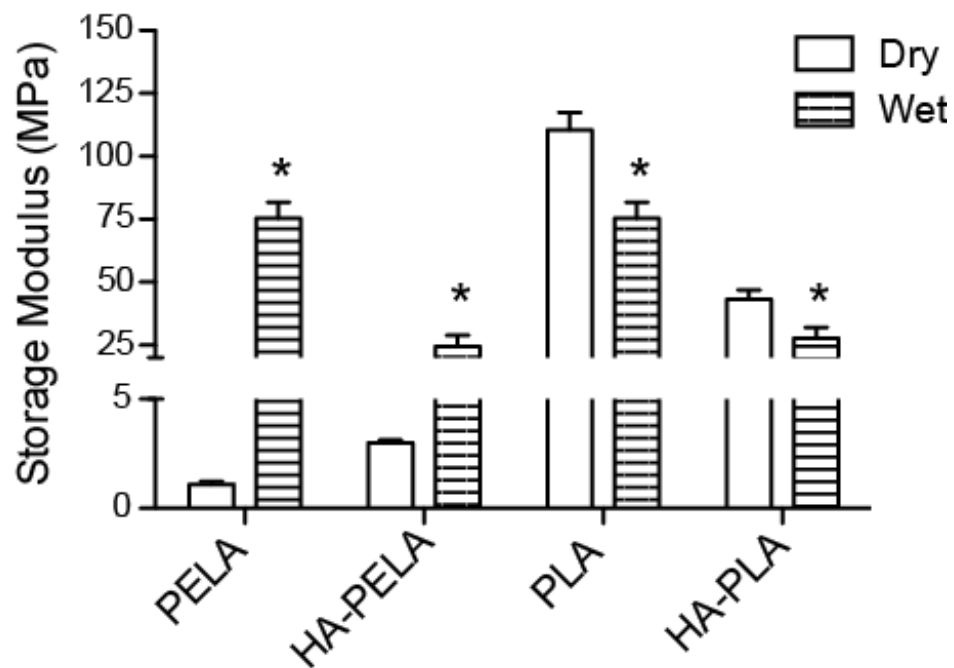


3.6 Hydration dependent mechanical properties of HA-PELA vs. HA-PLA

The differences in surface properties between HA-PELA and HA-PLA upon hydration were also accompanied by drastic mechanical property alterations. Dynamic mechanical testing was used to assess the tensile storage modulus of both dry and hydrated samples at 37 °C (Fig. 2.7). The storage modulus of the dry PELA increased from 1.1 MPa to 2.99 MPa with the incorporation of HA. By contrast, addition of HA significantly deteriorated the tensile storage modulus of dry PLA scaffolds from 110 MPa to 43 MPa. Strikingly, the amphiphilic PELA and HA-PELA scaffolds exhibited 75-fold and 8-fold increases in storage modulus upon hydration, respectively. As expected, hydration of PLA and HA-PLA resulted in significant storage modulus reductions.

Figure 2.7. Mechanical property changes of electrospun PELA and PLA composite scaffolds upon hydration. Storage modulus (n=3) of dry and hydrated scaffolds at 37 °C determined by dynamic tensile mechanical analysis (0.02% strain, 1 Hz). * p<0.05 (One-way ANOVA with Tukey post-hoc).

Figure 2.7

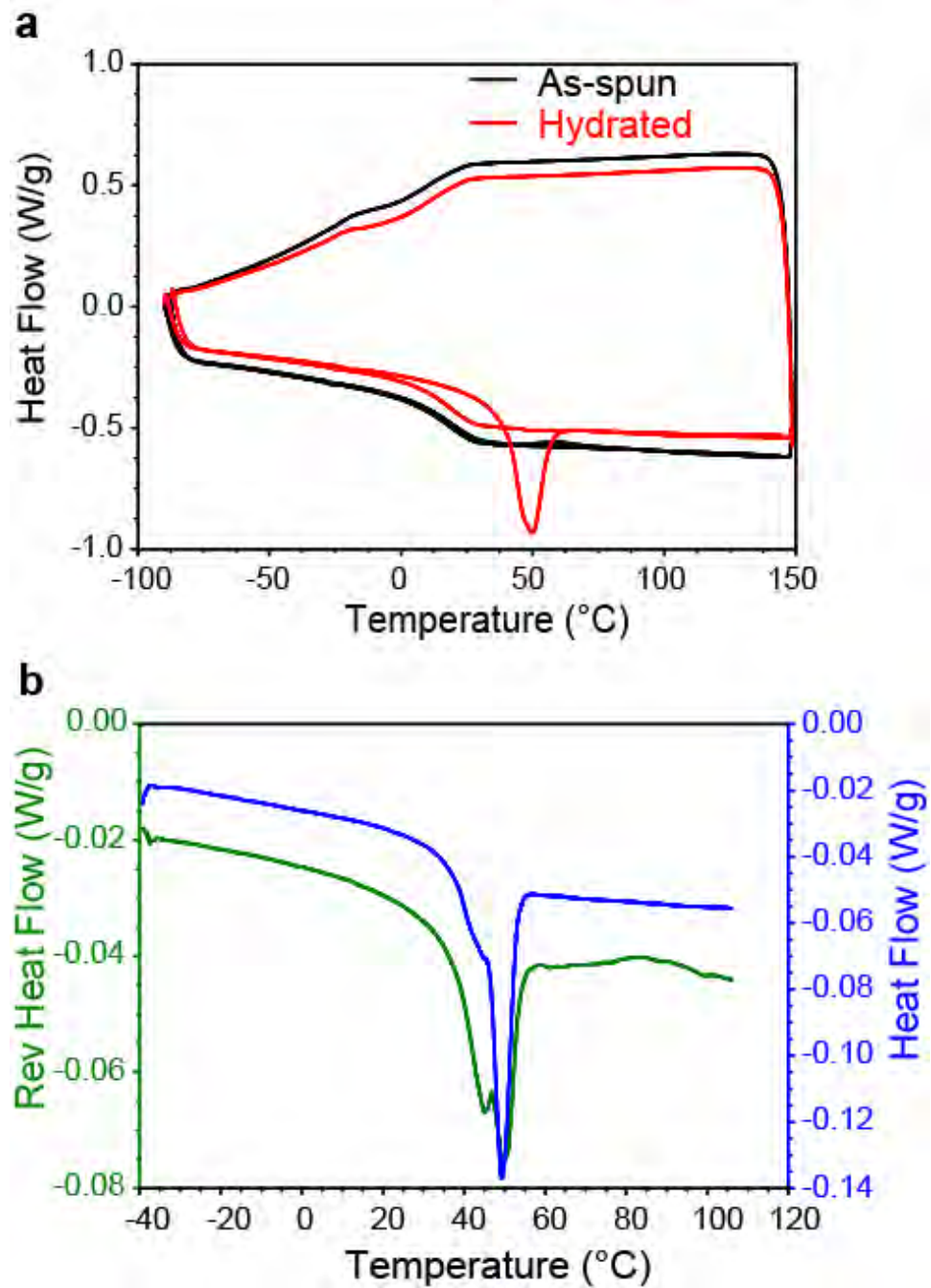


3.7 DSC and MDSC analysis of the hydration dependent rearrangement in PELA

Conventional and modulated DSC was carried out on scaffolds with and without prior hydration history to assess possible hydration-induced thermal behavior changes and the underlying structural rearrangements. Conventional DSC revealed an endothermic peak around 50 °C only with previously hydrated PELA specimens (Fig. 2.8a). To assess the nature of this transition, whether a reversible crystalline melting or an irreversible transition such as polymer aging, MDSC was carried out. MDSC confirmed that this sharp transition was present in the reversible heat flow, consistent with a typical crystalline melting peak (Fig. 2.8b).

Figure 2.8. Crystallization behavior of PELA scaffolds upon hydration. (a) DSC curves of electrospun PELA scaffolds with or without hydration history. Hydrated PELA samples were equilibrated in deionized water @ 37 °C for 24 h and lyophilized. (b) MDSC curves of lyophilized electrospun PELA after water equilibration depicting reversible heat flow (green) and total heat flow (blue).

Figure 2.8



3.8 In vitro hydrolytic degradation of HA-PELA and HA-PLA composites

The *in vitro* hydrolytic degradation behavior of the HA-PELA and HA-PLA scaffolds (n=3) was examined by monitoring mass loss upon incubation in PBS at 37 °C over a period of 12 weeks. ¹H NMR analysis showed a strong PEG peak in the PELA degradation solution (Fig. 2.9). The PELA and HA-PELA scaffolds lost ~20% of their mass over 12 weeks, whereas HA-PLA only lost ~3% of its mass during the same period (Fig. 2.10a). SEM monitoring of structural changes of the incubated scaffolds revealed the least change in HA-PELA fiber morphology by 3 weeks, while PELA fibers fused at their contact points and HA-PLA fibers aggregated together (Fig. 2.10b). The addition of HA effectively reduced the degree of fusing of the PELA fibers.

Figure 2.9. ^1H NMR (CDCl_3) of PELA and PELA degradation products.

In order to obtain NMR spectra of the PELA degradation products, electrospun PELA was incubated in PBS at 37 °C. Following 12 weeks of incubation, the PBS degradation solution was lyophilized, degradation products were dissolved in CDCl_3 , and salts were filtered out with a .2 μm PTFE filter. The NMR spectrum of the degradation products indicates a PEG peak. Lactic acid is not readily apparent by NMR, likely due to the poor solubility of lactic acid in CDCl_3 .

Figure 2.9

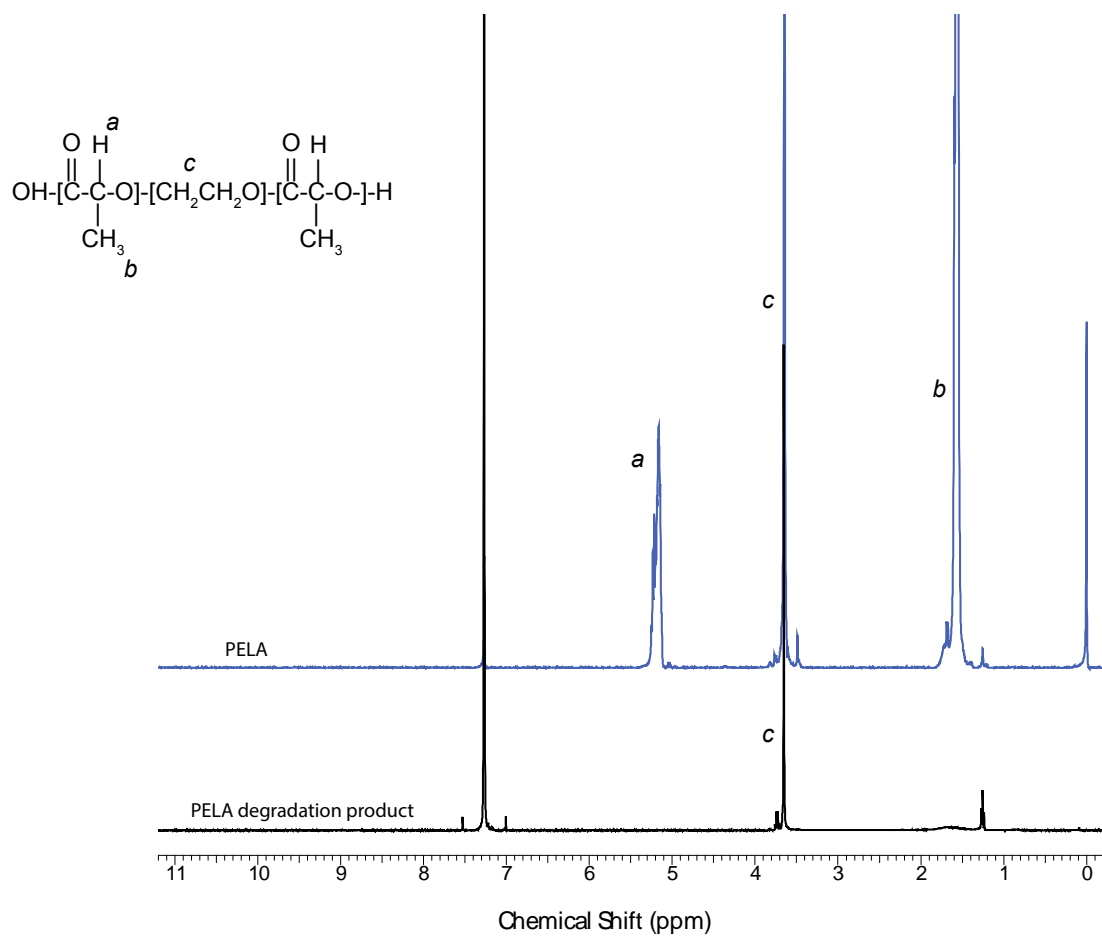
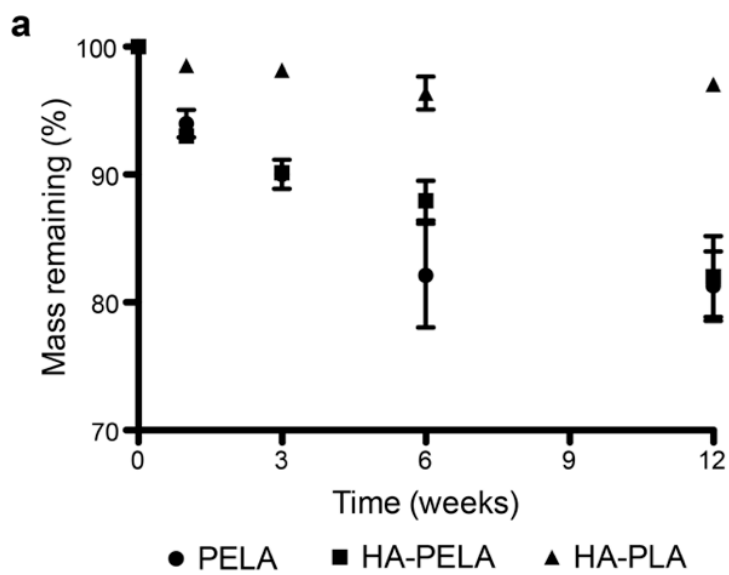
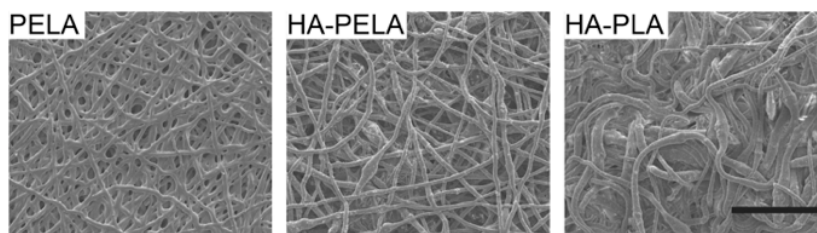


Figure 2.10. Hydrolytic degradation of HA-PELA and HA-PLA scaffolds in PBS. (a) Mass loss over 12 weeks. (b) SEM micrographs of PELA, HA-PELA, and HA-PLA scaffolds following a 3-week incubation in PBS (pH 7.4, $\text{Ca}^{2+}/\text{Mg}^{2+}$ -free) at 37 °C. Scale bar = 50 μm .

Figure 2.10



b

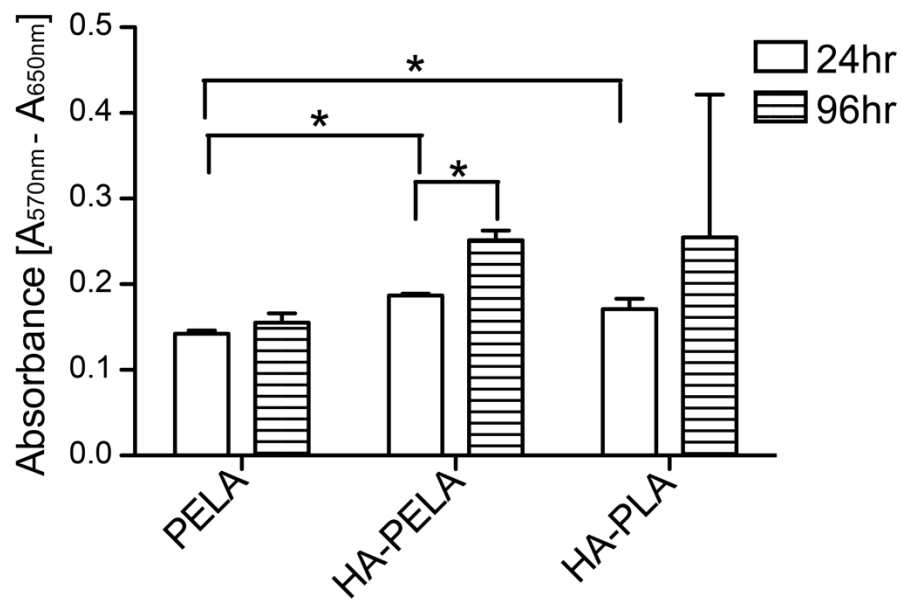


3.9 The role of PEG and HA on rMSC proliferation

rMSCs were seeded onto the PELA and HA-PELA scaffolds (n=3) and the viability of adherent cells was quantified by MTT assay at 24 and 96 h and compared with those adhered to HA-PLA (Fig. 2.11). More viable cells were adhered to HA-PELA than to PELA at 24 h. rMSCs adhered on all substrates were able to proliferate to some degree as indicated by MTT cell viability at 96 h. However, the increase in MTT absorbance from 24 h to 96 h was only significant for HA-PELA.

Figure 2.11. rMSC attachment and early proliferation on electrospun PELA, HA-PELA, and HA-PLA scaffolds (n=3) as determined by MTT cell viability assay at 24 and 96 h after initial cell seeding. * $p < 0.05$ (One-way ANOVA with Tukey post-hoc).

Figure 2.11

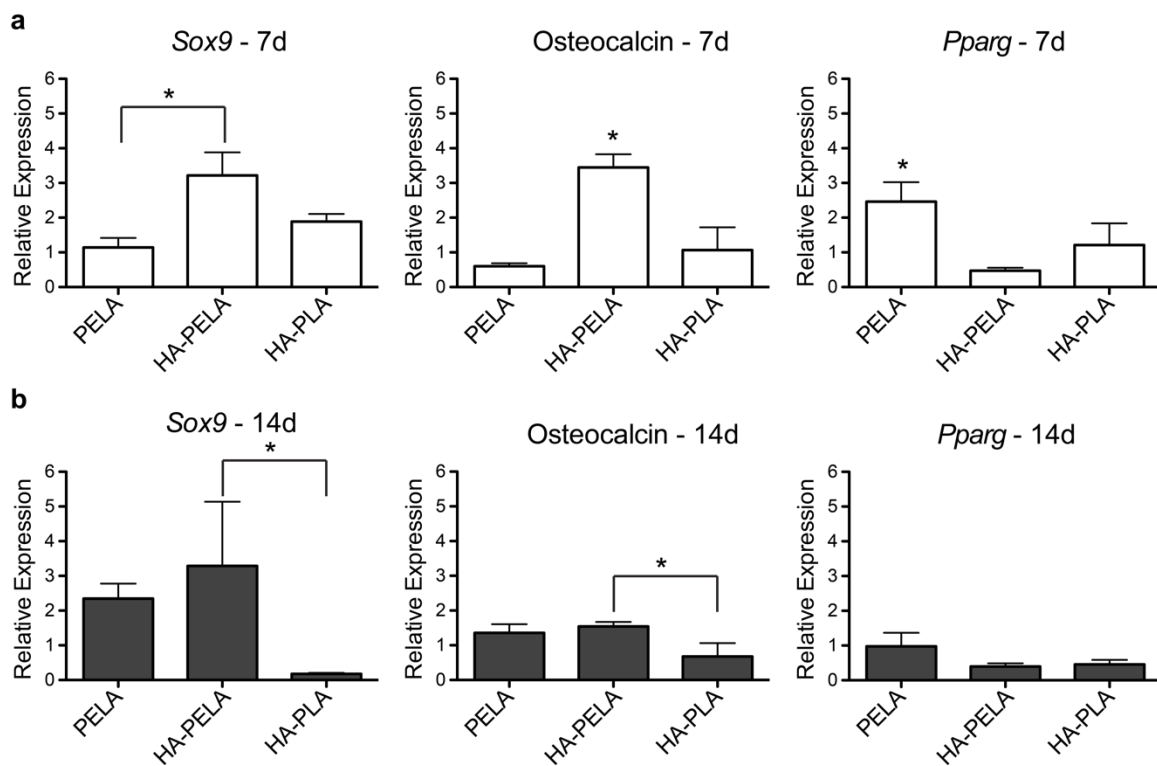


3.10 The role of PEG and HA on the lineage commitment and induced osteogenic differentiation of rMSCs.

To examine the effects surface chemistry and HA incorporation on the spontaneous lineage commitment of MSCs, we cultured rMSCs on PELA and HA-PELA scaffolds along with HA-PLA control in expansion medium without differentiation-inducing supplements. Gene expression of typical osteoblast, chondrocyte, and adipocyte markers was analyzed by qPCR at 7 and 14 days to determine the temporal nature of the rMSC response to the PELA, HA-PELA, and HA-PLA scaffolds. Data were normalized to those obtained from the rMSCs prior to seeding on the various substrates (time 0). For the PELA scaffolds, HA incorporation resulted in significantly increased expression of the chondrogenic marker *Sox9* and the osteogenic marker *Bglap* (osteocalcin) mRNA as early as 7 days (Fig. 2.12a). Expression of *Sox9* and osteocalcin was significantly higher for MSCs cultured on HA-PELA scaffolds than for those cultured on HA-PLA. Although the expression level of osteocalcin by MSCs cultured on HA-PELA decreased from day 7 to day 14 (Fig. 2.12b), it was still significantly higher than those observed with MSCs cultured on HA-PLA. The differences in the expression of *Sox9* by MSCs cultured on HA-PELA vs. HA-PLA, on the other hand, was even more pronounced by day 14. The adipogenic marker *Ppparg* was significantly higher at day 7 on PELA than on HA-PELA, but the differences were not sustained to day 14.

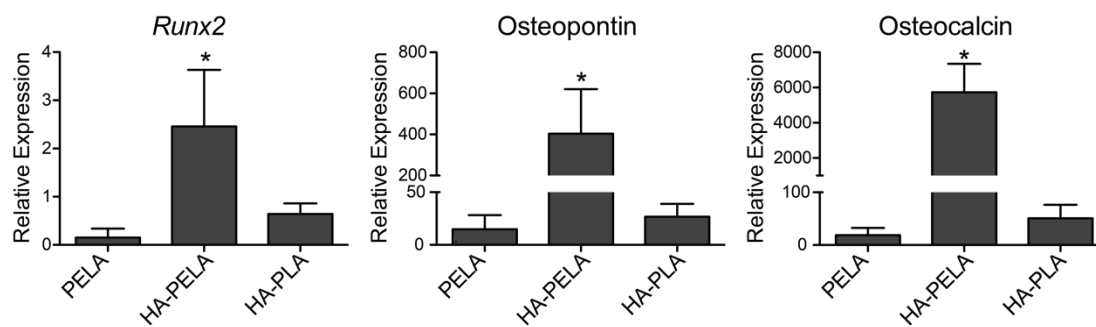
Figure 2.12. Effect of scaffold composition (polymer chemistry and HA) on the lineage commitment of rMSCs in un-stimulated culture. Expression of *Sox9*, osteocalcin, and *Pparg* following (a) 7 or (b) 14 days culture in expansion medium, as determined by qPCR. Data are normalized with housekeeping gene GAPDH and plotted as expression relative to that of rMSCs at time 0 (prior to seeding onto scaffolds). * $p < 0.05$ (One-way ANOVA with Tukey post-hoc).

Figure 2.12



Finally, we examined the impact of HA and PEG on the potency of induced osteogenic differentiation of rMSCs for potential bone tissue engineering applications. PELA, HA-PELA, and HA-PLA scaffolds were cultured with rMSCs for 14 days in osteogenic medium and total RNA was isolated. We used qPCR to quantify the expression of *Runx2*, osteopontin, and osteocalcin (Fig. 2.13). rMSCs adhered on HA-PELA expressed significantly higher levels of all these marker genes than those adhered on PELA or HA-PLA. The expression of osteopontin and osteocalcin was over two orders of magnitude higher for MSCs adhered on HA-PELA than either PELA or HA-PLA on day 14.

Figure 2.13. Effect of scaffold composition (polymer chemistry and HA) on the osteogenic differentiation of rMSCs under induced differentiation culture conditions. Expression of *Runx2*, osteopontin, and osteocalcin following a 14-day culture in osteogenic medium. Data are normalized with housekeeping gene GAPDH and plotted as expression relative to that of rMSCs at time 0 (prior to seeding onto scaffolds). * $p < 0.05$ (One-way ANOVA with Tukey post-hoc).

Figure 2.13

4. Discussion

PLA is a widely used material in the field of tissue engineering due to favorable properties such as biocompatibility, biodegradability, and ease of processing into diverse architectures. However, the intrinsic hydrophobicity of PLA compromises its aqueous dimensional stability and its ability to support cell seeding, growth factor and hydrophilic drug loading, and direct blending with hydrophilic materials such as HA.[169] We tested the hypothesis that by chemically inserting a hydrophilic PEG block within PLA, the resulting amphiphilic triblock co-polymer PELA will favorably interact with HA and be readily electrospun into HA-PELA composite scaffolds with improved physical and biological properties over HA-PLA composites or PELA alone.

We chose racemic D,L-lactide over L-lactide due to its accelerated degradation profile and a lack of crystalline degradation by-products which can elicit adverse tissue responses during potential *in vivo* applications.[48,121] By simply changing the initiator (PEG vs ethylene glycol), we were able to synthesize both the PELA and PLA with similar molecular weights and polydispersity. This allowed us to investigate the effect of polymer chemistry on the HA-composite scaffold properties without additional confounding factors. The facile synthesis and purification of PELA is advantageous for subsequent scale-up for clinical use.

In order to reproducibly fabricate a uniform HA-polymer composite scaffold by electrospinning, the HA needs to be homogeneously dispersed in the

electrospinning solution. A manifestation of poor adhesion between a polymer and HA is that the HA would rapidly settle out of the suspension, as was observed with HA-PLA. We demonstrated that with PELA, a stable HA suspension could be achieved even at HA contents as high as 33 wt.%, in the absence of any surfactants. Such stability is one manifestation of the improved interfacial adhesion between PELA and HA. Consequently, electrospinning of the stable HA-PELA suspension resulted in a scaffold with more uniform fiber morphology and more predictable HA content than electrospun HA-PLA (Fig. 2.3 b&c).

The robust blending and interfacial adhesion between HA and PELA was further manifested in the storage modulus enhancement of the HA-PELA composite over PELA, in contrast to the mechanical strength deterioration of HA-PLA compared to PLA (Fig. 2.7). In addition, HA-PELA exhibited a 5-fold higher ultimate tensile strain and a 10-fold higher ultimate tensile stress than HA-PLA (Fig. 2.5). The far more brittle nature of the HA-PLA composite reflects the inadequate interfacial adhesion between PLA and HA.[169] The significantly enhanced extensibility and ultimate tensile strength of electrospun HA-PELA compared to those of HA-PLA is advantageous for potential surgical manipulation.

The amphiphilic nature of PELA is expected to lead to hydration-induced structural rearrangement of the polymer chains[183,184] and corresponding changes in surface wettability and mechanical properties, which are important for

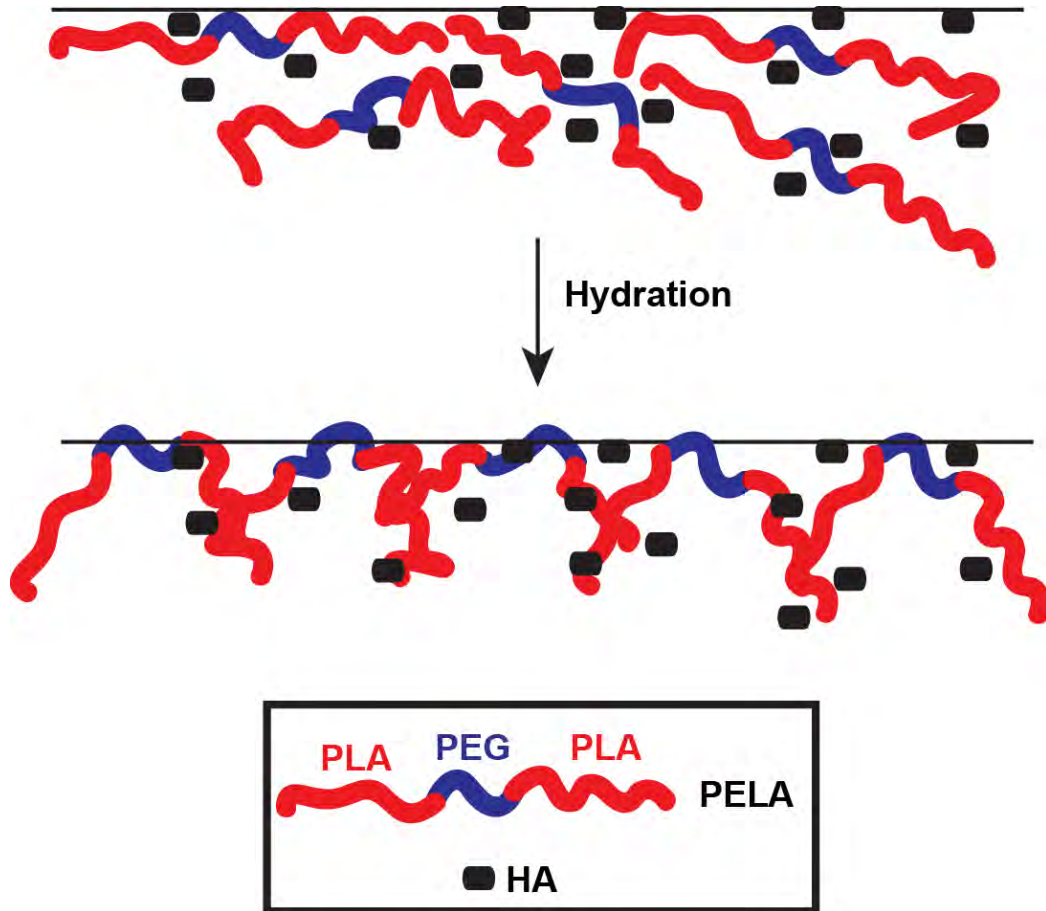
tissue engineering applications. As expected, the chemical incorporation of PEG into PLA reduced the water contact angle of the scaffold compared to PLA. A striking observation was that prior hydration conferred superhydrophilicity to electrospun HA-PELA (Fig. 2.6b), with its water contact angle approaching 0° , pointing to a possible hydration-induced structural rearrangement of the amphiphilic polymer that exposes the hydrophilic PEG to the surface (Scheme 2). The water contact angle of PELA was also reduced upon hydration, although the effect was less dramatic than that observed with HA-PELA, suggesting that the HA plays a role in stabilizing hydration-induced structural rearrangement of the amphiphilic polymer and/or affecting the morphology of the scaffold. We found that the nanofibrous morphology of the HA-PELA scaffolds was indeed important for acquiring hydration-induced superhydrophilicity as the water contact angle drop decrease was far less dramatic on solvent cast HA-PELA films. Contact angle measurement of the PLA scaffold after the water equilibration could not be obtained because the hydrophobic scaffold shrank dramatically upon hydration. Such an observation is consistent with previously reported dimensional instability of electrospun poly(D,L-lactic acid) scaffolds in aqueous environments.[185–187] The extent of shrinkage of the HA-PLA was milder, likely due to the stabilizing effect of the HA within the composite scaffold. The superhydrophilicity combined with the dimensional stability of HA-PELA is advantageous for the loading of cells and aqueous therapeutics, allowing them to be readily absorbed into the scaffold.

We also observed striking storage modulus increases in the PELA and HA-PELA scaffolds upon hydration (Fig. 2.7). The storage modulus of the electrospun PLA and HA-PLA scaffolds, on the other hand, expectedly reduced upon hydration, likely due to a combination of the plasticizing effect of water and the amorphous nature of PLA.[188] We hypothesize that the hydration-induced structural rearrangement of the amphiphilic polymer chains that exposes the hydrophilic PEG blocks to the surface, thereby reducing interfacial energy and lowering the water contact angle, also resulted in the reinforcement of the storage modulus of the material (Fig. 2.14). Indeed, using conventional DSC, we showed that while the as-spun dry PELA specimen only possessed a single glass transition, the specimen with prior hydration history had an extra endothermic peak in the DSC spectrum around 50 °C (Fig. 2.8a). This thermal transition, also present in the reversible MDSC heat flow (Fig. 2.8b), is consistent with a crystalline melting temperature (T_m) of PEG, the only crystalline component in the PELA triblock copolymer. It has been previously reported that the T_m for PEG in a PEG-PLA diblock polymer was 50 °C as opposed to 60 °C for pure PEG. [181] This melting peak indicates that the concentration and orientation of surface exposed PEG was sufficient to induce crystallization. In turn, this hydration-induced structural rearrangement permitted load-transfer in the polymer network, as described for other amphiphilic polymer systems.[189] The hydration-induced stiffening of the HA-PELA scaffolds is potentially advantageous for applications such as scaffold-guided skeletal/dental bone

regeneration. The elastic membrane, upon surgical delivery to fill in or cover an osseous defect, would stiffen within the physiological environment of the defect to prevent soft tissue collapse, thereby maintaining adequate space for bone regeneration.

Figure 2.14. Depiction of a proposed structural rearrangement of the PELA block copolymer chains within HA-PELA composites upon hydration.

Figure 2.14



As the HA-PELA scaffolds are designed to be biodegradable, we evaluated their *in vitro* degradation in PBS over 12 weeks (Fig. 2.10a). HA-PELA exhibited an accelerated degradation compared to HA-PLA, resulting in ~20% mass reduction in 3 months. Such a degradation profile is desired for scaffold-assisted repair of long bone fractures where the maturation/remodeling of bony calluses typically takes place 3-4 months following injury in adults.[121] It ensures that the scaffold fully exerts its templating role during the early stage of scaffold-assisted repair and only degrades at the desired later stage of callus remodeling. The accelerated degradation of PELA and HA-PELA compared to HA-PLA can be attributed to a combination of the more effective water penetration throughout the amphiphilic scaffold enabled by the hydrophilic PEG blocks, and the clearance of the cleaved water-soluble PEG segments from the polymer, as previously described.[190–192] ^1H NMR monitoring of the degradation products confirmed clearance of the PEG segments (Fig. 2.9). Monitoring of microstructural changes of the scaffolds by SEM upon incubation in PBS for 3 weeks revealed that the HA-PLA scaffolds suffered from hydrophobicity-driven collapse of the fibers while the HA-PELA fiber morphology was maintained (Fig. 2.10b). The PELA scaffold without HA exhibited some degree of fiber fusions upon incubation in PBS, although to a much lesser extent compared to HA-PLA. The PEG blocks in PELA have likely prevented more dramatic hydrophobicity-driven fiber aggregation observed with PLA or HA-PLA, while the dynamic rearrangement and crystallization of PEG blocks in aqueous

buffer may have resulted in the fusing of the amphiphilic fibers around their physical contact points. The maintenance of HA-PELA fiber morphology upon PBS incubation further demonstrates the structural stabilizing effect of HA on the amphiphilic scaffold. This combination of dimensional stability, superhydrophilicity, and superior mechanical integrity of HA-PELA composites in an aqueous environment establish HA-PELA composites as far more advantageous scaffolds for tissue engineering applications than the conventional HA-PLA composites.

To further evaluate the applicability of HA-PELA composites for skeletal tissue engineering applications, we compared the ability of HA-PELA and HA-PLA composite scaffolds to support the attachment and guide lineage-specific differentiation of mesenchymal stem cells (MSCs) for the regeneration of bone or cartilage tissues. MSCs residing in the bone marrow are capable of differentiating into a variety of cell types including osteoblasts, chondrocytes, adipocytes, and myoblasts.[193] They can be readily isolated and enriched as adherent bone marrow stromal cells, and expanded and used as a progenitor cell source for musculoskeletal tissue engineering.[194]

The non-fouling PEG block and the osteoconductive HA component of the HA-PELA composites are expected to exhibit opposite effects on protein and cell adhesion. For instance, un-mineralized di-block or tri-block PELA have been used as anti-adhesion membranes,[62] with their low protein adsorption characteristics attributed to the PEG exposed on the surface in the aqueous

environment.[195,196] Meanwhile, HA is known for its ability to absorb a wide range of proteins due to its dynamic surface properties (e.g. pH-dependent zeta potential) and large surface area (for HA nanocrystals), promoting cell attachment.[125,197,198] We hypothesized that the incorporation of HA could improve rMSC attachment on PELA. We showed by MTT assay that the addition of HA to PELA indeed increased the attachment of rMSCs (Fig. 2.11). HA also supported the rMSC proliferation with a significant increase in cell viability from 24 h to 96 h on HA-PELA. It has been reported previously that rMSC proliferation is reduced on PEG-PLA materials.[195] In our study, this effect was offset by the incorporation of HA. It is also worth noting that high standard deviation was observed for the cell viability at 96 h in the HA-PLA group, reflecting the poor HA dispersion within the inhomogeneous HA-PLA scaffold.

The addition of HA to synthetic scaffolds has been shown to promote osteochondral lineage commitment of MSCs in un-stimulated culture[131,132,172] or more potent chondrogenesis/osteogenesis of MSCs in response to chondrogenic/osteogenic inductions in culture and skeletal tissue repair *in vivo*. [135,199–202] However, such an effect has not been consistently established, potentially due to the inhomogeneous distribution of HA within many of the hydrophobic degradable polymer scaffolds utilized for such investigations. Further, how amphiphilic polymer-HA scaffolds impact the gene expression of MSCs under un-stimulated culture conditions is largely unknown.

We cultured rMSCs in expansion medium on the PELA, HA-PELA, and HA-PLA scaffolds and used qPCR to quantify changes early (7 d) and later (14 d) gene expression changes in osteogenesis, chondrogenesis and adipogenesis markers. By using expansion medium free of differentiation inductive agents, we can examine the effect of scaffold composition on guiding rMSC differentiation towards a particular lineage. We showed that MSCs cultured on HA-PELA scaffolds expressed consistently higher expression of the chondrocyte marker SOX9 and the osteoblast marker osteocalcin throughout the 14-day culture (Fig. 2.12). However the difference was not statistically significant at day 14, possibly due to the unstimulated culture conditions being insufficient to sustain the spontaneous osteogenic differentiation over time. The increased osteochondral gene expression at day 7 with the addition of HA to PELA is in contrast with prior reports using materials such as electrospun HA-PCL or poly(ethylene oxide terephthalate)–poly(butylene terephthalate)-HA, where the addition of HA had little or no effect on MSC gene expression.[132,203] Another observation is that the expression of adipogenic marker PPARG significantly decreased upon the addition of HA to PELA at 7 days. Furthermore, the expression of PPARG trends higher at 7 days for rMSCs cultured on HA-PLA than those cultured on the HA-PELA. These results suggest that the osteochondral-inductive properties of HA are more effectively manifested on HA-PELA where polymer-HA interfacial adhesion and dispersion is improved over HA-PLA.

To examine the role of polymer chemistry and HA incorporation in promoting osteogenesis of MSCs upon culture induction, we quantified the osteogenic gene expression of rMSCs cultured on PELA, HA-PELA and HA-PLA in osteogenic medium. The expression of early (*RUNX2*), middle (osteopontin), and late stage (osteocalcin) osteogenesis markers were all significantly up-regulated on HA-PELA compared to PELA or HA-PLA scaffolds (Fig. 2.13).[204,205] In particular, the expression of osteopontin and osteocalcin was increased over two orders of magnitude on HA-PELA. Prior work on MSCs attached to electrospun HA-PLLA (calcium deficient) scaffolds showed increased osteogenic gene expression with increasing HA content in expansion medium while the effects were abrogated in osteogenic medium.[131] By contrast, here we show that the HA-PELA scaffolds promoted osteogenic gene expression in MSCs in both stimulated and unstimulated cultures. More homogenous HA distribution within the amphiphilic HA-PELA scaffold as opposed to the uneven distribution of aggregated HA within the HA-PLA scaffold may translate into a higher surface area of the osteoconductive HA interacting with adherent MSCs. Furthermore, prior work has shown that PEG/PLA diblock co-polymers or PEG/PLA blends promote the osteogenic differentiation of MSCs.[196,206] Here we show that the synergy between HA and PEG supported an even more potent osteogenic MSC response. By sensitizing the response of MSCs to osteogenic induction,[204] it may be possible to deliver exogenous osteogenic inductive agents such as bone morphogenetic protein (rhBMP-2) via HA-PELA with

reduced loading doses for enhanced safety and reduced cost. Taken together, HA-PELA composites exhibit unique handling properties (elasticity, superhydrophilicity, hydration-induced stiffening) and bioactivity (rMSC attachment, osteochondral gene expression) ideal for osteochondral tissue engineering and *in vivo* application.

5. Conclusions

A biodegradable electrospun HA-PELA composite was designed for skeletal tissue engineering applications. We showed that favorable interactions between HA and the PEG component of the amphiphilic block copolymer dictated the physical and biological performance of the composites. The hydrophilic PEG block improved HA blending and adhesion to the polymer, facilitating the preparation of composite fibrous scaffolds with uniform fiber dimensions and HA distribution by electrospinning. The incorporation of well integrated HA with PELA improved the dimensional stability and reinforced the tensile storage moduli of the electrospun composites while maintaining tensile elasticity. The hydrophilicity and mechanical integrity of HA-PELA further improved in an aqueous environment, likely resulting from hydration-induced structural rearrangement of the PEG domains that may have been more effectively stabilized by HA. The combination of dimensional stability, mechanical integrity, superhydrophilicity, and tensile elasticity exhibited by HA-PELA can be exploited to facilitate cell seeding, drug delivery and convenient surgical manipulations of the composite scaffold. Finally, HA incorporation improved cell

attachment to the relatively low-fouling PELA, and the HA-PELA composite, unlike HA-PLA, promoted osteochondral lineage commitment of MSCs and supported more potent osteogenic gene expression upon induction. The combination of improved handling characteristics and biological performance positions HA-PELA as a more suitable bone tissue engineering scaffold than HA-PLA. Indeed, the facile synthesis of PELA, the consistent properties of electrospun HA-PELA, and the established safety profile of the constituents of the composite scaffold are appealing characteristics for successful clinical translation. Overall, this study demonstrates the importance of rational selection and assembly of key structural components with synergistic interactions in the design of effective tissue engineering scaffolds.

Acknowledgments

I would like to thank Dr. Jianwen Xu for technical assistance with polymer synthesis. This research was supported in part by the National Institutes of Health Grant R01AR055615 and by the Department of Defense Congressionally Directed Medical Research Programs under award number W81XWH-10-0574. Core resources supported by the National Center for Research Resources Grant S10RR021043 were used.

**CHAPTER III: Spiral-wrapped electrospun amphiphilic polymer-
hydroxyapatite scaffold for templated repair of long bone defects in rats**

Preface

This chapter has been adapted from a manuscript in preparation:

Kutikov AB, Skelly J, Ayers DC, Song J. "Spiral-wrapped electrospun amphiphilic polymer-hydroxyapatite scaffold delivering MSCs or rhBMP-2 for the templated repair of long bone defects in rats"

Dr. Jie Song and Artem Kutikov designed the experiments in this work. Dr. David Ayers contributed to conception of the work and review of the manuscript. Artem Kutikov and Jordan Skelly performed rat surgeries. Jordan Skelly performed the micro-computed tomography scans. Artem Kutikov performed the remainder of the work.

Abstract

Effective repair of critical size long bone defects presents a significant clinical challenge. Electrospun scaffolds with adequate hydrophilicity, high surface area, and osteoconductivity can be exploited to deliver protein therapeutics and stem/progenitor cells, but their standalone application for long bone repair is hampered by limited thickness. The electrospun composite of amphiphilic PELA and HA supports cell/therapeutics loading and osteogenic differentiation of MSCs. Here we explore the strategy of spiral-wrapping electrospun HA-PELA to fit in 5-mm rat femoral segmental defects and compare the effectiveness of delivering exogenous MSCs versus a low dose of rhBMP-2 for guiding new bone formation. HA-PELA with pre-seeded MSCs resulted in laminated endochondral ossification directly templated by the spiral-wrapped scaffold layers across the longitudinal span of the defect. Using GFP-labeling, we confirmed that the exogenous MSCs survived 7 days post-implantation. When loaded with 500-ng rhBMP-2, HA-PELA spirals led to more robust but less templated bone formation than MSCs, with bone bridging over the defect by 12 weeks. The biodegradable scaffold did not elicit allergic reactions or chronic inflammation. These outcomes support spiral-wrapped electrospun HA-PELA as a promising strategy for therapeutics delivery and templated long bone repair.

1. Introduction

There remains a significant clinical need for better strategies to repair critical-size bone defects resulting from congenital conditions, trauma, or tumor resection. Autografting procedures are considered the gold standard but they can lead to significant donor site morbidity and are limited by autograft supply.[24] Allografts, obtained from human donors, are alternatives to autografts but carry an inherent risk for disease transition and suffer from long-term failure rates as high as 60% over 10 years.[14] Current commercially available bone graft substitutes are typically weak and brittle gels or foams[25] that possess poor handling characteristics (e.g. inconvenient surgical insertion and inadequate graft fixation). Adequate bone healing facilitated by these materials typically will require high doses of exogenous growth factors such as recombinant human rhBMP-2. The performance of bone graft substitutes can potentially be improved by integrating biomaterials exhibiting desired physical and biological properties with appropriate scaffold configurations and a safe loading dose of biological factors and/or skeletal progenitor cells.

Electrospinning is a widely used technique to manufacture tissue engineering scaffolds with nanofibrous morphology similar to that of native extracellular matrices.[83] Such scaffolds provide a high surface area for cell attachment and proliferation,[83] and when properly engineered, can also support stem cell differentiation.[207–209] As growth factor delivery vehicles, the high surface area of electrospun scaffolds is also desired for protein adsorption

and improved sustained release.[87] Another advantage of electrospinning is the versatility of fabricating scaffolds from a variety of polymers and composite materials. For bone tissue engineering, electrospun composites combining degradable polymers with osteoconductive minerals such as HA have long been sought after, with recent attention focused on achieving improved polymer-mineral blending and interfacial adhesion.[131,141,209] The incorporation of HA has been shown to promote cell attachment, proliferation, and osteogenic differentiation on electrospun polymer scaffolds, especially when they are well-integrated with the polymer matrix.[131,209–211] Such electrospun materials have been used for containing soft hydrogels,[212,213] delivering platelet rich plasma,[214] or guiding regeneration of non-weight bearing cranial/mandibular defects.[215–218] However, their standalone uses for long bone regeneration, a challenging clinical problem in orthopedic trauma care,[219] have been lacking due to the limited thickness and inadequate mechanical properties of electrospun materials.

We hypothesized that spiral-wrapping electrospun scaffolds may be a promising approach for taking advantage of both the high surface area of electrospun materials to deliver therapeutics / support cellular adhesion and the defined 3-D configuration of the spiral to guide the regeneration of critical long bone defects. Furthermore, the relatively low quantity of polymer used to fabricate electrospun materials may also mitigate potential adverse immune responses to the degradation products of degradable polymer scaffolds.[220]

Spiral-wrapped scaffolds in combination with other materials have been studied for potential tissue engineering applications *in vitro*. [93,221–224] Zhang *et al.* and Wang & Xu have described spiral-wrapped electrospun PCL/salt-leached PCL film composites and electrospun PCL/sintered PLGA scaffolds, respectively, [222–224] although neither design was tested *in vivo*. Jiang *et al.* employed an electrostatic assembly strategy to fabricate a spiral-wrapped membrane composed of chitosan/cellulose/HA and tested their performance in augmenting the repair of rabbit radius defects. [93] However, the non-critical defect size they employed makes the efficacy of the scaffold difficult to interpret as the no-scaffold defect control also healed. Piskin *et al.* used spiral-wrapped electrospun PCL scaffolds containing simvastatin to aid the healing calvarial defects in rats, however, defect closure was not achieved by 6 months post-op. [221] Overall, *in vivo* studies that examine the efficacy of standalone 3-D electrospun scaffolds in a clinically relevant critical long bone defect model are lacking.

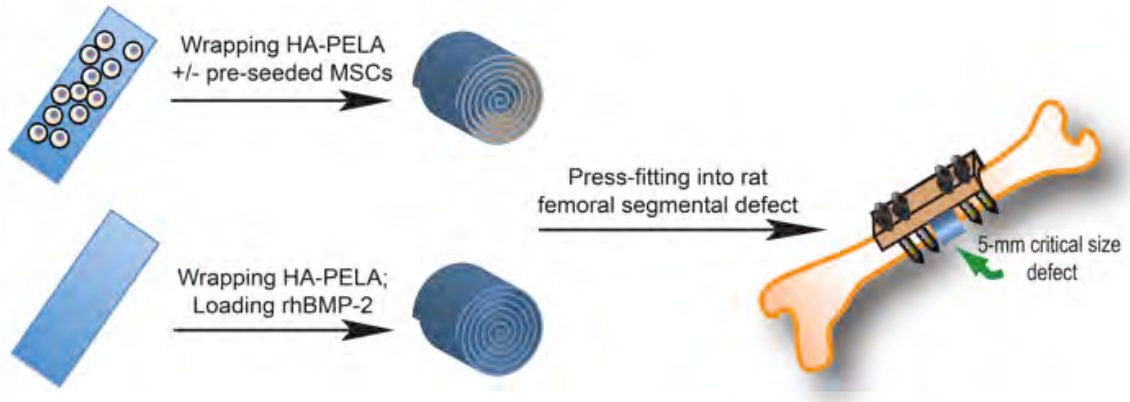
We recently prepared a well-integrated electrospun composite of HA and biodegradable amphiphilic tri-block copolymer PELA. [209] The hydrophilic PEG segment was chosen to enable the dispersion and binding with the hydrophilic HA mineral while the hydrophobic PDLA blocks provided biodegradability and aqueous stability. These electrospun HA-PELA composites supported far more potent osteogenic differentiation of rMSCs *in vitro* than conventional electrospun HA-PLA composites. Meanwhile, we also observed super-hydrophilicity (water

contact angle $\sim 0^\circ$), high elasticity ($>200\%$ ultimate strain), and hydration-induced stiffening of the HA-PELA composite [209]. These physical properties could facilitate absorption of aqueous suspensions of cells and growth factors, and enable easy surgical handling and stable fixation (e.g. wrapping around a defect, fitting within a confined defect,[225] etc.). This combination of bioactivity and handling characteristics makes electrospun HA-PELA a promising material for bone repair.

Here we exploit the unique handling characteristics (super-hydrophilicity, elasticity, hydration-induced stiffening) and *in vitro* bioactivity of electrospun HA-PELA [209] in the form of 3-D spirals for augmenting the repair of critical-size long bone defects. We test the hypothesis that electrospun spiral-wrapped scaffolds can be readily fit within critical long bone defects and guide bone formation throughout the spiral template. Furthermore, we compare the robustness of bone formation templated by progenitor cell-seeded scaffolds versus osteogenic growth factor-loaded scaffolds. We hypothesized that whereas the local sustained release of rhBMP-2 from the HA-PELA scaffold may result in more potent osteogenesis throughout the defect, the delivery of exogenous MSCs via the scaffold may lead to more organized new bone formation intimately templated by the cell-seeded spiral template. We tested these hypotheses by comparing the performance of spiral-wrapped HA-PELA scaffolds with or without pre-seeded rMSCs to scaffolds loaded with a low dose of rhBMP-2 (500 ng) in healing 5-mm critical-size femoral segmental defects in rats (Figure 3.1).

Figure 3.1. Schematic of the spiral-wrapping of HA-PELA scaffolds with or without pre-seeded cells or absorbed rhBMP-2 for implantation into a 5-mm rat femoral segmental defect stabilized by a PEEK fixation plate.

Figure 3.1



2. Materials and Methods

2.1 Scaffold fabrication

PELA was synthesized and electrospun with HA as previously described.[209] Briefly, PELA was synthesized by ring opening polymerization of 3,4-Dimethyl-1,4-dioxane-2,5 dione (D,L-Lactide; Sigma Aldrich, St. Louis, MO) initiated by PEG (20,000 Dalton; Fluka BioUltra, Switzerland) and catalyzed by Sn(II) 2-ethylhexanoate (500ppm; Sigma Aldrich, St. Louis, MO). The resulting polymer (MW: 131,800 Da, PDI: 1.43) was dissolved in chloroform, purified by precipitation in methanol, and dried in a vacuum oven. HA-PELA composite scaffolds were fabricated by electrospinning a homogenous suspension of 10 wt%HA in PELA using 1:4 (v/v) dimethylformamide/chloroform as a solvent.[209] The suspension was electrospun through a 22 G needle at 12 kV onto a grounded aluminum collector positioned 15 cm away. After 2 h of electrospinning, the scaffolds were dried in a vacuum oven for 48 h to remove any residual solvent and stored in a desiccator at 4 °C.

2.2 Rat bone marrow stromal cell (rMSC) isolation

rMSCs were isolated from the long bones of 4 week old male Charles River SASCO SD rats according to the protocol approved by the University of Massachusetts Medical School Institutional Animal Care and Use committee, as previously described.[153] Bone marrow was flushed with cold minimal essential medium (α MEM; Life Technologies, Carlsbad, CA). Prior to plating, red blood

cells were lysed with sterile water, cells were re-suspended in MSC expansion medium (α MEM without ascorbic acid, supplemented with 20% fetal bovine serum, 2% L-glutamine, and 1% penicillin-streptomycin), and passed through a sterile strainer. Non-adherent cells were removed after 4 days of culture and the remaining adherent cells were expanded until 70% confluent prior to use.

2.3 Scaffold preparation

Scaffolds were sterilized by exposure to UV light (254 nm) for 30 min on each side and equilibrated overnight in MSC expansion medium prior to use. For rMSC loaded scaffolds, 100,000 rMSCs/cm² in 50 μ L expansion medium were seeded onto scaffolds (5.3 mm \times 40 mm \times 0.10 – 0.12 mm) which were placed in 6-well ultra-low cell attachment plates (Corning Inc., Corning, NY). Following 30 min of incubation (37 °C, 5% CO₂), 2 mL of expansion medium was added to the wells and the scaffolds were incubated for an additional 24 h. Scaffolds were washed 3 times with PBS prior to implantation. Cell-free and rhBMP-2 loaded scaffolds were processed in the same manner but without rMSCs. Loading of rhBMP-2 (CHO-derived; R&D Systems, Minneapolis, MN; 500 ng in 50 μ L PBS) was performed 15 min prior to implantation.

2.4 rMSC attachment and viability on spiral-wrapped HA-PELA

rMSCs were seeded onto electrospun HA-PELA scaffolds as described above. After 24 h, scaffolds were spiral-wrapped into 3-D cylinders or cultured on unperturbed electrospun meshes in the ultra-low attachment 6-well plates. At

each time point, fresh medium containing 9% (v/v) Cell Counting Kit-8 reagent (CCK-8; Dojindo Molecular Technologies Inc., Japan) was added to the wells. After 4-h incubation, 100 μ L of medium was removed for measurement of absorbance at 450 nm with 650-nm background correction on a Multiskan FC microplate photometer (Thermo Scientific, Billerica, MA). The remainder of the medium was aspirated, the scaffolds were washed with PBS, and medium was replaced for continued culture up to 14 days. The CCK-8 assay was carried out at day 1, 7 and 14. Following the 14-day culture, the spiral-wrapped scaffolds were unwrapped and the adherent cells were labeled with Alexa Fluor 488 Phalloidin and DAPI (Life Technologies, Carlsbad, CA), and imaged on an inverted epifluorescence microscope (Zeiss Axiovert 40 CFL; Carl Zeiss, Germany).

2.5 *In vitro* rhBMP-2 release from HA-PELA

Electrospun HA-PELA scaffolds (n=3) were punched into 0.32 cm² circles, sterilized 30 min/side with UV, and equilibrated overnight in deionized water at 37 °C. They were then air dried in a biosafety cabinet, placed in ultra-low attachment 24-well plates (Corning Inc., Corning, NY), and loaded with 75 ng rhBMP-2 in 5 μ L of PBS. One milliliter of PBS was then added to each well and the plate was incubated at 37 °C. For each time point, the release buffer (1 mL) was collected and replenished with fresh PBS. The release buffer was frozen and stored at -80 °C prior to rhBMP-2 measurement. At the end of the release experiment, all collected release buffers were thawed and the rhBMP-2

concentration was determined using a rhBMP-2 ELISA kit (R&D Systems, Minneapolis, MN).

2.6 *In vitro* bioactivity of rhBMP-2 retained on HA-PELA following 7-day incubation in PBS

The HA-PELA scaffolds, retrieved after 7-day PBS incubation from the BMP-2 release study, were then assessed for their ability to support C2C12 transdifferentiation in order to confirm the osteogenic bioactivity of the rhBMP-2 retained on the scaffolds. C2C12 cells were seeded directly onto the scaffolds (20,000 cells/cm²) that were placed in ultra-low attachment 96-well plates (Corning Inc., Corning, NY), and cultured in DMEM containing 5% fetal bovine serum and 1% penicillin-streptomycin for 72 h. The scaffolds were fixed in periodate-lysine-paraformaldehyde (PLP) fixative[226] and alkaline phosphate (ALP) activity was stained using a Leukocyte Alkaline Phosphatase Kit (Sigma-Aldrich, St. Louis, MO). Following staining, the scaffolds were imaged on an inverted microscope (Zeiss Axiovert 40).

2.7 *In vivo* study design and surgical procedure

Electrospun HA-PELA alone (n=12), pre-seeded with rMSCs (n=11), or loaded with rhBMP-2 (n=11) were rolled into 5.3-mm long and 3-mm wide spirals and press-fit into 5-mm segmental femoral defects in rats. Bone healing was monitored over time with a Scanco VivaCT75 *in vivo* microCT scanner every 4 weeks and also radiographed every 2 weeks. Animals were sacrificed at 4 or 12

weeks for histology (n=2 per treatment group / time point). A subset of animals was sacrificed at 12 weeks for torsion testing (n=4 for HA-PELA with pre-seeded MSCs; n=7 for HA-PELA with rhBMP-2). In order to track the fate of transplanted rMSCs, a subset of animals received scaffolds seeded with GFP-transduced rMSCs and were sacrificed at 2 days, 7 days, or 4 weeks post-op for histology (n=2).

All animal procedures were approved by the University of Massachusetts Medical School Institutional Animal Care and Use Committee. Male Charles River SASCO SD rats (290-300 g) were sedated with 5% isoflurane-oxygen and maintained at 2% isoflurane-oxygen during surgery. A 5-mm critical sized femoral defect was created and stabilized with a polyetheretherketone (PEEK) fixation plate as previously described.[135] Briefly, the femur was exposed by a combination of sharp and blunt dissection. The periosteum was circumferentially removed in order to emulate a challenging healing environment. A PEEK fixation plate was secured with 2 stainless steel bicortical screws flanking each side of the defect and with the two immediately adjacent to the defect further stabilized with hex nuts. The 5-mm defect was created with an oscillating Hall saw and bone debris was removed by copious irrigation with sterile saline. The empty, MSC-loaded, or rhBMP-2 loaded spiral wrapped scaffolds were then fit into the defect. The wounds were closed with sutures and the rats were given cefazolin (20 mg/kg, once per day) and buprenorphine (0.08 mg/kg, every 8 h)

subcutaneously for 2 days. Rats were radiographed immediately following surgery to confirm proper PEEK plate fixation.

2.8 Micro-computed tomography (μ -CT)

Every 4-weeks following surgery, animals were sedated and maintained with 2% isoflurane-oxygen for scanning of the femurs on a Scanco vivaCT 75 μ -CT system (Scanco Medical, Switzerland) at a voxel size of 30 x 30 x 30 μm^3 . Scans were also performed on 12-week explants with the same scanning resolution. A total of 167 30- μm slices within the defect site, totaling 5.01 mm, were used to construct the region of interest (ROI) for analysis. A global threshold was applied to remove soft tissue and scaffold background for quantification and reconstructing 3-D images. Bone volume and bone mineral density within the ROI were calculated using Scanco Medical's 3D analysis software.

2.9 Histology

Explants were fixed in PLP fixative[226] at 4 °C for 2 days and subsequently decalcified in 18% aqueous ethylenediaminetetraacetic acid (EDTA) (pH 8.0) for 4 weeks with exchanges of fresh EDTA solution twice a week. Following removal of the PEEK fixation plates, the explants were subjected to serial dehydration, paraffin embedding and sectioning. Six-micrometer thick sections were stained by hematoxylin and eosin (H&E) or toluidine blue.

To identify any potential negative systemic effects of HA-PELA and its degradation products, heart, kidney, liver, lung, spleen, and pancreas tissues were retrieved from the sacrificed rats at 12 weeks and 24 weeks after receiving the implants. The organs were fixed in periodate-lysine-paraformaldehyde fixative at 4 °C for 2 days then paraffin embedded, sectioned, and stained with hematoxylin and eosin for pathological evaluation.

2.10 Biomechanical testing

Using a Dremel drill, the center of the PEEK plates fixating the explants were thinned to minimal attachment to facilitate the handling of those explants that were not fully bridged with calcified callus during potting. The explants were then potted in zinc-coated aluminum hex nuts with bone cement following literature protocol.[227] After both ends were potted, the thinned center of the PEEK plate was carefully trimmed with scissors without damaging the underlying graft/callus. Using a mini-torsion tester equipped with an eP2 controller (Admet), the explants were torqued to failure at 1°/s. Maximum torque recorded was reported as the failure torque, torsional stiffness was determined from the linear region of the torque/displacement curve, and torsional energy was determined from the area under the torque/displacement curve.

2.11 Lentiviral GFP transduction of rMSCs and tracking of implanted GFP-rMSCs

rMSCs were transduced with lentiviral vectors (Cellomics Technology) expressing enhanced green fluorescent protein (GFP) driven by cytomegalovirus (CMV), elongation factor-1 alpha (EF1 α), or ubiquitin C (UBC) promoters. Cells were transduced with the virus at a multiplicity of infection of 5, 25, or 50. Passage 1 rMSCs were seeded at a density of $\sim 10,000$ cells/cm² in transduction medium (α MEM, 20% heat-inactivated FBS, 1% L-Glutamine) and cultured for 24 h before the respective lentiviral vectors were added. The culture plates were spun for 30 min in a centrifuge (1200 \times g, 32 °C) to increase transduction efficiency before subjected to continued culture for 24 h in transduction medium. The medium were then changed to MSC expansion medium and the cells were cultured for an additional 24 h prior to use. Transduction efficiency (% of cells transfected as revealed by green fluorescence) was examined by epifluorescence microscopy (Zeiss Axiovert 40 CFL) in 3 randomly selected fields of view at 100X magnification.

MTT cell viability assay (Roche, Indianapolis, IN) was performed to quantify cell viability 24 h after lentiviral transduction. Percent cell viability was normalized to untreated rMSC controls. Cell proliferation over 72 h was quantified by MTT (n=3) and presented as fold-change from initial cell viability (24 h following lentiviral transduction).

In order to track the viability of MSCs seeded on the scaffold and implanted in the rat femoral segmental defect, GFP-rMSCs were seeded on HA-PELA as described above. One of the GFP-rMSC seeded scaffolds, prepared at the same time as the scaffolds to be implanted, was rinsed with PBS and imaged on a fluorescent microscope (Zeiss Axiovert 40 CFL) to obtain pre-implantation GFP signal control. Remaining scaffolds were rolled into 3-D cylinders and implanted into the rat critical size femoral defects as described above. At 2 days, 7 days and 4 weeks post-op, animals were sacrificed and the scaffolds were excised from the defects, carefully unrolled, and mounted on a microscope slide for GFP imaging.

Immunohistochemical staining was used to track GFP-rMSCs at 4 weeks post-op. Explants were fixed, decalcified, and processed for histology as described above. The sections were deparaffinized, unmasked in 10 mM sodium citrate buffer (pH 6.0) and treated with rabbit polyclonal GFP antibody (#2555; Cell Signaling Technology) in SignalStain Antibody Diluent (Cell Signaling Technology). SignalStain Boost (Cell Signaling Technology) was used for detection of the rabbit antibodies. SignalSlide GFP IHC controls (Cell Signaling Technology) were used as positive controls.

2.11 Statistical analysis

All statistical analysis was performed with Prism 6.0 (GraphPad Software Inc., La Jolla, CA). Grubbs' testing ($\alpha = 0.05$) identified one outlier in the μ -CT quantification of the HA-PELA group, which was removed from subsequent

analyses. Shapiro-Wilk testing confirmed that the data in all groups followed a normal distribution. One-way analysis of variance (ANOVA) with Tukey post-hoc testing was thus used for all statistical comparisons.

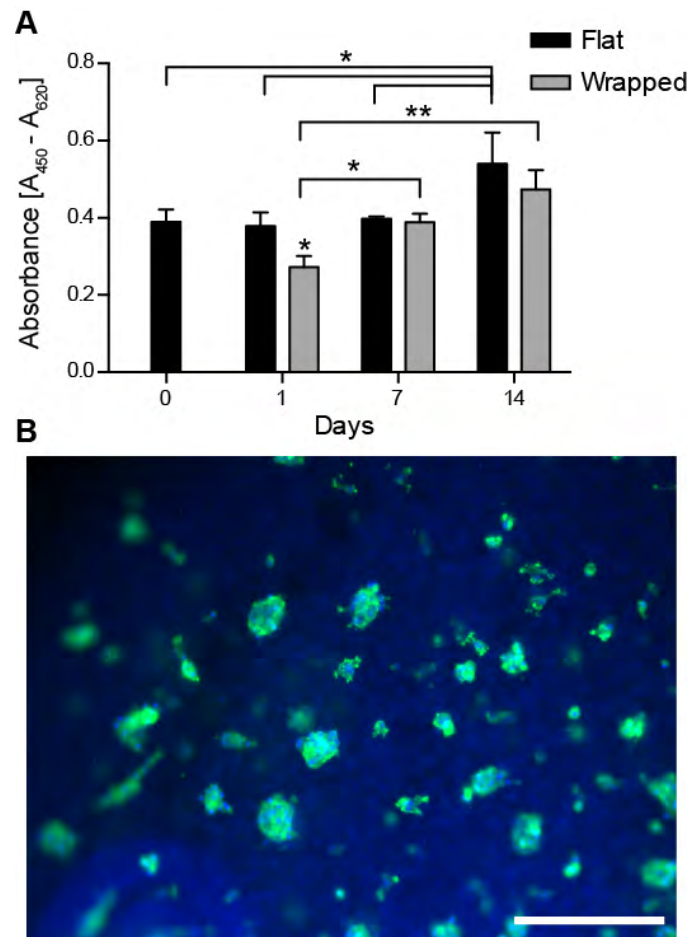
3. Results

3.1 MSC attachment and viability

MSCs readily adhered to the HA-PELA scaffolds. Although cell viability was significantly reduced (by 30%) at 24-h post spiral-wrapping, comparable numbers of viable cells were present on flat and spiral-wrapped scaffolds by 7 and 14 days in culture (Fig. 3.2A). MSCs adhered on scaffolds after 14 days in culture were visualized by staining F-actin (fluorescent phalloidin) and nuclei (DAPI) (Fig. 3.2B). Substantial non-specific absorption of DAPI onto the electrospun scaffold was observed.

Figure 3.2. Viability of rMSCs adhered to flat and spiral-wrapped HA-PELA scaffolds over time. (A) CCK-8 cell viability over 14 days (n=3). Day 0 cell viability was determined prior to spiral-wrapping the scaffolds. * $p < 0.05$, ** $p < 0.01$ (ANOVA with Tukey post-hoc) (B) Actin staining of adhered rMSCs on the spiral-wrapped scaffold after 14 days in culture. Scale bar = 250 μm .

Figure 3.2

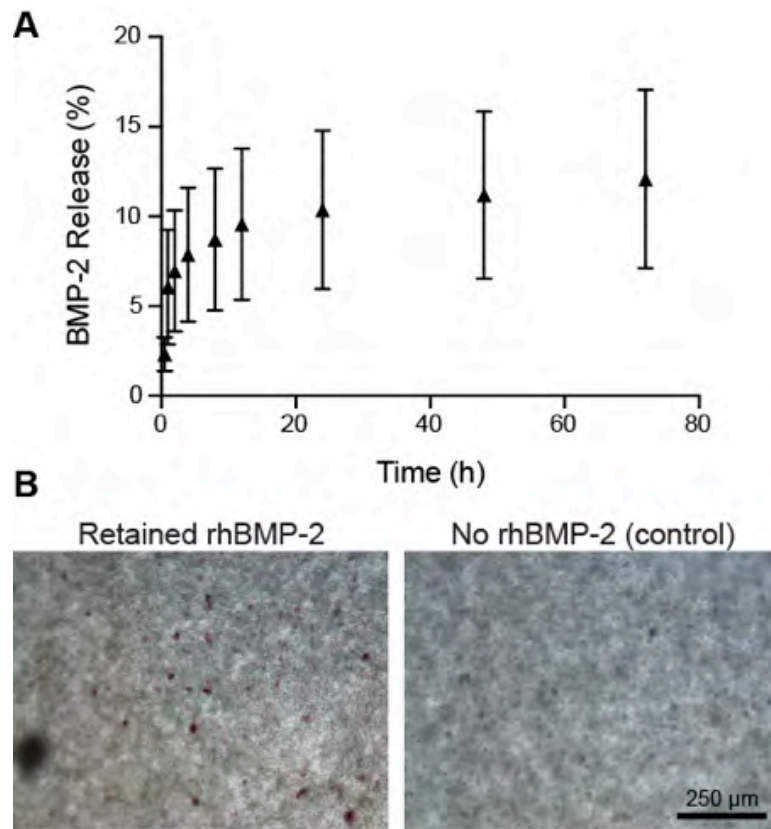


3.2 Retention and release of rhBMP-2 from HA-PELA

A slow yet sustained release of rhBMP-2 from the HA-PELA scaffold was detected by ELISA over 72 h (Fig. 3.3A). Only ~10% of the rhBMP-2 stably absorbed to the scaffold was released within the first 24 h and a cumulative 12% was released by 72 h. The rhBMP-2 retained on the scaffolds remained bioactive and was able to induce the osteogenic transdifferentiation of C2C12 myoblasts, as evidenced by the positive staining for the osteogenic marker ALP on the cells cultured on the scaffold pre-loaded with rhBMP-2 and subjected to 7-day prior incubation in PBS (Fig. 3.3B). ALP staining was not detected with the cells cultured on the scaffold without rhBMP-2 loading.

Figure 3.3. rhBMP-2 release and bioactivity. (A) Cumulative percentage of rhBMP-2 (75 ng loading dose) released from HA-PELA (n=3) in PBS at 37 °C. (B) Alkaline phosphatase staining of the C2C12 myoblasts cultured on HA-PELA with or without pre-absorbed rhBMP-2- for 3 days. The scaffolds bearing 75 ng rhBMP-2 were incubated in PBS for 7 days before being retrieved and seeded with C2C12 cells.

Figure 3.3

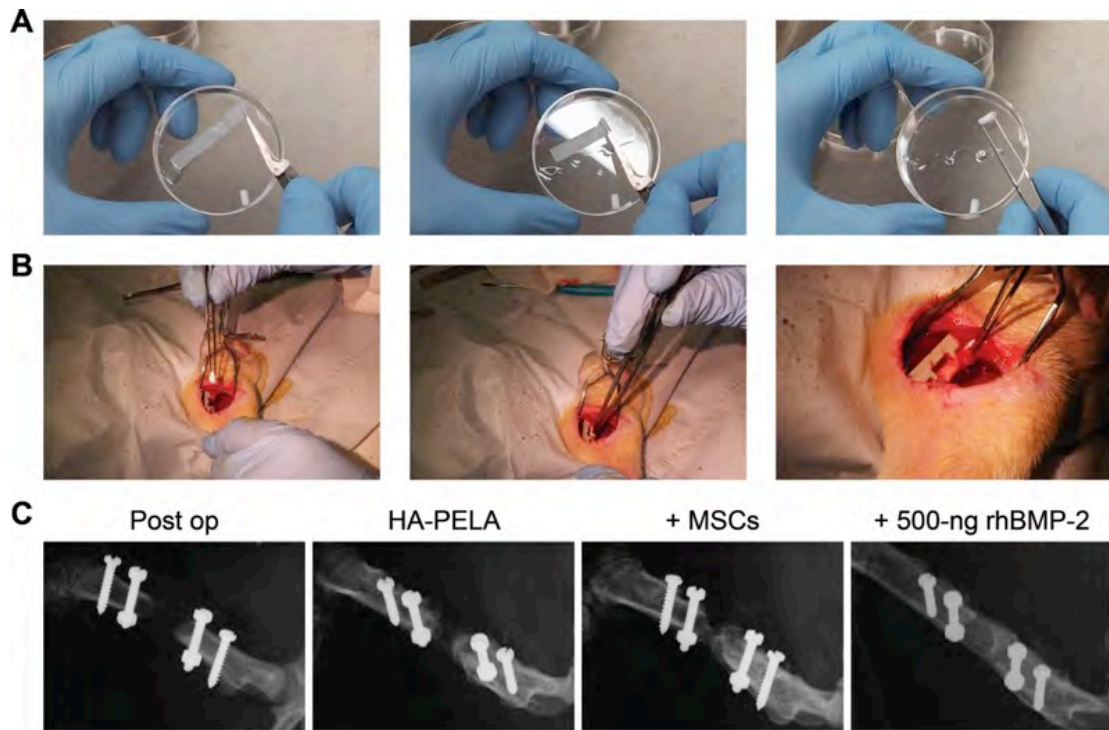


3.3 Radiographic follow-up of implanted spiral-wrapped HA-PELA with/without pre-seeded MSCs or rhBMP-2

HA-PELA scaffolds, with or without pre-seeded MSCs or absorbed rhBMP-2, were manually wrapped into cylindrical spirals (Fig. 3.4A) and implanted into 5-mm rat femoral defects (Fig. 3.4B). The implanted scaffolds could not be readily visualized by post-op x-ray radiographs due to the relatively low density of the HA (10 wt%) within the HA-PELA scaffold (Fig. 3.4C). New bone formation was visible by radiography in all treatment groups by 12 weeks post-op (Fig. 3.4C). The greatest amount of bridging bony callus was detected in the groups treated with HA-PELA and 500 ng of rhBMP-2. Of note, for the group treated with HA-PELA and MSCs, the new bone formation appeared to have occurred within, instead of surrounding the outer surface of, the spiral-wrapped scaffold.

Figure 3.4. Spiral-wrapping and surgical implantation of HA-PELA scaffolds and post-op radiographical follow-ups of the site of implantation. (A) Wrapping HA-PELA scaffolds into cylindrical spirals prior to surgery. (B) Implantation of spiral-wrapped HA-PELA scaffolds into 5-mm rat femoral segmental defects. (C) Radiographs of the scaffold-filled defects immediately post-op and after 12 weeks.

Figure 3.4



3.4 Histological evaluation of the cellularity and new bone formation within and surrounding the HA-PELA scaffold with/without MSCs or rhBMP-2

Histological sections were cut longitudinally, revealing the new bone/scaffold morphology across the length of the 5-mm defect (Fig. 3.5A). HA-PELA scaffolds remained visible at the defect site in all treatment groups by 12 weeks (Fig. 3.5B). Immune cells infiltrated within these HA-PELA scaffolds consisted primarily of macrophages and foreign body giant cells (*, Fig. 3.5B). No lymphocytes, neutrophils, eosinophils or mast cells were detected. Consistent with this mild local immune response, the implantation of HA-PELA also did not lead to gross changes to vital/scavenger organs by up to 24 weeks post-implantation (Fig. 3.6).

Substantial new bone formation at the scaffold/cortical bone interface, accompanied with neovessel formation (arrowheads, Fig. 3.5B) was readily detected in all treatment groups by 12 weeks (visible as early as 4 weeks) as revealed by H&E and polarized light microscopy. The new bone formed within the HA-PELA scaffolds, however, differed significantly in both morphology and maturity among the 3 treatment groups. The new bone formed within the HA-PELA scaffold was randomly aligned and remained immature by 12 weeks as reflected by the lack of strong birefringence under polarized light. By contrast, the new bone formed at the center of the scaffold pre-seeded with MSCs was well-aligned with and encapsulated between adjacent scaffold layers. The new bone formation templated by MSC-seeded HA-PELA, however, was still characterized

with a weak birefringent signal at 12 weeks. New bone formation was also visible within the HA-PELA scaffold absorbed with rhBMP-2, although they did not appear to be clearly templated by the spiral wrapped scaffold morphology. With the delivery of rhBMP-2, strong birefringence at both the cortical-scaffold junction and along the outer periphery of the scaffold indicative of aligned collagen fibers and more mature bone was observed under polarized light. Finally, purple toluidine blue staining for cartilaginous matrix was detectable in all areas of new bone formation, most notably at the cortical bone-scaffold junctions in all treatment groups.

Figure 3.5. Histological analysis of cellular infiltration and bone formation within/around the scaffold-filled defect at 12 weeks post-op. (A) Schematic of the histological sectioning along the longitudinal direction to enable examination of new bone formation across the full length of the defect; (B) Bright field and polarized light (PL) micrographs of hematoxylin & eosin (H&E) and toluidine blue (Tol Blue) stained sections. For each treatment group (HA-PELA, HA-PELA + rMSCs, and HA-PELA + rhBMP2), images were taken both at the cortical bone-scaffold junction and within the center of the scaffold. Arrowheads indicate blood vessels and * indicates macrophages/foreign body giant cells. Scale bar = 500 μm for micrographs taken at 50X magnification and 150 μm for those taken at 200X magnification. Inset images show a representative blood vessel in the HA-PELA group and a representative foreign body giant cell in the HA-PELA + rMSCs group. Inset scale bars = 20 μm .

Figure 3.5

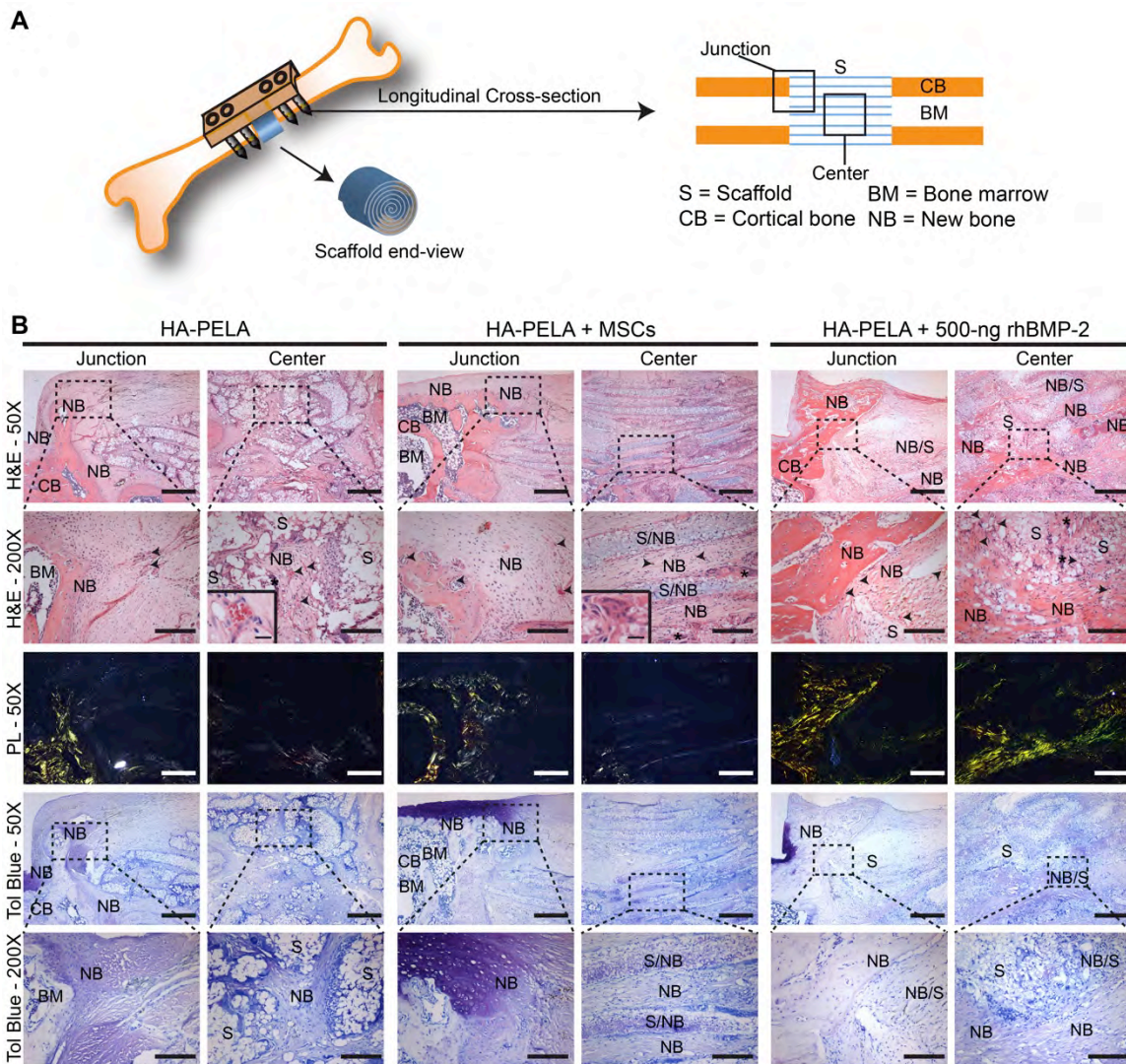
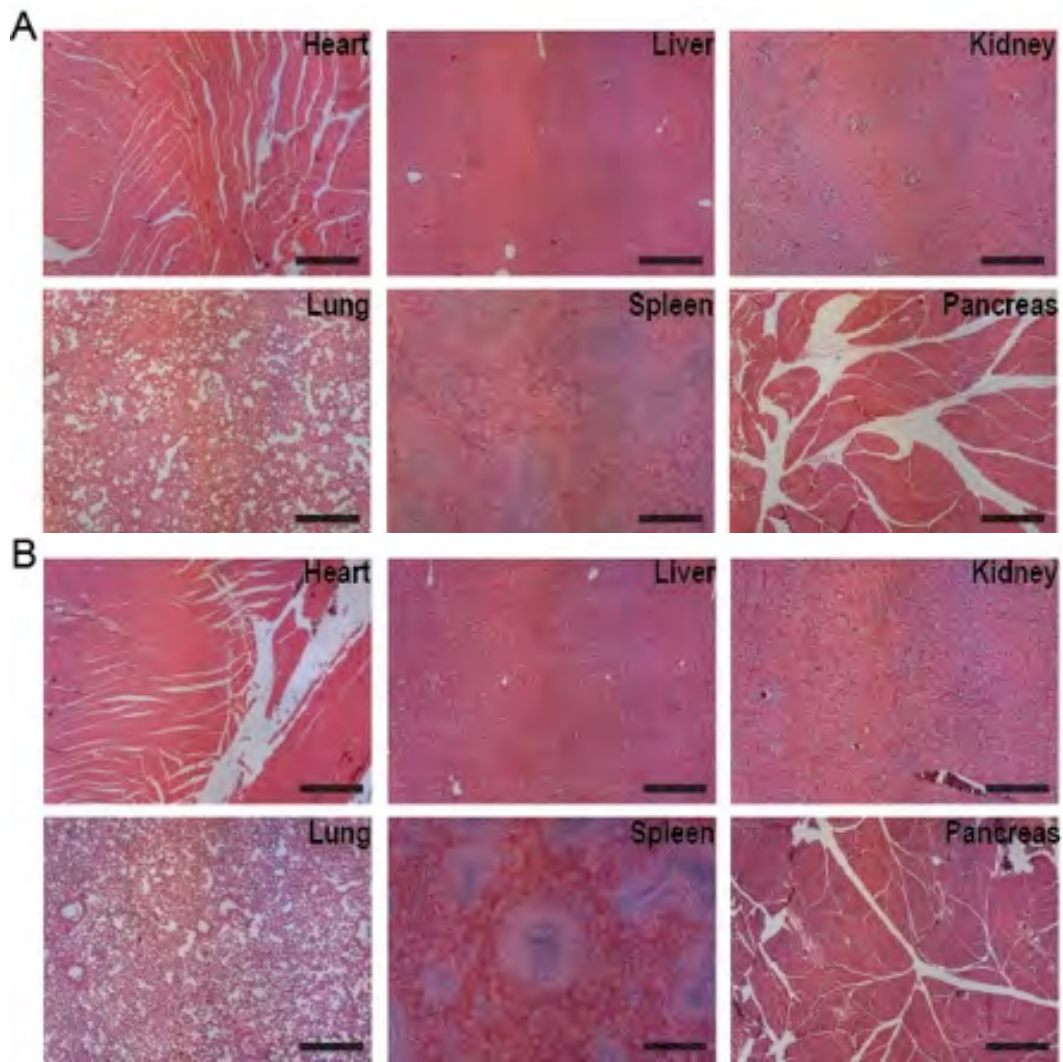


Figure 3.6. Hematoxylin and eosin staining of vital/scavenger organs (heart, liver, kidney, lung, spleen and pancreas) collected at (A) 12 weeks and (B) 24 weeks after implantation of HA-PELA. No abnormality was detected compared to un-operated healthy controls [135].

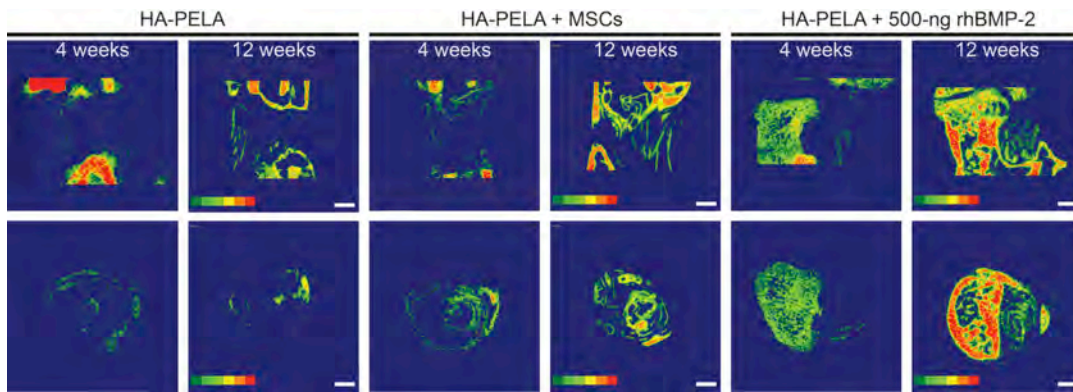
Figure 3.6



3.5 μ -CT analyses

Bone mineral density mapping of the longitudinal and axial center slices of the reconstructed ROI at 4 and 12 weeks post-op was used to visualize the morphology and maturity the new bone formed around/within the scaffold-filled defects over time (Fig. 3.7). The color mapping revealed that new bone formed at the scaffold/cortical bone interface and within the scaffold-filled defect in all treatment groups after 4 weeks. Most robust and mature bone formation was observed with the group absorbed with rhBMP-2, with the recanalization of the new bone clearly visible at 12 weeks. More robust new bone appeared to be localized on the side opposite the PEEK fixation plate. In the absence of rhBMP-2, bone formation was more clearly templated by the spiral scaffolds for both the HA-PELA alone and HA-PELA + MSCs groups. The templated spiral new bone growth in these treatment groups can be visualized by the vertical lines and concentric lines in the longitudinal and axial color maps, respectively. Maturation of the new bone from 4 to 12 weeks was observed for all groups, as evidenced by the increased red color in the mineral density color mapping.

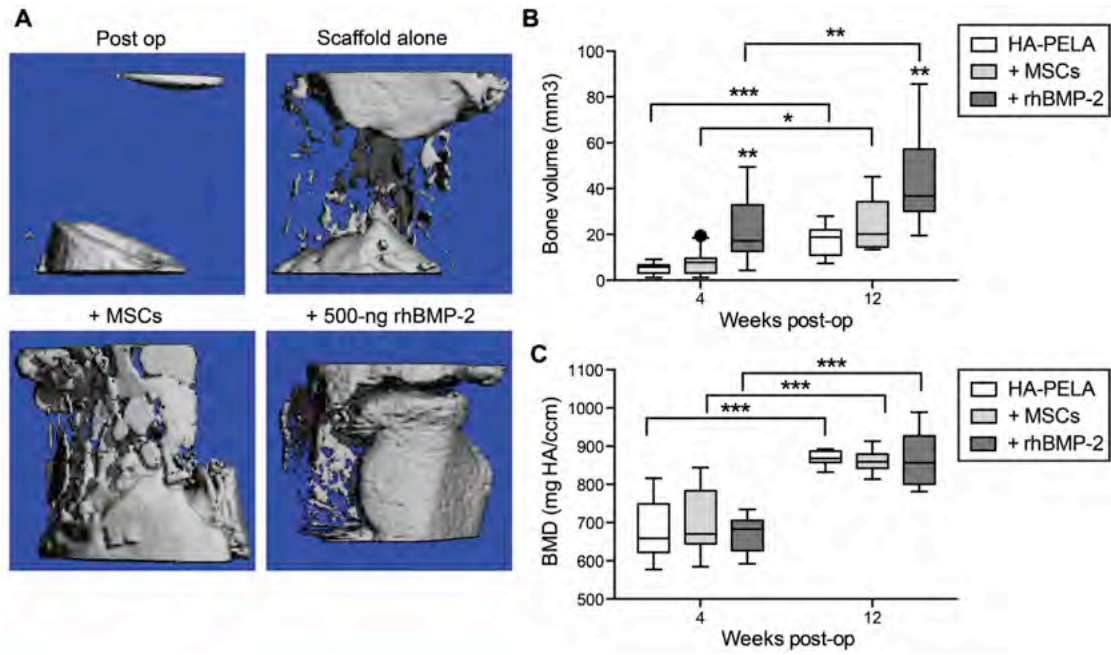
Figure 3.7. Two-dimensional bone mineral density color maps of the scaffold-filled defect over time (red representing higher mineral density). Longitudinal (top) and axial (bottom) mid-slices of the defect treated with HA-PELA, HA-PELA + rMSCs, and HA-PELA + 500 ng rhBMP-2 at 4 weeks and 12 week post-op are shown. Scale bars = 1 mm.

Figure 3.7

Reconstructed 3-D μ -CT images confirmed the bony callus formation at the graft-cortical bone interface and some degrees of scaffold-templated growth toward the center of the defect in the HA-PELA group (Fig. 3.8A). Greater amounts of scaffold-templated new bone formation were visible at the center of the defect by 12 weeks with pre-seeded MSCs, consistent with X-ray radiograph observations (Fig. 3.4C). The most robust bony callus formation bridging over the defect was observed with the HA-PELA + rhBMP-2 treatment group. Bone volume and bone mineral density in all treatment groups increased over the 12-week post-op monitoring period (Fig. 3.8B & C). The HA-PELA + rhBMP-2 group resulted in significantly greater bone volume than HA-PELA alone or HA-PELA + MSCs at both 4 and 12 weeks post-op (Fig. 3.8B). There was no significant difference in bone mineral density among the three treatment groups at a given time point examined (Fig. 3.8C).

Figure 3.8. *In vivo* μ -CT monitoring of the scaffold-filled defects over time. (A) μ -CT 3-D reconstructions of the ROI immediately post-op and those containing HA-PELA, HA-PELA + rMSCs, or HA-PELA + rhBMP-2 at 12 weeks post-op. Extra slices from the adjacent cortical bone were included for the reconstruction of the post-op ROI for convenient visual reference. For all treatment groups at 12 weeks, only the 5-mm defect site is shown. Global thresholding was applied to exclude the HA-PELA scaffold within the defect. (B-C) μ -CT quantification of new bone volume (mm^3) and bone mineral density (BMD; mg HA/cm^3) in the ROI at 4 and 12 weeks post-op (n=11). Data are graphed as Tukey box and whisker plots where whiskers represent the lower and upper 1.5 interquartile ranges (IQR). Data points outside the 1.5 IQR are plotted as individual points. * $p < 0.05$. ** $p < 0.01$. *** $p < .001$.

Figure 3.8

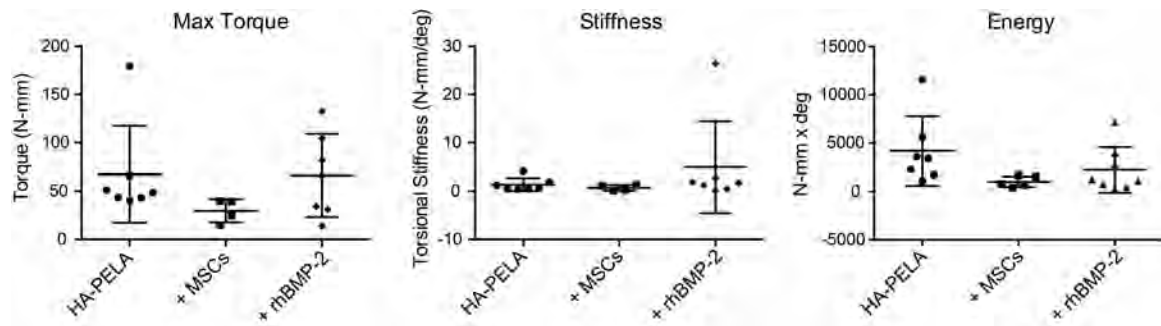


3.6 Torsional testing of treated femurs

Explants from all three treatments groups were potted in bone cement and ramped to failure under torsion. There was no significant difference in maximum torque, stiffness, or energy to failure between groups (Fig. 3.9).

Figure 3.9. Torsional testing of 12-week explants as a function of treatment (HA-PELA alone, MSCs, 500-ng rhBMP-2). Data are presented as scatter plots with mean \pm standard deviation.

Figure 3.9

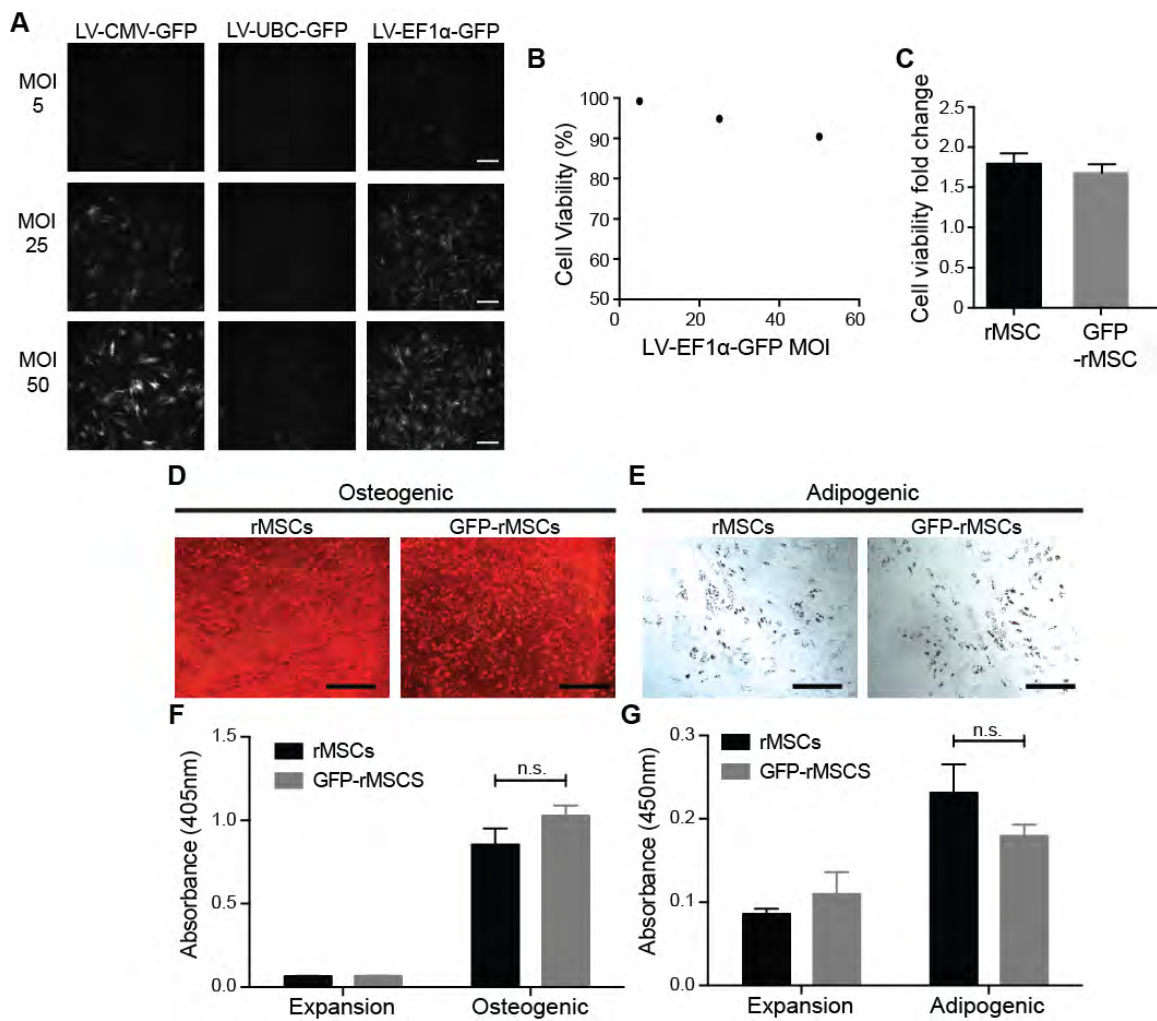


3.7 Tracking GFP-labeled MSCs *in vivo*

We compared the labeling efficacy of GFP driven by cytomegalovirus (CMV), elongation factor 1-alpha (EF1 α), and ubiquitin C (UBC) promoters at three multiplicities of infection (MOI; 5, 25, 50) to optimize lentiviral GFP transduction of MSCs. CMV and EF1 α promoters resulted in the highest levels of GFP signal with high labeling efficiency (>90%) (Fig. 3.10A). EF1 α -GFP at an MOI of 25 was chosen for all subsequent MSC labeling due to the uniform GFP signal, low cytotoxicity (Fig. 3.10B), and minimal effects on cell proliferation (Fig. 3.10C). There was no significant compromise in the potency of induced osteogenic or adipogenic differentiations of the MSCs upon GFP-labeling (Fig. 3.10D-G).

Figure 3.10. Lentiviral GFP labeling of rMSCs. (A) Fluorescence microscopy of rMSCs transduced with lentiviral vectors driving GFP expression by CMV, UBC, or EF1 α promoters with increasing MOI's. Scale bar = 150 μ m. (B) Viability of rMSCs upon 24-h exposure to various MOI's of EF1 α -GFP lentivirus relative to untreated controls. (C) Fold change in cell viability of GFP-rMSCs (transduced with LV-EF1 α -GFP at MOI = 25) vs. untreated rMSCs over 72 h. (D) Alizarin red S staining of untreated rMSCs and GFP-labeled rMSCs following 14-day culture in osteogenic medium; Scale bar = 250 μ m. (E) Oil red O staining of untreated rMSCs and GFP-labeled rMSCs following 14-day culture in adipogenic medium; Scale bar = 250 μ m. (F) Quantification of alizarin red stains in the rMSC and GFP-rMSCs cultures after 14 days in expansion (negative control) and osteogenic medium. The stains were released by acid treatment for spectroscopic quantifications. (G) Quantification of Oil red stains in the rMSC and GFP-rMSCs cultures after 14 days in expansion (negative control) and adipogenic medium. The stains were released by isopropanol for spectroscopic quantifications.

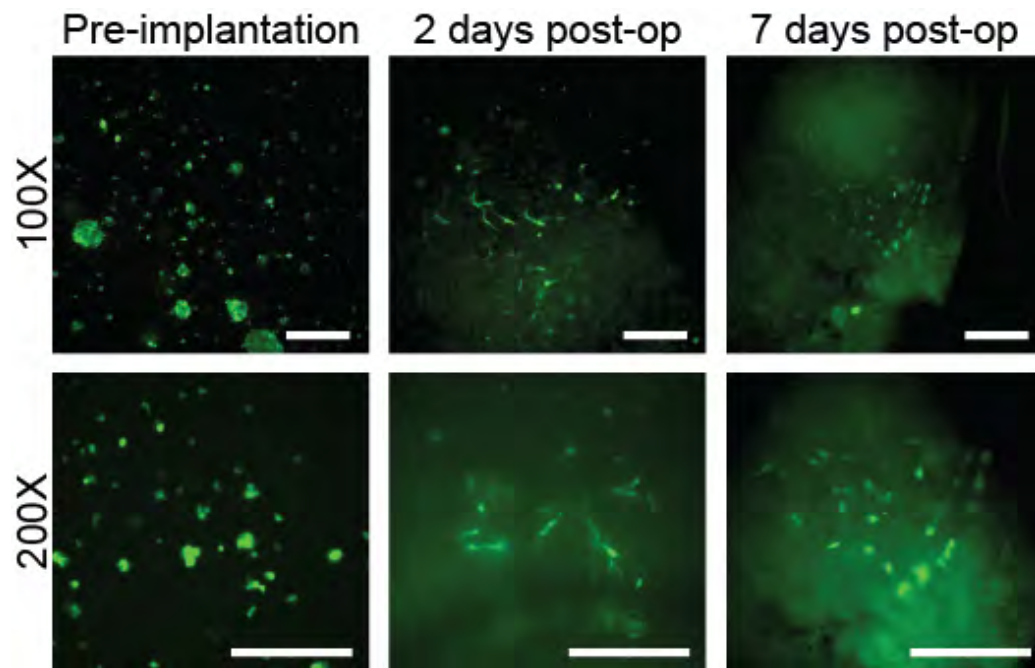
Figure 3.10



GFP-labeled cells were seeded on HA-PELA and implanted in the 5-mm femoral segmental defect and their fate was tracked over 4 weeks post-implantation. GFP-MSCs remained detectable on the scaffold at 2 and 7 days after implantation (Fig. 3.11) as shown by fluorescent microscopy, although the number of GFP-positive cells decreased over time. Morphology of the GFP-labeled cells attached to the scaffolds changed from a rounded shape pre-implantation to a more extended/spindle shape, supporting their ready adhesion and spreading on the osteoconductive scaffolds. No labeled cells were detected at 4 weeks post-op by immunohistochemistry with anti-GFP antibodies (data not shown).

Figure 3.11. Fluorescence microscopy of GFP-labeled rMSCs adhered to HA-PELA scaffolds before and after implantation. Scale bars = 300 μm .

Figure 3.11



4. Discussion

We hypothesized that a spiral-wrapped electrospun scaffold would support templated bone formation to augment the repair of long bone defects. To test this hypothesis, we used a 5-mm rat femoral segmental defect which has been validated as a critical long bone defect model to test the performance of bone tissue engineering scaffolds by our group and others [22,135,166,228]. The critical size of the defect, coupled with the removal of the surrounding periosteum, serves to emulate a challenging clinical scenario [229] precluding healing without proper intervention [230]. In our prior work we demonstrated that the handling properties (aqueous wettability and stability, tensile elasticity) and bioactivity (osteoconductivity and osteoinductivity) of electrospun degradable polymer/HA composites can be significantly improved by using an amphiphilic PELA block co-polymer instead of the conventional PLA [209]. Here we demonstrated that these handling and bioactivity characteristics made electrospun HA-PELA uniquely suited for the spiral-wrapped bone repair strategy.

Specifically, the hydrophilic surface and osteoconductive nature of HA-PELA allowed for easy loading of the MSC suspension and supported cellular adhesion and spreading (Fig. 3.2B & Fig. 3.11). The elastic properties of HA-PELA facilitated the spiral-wrapping of HA-PELA without brittle fracture. Manual rolling of the scaffold did not compromise the viability of the cells seeded on the scaffolds as revealed by *in vitro* monitoring of cell viability and proliferation over

the course of 14 days after the spiral-wrapping (Fig. 3.2). Furthermore, the aqueous wettability of HA-PELA and high surface area of the well-integrated nanocrystalline HA (known for affinity for a wide range of proteins)[135] and amphiphilic polymer also enabled facile loading and stable retention of aqueous rhBMP-2. The HA-PELA exhibited a slow yet sustained *in vitro* release of 10-15% of the loaded rhBMP-2 (235.8 ng/cm², same as the *in vivo* loading dose applied) over the first 3 days (Fig. 3.3A). Such an early release profile was in stark contrast to the burst release profile of conventional scaffolds (e.g. 100% release from clinically used collagen sponge after 2 days *in vitro*)[22] that are known to cause significant local and systemic side effects including ectopic bone formation.[20,231–233] Importantly, we also showed that the rhBMP-2 retained on the scaffold after 7-day incubation in PBS remained bioactive as evidenced by their ability to induce osteogenic transdifferentiation of adhered C2C12 myoblasts (Fig. 3.3B).[234] Uncompromised rMSC viability and sustained release of bioactive rhBMP-2 supported by HA-PELA allowed us to effectively compare how these therapeutic modalities could augment the healing of HA-PELA spiral-filled rat femoral segmental defects.

The spiral-wrapped scaffold, with a structure closely matching with that of the removed femoral shaft, could be press-fit within the 5-mm segmental defect and remained stably fixed throughout the course of the 12-week study. The implanted scaffolds were still visible by histology at 12 weeks post-op (Fig. 3.5), consistent with prior *in vitro* findings of only >20% mass loss after 12-week

incubation in PBS.[209] Macrophages and foreign body giant cells but no neutrophils or eosinophils were detected from the cells infiltrated to the scaffolds, consistent with mild foreign body and immunogenic responses to HA-PELA and its degradation products and the lack of severe chronic inflammation or allergic reactions.[48] Degradation-induced immune response to PLA-based materials is well documented.[48,235] It has been hypothesized that calcium phosphate minerals including HA can buffer the acidic degradation products of PLA thereby mitigating their immunogenicity.[236] It is unclear whether the mild local immune responses observed could be partially attributed to the buffering effect of the 10 wt% HA incorporated into the amphiphilic scaffold or if it was merely a result of incomplete degradation of the scaffold by 12 weeks.

All treatment groups, including the HA-PELA scaffold alone, facilitated new bone formation via an endochondral ossification mechanism within the defect site, as revealed by histology (Fig. 3.5) and μ -CT analyses (Fig. 3.7, Fig. 3.8). The new bone formation resulting from the treatment with HA-PELA alone, particularly beyond the scaffold-cortical bone junction, supports the osteoconductivity of the scaffold.[135] The delivery of MSCs via the HA-PELA spiral resulted in substantial increase of new bone formation away from the cortical/implant junctions. In agreement with our hypothesis, the new bone appeared to be directly templated by the spiral-wrapped scaffold as confirmed by histology (Fig. 3.5B) and μ -CT 2-D bone mineral density mapping (Fig. 3.7). Such uniform distribution of new bone across the longitudinal span of the defect,

concentrically separated by the spiral-wrapped electrospun scaffold and apparently promoted by the pre-seeded MSCs, has not been reported previously. Despite the unique morphology of the new bone, the delivery of rMSCs alone did not result in significantly higher bone volume or bone mineral density or the complete bridging of the defect by 12 weeks (Fig. 3.86B & C). The not-yet degraded spiral-wrapped scaffold could have prevented the concentrically formed new bone from continuously growing across the axial space and fusing together.

It is widely accepted that exogenous MSCs can improve bone formation in critical-size defects,[237–239] although some fail to show statistically significant improvement in bone formation with cell-seeded constructs over cell-free constructs.[240] It is still under intense debate as to whether exogenous MSCs locally delivered to the defect site contribute to healing via paracrine effect (e.g. secreted factors) or by direct participation in osteo/chondral differentiation, with the former receiving more recent attention.[241–243] Whereas literature reports on the fate of transplanted MSCs vary, they generally show that implanted exogenous cells have a limited lifetime within the defect site and do not substantially differentiate into osteoblast-like cells.[238,244,245] Here, by tracking GFP-labeled MSCs delivered by the same method into the 5-mm femoral segmental defect, we showed that viable exogenous cells could still be detected up to 7 days post-implantation, although their number decreased over time. These cells also changed from a rounded shape immediately after cell

seeding on HA-PELA to a spindle shape over time, and such improved cell spreading is likely due to the absorption of endogenous cell-adhesive proteins from the tissue microenvironment onto the scaffolds. Agreeing with literature reports that exogenous cells seeded on a mineral-based carrier cannot be detected 14 days post- subcutaneous implantation,[244] we also did not observe GFP-labeled rMSCs at later time points by IHC. It is unclear whether the failure of the new bone templated by HA-PELA + MSCs to completely bridge over the entire defect by 12 weeks was due to the poor survival of the transplanted cells, the relatively low numbers of MSCs seeded (<240,000 / scaffold), and/or the insufficient duration of paracrine effect exerted by the viable transplanted cells.

With an exceptionally low dose of rhBMP-2 delivered by HA-PELA (~10 fold lower than those used clinically with collagen sponges in humans, after scaling by defect dimensions)[18], we observed robust new bone formation across nearly the entire defect site. Our earlier study showed that HA-PELA could effectively sensitize the response of MSCs to osteogenic inductions by orders of magnitude compared to conventional degradable scaffolds *in vitro*. [209] It is conceivable that the HA-PELA spiral may have also sensitized the response of the endogenous progenitor cells that migrated and adhered onto the scaffold to the osteogenic induction by the locally released rhBMP-2 *in vivo*. The new bone formed with rhBMP-2 induction was not only significantly higher in volume than those templated by HA-PELA alone or HA-PELA + MSC (Fig. 3.8B), but also appeared more mature as revealed by polarized light microscopy (Fig. 3.5B)

and the substantial recanalization of new bone by 12 weeks (Fig. 3.7). However, in agreement with our hypothesis, the new bone formed by rhBMP-2 induction appeared less templated by the spiral configuration than the bone formed in the MSC group. This may be due to the released rhBMP-2 being less confined to the immediate vicinity of the spiral template, resulting in greater bone formation on the scaffold periphery. By contrast, the possible direct participation of exogenous MSCs may explain why the new bone formation was confined to the spiral template where these MSCs are adhered and confined.

It is worth noting that restoration of torsional strength of the defect was not achieved by 12 weeks in any of the treatment groups (Fig. 3.9). The 12-week timeframe in the current study was not sufficient to examine whether the spiral-templated new bone growth in-between adjacent scaffold layers would eventually merge into more mature and congruent bone as the scaffold fully degrades. Fusion of the concentrically distributed new bone layers could potentially be accelerated by introducing macropores in the spiral-wrapped electrospun scaffold, similar to the design proposed by Jiang et al.[93] Meanwhile, doubling the loading dose of rhBMP-2 from the exceptionally low 500-ng/defect applied in the current study, but still lower than the 2 μg to 11 μg per 5-mm segmental defect utilized with most literature scaffolds,[22,213,237,246–248] may expedite the functional healing of the defect. Finally, applying a combination of exogenous cells, therapeutic agents, or both to the spiral-wrapped scaffold to synergistically

stimulate the osteogenesis and angiogenesis may also present an opportunity to further improve the functional outcome of bone repair.

5. Conclusions

We explored the use of spiral-wrapped electrospun composite HA-PELA scaffolds for templating bone formation and promoting the repair of critical-size long bone defects. The HA-PELA scaffold was readily seeded with MSCs or loaded with rhBMP-2 and stably implanted into 5-mm mid-shaft femoral segmental defects in rats. We show that HA-PELA alone, pre-seeded with MSCs, or with a low dose of rhBMP-2 (500 ng) all supported varying degrees of bone formation within the defect. Bone formation was effectively templated by the scaffolds when combined with MSCs, resulting in the formation of laminated new bone sandwiched in-between adjacent electrospun scaffold layers. The most robust bone formation was obtained with the use of a single low dose of 500-ng rhBMP-2. These encouraging *in vivo* outcomes, coupled with the advantageous handling characteristics of HA-PELA (elasticity, hydrophilicity, hydration-induced stiffening), support spiral-wrapped electrospun HA-PELA scaffolds as promising materials for the repair of long bone defects.

Acknowledgements

I would like to thank April Mason-Savas for histology support and Dr. Ali Akalin for assessment of immune cell penetration. This research was supported in part by the National Institutes of Health Grant R01AR055615 and by the

Department of Defense Congressionally Directed Medical Research Programs under award number W81XWH-10-0574. Core resources supported by the National Institutes of Health shared instrumentation grant S10RR027082 were used.

**CHAPTER IV: Rapid Prototyping Amphiphilic Polymer/Hydroxyapatite
Composite Scaffolds with Hydration-Induced Self-Fixation Behavior**

Preface

This chapter has been adapted from:

Kutikov AB, Guirjala A, Song J. "Rapid prototyping amphiphilic polymer/hydroxyapatite composite scaffolds with hydration-induced self-fixation behavior" *Tissue Engineering Part C: Methods* 2014.

doi:10.1089/ten.TEC.2014.0213

Dr. Jie Song and Artem Kutikov designed the experiments in this work. Anvesh Gurijala contributed to preliminary optimization of rapid prototyping parameters and CAD. Artem Kutikov performed the experiments in this work.

Abstract

Two major factors hampering the broad use of rapid prototyped biomaterials for tissue engineering applications are the requirement for custom-designed or expensive research-grade three-dimensional (3-D) printers and the limited selection of suitable thermoplastic biomaterials exhibiting physical characteristics desired for facile surgical handling and biological properties encouraging tissue integration. Properly designed thermoplastic biodegradable amphiphilic polymers can exhibit hydration-dependent hydrophilicity changes and stiffening behavior, which may be exploited to facilitate the surgical delivery/self-fixation of the scaffold within a physiological tissue environment. Compared to conventional hydrophobic polyesters, they also present significant advantages in blending with hydrophilic osteoconductive minerals with improved interfacial adhesion for bone tissue engineering applications. Here we demonstrated the excellent blending of biodegradable, amphiphilic PELA triblock co-polymer with HA and the fabrication of high-quality rapid prototyped 3-D macroporous composite scaffolds using an unmodified consumer-grade 3-D printer. The rapid prototyped HA-PELA composite scaffolds and the PELA control (without HA) swelled (66% and 44% volume increases, respectively) and stiffened (1.38-fold and 4-fold increases in compressive modulus, respectively) in water. To test the hypothesis that the hydration-induced physical changes can translate into self-fixation properties of the scaffolds within a confined defect, a straightforward in vitro pull-out test was designed to quantify the peak force required to dislodge

these scaffolds from a simulated cylindrical defect at dry vs. wet states. Consistent with our hypothesis, the peak fixation force measured for the PELA and HA-PELA scaffolds increased 6-fold and 15-fold upon hydration, respectively. Furthermore, we showed that the low-fouling 3-D PELA inhibited the attachment of NIH3T3 fibroblasts or MSCs while the HA-PELA readily supported cellular attachment and osteogenic differentiation. Finally, we demonstrated the feasibility of rapid prototyping biphasic PELA/HA-PELA scaffolds for potential guided bone regeneration where an osteoconductive scaffold interior encouraging osteointegration and a non-adhesive surface discouraging fibrous tissue encapsulation is desired. This work demonstrated that by combining facile and readily translatable rapid prototyping approaches with unique biomaterial designs, biodegradable composite scaffolds with well-controlled macroporosities, spatially defined biological microenvironment, and useful handling characteristics can be developed.

1. Introduction

Bone tissue engineering approaches aim to overcome the limitations of autografts (donor site morbidity, limited quantity) and allografts (high failure rate, risk for infections) for the repair of critical-size bone defects.[24] Tissue engineering typically employs degradable biomaterial scaffolds to support the delivery of cells/therapeutics to the defect site to guide/promote tissue regeneration and eventually be replaced by the regenerated tissue of interest.[27] The performance of such scaffolds is dependent not only on the chemical and structural properties of the biomaterial (e.g. chemical composition, network structure, and interfacial adhesion in the case of composites), but also the physical design (e.g. scaffold architecture, porosity), biological performance (e.g. osteoconductivity) and handling characteristics of the scaffold. Rational design that takes into consideration all of these factors is more likely to produce scaffolds that could meet clinical needs and are readily translatable (scalable, off-the-shelf).

The bioactivity of synthetic polymeric materials for orthopedic applications can be improved by structurally incorporating calcium apatite minerals such as HA, the principle mineral component in bone. Besides the intrinsic osteoconductivity of HA[249] that encourages osteoblast/progenitor cell recruitment and growth,[132] the unique pH-dependent surface potential of HA also translates into the ability to enrich a wide range of endogenous protein factors and deliver exogenous protein therapeutics including osteogenic growth

factors.[135,250] For polymer/HA composite materials, adequate interfacial adhesion between the polymer and mineral components is essential for achieving robust handling characteristics and mechanical properties.[138,151,169] However, most biodegradable polymers used to fabricate resorbable scaffolds are hydrophobic. This hydrophobicity/hydrophilicity mismatch results in poor interfacial adhesion and brittle composites with poor handling characteristics (i.e. difficulty to be press-fit into defects, prone to brittle fractures). Furthermore, hydrophobic materials cause difficulty in loading aqueous solutions (cells and/or growth factors) into the scaffold and may potentially change protein conformations via hydrophobic interactions, resulting in compromised bioactivity of the absorbed protein therapeutics.[251,252]

With the aim of developing an improved biodegradable polymer/HA composite, we recently reported the a biodegradable amphiphilic block copolymer, PELA-based HA composite.[209] By blending PELA with HA and electrospinning the stable suspension, we produced non-woven fibrous meshes with more uniform morphologies, increased elasticity, and enhanced osteoconductivity and osteoinductivity when compared to electrospun HA-poly(D,L-lactic acid) composites. Interestingly, we also discovered that the amphiphilic nature of the electrospun scaffolds translated into super-hydrophilicity (water contact angle $\sim 0^\circ$) and an increased elastic modulus upon hydration. While electrospun HA-PELA would find unique orthopedic applications (e.g. as synthetic periosteal membrane wrapped around structural allografts),

their limited thickness and porosity[66,95,253] make them less suited for treating large defects where sufficient nutrient transport and cellular ingrowth throughout a 3-D macroporous scaffold is desired.

Rapid prototyping techniques such as selective laser sintering (SLS),[254] powder-based three-dimensional printing (3DP),[106] and fused deposition modeling (FDM) have been employed in the fabrication of large 3-D scaffolds for bone tissue engineering. These rapid prototyping approaches have typically required custom-designed or expensive (>\$100,000) research-grade printers, limiting their widespread uses by the research community. Nevertheless, such techniques enable the formation of HA or HA/polymer composite scaffolds with defined geometries and controlled interconnected pore architecture. This scaffold design enables more homogenous cell distribution and ensures consistent mechanical properties that are not attainable by less-controlled fabrication techniques such as salt leaching or gas foaming.[255,256] While rapid prototyping technology has become increasingly refined, the selection of biomaterials suitable for prototyping has remained limited. The most widely prototyped polymers are hydrophobic polyesters such as PCL,[257–261] PLLA,[262] or PLGA.[263] Rapid prototyped amphiphilic polymer scaffolds composed of polyethyleneoxide-terephthalate (PEOT) and polybutylene-terephthalate (PBT) (PEOT/PBT) using a specialized printer have been explored for cartilage tissue engineering.[264–266] However, the PBT component is not biodegradable, resulting in crystalline, hard-to-resorb remnants upon degradation

in vivo. [267] Furthermore, rapid prototyping HA-PEOT/PBT composite scaffolds for bone tissue engineering was not explored. We hypothesize that rapid prototyping HA-PELA scaffolds offers a unique opportunity to combine the outstanding biological properties (osteoconductivity and osteoinductivity) of HA-PELA with a well-defined 3-D macroporous architecture. Furthermore, we expect that the 3-D HA-PELA scaffold would exhibit novel self-fixation behavior derived from the unique hydration-induced swelling and stiffening behavior of the amphiphilic composite.

Here we report the rapid prototyping of interconnected macroporous PELA and HA-PELA scaffolds using an unmodified consumer-grade 3-D printer. We examined the swelling behavior and mechanical properties of the scaffolds. We also quantitatively evaluated the hydration-induced self-fixation (as a result of hydration-induced swelling and stiffening) of the scaffolds using a custom-designed *in vitro* pull-out test employing a sample holder simulating a confined tissue defect. To demonstrate the utility of the 3-D HA-PELA and PELA scaffolds for applications where opposing cell adhesive properties are desired (e.g. guided bone regeneration), [268] we examined their respective ability to support the attachment and proliferation of NIH3T3 fibroblasts. For potential bone tissue engineering applications, we examined the attachment and osteogenic differentiation of rMSCs on HA-PELA. Finally, we demonstrated the feasibility of fabricating biphasic HA-PELA/PELA scaffolds by rapid prototyping using this consumer-grade 3-D printer.

2. Materials and Methods

2.1 Materials

3,6-Dimethyl-1,4-dioxane-2,5-dione (D,L-lactide) was purchased from Sigma-Aldrich (St. Louis, MO), purified by recrystallization twice in anhydrous toluene, and dried under vacuum prior to use. PEG (20,000 Dalton, BioUltra) was purchased from Fluka (Switzerland). Polycrystalline hydroxyapatite powder (consisting of loose aggregates of ~100-nm crystallites) was purchased from Alfa Aesar (Ward Hill, MA). All other solvents and reagents were purchased from Sigma-Aldrich (St. Louis, MO) and used as received.

2.2 Polymer synthesis

PELA tri-block copolymer was synthesized and characterized as previously described.[209] Briefly, melt ring opening polymerization of D,L-lactide (0.12 mol) was initiated by poly(ethylene glycol) (20,000 Dalton, 0.2 mmol) with Sn(II) 2-ethylhexanoate (~95%, 0.06 mmol) catalysis. The reaction proceeded at 130 °C for 5 hours under argon. The crude PELA was dissolved in chloroform, purified by precipitation in methanol, and dried under vacuum before being subjected to GPC characterizations (described in 2.4).

2.3 Scaffold fabrication

The manufacturing process for 3-D PELA, HA-PELA, and PELA/HA-PELA biphasic scaffolds is depicted in Figure 4.1. Briefly, PELA/HA blends were solvent cast into films, extruded into filaments through a capillary rheometer, and

then rapid prototyped into 3-D scaffolds by FDM in a sub-ambient printing environment.

2.3.1 Preparation of PELA and HA-PELA films

PELA and HA-PELA dense films (~1.6 mm thick) were produced by solvent casting and sectioned into $\sim 0.5 \times 0.5 \text{ cm}^2$ pellets for filament extrusion. For the fabrication of HA-PELA composite films, HA (3.3 g, 25% w/w PELA) was bath-sonicated in 20 mL chloroform for 30 min. PELA (10 g) was added and the mixture was stirred overnight. The HA-PELA mixture was subsequently poured into Teflon molds. The chloroform was evaporated in a fume hood at room temperature overnight and subsequently in a vacuum oven at 60 °C for 24 h. PELA films were prepared by evaporating a chloroform solution of PELA without HA in the same mold followed by vacuum drying under identical conditions.

2.3.2 Filament extrusion

The PELA and HA-PELA filaments were extruded using a LCR7000 capillary rheometer (Dynisco Instruments, Franklin, MA) through a 2.81-mm diameter die. The barrel was preheated at 130 °C (for PELA) or 140 °C (for HA-PELA) for ~90 sec before the PELA or HA-PELA pellets were loaded, followed by continued heating at the respective temperatures for 120 s. The filaments were extruded through the die with a 120 s run time and a barrel piston speed of 32.84-mm min^{-1} and collected manually.

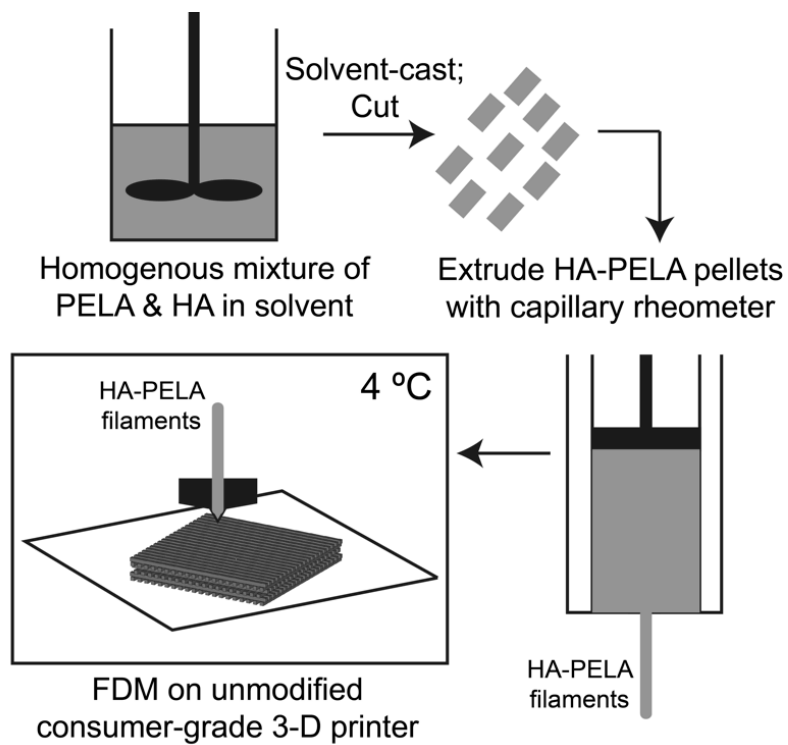
2.3.3 3-D Scaffold fabrication

A 3-D CAD model of a 16 mm × 16 mm square prism (Fig. 4.2a, 2.4 mm or 4 mm in height) was designed in 3-Matics (Materialise, Belgium) and converted into g-code instructions by MakerWare (MakerBot Industries, Brooklyn, New York). A MakerBot® Replicator™ 2X 3-D printer (MakerBot Industries, Brooklyn, New York) cooled in a deli refrigerator at 4 °C was used to print the scaffolds using the PELA or HA-PELA filaments. The sub-ambient printing environment was required to cool PELA below its T_g (~19 °C) so that the filament could be continuously fed into the printer without undesired softening before reaching the heated printing nozzle. Nozzle temperatures of 130 °C and 160 °C were applied to print the PELA and HA-PELA, respectively. The build platform was maintained at 30 °C to ensure stable adhesion of the bottom printed layer to the platform. Scaffolds were printed with a platform feed rate of 90 mm sec⁻¹.

Biphasic PELA/HA-PELA scaffolds were fabricated by extruding 3 layers of HA-PELA followed by 3 layers of PELA. PELA and HA-PELA filaments were loaded into separate nozzles of the Replicator™ 2X. The same printing conditions described above for printing PELA and HA-PELA were applied accordingly.

Figure 4.1. Depiction of the preparation of PELA and HA-PELA 3-D scaffolds by rapid prototyping.

Figure 4.1



2.4 Gel permeation chromatography

PELA and HA-PELA composites were dissolved in tetrahydrofuran, centrifuged (720x g, 5 min) to pellet the HA, before the supernatant was collected and filtered with a 0.4- μm Teflon filter for gel permeation chromatography (GPC) analyses. Molecular weights and polydispersity of PELA was determined by GPC on a Varian Prostar HPLC system equipped with two 5-mm PLGel MiniMIX-D columns (Agilent, Santa Clara, CA) and a PL-ELS2100 evaporative light scattering detector (Polymer Laboratories, UK). Tetrahydrofuran was used as an eluent at 0.3 mL h⁻¹ at room temperature. Molecular weight and polydispersity calculations were calibrated with EasiVial polystyrene standards (Agilent, Santa Clara, CA).

2.5 Scaffold characterization

2.5.1 Optical imaging

Macroscopic optical images of the HA-PELA, PELA, and the biphasic scaffolds were taken on a Leica M50 stereomicroscope equipped with a Leica DFC295 digital camera (Leica Microsystems, Germany).

2.5.2 Scanning electron microscopy and associated energy-dispersive x-ray spectroscopy (EDX)

HA-PELA, PELA, and PELA/HA-PELA biphasic scaffolds were coated with 3 nm of carbon and imaged on a Quanta 200 FEG MKII scanning electron microscope (FEI Inc., Hillsboro, OR) under high vacuum at 10 kV. EDX was

carried out to map the elemental compositions (Ca and P) of the biphasic scaffold at 15 kV with an Oxford-Link INCA 350 x-ray spectrometer (Oxford Instruments, United Kingdom).

2.5.3 Porosity calculation

The theoretical porosity (P) of the scaffolds was calculated by determining the percentage (%) of scaffold volume that is occupied by the polymer rods, as described by Zein et al.[110] and shown in equation (1):

$$P = \frac{V_a - V_t}{V_a} \times 100\% \quad (1)$$

where V_a (mm^3) is the apparent scaffold volume and V_t is the scaffold true volume taken up by polymer. Assuming that the FDM polymer rods are cylindrical in shape with a uniform diameter, the true volume taken up by polymer (V_t) in a square prism can be calculated as

$$V_t = L \times N \times V_{rw} \quad (2)$$

where L is the number of rods per layer, N is the number of layers, and V_{rw} is the volume of each cylindrical rod which is determined by the printed line width and length.

2.6 Swelling behavior

The height and diameter (averaged from 3 measurements) of dry PELA and HA-PELA scaffolds ($n=3$), cored from the square prism FDM blocks using a biopsy punch, was measured with a digital caliper. Line width was averaged from 5 measured lines per scaffold using a light microscope (Axioscop 2 MAT; Carl

Zeiss, Germany) and ImageJ (National Institutes of Health, Bethesda, MD). Scaffold mass was weighed using an analytical balance (ML104; Mettler-Toledo, Columbus, OH). Hydrated scaffold dimensions and mass were measured at various time intervals following incubation in de-ionized water at 37 °C. Residual water was removed prior to weighing by briefly blotting the scaffolds on KimWipes. Change in mass (M/M_0) was calculated by dividing the mass following water equilibration (M) by the initial mass of a scaffold briefly submerged in water (M_0). Change in volume (V/V_0) was calculated in the same manner. Hydrated line width was measured following 24-h incubation in 37 °C deionized water.

2.7 Mechanical testing

The compressive modulus of PELA and HA-PELA scaffolds ($n=3$) was determined on a Q800 DMA equipped with a liquid nitrogen gas cooling accessory (TA Instruments, New Castle, DE). Cylindrical specimens 6 mm in diameter and 4 mm in height, the dimensions used by Moroni et al. for characterizing mechanical properties of macroporous scaffolds,[256] were cored from the square prism FDM blocks. Unconfined compressive testing ($N=3$) was performed at 37 °C for both dry (as-printed) and hydrated (24 h in deionized water) scaffolds. The height and diameter of each specimen was measured with a digital caliper prior to testing. Each specimen was held isothermal at 37 °C for 30 min before being pre-loaded with a force of 0.001N and ramped at a rate of 1.0 N/min to 10 N. The compressive modulus was recorded as the slope of the linear region (0 to 0.5% strain) of the stress/strain curve.

2.8 Pull-out test

A custom sample holder (Fig. 4.5A) simulating a confined circular tissue defect was developed to enable quantitative measurement of the hydration-induced swelling/stiffening effect of the scaffolds via a pull-out test. A CAD model of the sample holder was designed in 3-Matics and fabricated on a MakerBot Thing-O-Matic™ 3-D printer using acrylonitrile butadiene styrene (ABS). In order to ensure consistent specimen placement, the specimen holder portion of the ABS prototype was tight-fitted with a standard cylindrical aluminum spacer (12.7 mm OD x 6.35 mm ID x 4.76 mm H, W.W. Grainger Inc., Chicago, IL). Cylindrical PELA or HA-PELA scaffolds 6 mm in diameter and 4 mm in height, cored from square prism FDM blocks using a biopsy punch, were each drilled with a center axial hole 1.6 mm in diameter to enable the insertion of a drywall nail (1.6 mm diameter, 32 mm long, 3.8 mm diameter head, Fig. 4.5B). The specimen was inserted into the aluminum spacer, and either tested dry or equilibrated in deionized water within the holder for 2 h at 37 °C prior to test. The bottom stem of the custom ABS holder and the sharp end of the inserted nail were secured between the grips of a MTS Bionix 370 mechanical testing system (MTS Systems Corporation, Minneapolis, MN), respectively (Fig. 4.5C). Specimens were ramped at a rate of 50 mm min⁻¹ until they were completely pulled out of the ABS/aluminum holder to determine the peak force as recorded by a 250N load cell (Interface, Scottsdale, AZ).

2.9 NIH3T3 cell attachment and proliferation

HA-PELA and PELA scaffolds (6.3 mm in diameter, 2.4 mm in height) were washed 3 times in deionized water (5 min per wash), sterilized in 70% ethanol, and allowed to air dry in a laminar flow hood. Residual ethanol was removed with a wash in PBS followed by equilibration overnight in Dulbecco's Modified Eagle Medium (DMEM, high glucose; Life Technologies, Grand Island, NY) supplemented with 10% bovine calf serum and 1% penicillin/streptomycin. Immediately prior to cell seeding, media were removed from the scaffolds by vacuum and the scaffolds were transferred to ultra low-attachment 24-well plates (Corning Inc., Corning, NY). NIH3T3 fibroblasts were trypsinized from adherent culture and seeded on the scaffolds (200,000 cells in 50 μ L of medium), and allowed to attach in an incubator (37 °C, 5% CO₂) for 1 h.

A Cell Counting Kit-8 assay (CCK-8; Dojindo Molecular Technologies Inc., Japan) was performed to assess the viability of cells attached on the scaffolds. At each time point, cell-laden scaffolds were transferred to a fresh well containing 0.7 mL of medium and 9% (v/v) CCK-8 reagent. After 4-h incubation, 100 μ L of medium was removed for measurement of absorbance at 450 nm with 650 nm background correction on a Multiskan FC microplate photometer (Thermo Scientific, Billerica, MA). The remainder of the medium was aspirated, the scaffolds were washed with PBS, and replaced with fresh medium for continued culture up to 14 days. The CCK-8 assay was carried out at day 1, 3, 5, 7 and 14.

NIH3T3 attachment on the HA-PELA and PELA scaffolds was also visualized by staining the viable cells with formazan dye using a MTT kit (Cell Proliferation Kit I; Roche, Indianapolis, IN). At 24 h post seeding, scaffolds were transferred to a fresh well containing medium with 9% (v/v) MTT labeling reagent. After 3 h of incubation, the scaffolds were imaged on a Leica M50 stereomicroscope equipped with a Leica DFC295 digital camera (Leica Microsystems, Germany).

2.10 rMSC attachment and osteogenic differentiation

rMSCs were isolated from 289-300g male Charles River SD rats according to the procedure approved by the University of Massachusetts Medical School Institutional Animal Care and Use Committee, and enriched by adherent culture as previously described.[153] The cells were cultured in MSC expansion medium (α MEM without ascorbic acid, containing 20% FBS, 1% penicillin–streptomycin and 2% L-glutamine). Passage 3 MSCs were seeded onto the scaffolds (200,00 cells in 50 μ L of medium), and a CCK-8 assay was performed after 24 h as described in the previous section.

In a separate set of experiments, rMSCs were seeded onto the HA-PELA scaffolds (400,000 cells in 50 μ L medium) and allowed to attach in a humidified incubator (37 °C, 5% CO₂) for 1 h. Following attachment, 0.7 mL of fresh expansion medium was added and the scaffolds were cultured for 24 h. To induce osteogenic differentiation, the medium then was replaced with MSC expansion medium supplemented with 10 nM of dexamethasone, 20 mM of β -

glycerol phosphate, and 50 μ M of L-ascorbic acid 2-phosphate. The scaffolds were cultured in either expansion or osteogenic medium for 14 days with medium changes twice a week. Alkaline phosphatase staining was performed with an Alkaline Phosphatase Leukocyte kit according to manufacturer's instructions (Sigma Aldrich). The protocol was modified to fix the scaffolds in 4% neutral buffered formalin for 15 min rather than in the Citrate-Acetone-Formaldehyde fixative because the scaffolds are soluble in acetone. Alkaline phosphatase stained scaffolds were imaged on a stereomicroscope.

For observation of the microscopic morphology of the adherent cells and the deposited extracellular matrices by scanning electron microscopy (SEM), the scaffolds were air dried, sputter coated with Au (~ 12nm), and imaged on a Quanta 200 FEG MKII scanning electron microscope under high vacuum at 5 kV.

2.11 Statistical analysis

All data are presented as mean \pm standard deviation. Statistical analysis was performed using ANOVA with Tukey post-hoc.

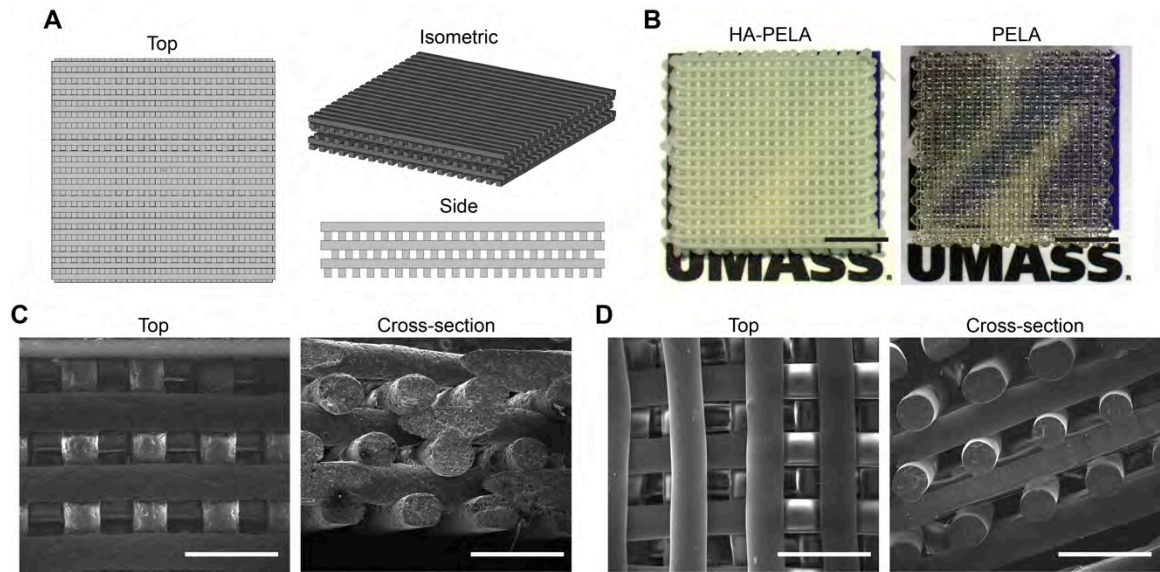
3. Results

3.1 Fabrication and characterization of PELA and HA-PELA scaffolds

CAD software was used to design 16 mm × 16 mm square prism scaffolds with a staggered arrangement of lines (Fig. 4.2A). The line width and height was set to 0.4 mm, the same as the printing nozzle diameter. The perpendicular and staggered line arrangements between neighboring and alternating layers, respectively, were designed to maximize the retention of cells during initial cell seeding. Line spacing of 0.4 mm, which was shown to be advantageous over large spacing (e.g. 0.8 mm) in achieving sufficient seeding efficiency, was used to give a theoretical scaffold porosity of 61.7%. Six-layer (2.4 mm high) scaffolds were designed for all cell culture studies and 10-layer (4.0 mm high) scaffolds were designed for all physical characterizations. The scaffolds were rapid prototyped based on the CAD models by FDM on an unmodified consumer-grade 3-D printer. Macroscopic images of the scaffolds (Fig. 4.2B) revealed that their line width was consistent with the CAD model (0.4 mm). Scanning electron micrographs showed a roughened fiber appearance for the HA-PELA composite scaffolds (Fig. 4.2C) and a smooth fiber appearance for the un-mineralized PELA scaffold (Fig. 4.2D). Cross-sections of both scaffolds revealed circular fibers with open pores between fibers (Fig. 4.2C & D).

Figure 4.2. Images of the CAD model and the rapid prototyped scaffolds. (A) Top, isometric, and side views of scaffold CAD model. (B) Stereomicroscopy images of rapid prototyped HA-PELA and PELA scaffolds. Scale bars = 5 mm. (C) Scanning electron micrographs of the HA-PELA scaffold. Scale bars = 1 mm. (D) Scanning electron micrographs of the PELA scaffold. Scale bars = 1 mm.

Figure 4.2



GPC was used to determine the effect of filament extrusion and rapid prototyping on the molecular weight and polydispersity of PELA (Table 4.1). PELA underwent a slight decrease in molecular weight, while the molecular weight of HA-PELA was minimally affected by the fiber extrusion at elevated temperatures (130 °C for PELA and 140 °C for HA-PELA). The rapid prototyping of PELA at the same nozzle temperature of 130 °C, however, did not lead to further decreases in the molecular weight of the printed PELA scaffold. No significant changes in the molecular weight distributions of PELA and HA-PELA were detected throughout the extrusion and rapid prototyping.

Table 4.1. Molecular weight distribution during the processing of PELA and HA-PELA.

Table 4.1

PELA sample	Proc. Temp. ^a	M _n	M _w	M _n /M _w
As synthesized PELA		85,873	134,077	1.56
HA-PELA filament	140 °C	84,615	129,902	1.53
HA-PELA scaffold	160 °C	82,537	130,945	1.58
PELA filament	130 °C	75,553	116,465	1.54
PELA scaffold	130 °C	76,415	117,039	1.53

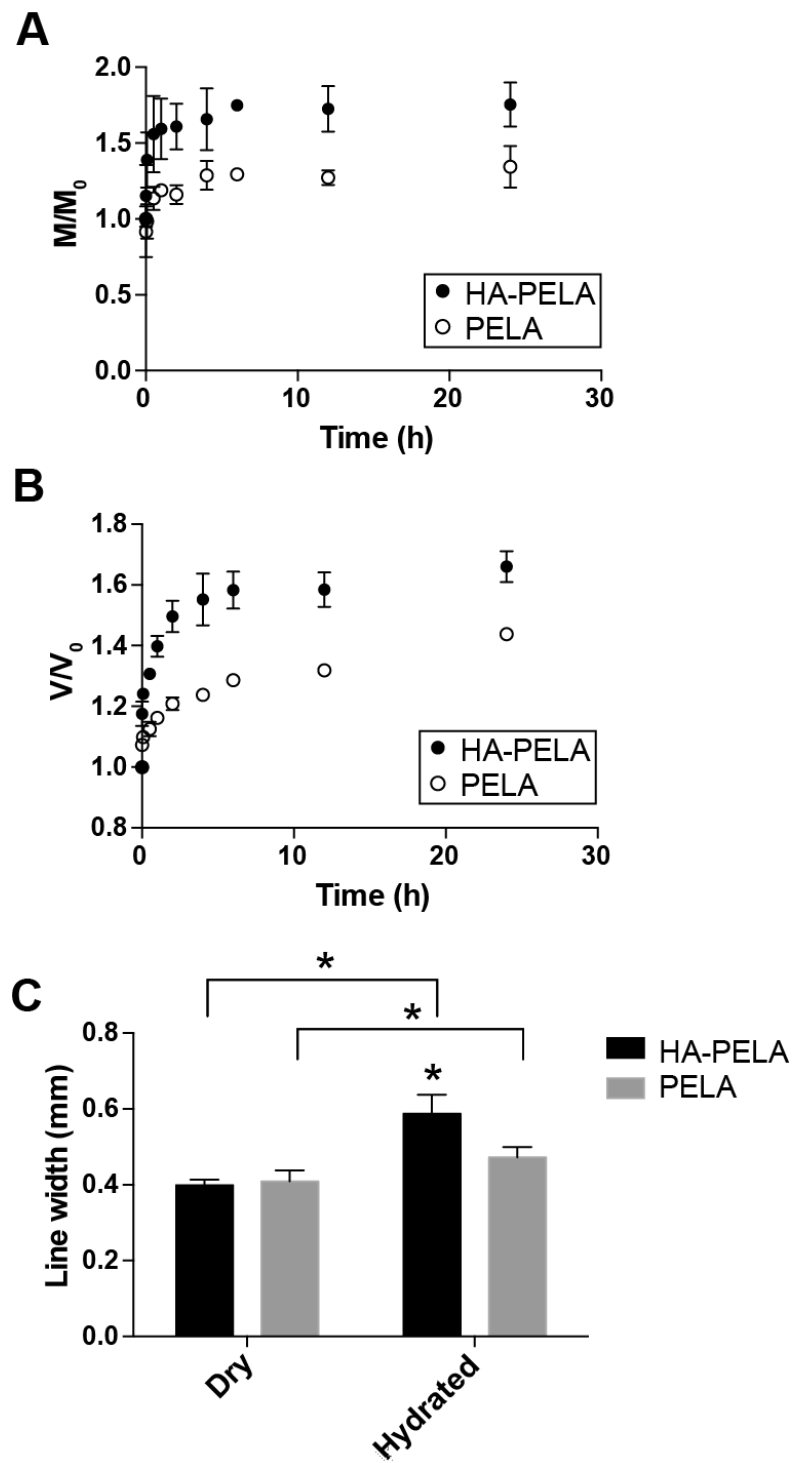
^a referring to the filament extrusion temperature or the nozzle temperature applied to the prototyping of the scaffolds.

3.2 Swelling behavior of HA-PELA and PELA

The swelling and water absorption behavior of the HA-PELA and PELA scaffolds (n=3) in deionized water at 37 °C was monitored over time (Fig. 4.3). The mass and volume of HA-PELA scaffolds increased more rapidly than PELA, resulting in a higher total swelling after 24 h (Fig. 4.3A & B). The mass and volume of both scaffolds increased more rapidly within the first 2-4 h, followed by slower but continued increases, reaching 75% (mass) and 66% (volume) for HA-PELA, and 34% (mass) and 43.8% (volume) for PELA by 24 h, respectively. The line width of the scaffolds also increased over the 24 h swelling period for both scaffolds (Fig. 4.3C), with the fully hydrated HA-PELA scaffold exhibiting significantly higher line width than that of PELA.

Figure 4.3 Swelling behavior of HA-PELA and PELA scaffolds (n=3). (A) Change in scaffold mass (swelled mass (M) / initial mass (M_0)) over time in deionized water at 37 °C. (B) Change in scaffold volume (swelled volume (V) / initial volume (V_0)) over time in deionized water at 37 °C. (C) Change in line width after 24 h hydration in deionized water at 37 °C. *P < 0.05.

Figure 4.3

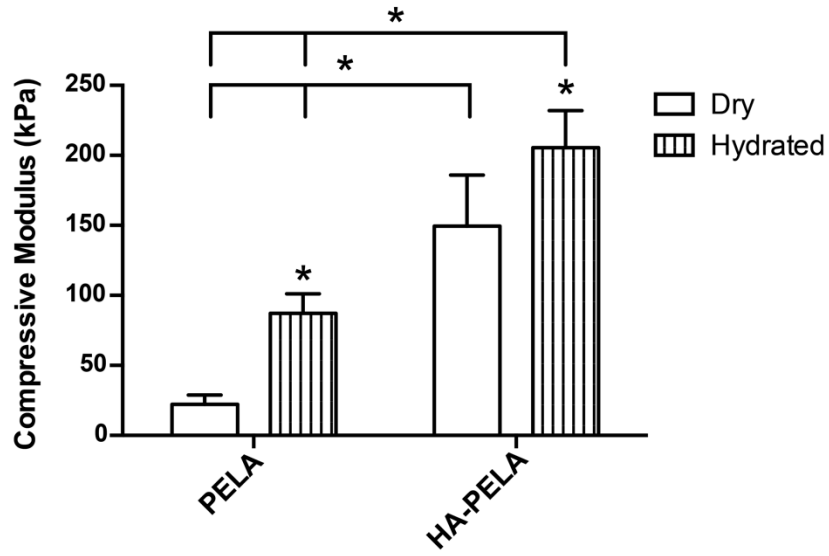


3.3 Hydration-induced stiffening of the scaffolds

The effect of hydration on the compressive modulus of HA-PELA and PELA scaffolds was determined by unconfined compressive testing at 37 °C. In both dry and hydrated states, HA-PELA exhibited a significantly higher compressive modulus than PELA (Fig. 4.4). After hydration in 37 °C deionized water for 24 h, the compressive moduli of both HA-PELA and PELA significantly increased. The magnitude of hydration-induced stiffening was higher for PELA than HA-PELA, with an increase in compressive modulus of 395% compared to 37.5%.

Figure 4.4. Compressive moduli of dry and hydrated PELA and HA-PELA scaffolds (n=3) at 37 °C. *P < 0.05.

Figure 4.4

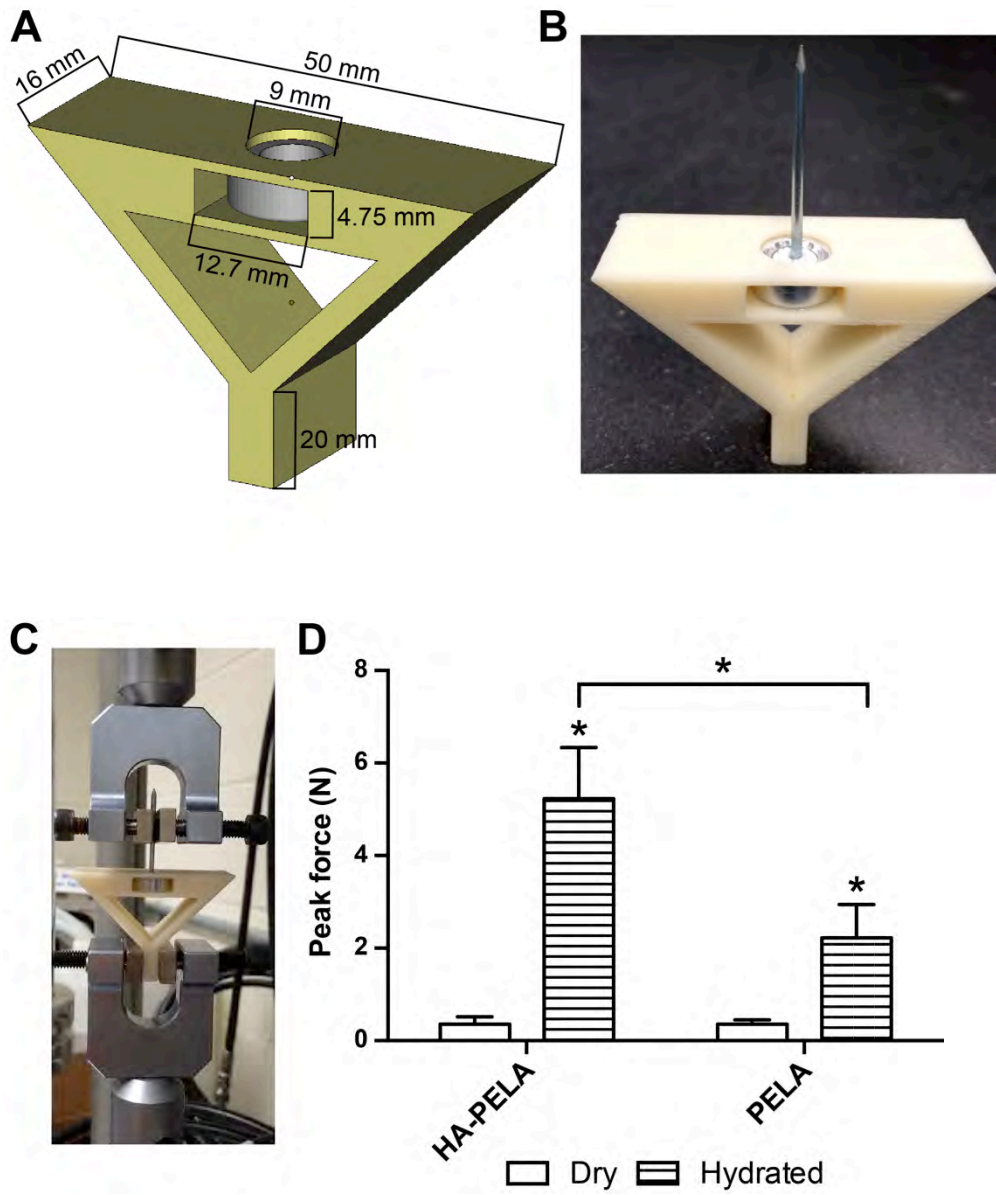


3.4 Hydration-induced self-fixation of scaffolds in a simulated confined defect

A device was designed to assess how the hydration-induced swelling and stiffening of the HA-PELA and PELA scaffolds may be exploited to facilitate their stable self-fixation into skeletal tissue defects as synthetic bone grafts. The CAD model and rapid prototyped ABS holder (Fig. 4.5A) incorporated a cylindrical aluminum spacer to hold a cylindrical test specimen with a bottom stem and a drywall nail penetrating through the center axis of the specimen (Fig. 4.5B) to fit in the grips of a MTS mechanical testing system. This design allows convenient placement of a test specimen in a precisely configured confined cylinder to allow for a pull-out test to be reproducibly carried out on any standard mechanical testing machine (Fig. 4.5C). The peak force required to pull the scaffold out of the specimen holder via the nail grip was determined. This force was measured for dry HA-PELA and PELA scaffolds and for scaffolds pre-swelled in the fixation device in deionized water at 37 °C for 2 h. The peak force increased by 15-fold and 6.3-fold following hydration of HA-PELA and PELA scaffolds in the fixation device, respectively (Fig. 4.5D). The peak fixation force of the hydrated HA-PELA scaffolds was significantly higher than that of the hydrated PELA scaffolds. The observed increase in peak force upon hydration, positively correlated with the difficulty of pulling out the specimen, is a potential indicator of how the specimens may swell/stiffen and become stably fixated within a tissue defect.

Figure 4.5. Hydration-induced self-fixation test. (A) CAD image of the self-fixation testing device with aluminum spacer. (B) Image of the rapid prototyped self-fixation testing device with HA-PELA scaffold inserted. (C) Image of the testing device secured to the grips of the MTS mechanical testing system. (D) Peak forces required to pull HA-PELA and PELA scaffolds (n=4) out of the self-fixation device before and after hydration. *P < 0.05.

Figure 4.5

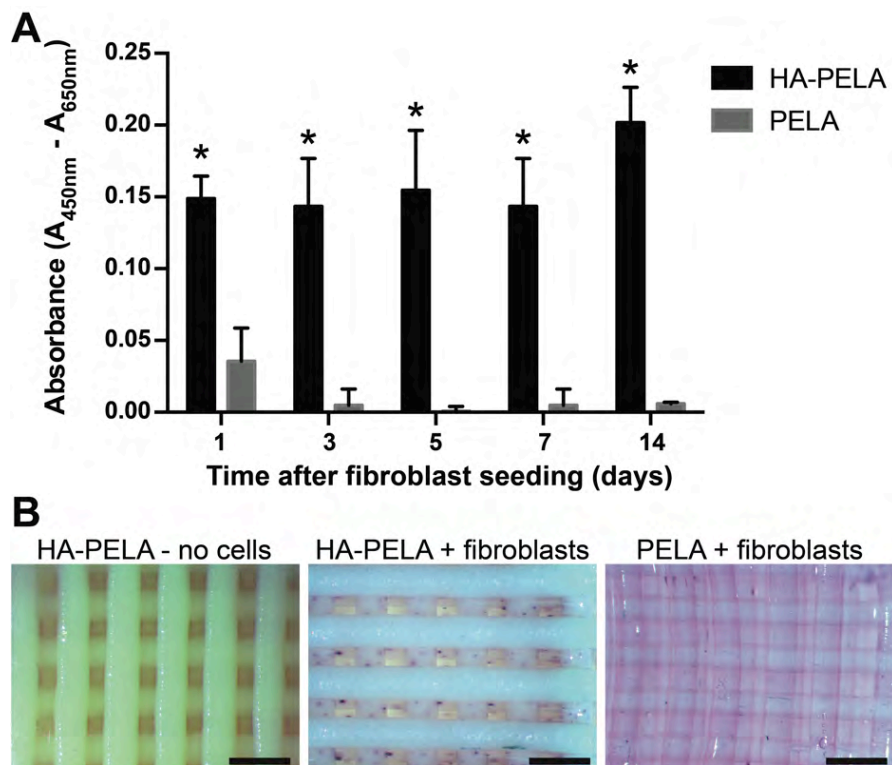


3.5 NIH3T3 attachment and proliferation on the rapid prototyped scaffolds

A CCK-8 assay was used to quantify the viability of NIH3T3 fibroblasts cultured on HA-PELA, PELA, and biphasic scaffolds (Fig. 4.6A). The CCK-8 reagent has low toxicity and the colored formazan product is soluble in medium, allowing the cellular viability on the same scaffolds to be longitudinally monitored in a non-destructive manner. Initial cell attachment was significantly higher on HA-PELA than PELA or the biphasic scaffolds, and the much higher cellular viability was maintained on HA-PELA for 14 days. The extremely poor cellular attachment on PELA left few viable cells on PELA by day 3. Differences in cell attachment between HA-PELA and PELA were further confirmed by staining viable cells with formazan dye (Fig. 4.6B). The HA-PELA scaffolds supported the attachment of viable cells evenly distributed across different layers of the composite scaffold. The PELA scaffold, however, only contained a small number of viable cells trapped within the pores, with few cells directly adhered to the low-fouling fibers.

Figure 4.6. CCK-8 cell viability assay of NIH3T3 attachment and proliferation on HA-PELA and PELA scaffolds (n=3). * $P < 0.05$. (B) Stereomicroscopy images of MTT stained scaffolds 24 h post NIH3T3 seeding. Dark purple stains denote viable cells adhered on the scaffolds. Scale bars = 1 mm.

Figure 4.6

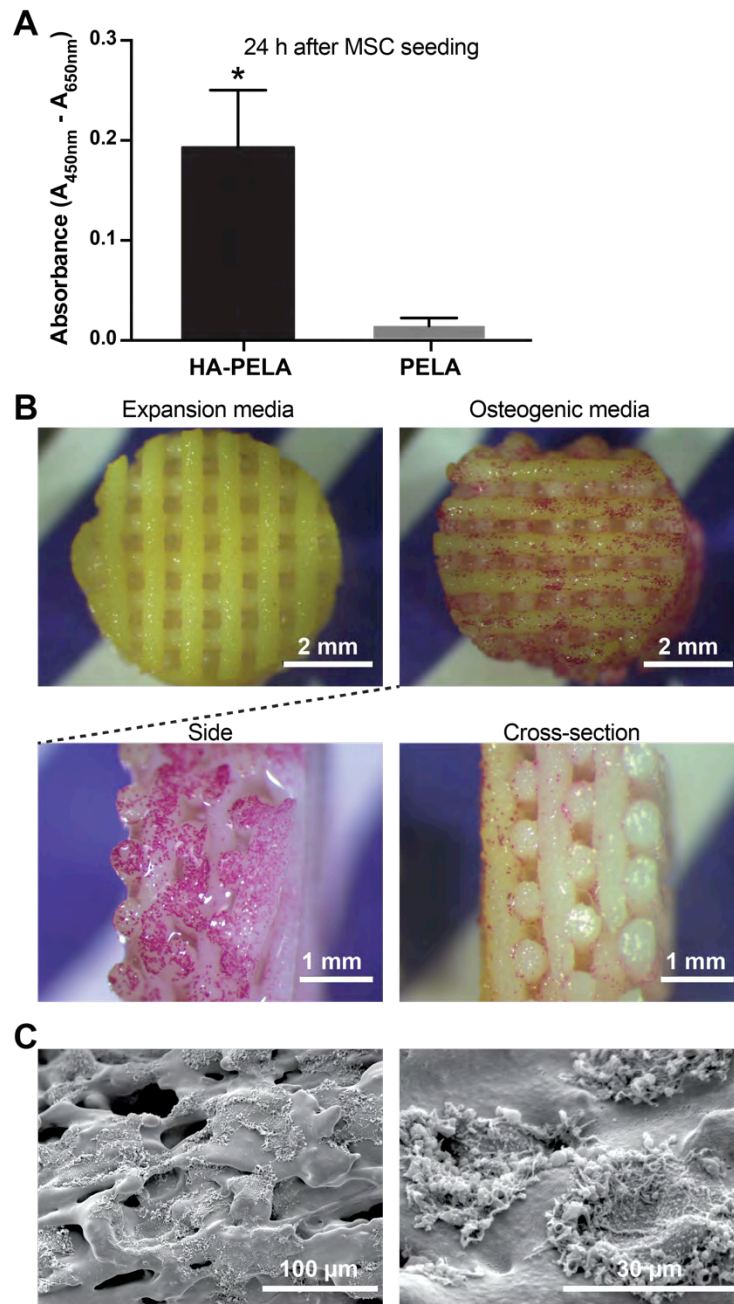


3.6 MSC attachment and osteogenic differentiation on the rapid prototyped scaffolds

The MSC attachment on HA-PELA was assessed in order to determine the suitability of HA-PELA for supporting potential stem/progenitor cell attachment and bone in-growth *in vivo*. CCK-8 assay revealed significantly higher (e.g. 16-fold increase in viable cells at 24 h) seeding efficiency of MSCs on the 3-D HA-PELA scaffolds than on the PELA scaffolds (Fig. 4.7A), further supporting the cell-adhesive nature/osteoconductivity of the former and the low-fouling nature of the latter. The ability of the HA-PELA scaffold to support osteogenic differentiation of rMSCs was examined by culturing the cells on the scaffolds in expansion or osteogenic medium for 14 days. Extensive positive (red) alkaline phosphatase staining detected throughout the 3-D macroporous scaffold (e.g. as revealed by surface, side and cross-section views) confirmed the osteogenic differentiation of the adherent rMSCs cultured in osteogenic medium (Fig. 4.7B). No non-specific staining was detected in the expansion medium control. SEM micrographs revealed the deposition of extracellular matrices including mineral nodules surrounding the rMSCs adhered to the scaffold after 14-day culture in osteogenic differentiation medium (Fig. 4.7C), further confirming that these rMSCs underwent osteogenic differentiation upon culture induction.

Figure 4.7. rMSC attachment and osteogenic differentiation on HA-PELA scaffolds. (A) CCK-8 cell viability assay of rMSCs attached to HA-PELA and PELA scaffolds at 24 h after initial seeding (n=3). * $P < 0.05$. (B) Alkaline phosphatase staining of rMSCs cultured on HA-PELA in expansion medium (left) or osteogenic medium (right) for 14 days. Side and cross section views of the stained scaffold cultured in osteogenic medium are shown below. (C) SEM micrographs of rMSCs cultured on HA-PELA in osteogenic medium for 14 days.

Figure 4.7

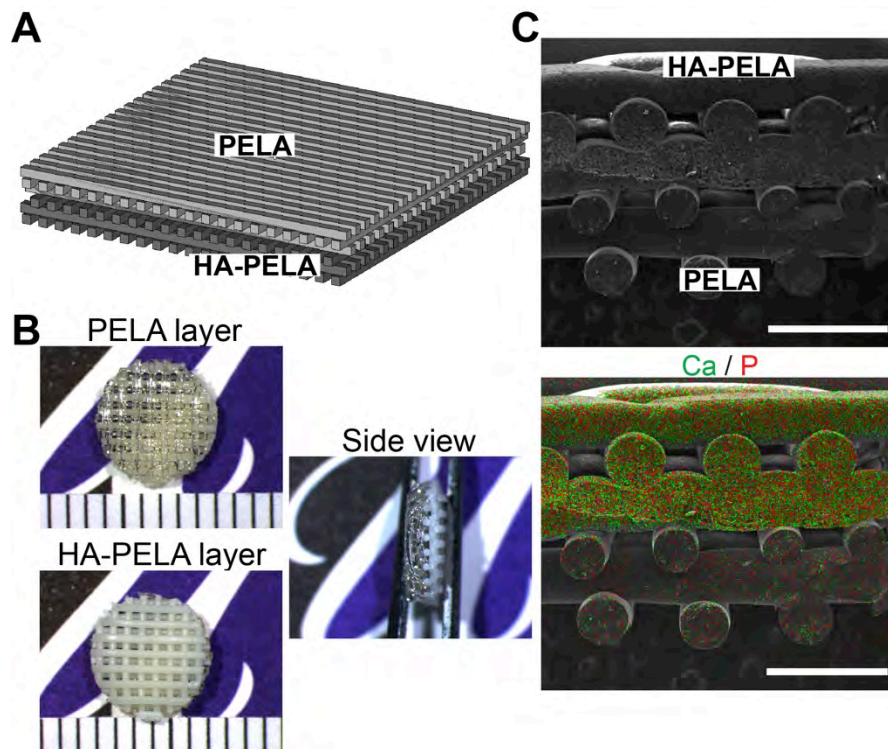


3.7 Rapid prototyping biphasic PELA/HA-PELA scaffolds

Biphasic scaffolds composed of 3 PELA layers and 3 HA-PELA layers were designed using CAD (Fig. 4.8A) and fabricated by FDM. Stereomicroscopy images showed distinct yet well-connected PELA and HA-PELA phases (Fig. 4.8B). Scanning electron microscopy and EDX mapping of the cross-section of the biphasic scaffold confirmed the distinct mineral composition in the HA-PELA fibers (Fig. 4.8C). The calcium (Ca) and phosphate (P) signals were clearly localized within and on the surface of the HA-PELA fibers while only minor background noise was detected in the adjacent PELA phase.

Figure 4.8. PELA/HA-PELA biphasic scaffold. (A) CAD model of the PELA/HA-PELA biphasic scaffold. (B) Stereomicroscopy images of a 6-mm core punched out from the biphasic scaffold. Scale markings = 1.0 mm (C) Scanning electron micrograph of a biphasic scaffold (top). Elemental mapping overlay (bottom) of calcium (green) and phosphate (red). Scale bars = 1 mm.

Figure 4.8



4. Discussion

Recent work from our group has demonstrated the potential of electrospun HA-PELA scaffolds for bone tissue engineering applications.[209] Compared to hydrophobic PLA, amphiphilic PELA exhibited significantly improved mechanical properties (10-fold increase in ultimate tensile strain), hydrophilicity, and bioactivity (osteoconductivity and highly sensitized response to the induction of osteogenesis of bone marrow stromal cells) when combined with HA.[209] Furthermore, the amphiphilic nature of PELA resulted in hydration-induced structural rearrangement (supported by DSC) and stiffening of the polymers,[209] a property that we hypothesize could be exploited to create scaffolds that can secure themselves within a confined bony defect (self-fixation). Stable graft fixation is important for preventing bone resorption,[269] and the fitting and fixation of bone grafts is a significant clinical problem, particularly in complex cranio-maxillofacial defects.[6,7]

Here we demonstrated facile fabrication of 3-D PELA, HA-PELA, and biphasic scaffolds with controlled macroporosity and architecture by FDM using a consumer-grade 3-D printer. We evaluated their swelling and mechanical properties under physiological conditions and designed a fixation test to examine the ability of the scaffolds to self-fixate within a confined cylindrical defect upon hydration *in vitro*. Furthermore, we evaluated these scaffolds' abilities to support cell adhesion/growth, thereby determining the suitability of the biphasic scaffold for applications such as guided bone regeneration.

The FDM process consists of feeding a thermoplastic polymer filament through a heated nozzle, guided by software instructions converted from the CAD model, and depositing thin rods of polymer layer by layer that fuse with one another at their contact points. We used an unmodified consumer-grade 3-D printer, MakerBot® Replicator™ 2X to fabricate the scaffolds. The only “customization” required for printing PELA and HA-PELA polymers are (1) the preparation of PELA and HA-PELA filaments to feed the 3-D printer, and (2) the identification of appropriate environmental and printing nozzle temperatures to support the smooth feeding (without premature softening) and printing (without degradation) of PELA/HA-PELA rather than ABS, the default polymer used for MakerBot® Replicator™ 2X.

In order to produce the filaments for FDM, a capillary rheometer was used to extrude the PELA and HA-PELA. The capillary rheometer or melt flow indexer allowed for smaller quantities of polymer (gram-scale vs. kilogram-scale required by conventional extruder) to be used. The melt flow indexer is also more cost-effective (<\$5,000) compared to micro-extruders (>\$100,000). We extruded pre-fabricated dense films obtained from solvent casting where loose aggregates of HA nanocrystals[153] were homogeneously blended with PELA in the composite. To ensure that the filament was smoothly fed into the heated printing nozzle without premature softening, we carried out the FDM in a deli refrigerator at 4 °C, well below the glass transition temperature of PELA (~19 °C). This temperature prevented the filament from softening/melting and sticking in the drive gear

before reaching the printing nozzle, the temperature of which was set at 130 °C for PELA and 160 °C for HA-PELA. With this approach, we were able to fabricate PELA and HA-PELA scaffolds with fiber dimensions precisely matching the CAD model (Fig. 4.2) without undesired line width widening/thinning due to inconsistent extrusion through the heated nozzle. GPC confirmed that the printing nozzle temperature chosen largely maintained the integrity of PELA and HA-PELA composite (Table 4.1). It is worth noting that the molecular weight of the HA-PELA composite decreased less than the molecular weight of PELA during the filament extrusion and subsequent processing, even though the processing temperatures for HA-PELA were higher, suggesting an insulating and protective effect of HA on the degradable polymer. This result is consistent with our prior observation that the electrospun HA-PELA meshes exhibited an increased thermal decomposition temperature compared to the PELA meshes as determined by TGA.[209]

PEG/PLA co-polymers are known to exhibit significant water absorption due to the hydrophilic PEG segment.[270,271] Additionally, we showed previously that electrospun PELA and HA-PELA scaffolds significantly stiffened upon hydration.[209] Here, we examined the swelling behavior and hydration-dependent mechanical properties of the rapid prototyped porous 3-D PELA and HA-PELA scaffolds at 37 °C. Both HA-PELA and PELA 3-D scaffolds were readily wetted by water and exhibited significant swelling in water within 2 h, with the prototyped line width increasing by 25% in 24 h (Fig. 4.3). The incorporation

of HA significantly increased the swelling of the scaffolds. This result may be attributed to the further increased hydrophilicity upon HA incorporation and the more roughened HA-PELA fiber morphologies that promoted better water penetration within HA-PELA. These observations support that the 3-D PELA-based scaffolds are highly hydrophilic, in agreement with prior water contact angle and swelling experiments carried out on electrospun PELA meshes and dense solvent-cast PELA films.[60,209]

Polymers typically soften upon hydration due to the plasticizing effect of water.[189] However, hydration-induced stiffening has been described previously for electrospun PELA[209] and other amphiphilic polymers.[189,272] This phenomenon is likely caused by hydration-induced phase separation of the hydrophilic PEG blocks from the hydrophobic segments,[189,209,273] which was confirmed by modulated differential scanning calorimetry with our electrospun PELA or HA-PELA fibrous meshes[209] and by small-angle x-ray scattering of other related amphiphilic systems.[189] We showed here that the compressive moduli of 3-D HA-PELA were higher than those of the PELA scaffolds in both dry and hydrated states (Fig. 4.4). The hydration-induced increase in compressive modulus was observed with both scaffolds, but the effect was more pronounced in PELA (~4-fold increase) than in HA-PELA (1.38-fold increase). However, the fully hydrated HA-PELA scaffold was more than twice as stiff as the hydrated PELA scaffold. The higher (by 6.7-fold) modulus of the dry HA-PELA scaffold compared to the dry PELA supported good structural integration of HA with the

amphiphilic polymer. The increase in modulus of the hydrated HA-PELA suggests that HA did not disrupt the hydration-induced phase separation of PELA.

The swelling behavior and hydration-induced stiffening of the rapid prototyped amphiphilic scaffolds led us to hypothesize that a dry HA-PELA or PELA scaffold readily placed within a confined tissue defect (with minimal resistance) could gradually conform to the defect upon swelling under physiological conditions and remain securely fixed within the defect as it stiffens. Such a gradual self-fixation would allow both convenient placement and better integration of an implant within the often-complex defect geometries. Inspired by push-out tests evaluating the fixation of osseous implants to surrounding native bone tissue,[274,275] we developed an *in vitro* pull-out test to quantify the hydration-induced self-fixation behavior. The test specimen was placed into a rapid prototyped testing device (Fig. 4.5B), allowed to swell in water, and the force required to pull it out of the testing device was measured. While this test does not fully recapitulate the environment of a tissue substrate, it provides a reproducible and facile method to quantitatively compare the self-fixation behavior of various scaffolds *in vitro*, thereby serving as a valuable, although imperfect, predictor. We observed significant fixation of both HA-PELA and PELA scaffolds after 2 h of hydration (Fig. 4.5D). The peak force required to remove the hydrated HA-PELA scaffold was 15-fold higher than that for the dry scaffold. The fixation force measured for the hydrated HA-PELA was also significantly higher

than that of hydrated PELA, likely due to a combination of the more pronounced swelling and the more substantial stiffening of the hydrated HA-PELA. To our knowledge, this is the first report of rapid prototyped biomaterial scaffold exhibiting well-characterized hydration-induced self-fixation behavior.

The low-fouling PEG component in PEG-PLA di-block films[60,195,196] and electrospun PELA[62,176] was previously shown to translate into low cellular adhesion. In our prior work, we showed that the electrospun HA-PELA meshes, unlike the low-fouling PELA counterpart, readily supported cellular adhesion and proliferation of bone marrow-derived stromal cells.[209] The substantial difference between PELA and HA-PELA in supporting cell adhesion could potentially be exploited for applications where varying degrees of tissue ingrowth are required on opposing sides of a biomaterial scaffold. One such application is guided bone regeneration (GBR).[268] The principle behind GBR is to exclude fibroblasts and soft tissue from occupying the bony defect while encouraging the defect be populated with osteogenic cells and filled with new bone.[276,277] We hypothesized that the low-fouling PELA, when properly incorporated into the scaffolds, would inhibit this fibroblast adhesion. Using a CCK-8 assay, we showed that the PELA scaffold indeed restricted the adhesion of fibroblasts (Fig. 4.6A). Only a small number of fibroblasts loosely adhered to the PELA scaffold, as visualized by MTT staining after 24 h (Fig. 4.6B), and they failed to proliferate over time (Fig. 4.6B). By contrast, nearly 5 times fibroblasts adhered to the HA-PELA upon cell seeding and they remained viable and stably attached to the

scaffold during the 14-day culture period (Figs. 4.6A & B), agreeing with the general trend we previously observed with electrospun PELA vs. HA-PELA scaffolds.[209]

We further confirmed that the osteoconductive HA-PELA readily supported the cellular adhesion and differentiation of MSCs. The incorporation of HA effectively offset the low-fouling effect of the PEG component of the amphiphilic composite, resulting in 10 times higher rMSC seeding efficiency on HA-PELA than on the PELA (Fig. 4.7A). The rMSCs remained adhered over long-term culture (14 days) and were able to differentiate and produce mineralized extracellular matrix in the presence of osteogenic medium (Fig. 4.7B & C). Combined with previously elucidated highly sensitized response of the MSCs adhered to HA-PELA (as opposed to PELA or HA-PLA) to osteogenic inductions,[209] these observations support 3-D HA-PELA as a promising scaffold for guiding bone regeneration upon surgical implantation to a bony defect. While the current study did not attempt to optimize of scaffold porosity and architecture, new computational modeling methods such as those based on triply periodic minimal surfaces could be employed to enable CAD of macroporous scaffolds with further improved cell seeding efficiency and mechanical properties.[102,278–280] Chemical modification of PELA with reactive groups to support techniques such as projection stereolithography would facilitate the fabrication of such next-generation scaffold designs.[101]

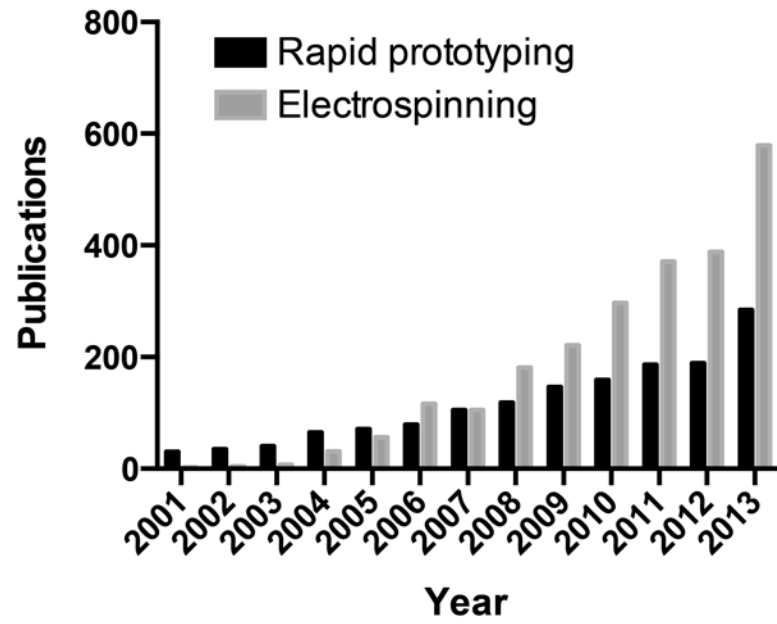
As a proof-of-concept, we fabricated a PELA/HA-PELA biphasic scaffold for potential GBR applications using the consumer-grade 3-D printing system (Fig. 4.8). The top low-fouling PELA phase was designed to prevent fibroblast adhesion/scar tissue encapsulation/soft tissue collapse into the defect *in vivo* while the bottom HA-PELA phase, upon insertion into a bony defect, was designed to support the attachment of osteoblasts or progenitors residing in the bony tissue environment to encourage bone ingrowth. Outstanding control in line width and clear separation of the distinct phases (Figs. 4.8B & C) was accomplished in the biphasic construct using the consumer-grade printer.

A PubMed search for prototyping publications in the past decade combining keyword search results from “fused deposition modeling”, “three-dimensional printing”, and “rapid prototyping” revealed an interesting trend indicative of the need for easier-to-use and more versatile rapid prototyping instrumentation in order to achieve broader and more sustained use of this technology (Fig. 4.9). The number of rapid prototyping-related publications appeared to have plateaued by 2010 with increasing numbers of publications in 2013. By comparison, the electrospinning technique, garnered initial attention from the research community almost 4 years later than rapid prototyping yet showed a much more rapid and sustained growth in terms of related publications (e.g. resulting in twice as many publications in 2013). This discrepancy in the number of publications may be in part due to the substantially lower investment (e.g. a few thousand dollars) required for an electrospinning setup than for

custom-designed or research-grade printing systems (e.g. could be >\$100,000). With the popularization of consumer-grade printers in the past few years, the use of rapid prototyping technology for fabricating novel biomaterial scaffolds by research laboratories as well as biotech industries could see a renewed upward trend.

Figure 4.9. Number of PubMed citations of rapid prototyping and electrospinning publications since 2001. Search results based on the key words “rapid prototyping”, “fused deposition modeling”, and “three-dimensional printing” were combined for the total rapid prototyping publications in each calendar year.

Figure 4.9



5. Conclusions

To the best of our knowledge, this study is the first to rapid prototype PELA or HA-PELA, a class of amphiphilic degradable biomaterials recently shown to exhibit exciting physical (e.g. hydrophilicity, mechanical integrity, and hydration-induced structural rearrangement and mechanical strengthening) and biological properties (e.g. osteoconductivity & up-regulated osteogenic gene expression),[209] into 3-D macroporous tissue engineering scaffolds. We describe the use of an unmodified, consumer-grade 3-D printer for the scaffold fabrication, facilitating the translation of this promising biomaterial to tissue engineering applications and promoting its wider use by the research community. Of note, the rapid prototyped PELA and HA-PELA composite scaffolds demonstrated unique swelling and mechanical properties that translated into hydration-induced self-fixation behavior. A customized specimen holder and a novel yet straightforward *in vitro* pull-out test was designed to quantify the self-fixation property resulting from hydration-induced swelling and stiffening of the amphiphilic scaffolds. The unique self-fixation behavior is attractive for scaffold-assisted tissue engineering applications where the ability of a scaffold to conform and secure itself within a tissue defect is desired for its stable implantation. We demonstrated differential abilities of rapid prototyped PELA and HA-PELA scaffolds to suppress or support the adhesion and proliferation of NIH3T3 fibroblasts and MSCs. Furthermore, MSCs adhered to HA-PELA were able to undergo potent osteogenic differentiation under *in vitro* culture induction. These

cell-adhesion properties can potentially be exploited in biphasic constructs with spatially controlled cell adhesion. Future work will explore the rapid prototyped biphasic constructs for guided bone regeneration where self-fixation and discrete cell adhesive properties may be exploited for facile scaffold implantation/stable fixation and promoting bone defect repair while preventing scar tissue encapsulation/soft tissue collapse.

6. Acknowledgments

This work was supported in part by the National Institutes of Health grants R01GM088678 and R01AR055615, and a University of Massachusetts Commercial Ventures & Intellectual Property Technology Award. Core resources supported by the National Center for Research Resources Grant S10RR021043 were used. I would like to thank Evanthia Fylaktou and Prof. Stephen McCarthy at the University of Massachusetts Lowell for the generous help in extruding the amphiphilic polymer filaments and the kind permission for access of the extruder by Metabolix, Inc.

CHAPTER V: Shape-Memory Performance of Thermoplastic Amphiphilic Triblock Copolymer Poly(D,L-lactic acid-co-ethylene glycol-co-D,L-lactic acid) (PELA)/Hydroxyapatite Composites

Preface

This chapter has been adapted from:

Kutikov AB, Reyer KA, Song J. "Shape memory performance of thermoplastic amphiphilic triblock copolymer poly(D,L-lactic acid-co-ethylene glycol-co-D,L-lactic acid) (PELA)/hydroxyapatite composites" *Macromolecular Chemistry and Physics* 2014. doi: 10.1002/macp.201400340

Dr. Jie Song and Artem Kutikov designed the experiments in this work. Kevin Reyer fabricated the PELA films, HA-PELA filament for 3-D printing, and assisted in mechanical testing and scanning electron microscopy. Artem Kutikov performed the remainder of the work.

Abstract

Biodegradable amphiphilic polymers and polymer/HA composites are promising materials for skeletal tissue engineering. When such materials possess thermal-responsive shape memory properties, they may be delivered in a minimally invasive temporary shape to a tissue defect and subsequently triggered to conform to the defect. Here we report the shape memory properties of high molecular weight (120 kDa) thermoplastic amphiphilic PELA and HA-PELA composites. The tensile and storage moduli of HA-PELA positively correlate with the HA content, supporting good structural integration of HA with PELA. Physical entanglements of the polymer chains enable their cold-deformation and stable fixation into temporary shapes at room temperature and rapid recovery (< 3 s) to their original shapes at $50\text{ }^{\circ}\text{C}$. Stable fixation of large deformations can be achieved at $-20\text{ }^{\circ}\text{C}$. Strain-controlled cyclic thermal mechanical testing reveals that while the rate of shape recovery from tensile deformations decreased with the higher HA content, all HA-PELA composites (up to 20 wt% HA) are able to achieve near complete shape recovery ($>90\%$) upon 10-min equilibration at $50\text{ }^{\circ}\text{C}$. Finally, the permanent shapes of HA-PELA composites can be reprogrammed at $50\text{ }^{\circ}\text{C}$ and rapid prototyped macroporous scaffolds can be fabricated with retained shape memory properties.

1. Introduction

Shape memory polymers (SMPs) can be programmed with a permanent shape, subsequently deformed into a stable temporary shape, and triggered to recover back to their permanent shape. In the case of thermal-responsive SMPs, the recovery trigger is a temperature above the transition temperature (T_{trans}), either glass transition temperature (T_g) or melting temperature (T_m), of the polymer. Programming the permanent shape is accomplished by casting the polymer into a mold for thermoset SMPs, or by deforming the polymer at a temperature above the T_m for thermoplastic SMPs. For both thermoset and thermoplastic SMPs, deforming the polymer above the T_g may program the temporary shape. The net-points (physical entanglement or chemical crosslinks) of a SMP network are responsible for setting the SMPs permanent shape while temperature sensitive switching domains fix the temporary shape.[281]

Engineering synthetic biomaterials with shape memory properties has the potential to enable more effective *in vivo* delivery of “smart” implants or tissue engineering scaffolds. The SMP implant could be delivered in a minimally invasive temporary shape to a tissue defect and subsequently thermally triggered to recover to its pre-programmed permanent shape precisely fitting the defect.

In order for thermal responsive SMPs to be safely applied for biomedical applications, two basic requirements of the SMPs must be met: 1) biocompatibility, and 2) reasonably narrow T_{trans} within a safe temperature range (<60°C).[282,283] In a bone environment, for example, exposure to temperatures

above 45 °C for one minute or short exposure to temperatures above 70 °C induce necrosis.[283] Therefore, the T_{trans} and rate of shape recovery are particularly important to reduce thermal damage to surrounding tissue. In addition, to facilitate clinical translation, versatile and scalable fabrication methods (e.g. a thermoplastic polymer would be more desired than thermoset in terms of the cost and ease of processing), bioactivity tailored for the specific application, physical properties enabling facile surgical handling (hydrophilicity, elasticity), and biodegradability are desired. Biodegradable SMPs have captivated the biomedical research community since they were exploited by Lendlein and Langer in 2001/2002 as resorbable self-tightening sutures.[284,285] A wide variety of SMPs have since been developed with varying mechanical properties, shape memory performance, and bioactivity.[281,286] We have previously shown that a degradable urethane-crosslinked SMP with GPa-glassy state storage modulus at body temperature can achieve stable temporary shape fixing at room or body temperature and full and rapid (<3 s) permanent shape recovery at ~50 °C.[287] This network was composed of polyhedral oligomeric silsesquioxane (POSS)-centered macromers grafted with 8 identical poly(D,L-lactic acid) (PLA) arms. However, while the POSS-PLA SMP is biocompatible, its degradation was shown to result in acute inflammation locally, which could be of a concern if it is used in large quantity in vivo.[48] This immune response is likely elicited by the acidic degradation byproducts of PLA.[235]

Calcium phosphates such as HA, the main mineral component in bone, have been blended with biodegradable polyesters to improve their bioactivity and buffer acidic degradation byproducts.[137,236,288,289] This HA/polymer composite strategy can be applied to improve the biological performance of biodegradable SMPs. The shape memory performance of HA-PLA composites has been studied extensively.[290–292] While such composites have shape memory behavior, they tend to exhibit slow permanent shape recovery (e.g. 100 s) even at relatively high triggering temperatures (e.g. 70 °C). Overall, biodegradable polymer/HA composites exhibiting an optimal combination of shape memory properties and biological performance are lacking. In our prior work, we blended high molecular weight (>100,000 Da) PELA amphiphilic triblock co-polymer with HA and electrospun the stable suspension into nano/micro fibrous scaffolds.[209] The HA-PELA scaffolds exhibited significantly improved handling characteristics (elasticity, hydrophilicity) and bioactivity (e.g. ability to support potent osteogenic differentiation of stem cells) than electrospun HA-PLA counterparts. Both the amphiphilic PELA and the incorporation of HA were critical for achieving the ultimate performance of the electrospun scaffolds, with the hydrophilic PEG block of PELA responsible for binding and dispersing the HA while the HA enhancing the osteoconductivity and osteoinductivity of the composite. The shape memory performance of PELA and its HA composites, however, has not been evaluated.

The shape memory behavior of amphiphilic polymers is a result of the phase separation between the hydrophilic and hydrophobic blocks.[293] By design, the phase exhibiting a higher thermal transition may act as the physical crosslinks or hard segments, while the other phase exhibiting the lower thermal transition could act as the switching phase or soft segments.[294] Amphiphilic polymer networks are often crosslinked to achieve sufficient mechanical integrity for shape memory and stability in aqueous solutions. For example, thiol-ene cross-linked PEG-PCL foams have been shown to exhibit shape memory properties at biologically relevant temperatures (40-50 °C).[295] The shape memory performance of photo-crosslinked amphiphilic gels composed of PEG and PCL or PEG and PLGA have also been reported.[296,297] In general, photopolymerized networks are not as amenable to polymer processing approaches such as extrusion or rapid prototyping as thermoplastics. When the amphiphilic polymers are of sufficiently high molecular weight to facilitate physical entanglement and achieve aqueous stability, tough and flexible thermoplastics can be fabricated.[192,270,271,298,299] Gu & Mather reported the shape memory behavior of high molecular weight ($M_n > 200,000$ Da) PCL-PEG thermoplastic polyurethanes.[293] Such materials can be cold-deformed to high strains (e.g. ~1240% strain) by a combination of elastic and plastic deformations at room temperature, which is above the T_g but below the T_m of both PCL and PEG blocks. Upon the release of the external stress, the material immediately recovered its elastic strain (from ~1240% loaded to 800% strain unloaded) while

the plastic deformations were fully recovered after 1 min at 70 °C, a temperature above the T_m for both blocks. The shape memory behavior of this system was a result of the physical crosslinks between the high molecular weight polymer chains (entanglements), acting as stable net points even above the T_m , and the recoverable stretching and recoiling of the PCL and PEG phases.

Here we hypothesized that a thermoplastic SMP can be generated with high molecular weight amphiphilic PELA and that HA can be incorporated with PELA while preserving shape memory properties. To test these hypotheses, we fabricated uniform composites of HA and PELA and examined their thermal mechanical properties and reprogrammable shape memory behavior around a physiologically relevant temperature, as a function of the HA content. To further assess their suitability for minimally invasive biomedical uses, the shape memory performance of rapid prototyped HA-PELA scaffolds was also examined.

2. Materials and Methods

2.1. Materials

3,6-Dimethyl-1,4-dioxane-2,5-dione (D,L-lactide) was purchased from Sigma–Aldrich (St. Louis, MO), purified by recrystallization twice in anhydrous toluene, and dried under vacuum prior to use. PEG (BioUltra, 20,000 Dalton) was purchased from Fluka (Switzerland). Polycrystalline HA powder was purchased from Alfa Aesar (Ward Hill, MA). All other solvents and reagents were purchased from Sigma–Aldrich (St. Louis, MO) and used as received.

2.2. PELA synthesis and characterization

2.2.1. Synthesis

PELA tri-block copolymer was synthesized by melt ring-opening polymerization as previously described.[209] Briefly, PEG (20,000 Dalton, 4 g, 0.2 mmol) was heated to 100 °C in a Schlenk flask and stirred under vacuum for 1 h to remove residual water. The melt was cooled to room temperature before Sn(II) 2-ethylhexanoate (~95%, 24.18 mg, 0.06 mmol) in anhydrous toluene was introduced by syringe. The toluene was removed by heating the mixture under vacuum at 100 °C for 15 min. The mixture was cooled to room temperature before D,L-lactide (17.295 g, 0.12 mol) was added under argon purge. The melt polymerization proceeded at 130 °C for 5 h under argon. The crude PELA was dissolved in chloroform, purified by precipitation in methanol, and dried under vacuum.

2.2.2. Characterization

The molecular weight and polydispersity of PELA was determined by gel-permeation chromatography on a Varian Prostar HPLC system equipped with two 5mm PLGel MiniMIX-D columns and a PL-ELS2100 evaporative light scattering detector (Polymer Laboratories). THF was used as an eluent at 0.3 ml/h at room temperature. Molecular weight and polydispersity calculations were calibrated with EasiVial polystyrene standards (Agilent, Santa Clara, CA). ¹H

NMR spectra were recorded on a Varian Mercury 400 MHz spectrometer at 298 K using CDCl_3 containing tetramethylsilane as the solvent.

2.3. PELA and HA-PELA films

2.3.1. Fabrication

Dense PELA and HA-PELA films were prepared by solvent casting. HA (0 to 20% w/w relative to PELA) was bath-sonicated in 4 mL chloroform for 30 min. PELA (1.25 g) was added and the mixture was stirred overnight. The HA-PELA mixture was subsequently poured into Teflon molds. The chloroform was evaporated in a fume hood at room temperature overnight and subsequently in a vacuum oven at 60 °C for 24 h. PELA films were prepared by evaporating a chloroform solution of PELA without HA in the same mold followed by vacuum drying under identical conditions. Films were stored at -20 °C prior to use.

2.3.2. Scanning electron microscopy (SEM)

The bottom surface of the solvent-cast films and their cross-sections were sputter coated with Au (~4 nm thick) and imaged on a Quanta 200 FEG MKII scanning electron microscope (FEI Inc., Hillsboro, OR) under high vacuum at 10 kV.

2.4. Mechanical testing

2.4.1. Tensile modulus / strength

The tensile modulus of PELA and HA-PELA films at room temperature was determined on a MTS Bionix 370 mechanical testing system (MTS Systems Corporation, Minneapolis, MN). ASTM D882-97 guidelines were followed with the exception of the initial grip displacement due to sample size constraints.[300] Specimens (5.3 mm × 35 mm × ~0.2 mm, n=3) were loaded into the MTS machine with an initial grip separation of 10 mm and subjected to a grip separation of 100 mm/min. The resulting force was recorded with a 250 N load cell (Interface, Scottsdale, AZ). The elastic modulus was calculated from the initial linear region of the stress-strain curve (1-5% strain). The initial toe region, if present, was excluded from the modulus calculation.

The tensile modulus at 37 °C was measured with a Q800 Dynamic Mechanical Analyzer (DMA) equipped with a gas cooling accessory (TA Instruments, New Castle, DE). Specimens (5.3 mm × 35 mm × ~0.2 mm) were loaded into a film tension fixture with a grip separation of 10 mm (n=3), equilibrated at 37 °C, held isothermally 10 min, then subjected to a 1-mN pre-load force. Tensile modulus was measured by ramping the specimens at a strain rate of 1 N /min. The modulus was calculated from the initial linear region of the stress strain curve (1-5% strain). The initial toe region, if present, was excluded from the modulus calculation.

2.4.2. Temperature-dependent storage modulus

The tensile storage moduli of PELA and HA-PELA were measured on a Q800 DMA equipped with a gas cooling accessory. Specimens (5.3 mm × 35 mm × ~0.2 mm) were loaded into a film tension fixture and equilibrated at -40 °C for 10 minutes before the temperature was ramped from -40 °C to 70 °C at a heating rate of 2 °C/min. The storage modulus was recorded at a strain amplitude of 0.02% and a frequency of 1 Hz.

2.4.3. Strain-controlled cyclic thermal mechanical testing

Shape memory characterization was performed under tension on a DMA Q800 equipped with a gas cooling accessory. Specimens (5.3 mm × 35 mm × ~0.2 mm) were equilibrated at 50 °C for 5 min and cooled to 25 °C and equilibrated for another 5 min prior to testing. The specimens were subjected to a 50% strain, and cooled at 2 °C/min to -20 °C while the constant strain of 50% was maintained. This yielded the elongated temporary shape ϵ_t . After being held at -20 °C for 5 min, the force on the sample was released to 0.01N and the resulting strain was recorded as the unloaded temporary shape ϵ_u . Shape recovery was triggered by heating the specimens at a rate of 2 °C/min to 50 °C and holding at 50 °C for 10 min. The recovered sample strain was recorded as ϵ_p . Each specimen was subjected to 3 consecutive cycles of testing. The second cycle was used to calculate the strain fixing ratio (R_f) and the strain recovery ratio (R_r) reported in Table 1. The R_f and R_r in a given cycle N were determined by using the following formulas:

$$R_f(N) = \frac{\varepsilon_u(N) - \varepsilon_p(N-1)}{\varepsilon_l(N) - \varepsilon_p(N-1)} \quad (1)$$

$$R_r(N) = \frac{\varepsilon_u(N) - \varepsilon_p(N)}{\varepsilon_u(N) - \varepsilon_p(N-1)} \quad (2)$$

2.4.4. Stress-controlled cyclic thermal mechanical testing

Specimens (5.3 mm × 35 mm × ~0.2 mm) were equilibrated at 50 °C for 5 min and cooled to 25 °C prior to testing. After being equilibrated at 25 °C for 5 min, the specimens were subjected to a 0.8 MPa tensile stress, and cooled at 2 °C/min to -20 °C while the constant stress was maintained. This yielded the elongated temporary shape under stress ε_l . After being held at -20 °C for 5 min, the stress was released to a 1-mN pre-load force. The resulting strain was recorded as the unloaded temporary shape ε_u . Shape recovery was triggered by heating the specimens at a rate of 2 °C/min to 50 °C and holding at 50 °C for 5 min. The recovered sample strain was recorded as ε_p . Each specimen was subjected to 4 consecutive cycles of testing. The R_f and R_r in a given cycle N were determined using formulas (1) and (2).

2.5. Demonstration of reprogrammable shape memory

A flat bar (5.3 mm × 35 mm × 0.2 mm) of HA-PELA (20 wt% HA) was deformed into a temporary spiral shape at room temperature. Shape recovery (to permanent flat bar) was initiated by submerging the specimen in 50 °C deionized water. In order to reprogram the permanent shape into a spiral, the specimen

was submerged in 50 °C deionized water and deformed into a spiral shape. The specimen was then allowed to cool to room temperature while the spiral shape was fixed. Subsequently, the specimen was deformed into a temporary flat bar shape at room temperature. Shape recovery (to reprogrammed permanent spiral) was initiated by submerging the specimen in 50 °C deionized water.

2.6. Demonstration of three-dimensional (3-D) rapid prototyped scaffold with shape memory behavior

2.6.1. Scaffold fabrication

A 3-D CAD model of a 16 mm × 16 mm × 2.4 mm square prism composed of a staggered arrangement of 0.4 mm lines was designed in 3-Matics (Materialise, Belgium, Fig. 6A) and converted into g-code instructions by MakerWare (MakerBot Industries, Brooklyn, New York). A MakerBot® Replicator™ 2X 3-D printer (MakerBot Industries, Brooklyn, New York) was used to fabricate the 3-D macroporous HA-PELA scaffolds (25 wt% HA) based on the CAD design, as we previously described.[225] A biopsy punch was used to core a 5-mm diameter specimen from the rapid prototyped prism.

2.6.2. Shape memory demonstration

The rapid prototyped HA-PELA scaffold was deformed at room temperature by manual compression into a collapsed cylinder shape. Recovery of the permanent expanded shape was triggered by submerging the scaffold in 50 °C deionized water.

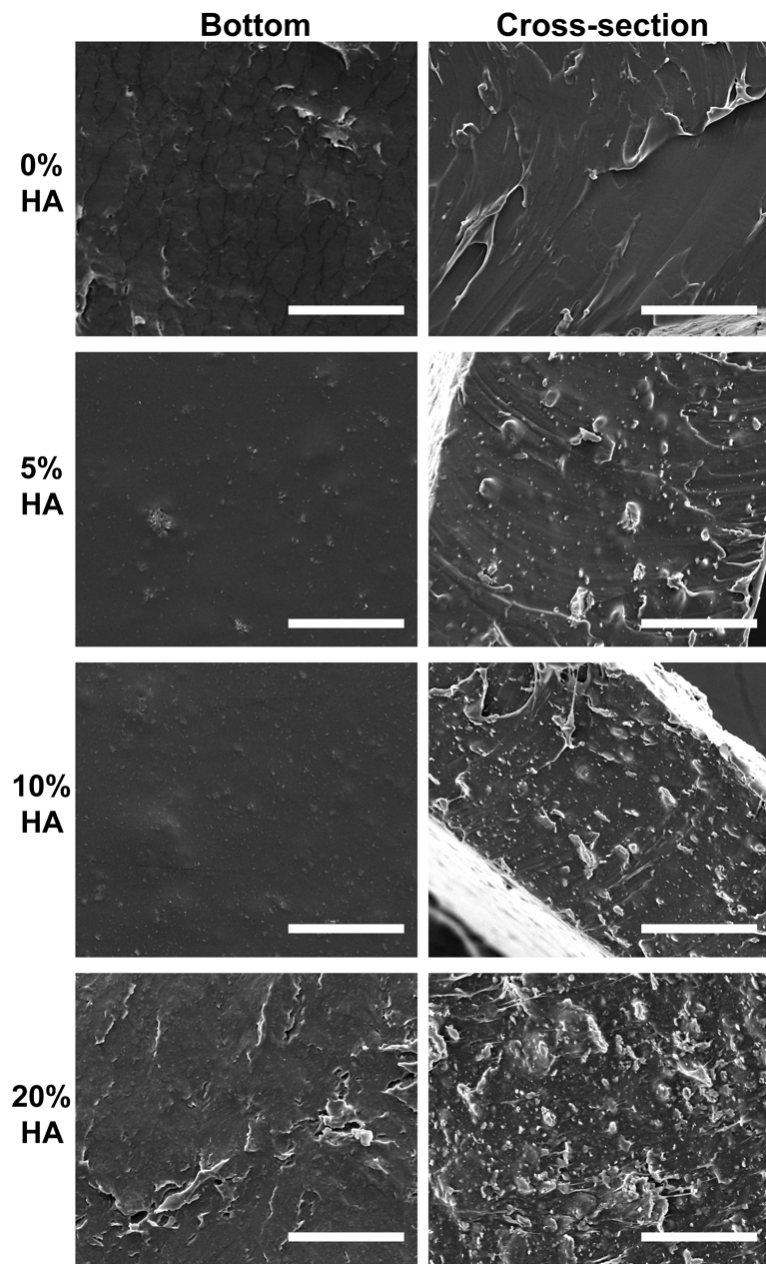
3. Results and Discussion

3.1. Characterization of PELA and HA-PELA composites

GPC and NMR characterizations confirmed the synthesis of high molecular weight PELA ($M_n = 120,000$ Da; $M_w = 190,000$ Da; $M_w/M_n = 1.56$; ^1H NMR (400 MHz, CDCl_3) δ 5.19 (m, 1126H), 3.65 (m, 1816H), 1.5 (m, 3921H) ppm.) We blended the PELA with various concentrations of HA (0 to 20 wt%), and solvent cast the composites into films. The favorable interaction between the hydrophilic PEG domain and hydrophilic HA mineral helped maintain the stable and uniform HA dispersion during the solvent casting procedure.[138] This was evidenced by the minimal settling of HA to the bottom face of the films (Fig. 5.1A), and the uniformly distributed HA across the thickness of the films (Fig 5.1B) as revealed by SEM micrographs of the cross-sections.

Figure 5.1. Scanning electron micrographs of the bottom surface (left) and cross-sections (right) of solvent-cast PELA films with 0-20 wt% of HA. Scale bars = 50 μm .

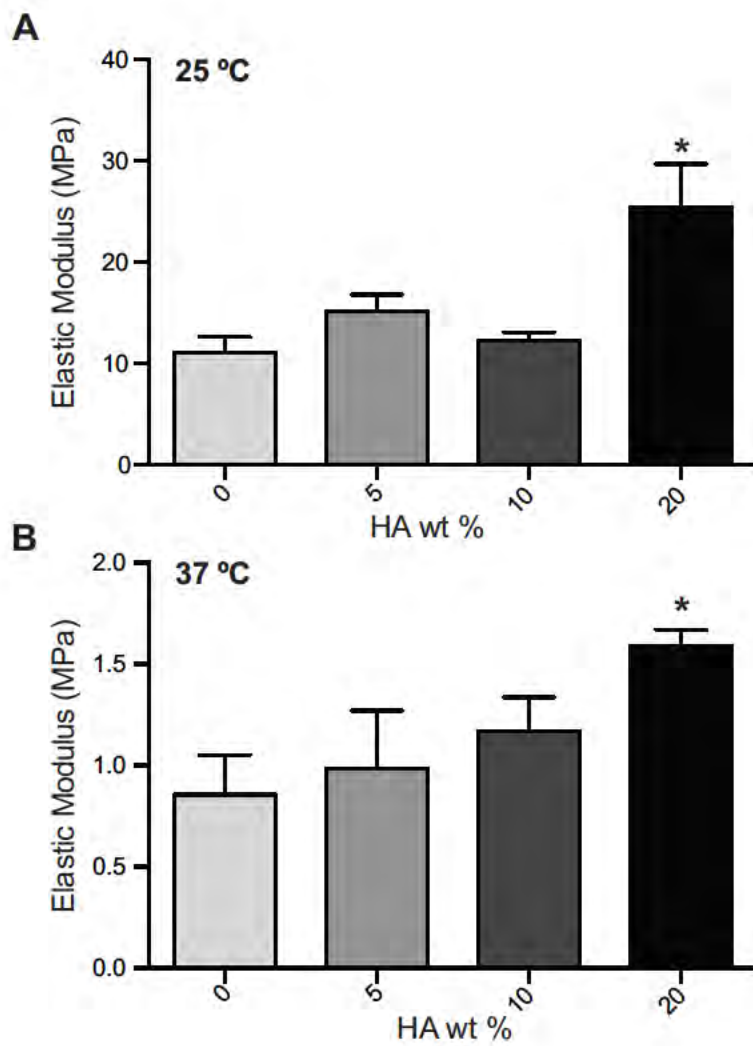
Figure 5.1



We examined the mechanical properties of the PELA and HA-PELA films by tensile testing. We aimed to test the films to failure under tension by following the ASTM D882-97 guidelines for thin plastic sheeting.[300] However, all films were highly elastic and either could not break within the limits of the MTS testing machine (~1000% strain) or broke at the grips. There was no significant difference in the elastic modulus of the films with lower HA contents (<10 wt% HA), however, the elastic modulus of the 20 wt% HA composite was significantly higher than all other groups (Figure 5.2A). We also examined the elastic modulus of the films at 37 °C to estimate their mechanical properties *in vivo* (Figure 5.2B). These films could not be strained to failure on the DMA (> 100% strain) at 37 °C, and their moduli were approximately an order of magnitude lower at 37 °C than those at 25 °C. The reinforcing effect of the structurally incorporated HA on the elastic modulus of the amphiphilic composites persisted at 37 °C, with the 20 wt% HA composite exhibiting significantly higher modulus.

Figure 5.2. Elastic moduli (n=3) of PELA films with 0-20 wt% of HA at (A) 25 °C or (B) 37 °C. Specimens (5.3 mm × 35 mm × ~0.2 mm) were ramped at 100 mm/min (25 °C) on an MTS mechanical testing system or at 1 N/min (37 °C) on a Q800 dynamic mechanical analyzer. * $p < 0.05$ (One way ANOVA with Tukey post-hoc).

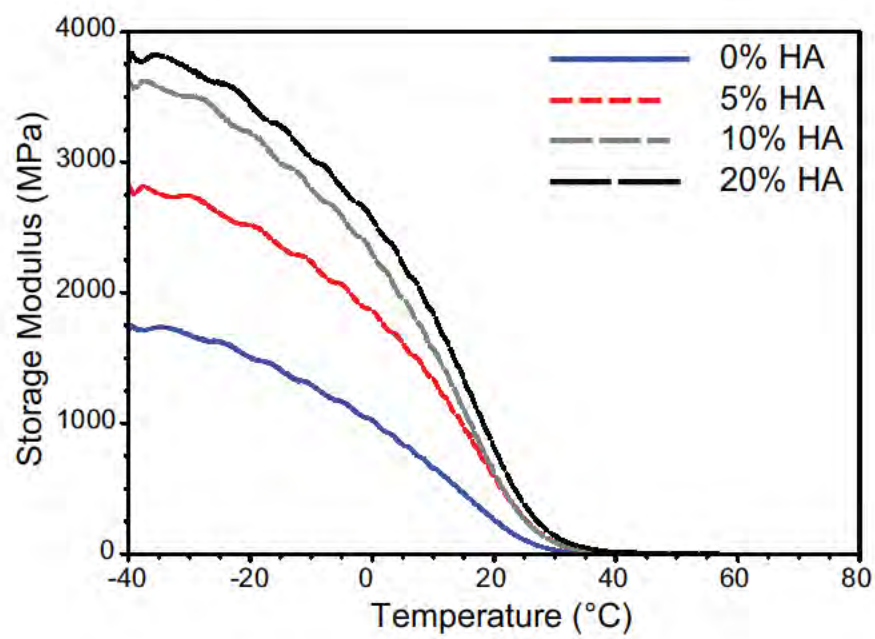
Figure 5.2



3.2. Thermal mechanical properties of PELA and HA-PELA composites

We examined the storage moduli of PELA and HA-PELA composites as a function of temperature to determine the suitable temperature range for programming shape memory. The storage modulus of PELA was expected to drop around its T_g (~ 19 °C, as we previously determined by DSC).[209] In agreement with the tensile strength results, the initial glassy state GPa-storage moduli (-40 °C) of the HA-PELA composites increased with increasing HA content (Figure 5.3). The storage moduli dropped by an order of magnitude around 19 °C, making it possible to deform the composites into temporary shapes at room temperature. This feature could allow the surgeon to deform the PELA or HA-PELA implant into a temporary shape desired for minimally invasive implantation at the surgical table without heating. Above 40 °C, the storage moduli descended into an elastic state plateau, supporting the feasibility of triggering shape recovery at this temperature. The storage modulus at 50 °C increased with the addition of HA (10 and 20 wt%), indicating that the reinforcing effect of HA was maintained at elevated temperatures. This reinforcement is likely a result of the HA particles limiting polymer chain motion.[301,302]

Figure 5.3. Temperature-dependent storage moduli of PELA films with 0-20 wt% of HA. Specimens (5.3 mm × 35 mm × ~0.2 mm) were subjected to 0.02% strain at a frequency of 1 Hz while temperature was ramped at 2 °C/min on a Q800 dynamic mechanical analyzer.

Figure 5.3

3.3. Shape memory performance of PELA and HA-PELA composites

Cyclic thermal mechanical testing was used to quantitatively assess the shape memory properties of PELA and HA-PELA composites. Prior to testing, we heated the films to 50 °C, and cooled them back to 25 °C to remove any potential thermal memory. Cyclic testing was performed under both strain-controlled (Figure 5.4A) and stress-controlled conditions (Figure 5.4B). The strain-controlled testing allows for a fair comparison of the shape memory behaviors among the samples with varying HA compositions by subjecting them to the same tensile strain. All calculations of shape fixation ratios and shape recovery ratios were based on the second cycle of strain-controlled testing (Table 5.1). The temporary shape of the films was programmed by deforming the specimens at 25 °C followed by cooling to -20 °C to fix the shape. Under these programming conditions, all films exhibited a shape fixation ratio (R_f) of >99% regardless of the HA content (Table 5.1). Stable fixation of a substantially strained (50% strain) temporary shape could not be accomplished at room temperature, possibly due to the elastic recovery of the strained polymer chains above their T_g (~19 °C). Shape recovery was initiated by heating the films to 50 °C. While incorporation of 20% HA reduced the recovery ratio of PELA by ~5%, all films recovered to >90% of their initial strain within 10 min at 50 °C. The incorporation of 5% and 10% HA had a negligible effect on the recovery ratio (~1-2%). However, HA incorporation reduced the rate of shape recovery as evident by the lower recovery ratio prior to the 10-min hold

at 50 °C. This is likely due to the HA particles slowing the movements of the polymer chains, as previously observed for HA/PLA composites.[290]

The cyclic testing under the stress-controlled mode takes into account the stiffening effect of the incorporated HA. The decreasing tensile strains achieved under the constant stress as a function of increasing HA content (Figure 5.4B) suggest that the polymer chain movement was restricted in the presence of HA. The shape fixation and recovery ratios of 20 wt% HA-PELA determined from strain-controlled (50% strain) and stress-controlled (~18% strain) testing were similar. The shape recovery ratio determined by the latter prior to and after a 5-min hold at 50 °C was 61.8% and 90.6%, respectively. This observation supports that good shape memory properties of PELA were largely retained despite the incorporation of HA content as high as 20%. Taken together, these cyclic thermal mechanical tests show that both PELA and HA-PELA films exhibited high shape fixation (>99%) and recovery ratios (>90%). For applications such as bone tissue engineering where the incorporation of osteoconductive HA is desired, up to 20 wt% HA can be blended with PELA while maintaining the shape memory behavior. However, to achieve optimal shape memory properties, the incorporation of < 10 wt% HA should be considered.

Figure 5.4. Shape memory behavior determined by (A) strain-controlled and (B) stress-controlled cyclic thermal mechanical testing of PELA films with 0-20 wt% of HA. Three consecutive cycles for each specimen (5.3 mm × 35 mm × ~0.2 mm) are shown.

Figure 5.4

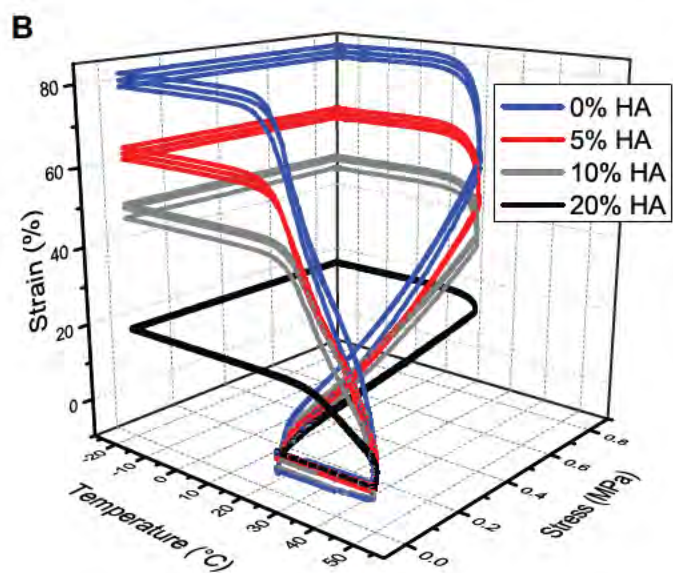
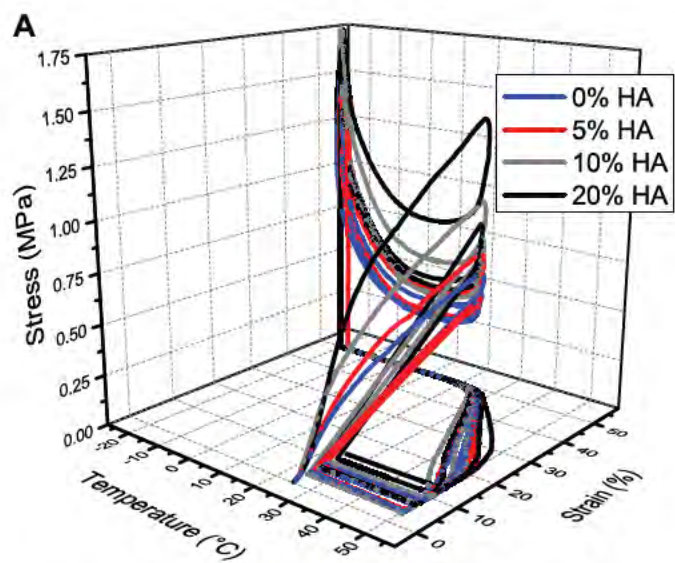


Table 5.1. Shape memory properties of HA-PELA films with varying HA contents determined from strain-controlled cyclic thermal mechanical testing.

Table 5.1

HA content (wt%)	Shape fixing ratio (R_f)	Recovery ratio at 50 °C (R_r) (no hold)	Recovery ratio (R_r) after 10 min hold at 50 °C
0	99.3%	85.3%	95.6%
5	99.4%	74.2%	94.2%
10	99.4%	75.8%	94.0%
20	99.4%	72.4%	90.6%

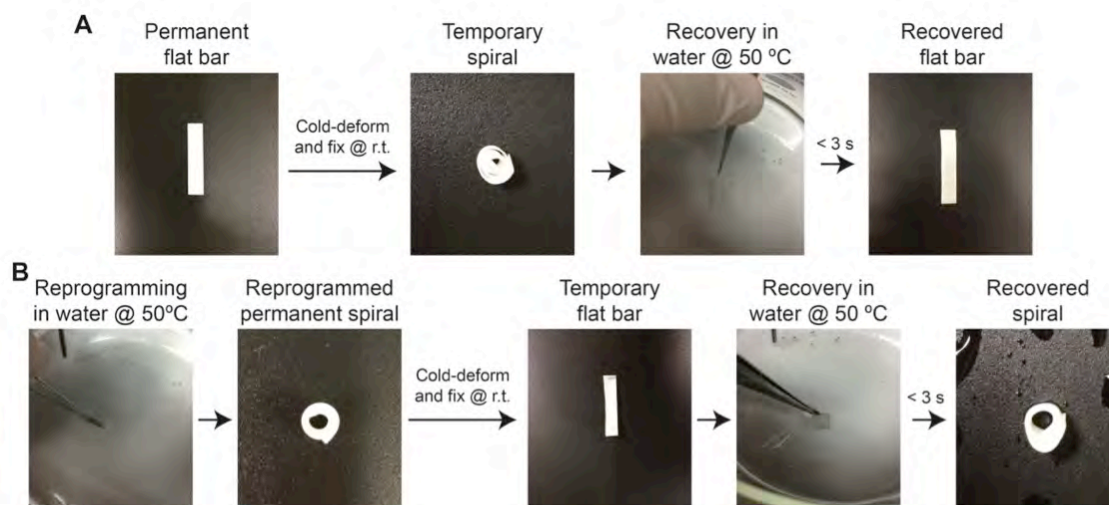
3.4. Demonstration of reprogrammable shape memory

The high molecular weight of PELA enables the formation of physical net-points within the polymer network, obviating the need for chemical crosslinking and permitting thermoplastic shape memory properties. The permanent shape of thermoplastic SMPs can be reprogrammed at elevated temperatures ($>T_m$). [285,303] This is advantageous because the permanent shape can be programmed after polymer processing/formation rather than being limited to the shape of the mold, as the case for thermoset SMPs. This can enable reuse/recycling of the SMP and fine-tuning of the shapes based on end-users' requirements. We demonstrated the ability to reprogram the permanent shape of HA-PELA (20 wt% HA) (Figure 5.5). The HA-PELA was first solvent cast into a flat bar shape, which defined its initial permanent shape. Cold-deforming the film into a spiral and fixing at room temperature programmed the temporary shape. Submerging the HA-PELA in 50 °C water triggered rapid recovery (< 3 s) back to the permanent flat bar shape (Figure 5.5A). To reprogram the permanent shape, the flat bar of HA-PELA was submerged in 50 °C water and deformed into a spiral (Figure 5.5B). The reprogrammed spiral shape was fixed upon cooling to room temperature. A stable temporary flat bar shape was programmed by simply un-rolling the spiral at room temperature. Submerging the flat bar in 50 °C water triggered rapid recovery (<3 s) to the reprogrammed permanent spiral shape. Of note, while we needed to cool the samples in order to maintain the strained temporary shape during cyclic stress-controlled testing, the spiral or flat bar

temporary shapes, without extensive tensile deformations, could be stably fixed at room temperature for over 24 h. This difference in shape fixation may be due to the varying amounts of plastic/elastic deformation between stretching the specimen under high strains vs. the spiral-wrapping. When wrapping the PELA or HA-PELA specimen into a spiral or unwrapping a spiral into a flat bar, the polymer chains were only exposed to relatively low strains, thus allowing for the lower energy deformations be adequately fixed at room temperature. When straining the samples under tension, the low content of PEG (~ 15 wt%) in PELA was insufficient to introduce enough crystallinity to prevent the release of stored energy within the polymer network and the spontaneous shape recovery at room temperature. In previously reported PCL-PEG composites, the semi-crystalline PCL combined with the higher content of crystalline PEG (>30 wt%) was sufficient to prevent complete elastic recovery at room temperature.[293]

Figure 5.5. Reprogrammable shape memory of HA-PELA films (20 wt% HA). (A) Cold-deformation and fixation into a temporary spiral at room temperature (r.t.) and rapid shape recovery to permanent flat bar shape (as cast) at 50 °C. (B) Reprogramming the flat bar into a permanent spiral shape at 50 °C, cold-deformation and fixation into a temporary flat bar at r.t., and subsequent rapid recovery back to reprogrammed permanent spiral.

Figure 5.5

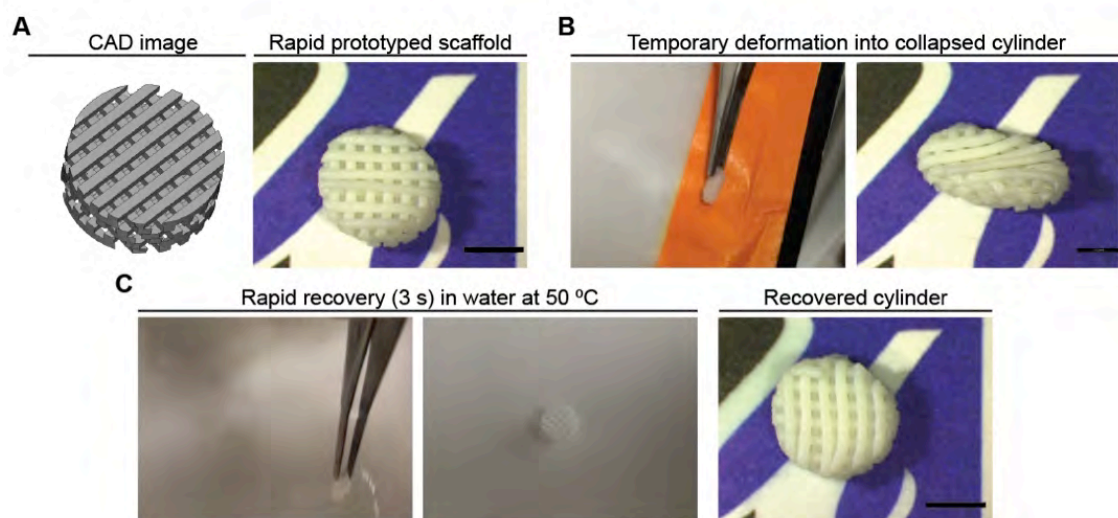


3.5. Shape memory rapid-prototyped macroporous HA-PELA scaffolds

Taking advantage of the thermoplastic nature of HA-PELA, we also prepared 3-D macroporous scaffolds by rapid prototyping. Tissue engineering scaffolds composed of a biodegradable SMP, delivered in a minimally invasive fashion to the defect site, could potentially minimize surgical morbidity. Here we show that the shape memory properties observed with the dense HA-PELA film are retained with the rapid prototyped 3-D scaffold (Figure 5.6). The macroporous HA-PELA cylindrical scaffolds were readily manually deformed into a compressed cylindrical shape at room temperature, and could rapidly (~ 3 s) recover to their original shape at 50 °C. Techniques such as solvent-casting/particulate leaching,[295,304] thermal induced phase separation,[305] and gas foaming[306] have been used to fabricate macroporous shape memory materials for tissue engineering applications. Compared to these techniques, rapid prototyping offers more precise control over pore size, pore interconnectivity, and scaffold shape. To our knowledge, this is the first report of a rapid prototyped biodegradable polymer-mineral composite scaffold exhibiting thermal responsive shape memory behavior.

Figure 5.6. Shape memory properties of a rapid prototyped macroporous cylindrical HA-PELA (25 wt% HA) scaffold. (A) CAD image (left) and stereomicroscopy image (right) of the rapid prototyped HA-PELA scaffold. (B) Cold-pressing and fixation of the HA-PELA scaffold into a collapsed disc at room temperature. (C) Rapid shape recovery of the collapsed disc into the original cylindrical shape in a 50 °C water bath. Scale bars = 3 mm.

Figure 5.6



4. Conclusions

We demonstrated the shape memory behavior of uncross-linked amphiphilic biodegradable thermoplastic polymer PELA and HA-PELA composites around physiologically relevant temperatures. Both PELA and HA-PELA composites were highly elastic and could be readily deformed at room temperature. Temporary shapes with small strain deformations could be stably fixed at room temperature while extensive tensile deformations required lower temperatures to fix. Both PELA and HA-PELA were able to rapidly recover their permanent shapes at a safe triggering temperature of 50 °C, around the T_m of the PEG component. Furthermore, the permanent shape of these thermoplastic materials could be readily reprogrammed at 50 °C, owing to the physical crosslinks within the high molecular weight PELA network. We demonstrated that the incorporation of HA (up to 10 wt% HA) had a minimal impact on the shape memory performance of PELA (e.g. no change in the nearly quantitative shape fixing ration; a slight decrease in recovery ratio from 95.6% to 94.0-94.2%). Higher HA content (20 wt%) increased the tensile modulus of the composites while preserving good shape memory properties (99.4% shape fixation, 90.6% shape recovery). Finally, we showed that the attractive shape memory behavior of HA-PELA was retained with macroporous scaffolds fabricated by rapid prototyping. The shape memory properties demonstrated with the HA-PELA composites, combined with their previously established osteoconductivity and osteoinductivity, make them uniquely suited for guided skeletal tissue

regeneration where the safe delivery and precise fitting of the scaffold within a complex defect is desired.

5. Acknowledgments

This work was supported in part by the National Institutes of Health grants R01GM088678 and a University of Massachusetts Commercial Ventures & Intellectual Property Technology Award. Core resources supported by the National Center for Research Resources Grant S10RR021043 were used.

CHAPTER V: DISCUSSION AND PERSPECTIVES

1. Summary of thesis work

The design of the biomaterial described in this thesis was guided by three basic objectives: 1) dispersion and binding of HA with hydrophilic polymer blocks, 2) biodegradation, 3) sufficient molecular weight and hydrophobic block length for uncross-linked aqueous stability and thermoplastic polymer processing. Importantly, in order to increase the likelihood of clinical translation, the biomaterial should be as simple and easy to produce as possible and be composed of materials that have been previously used in FDA-approved devices. In fulfilling these objectives, HA-PELA-based bone tissue engineering scaffolds highlight how the rational selection of biocompatible building blocks with synergistic interactions can result in smart (i.e. self-fitting / shape memory, guiding stem cell differentiation) tissue engineering scaffolds bearing a combination of unique handling properties and robust biological performance.

Chapters II and III described the *in vitro* and *in vivo* performance of electrospun HA-PELA scaffolds, respectively. Electrospinning was chosen as the scaffold fabrication strategy because it produces materials with ECM-mimetic microstructures and high surface areas for growth factor binding/release. The thin electrospun membranes can be used for guided bone regeneration,[175,307] to wrap around bone defects as synthetic periosteum,[308] or spiral-wrapped to fill long bone defects as described in this thesis. Unlike HA-PLA, the favorable dispersion of HA in PELA enabled the fabrication of HA-PELA scaffolds with uniform morphologies and HA content. The improved adhesion and dispersion of

HA with PELA and the amphiphilic nature of PELA resulted in improved handling properties (hydrophilicity, elasticity, aqueous stability) and bioactivity (more potent MSC differentiation) of HA-PELA compared to HA-PLA. While calcium phosphate bearing materials are known to guide the osteogenic differentiation of MSCs [126], the osteogenic gene induction from cells cultured on HA-PELA is markedly more robust than from other HA-containing synthetic biomaterials. For example, little or no differences in RUNX2 or osteocalcin mRNA expression were observed when adding calcium-deficient HA to electrospun PLLA scaffolds.[131] Similarly, little change in gene expression was observed when culturing human embryonic stem cell-derived MSCs on PLLA/PLGA scaffolds with varying HA contents.[309] HA-PELA's combination of enhanced bioactivity and handling properties is unmatched by other synthetic bone scaffold materials.

Indeed, the unique characteristics of HA-PELA translated into the ability of HA-PELA to serve as an effective scaffold for guiding bone regeneration *in vivo*. The elasticity of HA-PELA enabled it to be wrapped into spirals and stably press-fit into 5-mm critical size femoral defects in rats. The hydrophilicity of HA-PELA facilitated seeding of the electrospun scaffolds with MSCs or rhBMP-2 prior to implantation. The bioactivity of HA-PELA resulted in templated bone formation by MSCs along the bone defects and robust bone formation with a single low dose of rhBMP-2. There was a mild foreign body reaction to the degrading scaffolds at 12 weeks post-op but no evidence of systemic side effects or allergic reactions to the scaffold. Incomplete bridging of the defects by the MSC loaded scaffolds may

have been a result of the relatively low cell viability after implantation, as evidenced by tracking GFP-labeled MSCs. Taken together, chapters II and III of this thesis work demonstrate that electrospun HA-PELA is a promising scaffold for bone tissue engineering applications.

While electrospun scaffolds have distinct advantages, as previously described, they also suffer from dimensional constraints and limited macroporosity that impeded more timely restoration of the mechanical integrity of the long bone defect. Therefore, chapter IV described an alternative scaffold fabrication strategy, the rapid prototyping of PELA and HA-PELA into 3-D macroporous scaffolds. A method was developed to generate filaments of PELA and HA-PELA and fabricate 3-D scaffolds by FDM using a consumer-grade 3-D printer (MakerBot® Replicator2X™). The printing conditions were optimized such that uniform scaffolds with line widths matching the CAD model were generated. Both PELA and HA-PELA scaffolds swelled and stiffened in water, with greater swelling and compressive modulus for HA-PELA. Other amphiphilic polymers including PEG/PBT swell in water, a property that has been shown to improve bone apposition and bone ingrowth *in vivo*. [310] Hydration-induced modulus increases have been observed in a few amphiphilic non-degradable networks [189], and while PEG-PLA copolymers have been studied for decades, this hydration-induced stiffening behavior has only been observed for the molecular weight and composition of PELA designed in this dissertation. One reason that this novel PELA behavior has not been discovered until now is that most studies

used low molecular weight (<100 kDa) copolymers that do not have sufficient molecular entanglements and PLA weight ratios to stiffen upon hydration. This combination of swelling and increased modulus in a biodegradable amphiphilic polymer has not been previously reported.

The unique hydration-induced physical changes in 3-D HA-PELA were exploited for hydration-induced self-fixation, whereby the scaffolds could swell, stiffen and secure themselves in a simulated confined defect. This novel self-fixation behavior coupled with the compressibility of HA-PELA could facilitate its secure fitting in bone defects. The addition of HA effectively offset the low-fouling property of the PEG component and facilitated the attachment of fibroblasts or MSCs. Biphasic PELA/HA-PELA scaffolds were successfully prepared by rapid prototyping for potential applications where differential cell attachment is required, such as for preventing fibrous tissue ingrowth in guided bone regeneration. The PELA surface is designed to prevent fibroblast attachment and oppose soft tissue collapse, while the HA-PELA face exposed towards the bone space could support the adhesion and osteogenic differentiation of progenitor cells. Chapter IV of this thesis exemplifies how a simple and translatable polymer design can yield smart (self-securing / tailored cell attachment) tissue engineering scaffolds. Furthermore, the ability to rapid prototype PELA and HA-PELA on an unmodified consumer-grade printer enables the translation of this approach to the greater research community.

Chapter V examined the thermal responsive shape memory properties of PELA and HA-PELA. Shape memory scaffolds could be delivered in a minimally invasive (e.g. collapsed) temporary shape to the defect and then be triggered to recover to a preprogrammed permanent shape under a safe thermal trigger. However, SMPs are often thermoset materials that cannot be readily fabricated into porous scaffolds and/or are hydrophobic polyesters that have limited bioactivity and mix poorly with HA. Thermoplastic SMPs can be molded into diverse architectures above their transition temperature, enabling reprogramming of their permanent shape if needed. In a clinical setting, this could allow the surgeon to fine-tune the permanent shape prior to implantation. Due to the high molecular weight of PELA (>100,000 Da), physical entanglements in the polymer network act as net-points for the SMP. The addition of up to 10 wt.% HA had no impact on the shape memory efficiency of PELA, whereas the incorporation of 20 wt.% HA slowed the shape recovery rate, likely due to the HA particles restricting the movement of the polymer chains during recovery. The shape memory properties of HA-PELA were retained in rapid-prototyped macroporous 3-D scaffolds. Overall, chapter V demonstrates how the unique shape memory behavior of HA-PELA can be employed for potential minimally invasive delivery and stable fixation of the “smart” HA-PELA scaffolds for tissue engineering applications.

A search on PubMed for the term “bone tissue engineering” yields over 20,000 results but only ~8 bone biomaterials are in clinical use. This dichotomy is

due in part to either the failure to consider the multiple requirements for successful clinical translation and/or the overly complex and expensive biomaterials designs that are impractical for commercialization.[25] This thesis work changes the state of the field of bone tissue engineering by demonstrating how simple and scalable biomaterials can be engineered with smart delivery modalities and robust biological performance. Incorporating simplicity as a key element of biomaterial design has the potential to catalyze the translation of biomaterials from the bench to the bedside.

2. Future directions

2.2.1 Limitations of HA-PELA

The design and characterization of HA-PELA presented in this dissertation provides a framework for the design of high-performance bone tissue engineering biomaterials by using amphiphilic degradable polymers. However, there are a number of limitations to the current design of HA-PELA that should be acknowledged and overcome in future work.

Structural bone grafts are intended to provide mechanical support immediately following implantation. Typically composed of allogenic bone, they are indicated for large load-bearing defects or to supplement bone for revision total hip arthroplasty procedures.[311–313] HA-PELA's low elastic modulus (~200 kPa for HA-PELA versus ~17 GPa for human cortical bone [314]) makes it unsuitable for use as a weight-bearing structural bone grafting material. Therefore, HA-PELA alone would be indicated as a non-structural graft for maxillofacial or cranial sites. Alternatively, electrospun HA-PELA scaffolds pre-seeded with cells or growth factors could be used as a synthetic periosteum to wrap around structural allografts and improve their osteointegration.

PELA alone is relatively low-fouling and supports limited cell adhesion due to the presence of PEG. Whereas the addition of HA significantly increased cell adhesion onto PELA, cell adhesion could be further improved to facilitate the delivery of high densities of cells. This could be accomplished by strategies such as increasing the weight percentage of HA, decreasing the weight percentage or

molecular weight of PEG in PELA, or coating the scaffolds with cell-adhesive polydopamine [315].

Finally, while HA-PELA was designed as a biodegradable scaffold, the current degradation rate of HA-PELA (~ 1yr for complete degradation) is slower than the rate of normal new bone formation (3-4 months for healing [121]). Replacing the PLA block in PELA with PLGA could accelerate the scaffold degradation rate. By varying the ratio of the lactide and glycolide blocks, the degradation rate of PLGA can be varied from 1-4 months.[44] Incorporating PEG can further tune the degradation rate of PLGA.[316] An additional concern is the acidic pH surrounding degrading PLA implants which leads to secondary immune responses and potential bone resorption.[48] Indeed, immune cell infiltration was visible in the degrading electrospun HA-PELA scaffolds at 12 weeks post-op. This secondary immune response could potentially be mitigated by buffering the acidic degradation products with faster dissolving calcium phosphates such as tricalcium phosphate.[236]

2.2.2 Electrospun HA-PELA

The spiral-wrapped electrospun scaffold approach described in Chapter III is a promising strategy for healing long bone defects, however, functional restoration of the bone defect was not achieved by 12 weeks. In future studies, the spiral-wrapped scaffolds could be modified with macropores to increase bone fusion between layers, similar to a design used by Jiang et al.[93] Alternatively, the incorporation of sacrificial PEG fibers could increase the porosity of the

electrospun scaffolds. Another strategy to increase bone bridging could be to electrospin HA-PELA into aligned fibers that are oriented with the femoral defect. Lee et al. found that aligned fibers resulted in greater bone formation in mouse calvarial defects than randomly oriented fibers.[315] Regardless of scaffold design, future work should also explore how healing progresses at later time points, once the scaffolds are fully degraded. A recent *in vitro* degradation study (PBS @ 37 °C) of HA-PELA found a 30% mass loss at 24 weeks and ~96% at 46 weeks. Therefore, a one-year time point is appropriate for assessing the long-term responses to HA-PELA degradation *in vivo*.

By design, the spiral-wrapped HA-PELA scaffolds are readily amenable to testing combinations of growth factors and/or cells. One approach for improving bone healing is to increase angiogenesis in the defect by adding exogenous endothelial cells or pro-angiogenic growth factors. Bone is highly vascularized, with the blood flow supplying nutrients to the osteoblasts, osteocytes, and osteoclasts critical for bone maintenance and remodeling.[317] For a cell-based strategy to accelerate defect bridging, endothelial cells could be seeded with rMSCs or combined with rhBMP-2 in the spiral-wrapped HA-PELA scaffolds. Co-cultures of endothelial cells and MSCs have been shown to induce enhanced osteogenesis *in vitro* than MSCs alone.[318] *In vivo*, incorporating endothelial progenitor cells has been shown to increase early vascularization and bone formation in critical-size rat femoral defects.[319]

The addition of growth factor combinations or other therapeutics to HA-PELA could further accelerate bone healing. Patel et al. showed that the delivery of rhBMP-2 combined with vascular endothelial growth factor (VEGF) may accelerate bone defect bridging.[320] However, there was no difference in bone formation between the BMP-2 and BMP-2+VEGF groups at 12 weeks post-op. One potential reason for a limited beneficial effect at later stages is that VEGF promotes early vessel formation but may inhibit vessel maturation and stabilization.[317,321] Sphingosine 1-phosphate (S1P) is a phospholipid that has been shown to promote both the early and late stages of blood vessel formation,[322] and enhance healing in models of diabetes[323] and ischemic limb injury.[324] Our group recently used electrospun membranes of PELA and alkylated PELA block copolymers to improve the controlled release of S1P.[322] We found that unmodified PELA and PELA modified with 14-carbon bearing lactide units resulted in sustained release of bioactive S1P over 7 days. Based on the release characteristics of S1P from amphiphilic polymers such as PELA, future work will explore the synergistic effects of S1P and rhBMP-2 delivery from spiral-wrapped HA-PELA for healing critical size femoral defects in rats. Other potential additives to HA-PELA include bone anabolic factors such as prostaglandin E₂. Prostaglandin E₂ has been shown to stimulate bone formation and increase overall bone mass in both adolescent and aged rats.[325] However, the sustained release of Prostaglandin E₂ from bone tissue engineering scaffolds has not yet been explored.

2.2.3 Rapid prototyped PELA/HA-PELA

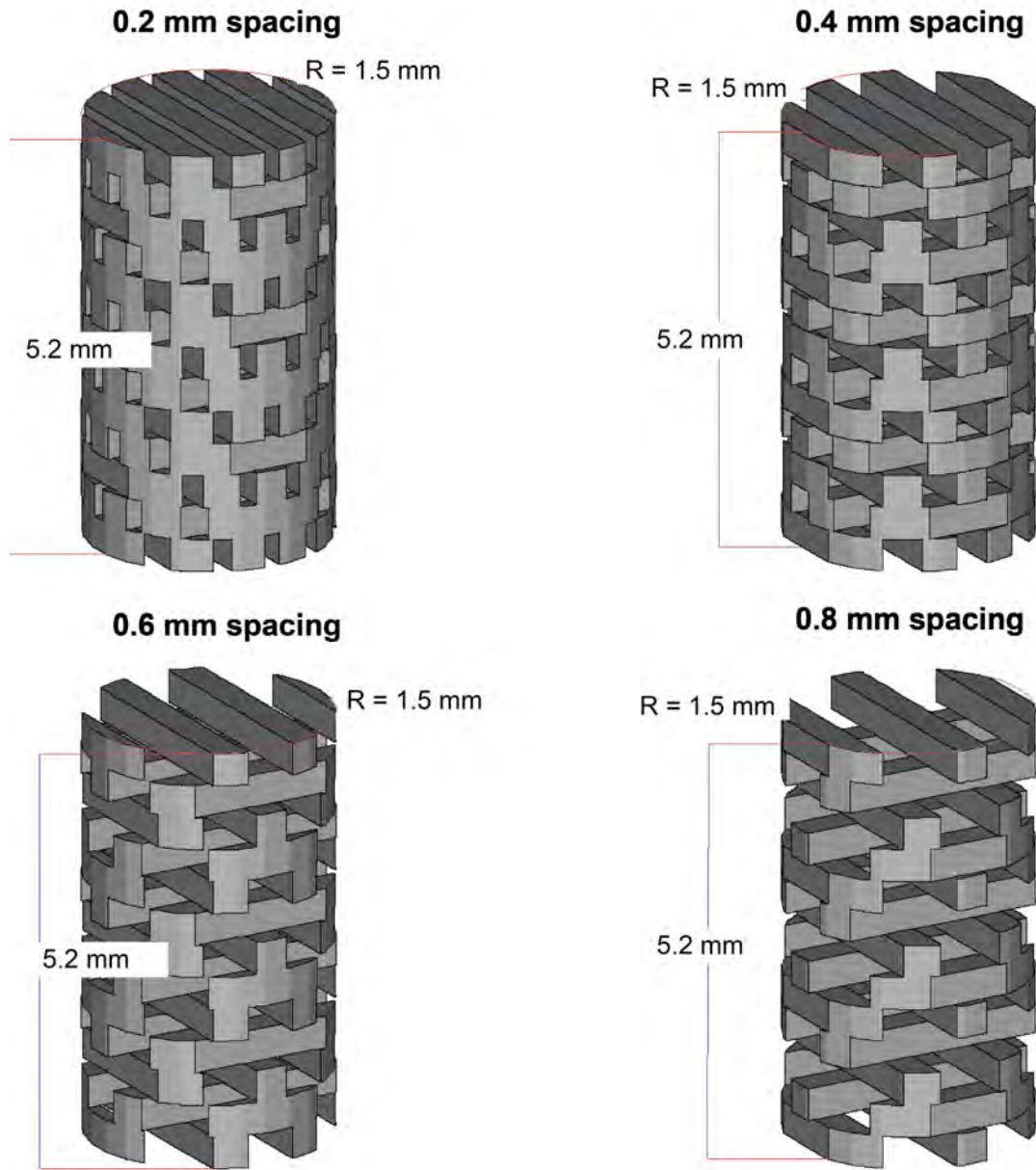
The promising preliminary results shown in Appendix I demonstrate the feasibility of healing mandibular defects with rapid prototyped HA-PELA and rhBMP-2, but warrant further study with an increased sample size to enable quantitative conclusions. It would be beneficial to monitor the healing at longer time points, for example 6 and 12 months, when the scaffold is expected to degrade. If 25 wt.% HA is insufficient to buffer the acidic degradation byproducts of PLA, there may be some inflammation and/or bone resorption at these later time points. If polymer degradation does result in poorer healing outcomes, future work should be to minimize the amount of foreign material required to provide a sufficient template for bone ingrowth. This may be accomplished through optimization of the HA-PELA scaffold morphology using CAD by adjusting the line spacing of the scaffolds. For example, Figure 6.1 shows CAD models of rat femoral defect sized (5 mm height, 3 mm diameter) scaffolds with increasing line spacing which correlates to increasing porosity and decreasing the mass of polymer. Further optimization of the scaffold morphology could be to explore different line arrangements, such as a staggered design, as shown in Figure 6.1, versus a straight-line arrangement.

While the FDM line size and spacing of 3-D HA-PELA scaffolds closely matches the CAD design, the dimensional accuracy and reproducibility of FDM fabricated HA-PELA implants based on patient-specific CT data will need to be validated. Rapid prototyped bone implants based on patient-specific CT data

have been FDA approved (i.e. OsteoFab™ by Oxford Performance Materials). Therefore, the resolution of CT scanning and reconstruction is sufficient for the fabrication of custom bone grafts. However, the OsteoFab™ implants are fabricated by the selective laser sintering of a non-degradable polymer. This fabrication process is very different from the 3-D HA-PELA process. FDM fabricated degradable bone implants have not yet been approved for clinical use.

Figure 6.1. CAD models of rat femoral defect sized scaffolds with increasing line spacing.

Figure 6.1



3. Concluding remarks

The hype surrounding tissue engineering has waxed and waned since the “Vacanti mouse” with an ear-shape tissue grown on its’ back garnered widespread media attention in 1997.[40] Cell sourcing, vascularization/nutrient transport, immune response, and scaffold degradation are just a few of the issues that need to be resolved to fully realize the promise of regenerating complex tissues and organs. Furthermore, while some tissue engineered products have entered clinical use (Carticel®, Apligraf®, Dermagraft®), the regulatory approval process and business constraints for such cell-based or cell-biomaterial combination therapies remain as significant hurdles.[118,326] The tissue engineering research in our laboratory has taken two paths: (1) the synthesis of novel biomaterials with unique functionalities to enable the design of next generation of tissue engineering scaffolds, (2) the strategic combination of building blocks previously used in FDA-approved devices with synergistic interactions to facilitate clinical translation. Both approaches will lead to better outcomes for patients; however, the second approach uses clinical translation as an essential design component and has the potential to make a more rapid impact. Designing biomaterials / tissue engineered therapies with translation in mind is important to realize the hope of tissue engineering.

The body of work presented in this thesis exemplifies how this strategic integration of simple components can produce smart tissue engineering scaffolds. Electrospun and rapid prototyped HA-PELA scaffolds are simple to

produce in large quantities, available off-the-shelf, easy to use (hydrophilic, moldable/press-fit), feature unique delivery modalities (self-fitting / shape-memory), and are bioactive. PLA, PEG, and HA are all used in FDA-approved implants, resulting in a potential 510(k) FDA-approval pathway for HA-PELA. This reduces the approximate cost of approval to \$1-50 million and 3-6 years, versus \$45-150 million and 5-8 years for a premarket approval (PMA) pathway.[118] The incorporation of exogenous cells or growth factors into HA-PELA would likely require PMA or regulation of it as a combination product and extend the approval time and cost. The clinical niche for HA-PELA, whether guided bone regeneration, cranio-maxillofacial bone grafting, synthetic periosteum, or other, should be worked out based on scientific evidence and clinical need/market analysis. Future studies should involve further collaboration with clinicians to define the clinical niche and validate the performance of HA-PELA in a large animal model.

REFERENCES

- [1] Marino JT, Ziran BH. Use of solid and cancellous autologous bone graft for fractures and nonunions. *Orthop Clin North Am* 2010;41:15–26.
- [2] Albee FH. *Bone-graft surgery*. W.B. Saunders Company; 1915.
- [3] Vaccaro AR. The role of the osteoconductive scaffold in synthetic bone graft. *Orthopedics* 2002;25:s571–8.
- [4] Silber JS, Anderson DG, Daffner SD, Brislin BT, Leland JM, Hilibrand AS, et al. Donor site morbidity after anterior iliac crest bone harvest for single-level anterior cervical discectomy and fusion. *Spine* 2003;28:134–9.
- [5] Sasso RC, LeHuec JC, Shaffrey C. Iliac crest bone graft donor site pain after anterior lumbar interbody fusion: a prospective patient satisfaction outcome assessment. *J Spinal Disord Tech* 2005;18 Suppl:S77–81.
- [6] Neovius E, Engstrand T. Craniofacial reconstruction with bone and biomaterials: review over the last 11 years. *J Plast Reconstr Aesthet Surg* 2010;63:1615–23.
- [7] Kellman RM. Safe and dependable harvesting of large outer-table calvarial bone grafts. *Arch Otolaryngol - Head Neck Surg* 1994;120:856–60.

- [8] Gruskay J a, Basques B a, Bohl DD, Webb ML, Grauer JN. Short-Term Adverse Events, Length of Stay, and Readmission Following Iliac Crest Bone Graft for Spinal Fusion. *Spine* 2014;1718–24.
- [9] Boyce T, Edwards J, Scarborough N. Allograft bone. The influence of processing on safety and performance. *Orthop Clin North Am* 1999;30:571–81.
- [10] Xie C, Reynolds D, Awad H, Rubery PT, Pelled G, Gazit D, et al. Structural bone allograft combined with genetically engineered mesenchymal stem cells as a novel platform for bone tissue engineering. *Tissue Eng* 2007;13:435–45.
- [11] Vastel L, Meunier A, Siney H, Sedel L, Courpied J-P. Effect of different sterilization processing methods on the mechanical properties of human cancellous bone allografts. *Biomaterials* 2004;25:2105–10.
- [12] Hofmann a, Konrad L, Hessmann MH, Küchle R, Korner J, Rompe JD, et al. The influence of bone allograft processing on osteoblast attachment and function. *J Orthop Res* 2005;23:846–54.
- [13] Nguyen H, Morgan D a F, Forwood MR. Sterilization of allograft bone: effects of gamma irradiation on allograft biology and biomechanics. *Cell Tissue Bank* 2007;8:93–105.

- [14] Wheeler DL, Enneking WF. Allograft bone decreases in strength in vivo over time. *Clin Orthop Relat Res* 2005;36–42.
- [15] Urist MR. Bone: Formation by Autoinduction. *Science* (80-) 1965;150:893–9.
- [16] Wozney J, Rosen V, Celeste A, Mitsock L, Whitters M, Kriz R, et al. Novel regulators of bone formation: molecular clones and activities. *Science* 1988;242:1528–34.
- [17] McKay WF, Peckham SM, Badura JM. A comprehensive clinical review of recombinant human bone morphogenetic protein-2 (INFUSE Bone Graft). *Int Orthop* 2007;31:729–34.
- [18] Suzuki S, Ikada Y. *Biomaterials for Surgical Operation*. Springer; 2011.
- [19] Sibiya SJ, Olivier EI, Duneas N. High yield isolation of BMP-2 from bone and in vivo activity of a combination of BMP-2/TGF- β 1. *J Biomed Mater Res A* 2013;101:641–6.
- [20] Epstein NE. Pros, cons, and costs of INFUSE in spinal surgery. *Surg Neurol Int* 2011;2:10.
- [21] Epstein NE. Complications due to the use of BMP/INFUSE in spine surgery: The evidence continues to mount. *Surg Neurol Int* 2013;4:S343–52.

- [22] Brown K V, Li B, Guda T, Perrien DS, Guelcher SA, Wenke JC. Improving bone formation in a rat femur segmental defect by controlling bone morphogenetic protein-2 release. *Tissue Eng Part A* 2011;17:1735–46.
- [23] Cho T-J, Gerstenfeld LC, Einhorn TA. Differential temporal expression of members of the transforming growth factor beta superfamily during murine fracture healing. *J Bone Miner Res* 2002;17:513–20.
- [24] Faour O, Dimitriou R, Cousins CA, Giannoudis P V. The use of bone graft substitutes in large cancellous voids: any specific needs? *Injury* 2011;42 Suppl 2:S87–90.
- [25] Place ES, Evans ND, Stevens MM. Complexity in biomaterials for tissue engineering. *Nat Mater* 2009;8:457–70.
- [26] Langer R, Tirrell DA. Designing materials for biology and medicine. *Nature* 2004;428:487–92.
- [27] Langer R, Vacanti J. Tissue engineering. *Science* 1993;260:920–6.
- [28] Khan Y, Yaszemski MJ, Mikos AG, Laurencin CT. Tissue engineering of bone: material and matrix considerations. *J Bone Joint Surg Am* 2008;90 Suppl 1:36–42.

- [29] Hutmacher DW, Schantz JT, Lam CXF, Tan KC, Lim TC. State of the art and future directions of scaffold-based bone engineering from a biomaterials perspective. *J Tissue Eng Regen Med* 2007;1:245–60.
- [30] Stevens MM. Biomaterials for bone tissue engineering. *Mater Today* 2008;11:18–25.
- [31] Hutmacher DW. Scaffolds in tissue engineering bone and cartilage. *Biomaterials* 2000;21:2529–43.
- [32] Vacanti C. The history of tissue engineering. *J Cell Mol Med* 2006;1:569–76.
- [33] Vacanti CA, Vacanti J. Chapter One - The history and scope of tissue engineering. *Princ. Tissue Eng.*, Elsevier; 2007, p. 3–6.
- [34] Genesis II. n.d.
- [35] Nerlich AG, Zink A, Szeimies U, Hagedorn HG. Ancient Egyptian prosthesis of the big toe. *Lancet* 2000.;356:2176–9.
- [36] Green WT. Articular cartilage repair. Behavior of rabbit chondrocytes during tissue culture and subsequent allografting. *Clin Orthop Relat Res* 1977:237–50.

- [37] Burke JF, Yannas I V, Quinby WC, Bondoc CC, Jung WK. Successful use of a physiologically acceptable artificial skin in the treatment of extensive burn injury. *Ann Surg* 1981;194:413–28.
- [38] Vacanti JP. Beyond Transplantation. *Arch Surg* 1988;123:545.
- [39] Vacanti JP, Morse MA, Saltzman WM, Domb AJ, Perez-Atayde A, Langer R. Selective cell transplantation using bioabsorbable artificial polymers as matrices. *J Pediatr Surg* 1988;23:3–9.
- [40] Cao Y, Vacanti JP, Paige KT, Upton J, Vacanti CA. Transplantation of chondrocytes utilizing a polymer-cell construct to produce tissue-engineered cartilage in the shape of a human ear. *Plast Reconstr Surg* 1997;100:297–302;303–4.
- [41] Furth ME, Atala A, Van Dyke ME. Smart biomaterials design for tissue engineering and regenerative medicine. *Biomaterials* 2007;28:5068–73.
- [42] Anderson DG, Burdick J a, Langer R. Materials science. Smart biomaterials. *Science* 2004;305:1923–4.
- [43] Ma PX. Scaffolds for tissue fabrication. *Mater Today* 2004;7:30–40.
- [44] Nair LS, Laurencin CT. Biodegradable polymers as biomaterials. *Prog Polym Sci* 2007;32:762–98.

- [45] Henton DE, Gruber P, Lunt J, Randall J. Polylactic Acid Technology. In: Mohanty AK, Misra M, Drzal LT, editors. Nat. Fibers, Biopolym. Biocomposites, Boca Raton, FL: Taylor & Francis; 2005, p. 527–78.
- [46] Engelberg I, Kohn J. Physico-mechanical properties of degradable polymers used in medical applications: A comparative study. *Biomaterials* 1991;12:292–304.
- [47] Maurus PB, Kaeding CC. Bioabsorbable implant material review. *Oper Tech Sports Med* 2004;12:158–60.
- [48] Fillion TM, Xu J, Prasad ML, Song J. In vivo tissue responses to thermal-responsive shape memory polymer nanocomposites. *Biomaterials* 2011;32:985–91.
- [49] Bergsma JE, de Bruijn WC, Rozema FR, Bos RR, Boering G. Late degradation tissue response to poly(L-lactide) bone plates and screws. *Biomaterials* 1995;16:25–31.
- [50] Woodruff MA, Hutmacher DW. The return of a forgotten polymer— Polycaprolactone in the 21st century. *Prog Polym Sci* 2010;35:1217–56.
- [51] Huang M-H, Li S, Hutmacher DW, Coudane J, Vert M. Degradation characteristics of poly(ϵ -caprolactone)-based copolymers and blends. *J Appl Polym Sci* 2006;102:1681–7.

- [52] Middleton JC, Tipton a J. Synthetic biodegradable polymers as orthopedic devices. *Biomaterials* 2000;21:2335–46.
- [53] Veronese FM, Pasut G. PEGylation, successful approach to drug delivery. *Drug Discov Today* 2005;10:1451–8.
- [54] Latour R. Biomaterials: Protein–Surface Interactions. *Encycl Biomater Biomed Eng* 2005:1–15.
- [55] Yamaoka T, Tabata Y, Ikada Y. Distribution and tissue uptake of poly(ethylene glycol) with different molecular weights after intravenous administration to mice. *J Pharm Sci* 1994;83:601–6.
- [56] Zhu J. Bioactive modification of poly(ethylene glycol) hydrogels for tissue engineering. *Biomaterials* 2010;31:4639–56.
- [57] Allen TM, Cullis PR. Drug delivery systems: entering the mainstream. *Science* 2004;303:1818–22.
- [58] Hans M., Lowman A. Biodegradable nanoparticles for drug delivery and targeting. *Curr Opin Solid State Mater Sci* 2002;6:319–27.
- [59] Oh JK. Polylactide (PLA)-based amphiphilic block copolymers: synthesis, self-assembly, and biomedical applications. *Soft Matter* 2011;7:5096.

- [60] Lee JH, Go AK, Oh SH, Lee KE, Yuk SH. Tissue anti-adhesion potential of ibuprofen-loaded PLLA-PEG diblock copolymer films. *Biomaterials* 2005;26:671–8.
- [61] Liu S, Hu C, Li F, Li X, Cui W, Fan C. Prevention of peritendinous adhesions with electrospun ibuprofen-loaded PELA fibrous membranes. *Tissue Eng Part A* 2012;19.
- [62] Yang D-J, Chen F, Xiong Z-C, Xiong C-D, Wang Y-Z. Tissue anti-adhesion potential of biodegradable PELA electrospun membranes. *Acta Biomater* 2009;5:2467–74.
- [63] Zhang Z, Ni J, Chen L, Yu L, Xu J, Ding J. Biodegradable and thermoreversible PCLA-PEG-PCLA hydrogel as a barrier for prevention of post-operative adhesion. *Biomaterials* 2011;32:4725–36.
- [64] Park S-N, Jang HJ, Choi YS, Cha JM, Son SY, Han SH, et al. Preparation and characterization of biodegradable anti-adhesive membrane for peritoneal wound healing. *J Mater Sci Mater Med* 2007;18:475–82.
- [65] Tessmar JK, Göpferich AM. Customized PEG-derived copolymers for tissue-engineering applications. *Macromol Biosci* 2007;7:23–39.
- [66] Karageorgiou V, Kaplan D. Porosity of 3D biomaterial scaffolds and osteogenesis. *Biomaterials* 2005;26:5474–91.

- [67] Murphy WL, Dennis RG, Kileny JL, Mooney DJ. Salt fusion: an approach to improve pore interconnectivity within tissue engineering scaffolds. *Tissue Eng* 2002;8:43–52.
- [68] Mikos AG, Thorsen AJ, Czerwonka LA, Bao Y, Langer R, Winslow DN, et al. Preparation and characterization of poly(L-lactic acid) foams. *Polymer (Guildf)* 1994;35:1068–77.
- [69] Mooney DJ, Baldwin DF, Suh NP, Vacanti JP, Langer R. Novel approach to fabricate porous sponges of poly(D,L-lactic-co-glycolic acid) without the use of organic solvents. *Biomaterials* 1996;17:1417–22.
- [70] Ma PX, Zhang R. Synthetic nano-scale fibrous extracellular matrix. *J Biomed Mater Res* 1999;46:60–72.
- [71] Cui H, Webber MJ, Stupp SI. Self-assembly of peptide amphiphiles: from molecules to nanostructures to biomaterials. *Biopolymers* 2010;94:1–18.
- [72] Pham QP, Sharma U, Mikos AG. Electrospinning of polymeric nanofibers for tissue engineering applications: a review. *Tissue Eng* 2006;12:1197–211.
- [73] Yeong W-Y, Chua C-K, Leong K-F, Chandrasekaran M. Rapid prototyping in tissue engineering: challenges and potential. *Trends Biotechnol* 2004;22:643–52.

- [74] Liu X, Ma PX. Polymeric scaffolds for bone tissue engineering. *Ann Biomed Eng* 2004;32:477–86.
- [75] Stevens B, Yang Y, Mohandas A, Stucker B, Nguyen KT. A review of materials, fabrication methods, and strategies used to enhance bone regeneration in engineered bone tissues. *J Biomed Mater Res B Appl Biomater* 2008;85:573–82.
- [76] Li D, Xia Y. Electrospinning of Nanofibers: Reinventing the Wheel? *Adv Mater* 2004;16:1151–70.
- [77] Formhals A. Process and apparatus for preparing artificial threads. US1975504 A, 1934.
- [78] Reneker DH, Chun I. Nanometre diameter fibres of polymer, produced by electrospinning. *Nanotechnology* 1996;7:216–23.
- [79] Wang Y, Gao R, Wang P-P, Jian J, Jiang X-L, Yan C, et al. The differential effects of aligned electrospun PHBHHx fibers on adipogenic and osteogenic potential of MSCs through the regulation of PPAR γ signaling. *Biomaterials* 2012;33:485–93.
- [80] Sun Z, Zussman E, Yarin a. L, Wendorff JH, Greiner a. Compound Core–Shell Polymer Nanofibers by Co-Electrospinning. *Adv Mater* 2003;15:1929–32.

- [81] Jana S, Zhang M. Fabrication of 3D aligned nanofibrous tubes by direct electrospinning. *J Mater Chem B* 2013;1:2575.
- [82] Lutolf MP, Hubbell JA. Synthetic biomaterials as instructive extracellular microenvironments for morphogenesis in tissue engineering. *Nat Biotechnol* 2005;23:47–55.
- [83] Li W-J, Laurencin CT, Caterson EJ, Tuan RS, Ko FK. Electrospun nanofibrous structure: a novel scaffold for tissue engineering. *J Biomed Mater Res* 2002;60:613–21.
- [84] Matthews JA, Wnek GE, Simpson DG, Bowlin GL. Electrospinning of collagen nanofibers. *Biomacromolecules* 2002;3:232–8.
- [85] Boland E, Wnek G, Simpson D, Pawlowski K, Bowlin G. Tailoring tissue engineering scaffolds using electrostatic processing techniques: A study of poly(glycolic acid) electrospinning. *J Macromol Sci Part A* 2001;38:1231–43.
- [86] Lim SH, Mao H-Q. Electrospun scaffolds for stem cell engineering. *Adv Drug Deliv Rev* 2009;61:1084–96.
- [87] Fillion TM, Kutikov A, Song J. Chemically modified cellulose fibrous meshes for use as tissue engineering scaffolds. *Bioorg Med Chem Lett* 2011;21:5067–70.

- [88] Cao H, McHugh K, Chew SY, Anderson JM. The topographical effect of electrospun nanofibrous scaffolds on the in vivo and in vitro foreign body reaction. *J Biomed Mater Res A* 2010;93:1151–9.
- [89] Woo KM, Chen VJ, Jung H, Kim T, Shin H, Baek J, et al. Comparative evaluation of nanofibrous scaffolding for bone regeneration in critical-size calvarial defects. *Tissue Eng Part A* 2009;15:2155–62.
- [90] Cai YZ, Wang LL, Cai HX, Qi YY, Zou XH, Ouyang HW. Electrospun nanofibrous matrix improves the regeneration of dense cortical bone. *J Biomed Mater Res A* 2010;95:49–57.
- [91] Zhong S, Zhang Y, Lim CT. Fabrication of Large Pores in Electrospun Nanofibrous Scaffolds for Cellular Infiltration: A Review. *Tissue Eng Part B Rev* 2011;00.
- [92] Ekaputra AK, Zhou Y, Cool SM, Hutmacher DW. Composite electrospun scaffolds for engineering tubular bone grafts. *Tissue Eng Part A* 2009;15:3779–88.
- [93] Jiang H, Zuo Y, Zou Q, Wang H, Du J, Li Y, et al. Biomimetic spiral-cylindrical scaffold based on hybrid chitosan/cellulose/nano-hydroxyapatite membrane for bone regeneration. *ACS Appl Mater Interfaces* 2013;5:12036–44.

- [94] Hong JK, Madhally S V. 3D Scaffold of Electrospun Fibers with Large Pore Size for Tissue Regeneration. *Acta Biomater* 2010.
- [95] Blakeney B a, Tambralli A, Anderson JM, Andukuri A, Lim D-J, Dean DR, et al. Cell infiltration and growth in a low density, uncompressed three-dimensional electrospun nanofibrous scaffold. *Biomaterials* 2011;32:1583–90.
- [96] Yokoyama Y, Hattori S, Yoshikawa C, Yasuda Y, Koyama H, Takato T, et al. Novel wet electrospinning system for fabrication of spongiform nanofiber 3-dimensional fabric. *Mater Lett* 2009;63:754–6.
- [97] Kim MS, Son J, Lee H, Hwang H, Choi CH, Kim G. Highly porous 3D nanofibrous scaffolds processed with an electrospinning/laser process. *Curr Appl Phys* 2014;14:1–7.
- [98] Baker BM, Shah RP, Silverstein AM, Esterhai JL, Burdick J a, Mauck RL. Sacrificial nanofibrous composites provide instruction without impediment and enable functional tissue formation. *Proc Natl Acad Sci U S A* 2012;109:14176–81.
- [99] Yang S, Leong K-F, Du Z, Chua C. The design of scaffolds for use in tissue engineering. Part II. Rapid prototyping techniques. *Tissue Eng* 2002;8:1–11.

- [100] Melchels FPW, Feijen J, Grijpma DW. A review on stereolithography and its applications in biomedical engineering. *Biomaterials* 2010;31:6121–30.
- [101] Melchels FPW, Bertoldi K, Gabbriellini R, Velders AH, Feijen J, Grijpma DW. Mathematically defined tissue engineering scaffold architectures prepared by stereolithography. *Biomaterials* 2010;31:6909–16.
- [102] Yoo D. New paradigms in internal architecture design and freeform fabrication of tissue engineering porous scaffolds. *Med Eng Phys* 2012;34:762–76.
- [103] Cooke MN, Fisher JP, Dean D, Rimnac C, Mikos AG. Use of stereolithography to manufacture critical-sized 3D biodegradable scaffolds for bone ingrowth. *J Biomed Mater Res B Appl Biomater* 2003;64:65–9.
- [104] Gauvin R, Chen Y-C, Lee JW, Soman P, Zorlutuna P, Nichol JW, et al. Microfabrication of complex porous tissue engineering scaffolds using 3D projection stereolithography. *Biomaterials* 2012;33:3824–34.
- [105] Chan V, Zorlutuna P, Jeong JH, Kong H, Bashir R. Three-dimensional photopatterning of hydrogels using stereolithography for long-term cell encapsulation. *Lab Chip* 2010;10:2062–70.

- [106] Butscher A, Böhner M, Hofmann S, Gauckler L, Müller R. Structural and material approaches to bone tissue engineering in powder-based three-dimensional printing. *Acta Biomater* 2011;7:907–20.
- [107] Sachs E, Cima M, Cornie J. Three-Dimensional Printing: Rapid Tooling and Prototypes Directly from a CAD Model. *CIRP Ann - Manuf Technol* 1990;39:201–4.
- [108] Inzana J a, Olvera D, Fuller SM, Kelly JP, Graeve O a, Schwarz EM, et al. 3D printing of composite calcium phosphate and collagen scaffolds for bone regeneration. *Biomaterials* 2014:1–9.
- [109] Boland T, Tao X, Damon BJ, Manley B, Kesari P, Jalota S, et al. Drop-on-demand printing of cells and materials for designer tissue constructs. *Mater Sci Eng C* 2007;27:372–6.
- [110] Zein I, Hutmacher DW, Tan KC, Teoh SH. Fused deposition modeling of novel scaffold architectures for tissue engineering applications. *Biomaterials* 2002;23:1169–85.
- [111] Serra T, Planell J a, Navarro M. High-resolution PLA-based composite scaffolds via 3-D printing technology. *Acta Biomater* 2013;9:5521–30.

- [112] Fedorovich NE, De Wijn JR, Verbout AJ, Alblas J, Dhert WJ a. Three-dimensional fiber deposition of cell-laden, viable, patterned constructs for bone tissue printing. *Tissue Eng Part A* 2008;14:127–33.
- [113] Dalton PD, Vaquette C, Farrugia BL, Dargaville TR, Brown TD, Hutmacher DW. Electrospinning and additive manufacturing: converging technologies. *Biomater Sci* 2013;1:171.
- [114] Park SH, Kim TG, Kim HC, Yang D-Y, Park TG. Development of dual scale scaffolds via direct polymer melt deposition and electrospinning for applications in tissue regeneration. *Acta Biomater* 2008;4:1198–207.
- [115] Ahn SH, Lee HJ, Kim GH. Polycaprolactone scaffolds fabricated with an advanced electrohydrodynamic direct-printing method for bone tissue regeneration. *Biomacromolecules* 2011;12:4256–63.
- [116] Brown TD, Dalton PD, Hutmacher DW. Direct writing by way of melt electrospinning. *Adv Mater* 2011;23:5651–7.
- [117] Bose S, Roy M, Bandyopadhyay A. Recent advances in bone tissue engineering scaffolds. *Trends Biotechnol* 2012;30:546–54.
- [118] Pashuck E, Stevens M. Designing Regenerative Biomaterial Therapies for the Clinic. *Sci Transl Med* 2012;4:1–12.

- [119] Mann S. *Biomineralization: Principles and Concepts in Bioinorganic Materials Chemistry*. Oxford University Press; 2001.
- [120] Robey PG, Boskey AL. The Composition of Bone. In: Rosen CJ, editor. *Prim. Metab. Bone Dis. Disord. Miner. Metab.*, Washington, D.C.: American Society for Bone and Mineral Research; 2008, p. 32–8.
- [121] Baroli B. From natural bone grafts to tissue engineering therapeutics: Brainstorming on pharmaceutical formulative requirements and challenges. *J Pharm Sci* 2009;98:1317–75.
- [122] Robling AG, Castillo AB, Turner CH. Biomechanical and molecular regulation of bone remodeling. *Annu Rev Biomed Eng* 2006;8:455–98.
- [123] Sabir MI, Xu X, Li L. A review on biodegradable polymeric materials for bone tissue engineering applications. *J Mater Sci* 2009;44:5713–24.
- [124] Kilpadi KL, Chang PL, Bellis SL. Hydroxylapatite binds more serum proteins, purified integrins, and osteoblast precursor cells than titanium or steel. *J Biomed Mater Res* 2001;57:258–67.
- [125] Gorbunoff M, Timasheff S. The interaction of proteins with hydroxyapatite III. Mechanism. *Anal Biochem* 1984;136:440–5.
- [126] Shih Y-R V., Hwang Y, Phadke A, Kang H, Hwang NS, Caro EJ, et al. Calcium phosphate-bearing matrices induce osteogenic differentiation of

stem cells through adenosine signaling. Proc Natl Acad Sci U S A
2014;111:990–5.

- [127] Costantino PD, Chaplin JM, Wolpoe ME, Catalano PJ, Sen C, Bederson JB, et al. Applications of fast-setting hydroxyapatite cement: cranioplasty. Otolaryngol Head Neck Surg 2000;123:409–12.
- [128] Oosterbos CJM, Rahmy AIA, Tonino AJ, Witpeerd W. High survival rate of hydroxyapatite-coated hip prostheses: 100 consecutive hips followed for 10 years. Acta Orthop Scand 2004;75:127–33.
- [129] Grote JJ. Reconstruction of the ossicular chain with hydroxyapatite implants. Ann Otol Rhinol Laryngol Suppl 1986;123:10–2.
- [130] Gaharwar AK, Dammu S a, Canter JM, Wu C-J, Schmidt G. Highly Extensible, Tough, and Elastomeric Nanocomposite Hydrogels from Poly(ethylene glycol) and Hydroxyapatite Nanoparticles. Biomacromolecules 2011;12:1641–50.
- [131] D'Angelo F, Armentano I, Cacciotti I, Tiribuzi R, Quattrocelli M, Del Gaudio C, et al. Tuning multi/pluri-potent stem cell fate by electrospun poly(L-lactic acid)-calcium-deficient hydroxyapatite nanocomposite mats. Biomacromolecules 2012;13:1350–60.

- [132] Polini A, Pisignano D, Parodi M, Quarto R, Scaglione S. Osteoinduction of Human Mesenchymal Stem Cells by Bioactive Composite Scaffolds without Supplemental Osteogenic Growth Factors. *PLoS One* 2011;6:e26211.
- [133] Xu J, Li X, Lian JB, Ayers DC, Song J. Sustained and localized in vitro release of BMP-2/7, RANKL, and tetracycline from FlexBone, an elastomeric osteoconductive bone substitute. *J Orthop Res* 2009;27:1306–11.
- [134] Zheng F, Wang S, Wen S, Shen M, Zhu M, Shi X. Characterization and antibacterial activity of amoxicillin-loaded electrospun nano-hydroxyapatite/poly(lactic-co-glycolic acid) composite nanofibers. *Biomaterials* 2013;34:1402–12.
- [135] Fillion TM, Li X, Mason-Savas A, Kreider JM, Goldstein SA, Ayers DC, et al. Elastomeric osteoconductive synthetic scaffolds with acquired osteoinductivity expedite the repair of critical femoral defects in rats. *Tissue Eng Part A* 2011;17:503–11.
- [136] Dorozhkin S V. Calcium orthophosphate-based biocomposites and hybrid biomaterials. *J Mater Sci* 2009;44:2343–87.
- [137] Ji W, Yang F, Seyednejad H, Chen Z, Hennink WE, Anderson JM, et al. Biocompatibility and degradation characteristics of PLGA-based

electrospun nanofibrous scaffolds with nanoapatite incorporation.

Biomaterials 2012;33:6604–14.

[138] Supová M. Problem of hydroxyapatite dispersion in polymer matrices: a review. J Mater Sci Mater Med 2009;20:1201–13.

[139] Wagoner Johnson AJ, Herschler B a. A review of the mechanical behavior of CaP and CaP/polymer composites for applications in bone replacement and repair. Acta Biomater 2011;7:16–30.

[140] Wang M. Developing bioactive composite materials for tissue replacement. Biomaterials 2003;24:2133–51.

[141] Kim H-W, Knowles JC, Kim H-E. Effect of biphasic calcium phosphates on drug release and biological and mechanical properties of poly(caprolactone) composite membranes. J Biomed Mater Res 2004;70A:467–79.

[142] Jeong SI, Ko EK, Yum J, Jung CH, Lee YM, Shin H. Nanofibrous poly(lactic acid)/hydroxyapatite composite scaffolds for guided tissue regeneration. Macromol Biosci 2008;8:328–38.

[143] Rodriguez G, Dias J, D'Ávila MA, Bártolo P. Influence of Hydroxyapatite on Extruded 3D Scaffolds. Procedia Eng 2013;59:263–9.

- [144] Kim H, Lee H, Knowles JC. Electrospinning biomedical nanocomposite fibers of hydroxyapatite/poly(lactic acid) for bone regeneration. *J Biomed Mater Res A* 2006;79:643–9.
- [145] Dupraz a M, de Wijn JR, v d Meer S a, de Groot K. Characterization of silane-treated hydroxyapatite powders for use as filler in biodegradable composites. *J Biomed Mater Res* 1996;30:231–8.
- [146] Dupraz AMP, v. d. Meer SAT, De Wijn JR, Goedemoed JH. Biocompatibility screening of silane-treated hydroxyapatite powders, for use as filler in resorbable composites. *J Mater Sci Mater Med* 1996;7:731–8.
- [147] Qiu X, Hong Z, Hu J, Chen L, Chen X, Jing X. Hydroxyapatite surface modified by L-lactic acid and its subsequent grafting polymerization of L-lactide. *Biomacromolecules* 2005;6:1193–9.
- [148] Wang Y, Dai J, Zhang Q, Xiao Y, Lang M. Improved mechanical properties of hydroxyapatite/poly(ϵ -caprolactone) scaffolds by surface modification of hydroxyapatite. *Appl Surf Sci* 2010;256:6107–12.
- [149] Chung W-J, Kwon K-Y, Song J, Lee S-W. Evolutionary Screening of Collagen-like Peptides That Nucleate Hydroxyapatite Crystals. *Langmuir* 2011;27:7620–8.

- [150] Song J, Malathong V, Bertozzi CR. Mineralization of synthetic polymer scaffolds: a bottom-up approach for the development of artificial bone. *J Am Chem Soc* 2005;127:3366–72.
- [151] Song J, Saiz E, Bertozzi CR. Preparation of pHEMA–CP composites with high interfacial adhesion via template-driven mineralization. *J Eur Ceram Soc* 2003;23:2905–19.
- [152] Song J, Saiz E, Bertozzi CR. A new approach to mineralization of biocompatible hydrogel scaffolds: an efficient process toward 3-dimensional bonelike composites. *J Am Chem Soc* 2003;125:1236–43.
- [153] Song J, Xu J, Filion T, Saiz E, Tomsia AP, Lian JB, et al. Elastomeric high-mineral content hydrogel-hydroxyapatite composites for orthopedic applications. *J Biomed Mater Res A* 2009;89:1098–107.
- [154] Skelly JD, Lange J, Filion TM, Li X, Ayers DC, Song J. Vancomycin-bearing Synthetic Bone Graft Delivers rhBMP-2 and Promotes Healing of Critical Rat Femoral Segmental Defects. *Clin Orthop Relat Res* 2014.
- [155] Li X, Xu J, Filion TM, Ayers DC, Song J. pHEMA-nHA Encapsulation and Delivery of Vancomycin and rhBMP-2 Enhances its Role as a Bone Graft Substitute. *Clin Orthop Relat Res* 2012.

- [156] Huebsch N, Arany PR, Mao AS, Shvartsman D, Ali OA, Bencherif SA, et al. Harnessing traction-mediated manipulation of the cell/matrix interface to control stem-cell fate. *Nat Mater* 2010;9:518–26.
- [157] Engler AJ, Sen S, Sweeney HL, Discher DE. Matrix elasticity directs stem cell lineage specification. *Cell* 2006;126:677–89.
- [158] Lutolf MP, Gilbert PM, Blau HM. Designing materials to direct stem-cell fate. *Nature* 2009;462:433–41.
- [159] Singh A, Zhan J, Ye Z, Elisseff JH. Modular Multifunctional Poly(ethylene glycol) Hydrogels for Stem Cell Differentiation. *Adv Funct Mater* 2012.
- [160] Yang PJ, Temenoff JS. Engineering orthopedic tissue interfaces. *Tissue Eng Part B Rev* 2009;15:127–41.
- [161] Huebsch N, Mooney DJ. Inspiration and application in the evolution of biomaterials. *Nature* 2009;462:426–32.
- [162] Weiner S, Wagner HD. The Material Bone: Structure-Mechanical Function Relations. *Annu Rev Mater Sci* 1998;28:271–98.
- [163] Thomson RC, Yaszemski MJ, Powers JM, Mikos G. Hydroxyapatite fiber reinforced poly(alpha-hydroxy ester) foams for bone regeneration. *Biomaterials* 1998;19:1935–43.

- [164] Holzwarth JM, Ma PX. Biomimetic nanofibrous scaffolds for bone tissue engineering. *Biomaterials* 2011;32:9622–9.
- [165] Ma PX, Zhang R, Xiao G, Franceschi R. Engineering new bone tissue in vitro on highly porous poly(alpha-hydroxyl acids)/hydroxyapatite composite scaffolds. *J Biomed Mater Res* 2001;54:284–93.
- [166] Rai B, Oest ME, Dupont KM, Ho KH, Teoh SH, Guldberg RE. Combination of platelet-rich plasma with polycaprolactone-tricalcium phosphate scaffolds for segmental bone defect repair. *J Biomed Mater Res A* 2007;81:888–99.
- [167] Rezwan K, Chen QZ, Blaker JJ, Boccaccini AR. Biodegradable and bioactive porous polymer/inorganic composite scaffolds for bone tissue engineering. *Biomaterials* 2006;27:3413–31.
- [168] Palmer LC, Newcomb CJ, Kaltz SR, Spoerke ED, Stupp SI. Biomimetic systems for hydroxyapatite mineralization inspired by bone and enamel. *Chem Rev* 2008;108:4754–83.
- [169] Neuendorf RE, Saiz E, Tomsia P, Ritchie RO. Adhesion between biodegradable polymers and hydroxyapatite: Relevance to synthetic bone-like materials and tissue engineering scaffolds. *Acta Biomater* 2008;4:1288–96.

- [170] Wei J, Liu A, Chen L, Zhang P, Chen X, Jing X. The surface modification of hydroxyapatite nanoparticles by the ring opening polymerization of gamma-benzyl-L-glutamate N-carboxyanhydride. *Macromol Biosci* 2009;9:631–8.
- [171] Hong Z, Zhang P, He C, Qiu X, Liu A, Chen L, et al. Nano-composite of poly(L-lactide) and surface grafted hydroxyapatite: mechanical properties and biocompatibility. *Biomaterials* 2005;26:6296–304.
- [172] Spadaccio C, Rainer A, Trombetta M, Vadalá G, Chello M, Covino E, et al. Poly-L-lactic acid/hydroxyapatite electrospun nanocomposites induce chondrogenic differentiation of human MSC. *Ann Biomed Eng* 2009;37:1376–89.
- [173] Peng F, Yu X, Wei M. In vitro cell performance on hydroxyapatite particles/poly(L-lactic acid) nanofibrous scaffolds with an excellent particle along nanofiber orientation. *Acta Biomater* 2011;7:2585–92.
- [174] Kim H. Biomedical nanocomposites of hydroxyapatite/polycaprolactone obtained by surfactant mediation. *J Biomed Mater Res A* 2007;83:169–77.
- [175] Yang F, Both SK, Yang X, Walboomers XF, Jansen J a. Development of an electrospun nano-apatite/PCL composite membrane for GTR/GBR application. *Acta Biomater* 2009;5:3295–304.

- [176] Yang D-J, Xiong C-D, Govender T, Wang Y-Z. Preparation and drug-delivery potential of metronidazole-loaded PELA tri-block co-polymeric electrospun membranes. *J Biomater Sci Polym Ed* 2009;20:1321–34.
- [177] Zhou S, Liao X, Li X, Deng X, Li H. Poly-d,l-lactide-co-poly(ethylene glycol) microspheres as potential vaccine delivery systems. *J Control Release* 2003;86:195–205.
- [178] Zhou S, Deng X, Yuan M, Li X. Investigation on preparation and protein release of biodegradable polymer microspheres as drug-delivery system. *J Appl Polym Sci* 2002;84:778–84.
- [179] Rathi SR, Coughlin EB, Hsu SL, Golub CS, Ling GH, Tzivanis MJ. Effect of midblock on the morphology and properties of blends of ABA triblock copolymers of PDLA-mid-block-PDLA with PLLA. *Polymer* 2012;53:3008–16.
- [180] Rathi S, Chen X, Coughlin EB, Hsu SL, Golub CS, Tzivanis MJ. Toughening semicrystalline poly(lactic acid) by morphology alteration. *Polymer* 2011;52:4184–8.
- [181] Lucke A, Tessmar J, Schnell E, Schmeer G, Göpferich A. Biodegradable poly(D,L-lactic acid)-poly(ethylene glycol)-monomethyl ether diblock copolymers: structures and surface properties relevant to their use as biomaterials. *Biomaterials* 2000;21:2361–70.

- [182] Meloan SN, Puchtler H. Chemical Mechanisms of Staining Methods: Von Kossa's Technique: What von Kossa Really Wrote and a Modified Reaction for Selective Demonstration of Inorganic Phosphates. *J Histotechnol* 1985;8:11–3.
- [183] Von Burkersroda F, Gref R, Göpferich a. Erosion of biodegradable block copolymers made of poly(D,L-lactic acid) and poly(ethylene glycol). *Biomaterials* 1997;18:1599–607.
- [184] Younes H, Cohn D. Morphological study of biodegradable PEO / PLA block copolymers. *Biomed Mater* 1987;21:1301–16.
- [185] Cui W, Zhu X, Yang Y, Li X, Jin Y. Evaluation of electrospun fibrous scaffolds of poly(dl-lactide) and poly(ethylene glycol) for skin tissue engineering. *Mater Sci Eng C* 2009;29:1869–76.
- [186] Jose M V, Thomas V, Johnson KT, Dean DR, Nyairo E. Aligned PLGA/HA nanofibrous nanocomposite scaffolds for bone tissue engineering. *Acta Biomater* 2009;5:305–15.
- [187] Xie Z, Buschle-Diller G, DeInnocentes P, Bird RC. Electrospun poly(D,L)-lactide nonwoven mats for biomedical application: Surface area shrinkage and surface entrapment. *J Appl Polym Sci* 2011;122:1219–25.

- [188] Steendam R, van Steenberghe MJ, Hennink WE, Frijlink HW, Lerk CF. Effect of molecular weight and glass transition on relaxation and release behaviour of poly(DL-lactic acid) tablets. *J Control Release* 2001;70:71–82.
- [189] Bedoui F, Widjaja LK, Luk A, Bolikal D, Murthy NS, Kohn J. Anomalous increase in modulus upon hydration in random copolymers with hydrophobic segments and hydrophilic blocks. *Soft Matter* 2012;8:2230.
- [190] Cohn D, Younes H. Compositional and structural analysis of PELA biodegradable block copolymers degrading under in vitro conditions. *Biomaterials* 1989;10:466–74.
- [191] Hu D, Liu H. Structural Analysis and Degradation Behavior in Polyethylene Glycol/Poly(L-lactide) Copolymers. *J Appl Polym Sci* 1994;51:473–82.
- [192] Li S, Rashkov I, Espartero J, Vert M, Manolova N. Synthesis , Characterization , and Hydrolytic Degradation of PLA/PEO/PLA Triblock Copolymers with Long Poly (L-lactic acid) Blocks. *Macromolecules* 1996;29:50–6.
- [193] Caplan AI. Mesenchymal stem cells. *J Orthop Res* 1991;9:641–50.
- [194] McCullen SD, Chow AGY, Stevens MM. In vivo tissue engineering of musculoskeletal tissues. *Curr Opin Biotechnol* 2011;22:715–20.

- [195] Göpferich A, Peter SJ, Lucke A, Lu L, Mikos AG. Modulation of marrow stromal cell function using poly(D,L-lactic acid)-block-poly(ethylene glycol)-monomethyl ether surfaces. *J Biomed Mater Res* 1999;46:390–8.
- [196] Lieb E, Tessmar J, Hacker M, Fischbach C, Rose D, Blunk T, et al. Poly (D, L-lactic acid)-poly (ethylene glycol)-monomethyl ether diblock copolymers control adhesion and osteoblastic differentiation of marrow stromal cells. *Tissue Eng* 2003;9:71–84.
- [197] Webster TJ, Celaletdin E, Doremus RH, Siegel RW, Bizios R. Specific proteins mediate enhanced osteoblast adhesion on nanophase ceramics. *J Biomed Mater Res* 2000;51:475–83.
- [198] Lee JH, Rim NG, Jung HS, Shin H. Control of osteogenic differentiation and mineralization of human mesenchymal stem cells on composite nanofibers containing poly[lactic-co-(glycolic acid)] and hydroxyapatite. *Macromol Biosci* 2010;10:173–82.
- [199] Fischer EM, Layrolle P, Van Blitterswijk CA, De Bruijn JD. Bone formation by mesenchymal progenitor cells cultured on dense and microporous hydroxyapatite particles. *Tissue Eng* 2003;9:1179–88.
- [200] Zhao F, Grayson WL, Ma T, Bunnell B, Lu WW. Effects of hydroxyapatite in 3-D chitosan-gelatin polymer network on human mesenchymal stem cell construct development. *Biomaterials* 2006;27:1859–67.

- [201] Xue D, Zheng Q, Zong C, Li Q, Li H, Qian S, et al. Osteochondral repair using porous poly(lactide-co-glycolide)/nano-hydroxyapatite hybrid scaffolds with undifferentiated mesenchymal stem cells in a rat model. *J Biomed Mater Res A* 2010;94:259–70.
- [202] Kim S-S, Sun Park M, Jeon O, Yong Choi C, Kim B-S. Poly(lactide-co-glycolide)/hydroxyapatite composite scaffolds for bone tissue engineering. *Biomaterials* 2006;27:1399–409.
- [203] Nandakumar A, Fernandes H, de Boer J, Moroni L, Habibovic P, van Blitterswijk C a. Fabrication of bioactive composite scaffolds by electrospinning for bone regeneration. *Macromol Biosci* 2010;10:1365–73.
- [204] Lian J, Stein G. Concepts of Osteoblast Growth and Differentiation: Basis for Modulation of Bone Cell Development and Tissue Formation. *Crit Rev Oral Biol Med* 1992;3:269–305.
- [205] Lian JB, Stein GS, Stein JL, van Wijnen a J. Transcriptional control of osteoblast differentiation. *Biochem Soc Trans* 1998;26:14–21.
- [206] Ni P, Fu S, Fan M, Guo G, Shi S, Peng J, et al. Preparation of poly(ethylene glycol)/polylactide hybrid fibrous scaffolds for bone tissue engineering. *Int J Nanomedicine* 2011;6:3065–75.

- [207] Lyu S, Huang C, Yang H, Zhang X. Electrospun fibers as a scaffolding platform for bone tissue repair. *J Orthop Res* 2013;31:1382–9.
- [208] Li W-J, Tuli R, Huang X, Laquerriere P, Tuan RS. Multilineage differentiation of human mesenchymal stem cells in a three-dimensional nanofibrous scaffold. *Biomaterials* 2005;26:5158–66.
- [209] Kutikov AB, Song J. An amphiphilic degradable polymer/hydroxyapatite composite with enhanced handling characteristics promotes osteogenic gene expression in bone marrow stromal cells. *Acta Biomater* 2013;9:8354–64.
- [210] Ngiam M, Liao S, Patil AJ, Cheng Z, Chan CK, Ramakrishna S. The fabrication of nano-hydroxyapatite on PLGA and PLGA/collagen nanofibrous composite scaffolds and their effects in osteoblastic behavior for bone tissue engineering. *Bone* 2009;45:4–16.
- [211] Phipps MC, Clem WC, Catledge S a, Xu Y, Hennessy KM, Thomas V, et al. Mesenchymal stem cell responses to bone-mimetic electrospun matrices composed of polycaprolactone, collagen I and nanoparticulate hydroxyapatite. *PLoS One* 2011;6:e16813.
- [212] Kolambkar YM, Dupont KM, Boerckel JD, Huebsch N, Mooney DJ, Hutmacher DW, et al. An alginate-based hybrid system for growth factor

delivery in the functional repair of large bone defects. *Biomaterials* 2011;32:65–74.

[213] Kolambkar YM, Boerckel JD, Dupont KM, Bajin M, Huebsch N, Mooney DJ, et al. Spatiotemporal delivery of bone morphogenetic protein enhances functional repair of segmental bone defects. *Bone* 2011;49:485–92.

[214] Berner a, Boerckel JD, Saifzadeh S, Steck R, Ren J, Vaquette C, et al. Biomimetic tubular nanofiber mesh and platelet rich plasma-mediated delivery of BMP-7 for large bone defect regeneration. *Cell Tissue Res* 2012;347:603–12.

[215] Shin M, Yoshimoto H, Vacanti JP. In vivo bone tissue engineering using mesenchymal stem cells on a novel electrospun nanofibrous scaffold. *Tissue Eng* 2004;10:33–41.

[216] Fu S, Ni P, Wang B, Chu B, Peng J, Zheng L, et al. In vivo biocompatibility and osteogenesis of electrospun poly(ϵ -caprolactone)-poly(ethylene glycol)-poly(ϵ -caprolactone)/nano-hydroxyapatite composite scaffold. *Biomaterials* 2012;33:8363–71.

[217] Ko EK, Jeong SI, Rim NG, Lee YM, Shin H, Lee B-K. In vitro osteogenic differentiation of human mesenchymal stem cells and in vivo bone formation in composite nanofiber meshes. *Tissue Eng Part A* 2008;14:2105–19.

- [218] Woo KM, Chen VJ, Jung H-M, Kim T-I, Shin H-I, Baek J-H, et al. Comparative evaluation of nanofibrous scaffolding for bone regeneration in critical-size calvarial defects. *Tissue Eng Part A* 2009;15:2155–62.
- [219] Horner E a, Kirkham J, Wood D, Curran S, Smith M, Thomson B, et al. Long bone defect models for tissue engineering applications: criteria for choice. *Tissue Eng Part B Rev* 2010;16:263–71.
- [220] Williams DF. On the mechanisms of biocompatibility. *Biomaterials* 2008;29:2941–53.
- [221] Pişkin E, Işoğlu IA, Bölgen N, Vargel I, Griffiths S, Cavuşoğlu T, et al. In vivo performance of simvastatin-loaded electrospun spiral-wound polycaprolactone scaffolds in reconstruction of cranial bone defects in the rat model. *J Biomed Mater Res A* 2009;90:1137–51.
- [222] Wang J, Valmikinathan CM, Liu W, Laurencin CT, Yu X. Spiral-structured, nanofibrous, 3D scaffolds for bone tissue engineering. *J Biomed Mater Res A* 2010;93:753–62.
- [223] Zhang X, Chang W, Lee P, Wang Y, Yang M, Li J, et al. Polymer-ceramic spiral structured scaffolds for bone tissue engineering: effect of hydroxyapatite composition on human fetal osteoblasts. *PLoS One* 2014;9:e85871.

- [224] Wang J, Yu X. Preparation, characterization and in vitro analysis of novel structured nanofibrous scaffolds for bone tissue engineering. *Acta Biomater* 2010;6:3004–12.
- [225] Kutikov AB, Gurijala A, Song J. Rapid Prototyping Amphiphilic Polymer/Hydroxyapatite Composite Scaffolds with Hydration-Induced Self-Fixation Behavior. *Tissue Eng Part C Methods* 2014.
- [226] Miao D, Scutt a. Histochemical Localization of Alkaline Phosphatase Activity in Decalcified Bone and Cartilage. *J Histochem Cytochem* 2002;50:333–40.
- [227] Nussbaum D a., Gailloud P, Murphy K. The Chemistry of Acrylic Bone Cements and Implications for Clinical Use in Image-guided Therapy. *J Vasc Interv Radiol* 2004;15:121–6.
- [228] Hsu WK, Sugiyama O, Park SH, Conduah a, Feeley BT, Liu NQ, et al. Lentiviral-mediated BMP-2 gene transfer enhances healing of segmental femoral defects in rats. *Bone* 2007;40:931–8.
- [229] Rodriguez-Merchan EC, Forriol F. Nonunion: general principles and experimental data. *Clin Orthop Relat Res* 2004:4–12.

- [230] Sato K, Watanabe Y, Harada N, Abe S, Matsushita T, Yamanaka K, et al. Establishment of Reproducible, Critical-Sized, Femoral Segmental Bone Defects in Rats. *Tissue Eng Part C Methods* 2014;1–5.
- [231] Winn S. Sustained release emphasizing recombinant human bone morphogenetic protein-2. *Adv Drug Deliv Rev* 1998;31:303–18.
- [232] Fu Y, Nie H, Ho M, Wang C-K, Wang C. Optimized bone regeneration based on sustained release from three-dimensional fibrous PLGA/HAp composite scaffolds loaded with BMP-2. *Biotechnol Bioeng* 2008;99:996–1006.
- [233] Jeon O, Song SJ, Yang HS, Bhang S-H, Kang S-W, Sung MA, et al. Long-term delivery enhances in vivo osteogenic efficacy of bone morphogenetic protein-2 compared to short-term delivery. *Biochem Biophys Res Commun* 2008;369:774–80.
- [234] Katagiri T, Yamaguchi A, Komaki M, Abe E, Takahashi N, Ikeda T, et al. Bone morphogenetic protein-2 converts the differentiation pathway of C2C12 myoblasts into the osteoblast lineage. *J Cell Biol* 1994;127:1755–66.
- [235] Suganuma J, Alexander H. Biological response of intramedullary bone to poly-L-lactic acid. *J Appl Biomater* 1993;4:13–27.

- [236] Agrawal CM, Athanasiou KA. Technique to control pH in vicinity of biodegrading PLA-PGA implants. *J Biomed Mater Res* 1997;38:105–14.
- [237] Yasko AW, Lane JM, Fellingner EJ, Rosen V, Wozney JM, Wang EA. The healing of segmental bone defects, induced by recombinant human bone morphogenetic protein (rhBMP-2). A radiographic, histological, and biomechanical study in rats. *J Bone Joint Surg Am* 1992;74:659–70.
- [238] Dupont KM, Sharma K, Stevens HY, Boerckel JD, García AJ, Guldberg RE. Human stem cell delivery for treatment of large segmental bone defects. *Proc Natl Acad Sci U S A* 2010;107:3305–10.
- [239] Kadiyala S, Jaiswal N, Bruder SSP. Culture-Expanded, Bone Marrow-Derived Mesenchymal Stem Cells Can Regenerate a Critical-Sized Segmental Bone Defect. *Tissue Eng* 1997;3:173–85.
- [240] Schantz J-T, Hutmacher DW, Lam CXF, Brinkmann M, Wong KM, Lim TC, et al. Repair of calvarial defects with customised tissue-engineered bone grafts II. Evaluation of cellular efficiency and efficacy in vivo. *Tissue Eng* 2003;9 Suppl 1:S127–39.
- [241] Tasso R, Augello A, Boccardo S, Salvi S, Caridà M, Postiglione F, et al. Recruitment of a host's osteoprogenitor cells using exogenous mesenchymal stem cells seeded on porous ceramic. *Tissue Eng Part A* 2009;15:2203–12.

- [242] Tasso R, Gaetani M, Molino E, Cattaneo A, Monticone M, Bachi A, et al. The role of bFGF on the ability of MSC to activate endogenous regenerative mechanisms in an ectopic bone formation model. *Biomaterials* 2012;33:2086–96.
- [243] Crisostomo PR, Markel T a, Wang Y, Meldrum DR. Surgically relevant aspects of stem cell paracrine effects. *Surgery* 2008;143:577–81.
- [244] Zimmermann CE, Gierloff M, Hedderich J, Açil Y, Wiltfang J, Terheyden H. Survival of transplanted rat bone marrow-derived osteogenic stem cells in vivo. *Tissue Eng Part A* 2011;17:1147–56.
- [245] Hwang SJ, Cho TH, Kim IS. In Vivo Gene Activity of Human Mesenchymal Stem Cells After Scaffold-Mediated Local Transplantation. *Tissue Eng Part A* 2014:1–15.
- [246] Zara JN, Siu RK, Zhang X, Shen J, Ngo R, Lee M, et al. High doses of bone morphogenetic protein 2 induce structurally abnormal bone and inflammation in vivo. *Tissue Eng Part A* 2011;17:1389–99.
- [247] Kirker-Head C, Karageorgiou V, Hofmann S, Fajardo R, Betz O, Merkle HP, et al. BMP-silk composite matrices heal critically sized femoral defects. *Bone* 2007;41:247–55.

- [248] Lee SS, Huang BJ, Kaltz SR, Sur S, Newcomb CJ, Stock SR, et al. Bone regeneration with low dose BMP-2 amplified by biomimetic supramolecular nanofibers within collagen scaffolds. *Biomaterials* 2013;34:452–9.
- [249] Furukawa T, Matsusue Y, Yasunaga T, Nakagawa Y, Okada Y, Shikinami Y, et al. Histomorphometric study on high-strength hydroxyapatite/poly(L-lactide) composite rods for internal fixation of bone fractures. *J Biomed Mater Res* 2000;50:410–9.
- [250] Filion TM, Song J. Scalable functional bone substitutes: strategic integration of key structural elements of bone in synthetic biomaterials, Chapter 12. In: Fazel R, editor. *Biomed. Eng. - Front. Challenges*, InTech; 2011, p. 233–48.
- [251] Roach P, Farrar D, Perry CC. Interpretation of protein adsorption: surface-induced conformational changes. *J Am Chem Soc* 2005;127:8168–73.
- [252] Lu DR, Park K. Effect of surface hydrophobicity on the conformational changes of adsorbed fibrinogen. *J Colloid Interface Sci* 1991;144:271–81.
- [253] Phipps MC, Clem WC, Grunda JM, Clines G a, Bellis SL. Increasing the pore sizes of bone-mimetic electrospun scaffolds comprised of polycaprolactone, collagen I and hydroxyapatite to enhance cell infiltration. *Biomaterials* 2012;33:524–34.

- [254] Leong KF, Cheah CM, Chua CK. Solid freeform fabrication of three-dimensional scaffolds for engineering replacement tissues and organs. *Biomaterials* 2003;24:2363–78.
- [255] Sun Y, Finne-Wistrand A, Albertsson A-C, Xing Z, Mustafa K, Hendrikson WJ, et al. Degradable amorphous scaffolds with enhanced mechanical properties and homogeneous cell distribution produced by a three-dimensional fiber deposition method. *J Biomed Mater Res A* 2012;100:2739–49.
- [256] Moroni L, de Wijn JR, van Blitterswijk C a. 3D fiber-deposited scaffolds for tissue engineering: influence of pores geometry and architecture on dynamic mechanical properties. *Biomaterials* 2006;27:974–85.
- [257] Shor L, Güçeri S, Wen X, Gandhi M, Sun W. Fabrication of three-dimensional polycaprolactone/hydroxyapatite tissue scaffolds and osteoblast-scaffold interactions in vitro. *Biomaterials* 2007;28:5291–7.
- [258] Williams JM, Adewunmi A, Schek RM, Flanagan CL, Krebsbach PH, Feinberg SE, et al. Bone tissue engineering using polycaprolactone scaffolds fabricated via selective laser sintering. *Biomaterials* 2005;26:4817–27.

- [259] Wiria FE, Leong KF, Chua CK, Liu Y. Poly-epsilon-caprolactone/hydroxyapatite for tissue engineering scaffold fabrication via selective laser sintering. *Acta Biomater* 2007;3:1–12.
- [260] Schantz J-T, Brandwood A, Hutmacher DW, Khor HL, Bittner K. Osteogenic differentiation of mesenchymal progenitor cells in computer designed fibrin-polymer-ceramic scaffolds manufactured by fused deposition modeling. *J Mater Sci Mater Med* 2005;16:807–19.
- [261] Heo S, Kim S-E, Wei J, Kim DH, Hyun Y, Yun H, et al. In vitro and animal study of novel nano-hydroxyapatite/poly(epsilon-caprolactone) composite scaffolds fabricated by layer manufacturing process. *Tissue Eng Part A* 2009;15:977–89.
- [262] Giordano RA, Wu BM, Borland SW, Cima LG, Sachs EM, Cima MJ. Mechanical properties of dense polylactic acid structures fabricated by three dimensional printing. *J Biomater Sci Polym Ed* 1996;8:63–75.
- [263] Kim J, McBride S, Tellis B, Alvarez-Urena P, Song Y-H, Dean DD, et al. Rapid-prototyped PLGA/ β -TCP/hydroxyapatite nanocomposite scaffolds in a rabbit femoral defect model. *Biofabrication* 2012;4:025003.
- [264] Woodfield TBF, Malda J, de Wijn J, Péters F, Riesle J, van Blitterswijk C a. Design of porous scaffolds for cartilage tissue engineering using a three-dimensional fiber-deposition technique. *Biomaterials* 2004;25:4149–61.

- [265] Moroni L, de Wijn JR, van Blitterswijk C a. Three-dimensional fiber-deposited PEOT/PBT copolymer scaffolds for tissue engineering: influence of porosity, molecular network mesh size, and swelling in aqueous media on dynamic mechanical properties. *J Biomed Mater Res A* 2005;75:957–65.
- [266] Leferink AM, Hendrikson WJ, Rouwkema J, Karperien M, van Blitterswijk CA, Moroni L. Increased cell seeding efficiency in bioplotting three-dimensional PEOT/PBT scaffolds. *J Tissue Eng Regen Med* 2013:n/a – n/a.
- [267] Deschamps AA, van Apeldoorn AA, Hayen H, de Bruijn JD, Karst U, Grijpma DW, et al. In vivo and in vitro degradation of poly(ether ester) block copolymers based on poly(ethylene glycol) and poly(butylene terephthalate). *Biomaterials* 2004;25:247–58.
- [268] Retzepi M, Donos N. Guided Bone Regeneration: biological principle and therapeutic applications. *Clin Oral Implants Res* 2010;21:567–76.
- [269] Phillips JH, Rahn BA. Fixation effects on membranous and endochondral onlay bone-graft resorption. *Plast Reconstr Surg* 1988;82:872–7.
- [270] Cohn D, Younes H. Biodegradable PEO/PLA block copolymers. *J Biomed Mater Res* 1988;22:993–1009.

- [271] Cohn D, Hotovely-Salomon a. Biodegradable multiblock PEO/PLA thermoplastic elastomers: molecular design and properties. *Polymer (Guildf)* 2005;46:2068–75.
- [272] Xu J, Bohnsack D a, Mackay ME, Wooley KL. Unusual mechanical performance of amphiphilic crosslinked polymer networks. *J Am Chem Soc* 2007;129:506–7.
- [273] Murthy NS, Wang W, Kohn J. Microphase separation in copolymers of hydrophilic PEG blocks and hydrophobic tyrosine-derived segments using simultaneous SAXS/WAXS/DSC. *Polymer (Guildf)* 2010;51:3978–88.
- [274] Thomas KA, Cook SD. An evaluation of variables influencing implant fixation by direct bone apposition. *J Biomed Mater Res* 1985;19:875–901.
- [275] Verheyen CC, de Wijn JR, van Blitterswijk CA, de Groot K, Rozing PM. Hydroxylapatite/poly(L-lactide) composites: an animal study on push-out strengths and interface histology. *J Biomed Mater Res* 1993;27:433–44.
- [276] Dimitriou R, Mataliotakis GI, Calori GM, Giannoudis P V. The role of barrier membranes for guided bone regeneration and restoration of large bone defects: current experimental and clinical evidence. *BMC Med* 2012;10:81.
- [277] Dahlin C, Linde A, Gottlow J, Nyman S. Healing of bone defects by guided tissue regeneration. *Plast Reconstr Surg* 1988;81:672–6.

- [278] Melchels FPW, Barradas AMC, van Blitterswijk C a, de Boer J, Feijen J, Grijpma DW. Effects of the architecture of tissue engineering scaffolds on cell seeding and culturing. *Acta Biomater* 2010;6:4208–17.
- [279] Yoo D. New paradigms in hierarchical porous scaffold design for tissue engineering. *Mater Sci Eng C Mater Biol Appl* 2013;33:1759–72.
- [280] Kapfer SC, Hyde ST, Mecke K, Arns CH, Schröder-Turk GE. Minimal surface scaffold designs for tissue engineering. *Biomaterials* 2011;32:6875–82.
- [281] Behl M, Razzaq MY, Lendlein A. Multifunctional shape-memory polymers. *Adv Mater* 2010;22:3388–410.
- [282] Rem a I, Oosterhuis J a, Journée-de Korver HG, van den Berg TJ, Keunen JE. Temperature dependence of thermal damage to the sclera: exploring the heat tolerance of the sclera for transscleral thermotherapy. *Exp Eye Res* 2001;72:153–62.
- [283] Berman AT, Reid JS, Yanicko DR, Sih GC, Zimmerman MR. Thermally induced bone necrosis in rabbits. Relation to implant failure in humans. *Clin Orthop Relat Res* 1984:284–92.

- [284] Lendlein A, Schmidt AM, Langer R. AB-polymer networks based on oligo(epsilon-caprolactone) segments showing shape-memory properties. Proc Natl Acad Sci U S A 2001;98:842–7.
- [285] Lendlein A, Langer R. Biodegradable, elastic shape-memory polymers for potential biomedical applications. Science 2002;296:1673–6.
- [286] Madbouly SA, Lendlein A. Shape-Memory Polymer Composites. In: Lendlein A, editor. Adv. Polym. Sci., Springer Berlin Heidelberg; 2010, p. 41–95.
- [287] Xu J, Song J. High performance shape memory polymer networks based on rigid nanoparticle cores. Proc Natl Acad Sci U S A 2010;107:7652–7.
- [288] Lin G, Cosimbescu L, Karin NJ, Tarasevich BJ. Injectable and thermosensitive PLGA-g-PEG hydrogels containing hydroxyapatite: preparation, characterization and in vitro release behavior. Biomed Mater 2012;7:024107.
- [289] Schiller C, Epple M. Carbonated calcium phosphates are suitable pH-stabilising fillers for biodegradable polyesters. Biomaterials 2003;24:2037–43.
- [290] Zheng X, Zhou S, Li X, Weng J. Shape memory properties of poly(D,L-lactide)/hydroxyapatite composites. Biomaterials 2006;27:4288–95.

- [291] Zheng X, Zhou S, Yu X, Li X, Feng B, Qu S, et al. Effect of in vitro degradation of poly(D,L-lactide)/beta-tricalcium composite on its shape-memory properties. *J Biomed Mater Res B Appl Biomater* 2008;86:170–80.
- [292] Zhou S, Zheng X, Yu X, Wang J, Weng J, Li X, et al. Hydrogen Bonding Interaction of Poly(d , l -Lactide)/hydroxyapatite Nanocomposites. *Chem Mater* 2007;19:247–53.
- [293] Gu X, Mather PT. Entanglement-based shape memory polyurethanes: Synthesis and characterization. *Polymer (Guildf)* 2012;53:5924–34.
- [294] Lendlein A, Kelch S. Shape-Memory Polymers. *Angew Chemie Int Ed* 2002;41:2034.
- [295] Baker RM, Henderson JH, Mather PT. Shape memory poly(ϵ -caprolactone)-co-poly(ethylene glycol) foams with body temperature triggering and two-way actuation. *J Mater Chem B* 2013;1:4916.
- [296] Nagata M, Kitazima I. Photocurable biodegradable poly(ϵ -caprolactone)/poly(ethylene glycol) multiblock copolymers showing shape-memory properties. *Colloid Polym Sci* 2005;284:380–6.
- [297] Feng Y, Zhang S, Zhang L, Guo J, Xu Y. Synthesis and characterization of hydrophilic polyester-PEO networks with shape-memory properties. *Polym Adv Technol* 2011;22:2430–8.

- [298] Bae YH, Huh KM, Kim Y, Park K. Biodegradable amphiphilic multiblock copolymers and their implications for biomedical applications. *J Control Release* 2000;64:3–13.
- [299] Saito N, Okada T, Toba S, Miyamoto S, Takaoka K. New synthetic absorbable polymers as BMP carriers: plastic properties of poly-D,L-lactic acid-polyethylene glycol block copolymers. *J Biomed Mater Res* 1999;47:104–10.
- [300] ASTM Standard D882-97. Standard Test Method for Tensile Properties of Thin Plastic Sheeting, West Conshohocken, PA: ASTM International; 1998.
- [301] Nazhat SN, Joseph R, Wang M, Smith R, Tanner KE, Bonfield W. Dynamic mechanical characterization of hydroxyapatite reinforced polyethylene: effect of particle size. *J Mater Sci Mater Med* 2000;11:621–8.
- [302] Kalfus J, Jancar J. Reinforcing mechanisms in amorphous polymer nanocomposites. *Compos Sci Technol* 2008;68:3444–7.
- [303] Wischke C, Schossig M, Lendlein A. Shape-memory effect of micro-/nanoparticles from thermoplastic multiblock copolymers. *Small* 2014;10:83–7.
- [304] Zhang D, Burkes WL, Schoener C a, Grunlan M a. Porous inorganic-organic shape memory polymers. *Polymer* 2012;53:2935–41.

- [305] Sauter T, Kratz K, Lendlein A. Pore-Size Distribution Controls Shape-Memory Properties on the Macro- and Microscale of Polymeric Foams. *Macromol Chem Phys* 2013;214:1184–8.
- [306] Singhal P, Rodriguez JN, Small W, Eagleston S, Van de Water J, Maitland DJ, et al. Ultra Low Density and Highly Crosslinked Biocompatible Shape Memory Polyurethane Foams. *J Polym Sci B Polym Phys* 2012;50:724–37.
- [307] Lee YJ, Lee J-H, Cho H-J, Kim HK, Yoon TR, Shin H. Electrospun fibers immobilized with bone forming peptide-1 derived from BMP7 for guided bone regeneration. *Biomaterials* 2013;34:5059–69.
- [308] Zhang X, Awad H a, O’Keefe RJ, Guldberg RE, Schwarz EM. A perspective: engineering periosteum for structural bone graft healing. *Clin Orthop Relat Res* 2008;466:1777–87.
- [309] Hwang NS, Varghese S, Lee HJ, Zhang Z, Elisseeff J. *Biomaterials* Directed In Vivo Osteogenic Differentiation of Mesenchymal Cells Derived from Human Embryonic Stem Cells. *Tissue Eng Part A* 2013.
- [310] Radder a M, Leenders H, van Blitterswijk C a. Interface reactions to PEO/PBT copolymers (Polyactive) after implantation in cortical bone. *J Biomed Mater Res* 1994;28:141–51.

- [311] Goldberg VM. Selection of Bone Grafts for Revision Total Hip Arthroplasty. Clin Orthop Relat Res 2000;381:68–76.
- [312] Gazdag A, Lane J, Glaser D, Forster R. Alternatives to Autogenous Bone Graft: Efficacy and Indications. J Am Acad Orthop Surg 1995;3:1–8.
- [313] Ring D, Roberge C, Morgan T, Jupiter JB. Osteotomy for malunited fractures of the distal radius: A comparison of structural and nonstructural autogenous bone grafts. J Hand Surg Am 2002;27:216–22.
- [314] Choi K, Kuhn JL, Ciarelli MJ, Goldstein S a. The elastic moduli of human subchondral, trabecular, and cortical bone tissue and the size-dependency of cortical bone modulus. J Biomech 1990;23:1103–13.
- [315] Lee J-H, Lee YJ, Cho H-J, Shin H. Guidance of In Vitro Migration of Human Mesenchymal Stem Cells and In Vivo Guided Bone Regeneration Using Aligned Electrospun Fibers. Tissue Eng Part A 2013.
- [316] Penco M, Marcioni S, Ferruti P, D' Antone S, Deghenghi R. Degradation behaviour of block copolymers containing poly(lactic-glycolic acid) and poly(ethylene glycol) segments. Biomaterials 1996;17:1583–90.
- [317] Krishnan L, Willett NJ, Guldberg RE. Vascularization Strategies for Bone Regeneration. Ann Biomed Eng 2014.

- [318] Gershovich J, Dahlin RL, Kasper FK, Mikos AG. Enhanced osteogenesis in co-cultures with human mesenchymal stem cells and endothelial cells on polymeric microfiber scaffolds. *Tissue Eng Part A* 2013.
- [319] Seebach C, Henrich D, Kähling C, Wilhelm K, Tami AE, Alini M, et al. Endothelial progenitor cells and mesenchymal stem cells seeded onto beta-TCP granules enhance early vascularization and bone healing in a critical-sized bone defect in rats. *Tissue Eng Part A* 2010;16:1961–70.
- [320] Patel ZS, Young S, Tabata Y, Jansen JA, Wong MEK, Mikos AG. Dual delivery of an angiogenic and an osteogenic growth factor for bone regeneration in a critical size defect model. *Bone* 2008;43:931–40.
- [321] Greenberg JI, Shields DJ, Barillas SG, Acevedo LM, Murphy E, Huang J, et al. A role for VEGF as a negative regulator of pericyte function and vessel maturation. *Nature* 2008;456:809–13.
- [322] Zhang J, Song J. Amphiphilic degradable polymers for immobilization and sustained delivery of sphingosine 1-phosphate. *Acta Biomater* 2014;10:3079–90.
- [323] Kawanabe T, Kawakami T, Yatomi Y, Shimada S, Soma Y. Sphingosine 1-phosphate accelerates wound healing in diabetic mice. *J Dermatol Sci* 2007;48:53–60.

- [324] Qi X, Okamoto Y, Murakawa T, Wang F, Oyama O, Ohkawa R, et al. Sustained delivery of sphingosine-1-phosphate using poly(lactic-co-glycolic acid)-based microparticles stimulates Akt/ERK-eNOS mediated angiogenesis and vascular maturation restoring blood flow in ischemic limbs of mice. *Eur J Pharmacol* 2010;634:121–31.
- [325] Vance J, Galley S, Liu DF, Donahue SW. Mechanical stimulation of MC3T3 osteoblastic cells in a bone tissue-engineering bioreactor enhances prostaglandin E2 release. *Tissue Eng* 1832;11:1832–9.
- [326] Lee MH, Arcidiacono JA, Bilek AM, Wille JJ, Hamill CA, Wonnacott KM, et al. Considerations for tissue-engineered and regenerative medicine product development prior to clinical trials in the United States. *Tissue Eng Part B Rev* 2010;16:41–54.

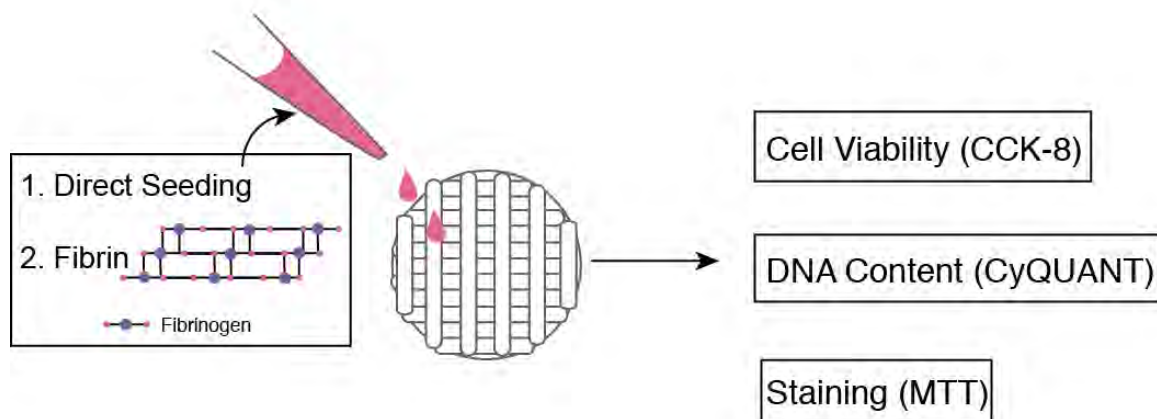
APPENDIX I: Ongoing work with 3-D HA-PELA scaffolds

This thesis work describes the development and characterization of HA-PELA-based bone tissue engineering scaffolds, however, significant work remains to achieve the ultimate goal of translating these smart materials to the clinic. Ongoing work includes improving the cell seeding efficiency on 3-D macroporous HA-PELA scaffolds and testing the performance of 3-D macroporous HA-PELA scaffolds in augmenting the repair of critical-size mandibular defects *in vivo*.

1.1 Optimizing cell seeding into rapid prototyped macroporous scaffolds

Chapter IV describes how 3-D HA-PELA scaffolds support the attachment and differentiation of MSCs. However, the large pore size of rapid prototyped scaffolds (~400 μm) compared to the size of a cell (~10-20 μm) results in sub-optimal entrapment of seeded cells within the scaffold. Therefore, cell seeding techniques, cell densities, and media volumes needed to be optimized in order to achieve optimal cell attachment and proliferation. Prior studies have explored the use of agarose treated plates,[1] dynamic culture,[1] cell sheets,[2] or fibrin glues[3,4] to improve seeding efficiency. We are currently developing a simple and reproducible protocol to improve seeding efficiency of rMSCs onto rapid prototyped macroporous scaffolds. We compared the efficiency of a direct seeding technique to that facilitated by fibrin glue by measuring cell viability (CCK-8), DNA content, and staining to visualize cell distribution (MTT) (Fig. 1).

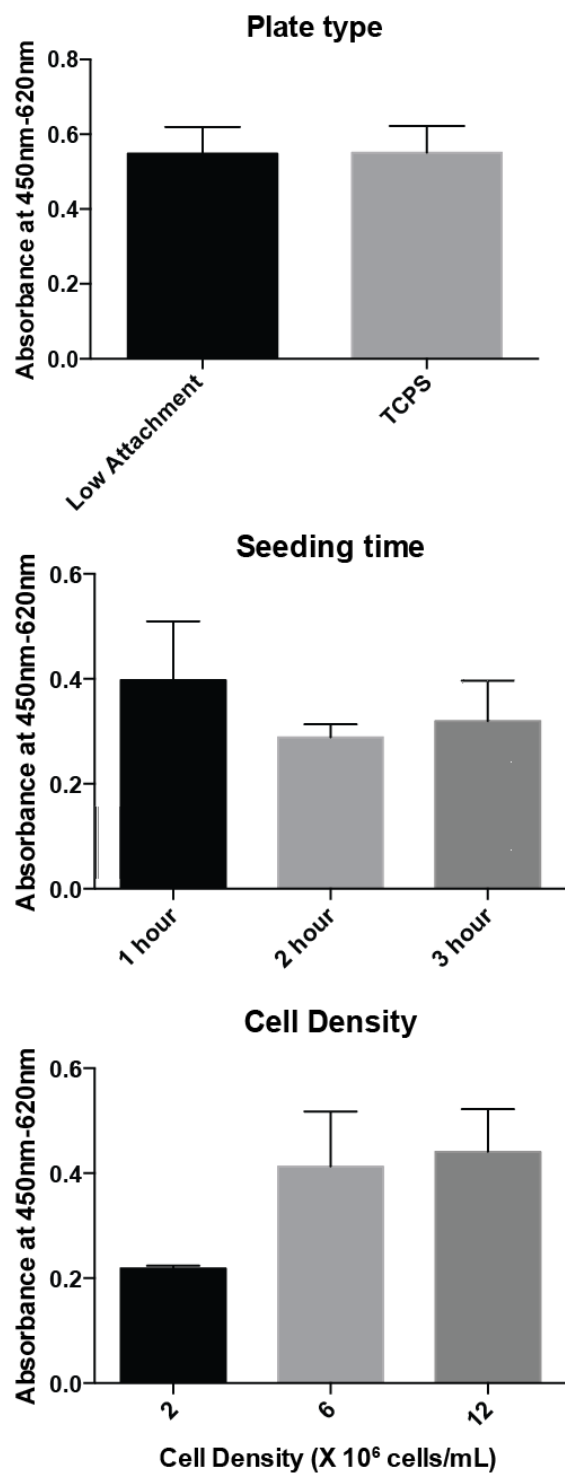
Figure 1. Experimental scheme for optimizing cell seeding onto HA-PELA scaffolds.

Figure 1

We previously showed by the CCK-8 cell viability assay that seeding cells on the macroporous scaffolds in pHEMA-coated low-attachment plates vs. in standard tissue culture polystyrene (TCPS) followed by immediate transfer of the cell-seeded scaffold to a new TCPS well results in no difference in cell seeding efficiency. Furthermore, allowing the cells to attach for varying period of time (1-3 h) prior to submerging in culture medium results in no difference in cell seeding efficiency (Fig. 2). We also found that increasing the cell suspension concentration from 2×10^6 cells/mL to 6×10^6 cells/mL in a 30- μ L volume improved the viability of the adherent cells on the macroporous scaffold, while further increasing the cell suspension concentration to 12×10^6 cells/mL did not provide further benefit. Thus, for all subsequent cell seeding experiments, pHEMA-coated low-attachment plates were used and 30 μ L of 6×10^6 cells/mL cell suspension and 1 h seeding time prior to the addition of culture medium were applied.

Figure 2. Optimizing direct seeding of a cell suspension onto HA-PELA.

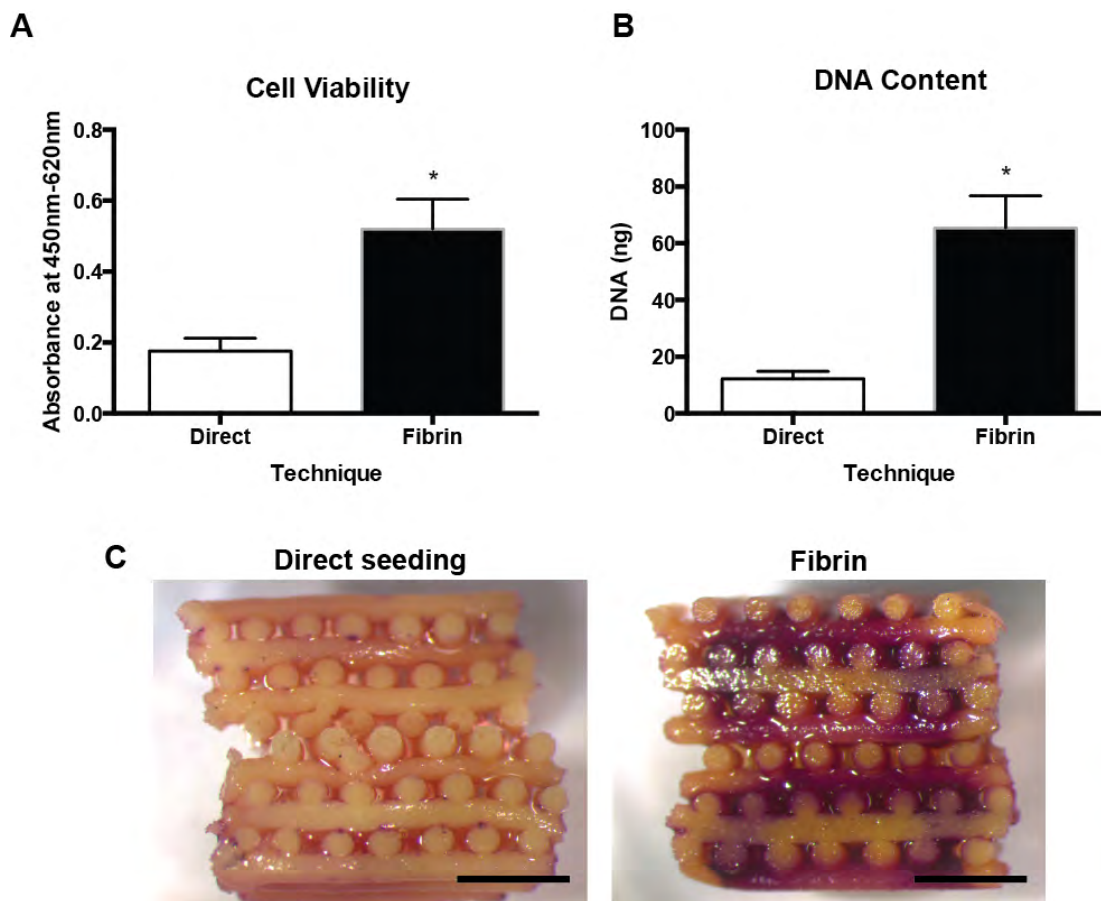
Figure 2



Our choice of fibrin as an auxiliary vehicle to improve cell seeding efficiency on HA-PELA scaffolds is inspired by the unique biological function of fibrin. During blood clotting, the serine protease thrombin cleaves soluble fibrinogen that polymerizes into a fibrin clot. This fibrin clot provides a scaffold for the initial stages of wound healing.[5] Fibrin glues are clinically used as hemostatic agents and tissue sealants. The intrinsic biocompatibility and cell-adhesiveness of fibrin has also led to applications as cell-delivery vehicles [6] and tissue engineering scaffolds.[7,8] Fibrin glues have also been widely used to improve the cell seeding efficiency and retention in synthetic polymer-based scaffolds.[4,9–11] We hypothesize that fibrin could also improve cell seeding efficiency on 3-D HA-PELA scaffolds. We compared the fibrin gel integrity when polymerizing 2 mg/mL to 10 mg/mL fibrinogen, in cell culture medium, with 0.83 U/mL thrombin in cell culture medium. Based on a tube inversion test, the 2 mg/mL fibrinogen solution did not form a solid gel even after 3 h at 37 °C but the 5 mg/mL and 10 mg/mL fibrinogen gelled rapidly (<2 min). Therefore, the 5 mg/mL fibrinogen concentration was chosen for cell seeding experiments. When comparing directly seeding cells in medium to seeding the cells in fibrin, the latter resulted in a significantly higher cell viability (CCK-8) and DNA content after 24 h (Fig. 3 A & B). These results were confirmed by visualizing viable cells with MTT reagent (Fig. 3 C).

Figure 3. Comparing (A) cell viability, (B) DNA content, and (C) MTT staining of cells seeded directly or with a fibrin gel.

Figure 3



An alternative strategy being explored is to use bio-orthogonally cross-linked fast-degrading synthetic hydrogels to improve the cell seeding efficiency. A PEG-based hydrogel platform developed in our laboratory can be cross-linked without the use of toxic initiators or UV light and has highly tunable and predictable degradation rates ensuring its timely disintegration.[12] We are comparing the efficacy of fibrin to these synthetic gels in enabling more effective cell seeding on macroporous scaffolds and their temporal effect on cellular behavior as they degrade.

1.2 Healing rat mandibular defects with 3-D HA-PELA

Cranio-maxillofacial sites are the most frequent sites of bone grafting due to tumor metastasis and subsequent tumor resection as well as developmental defects such as cleft palate [13] or trauma.[14] The difficulty of shaping and securing autografts and allografts into the often-complex cranio-maxillofacial defect geometries results in a significant clinical need for custom rapid prototyped or easily moldable synthetic bone grafts.[15–18] The ability to rapid prototype self-fitting shape memory HA-PELA scaffolds may make them uniquely suited for such cranio-maxillofacial grafting procedures.

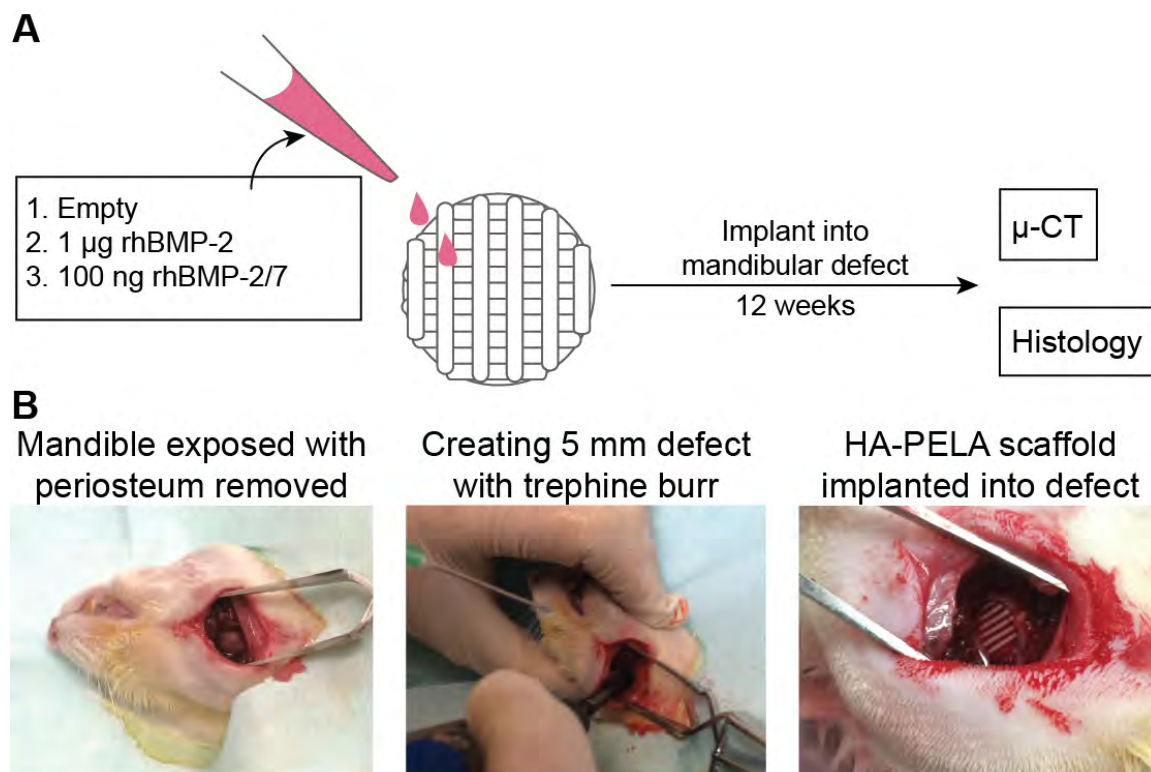
The bones of the skull and mandible are formed through an intramembranous ossification process, as opposed to endochondral ossification for long bones, and may have a different healing capacity from long bones.[19] Therefore, the femoral defect model described in this dissertation may be inappropriate for testing bone-grafting materials for cranio-maxillofacial

applications. A critical-size mandibular defect in rats was chosen as the *in vivo* model to test the efficacy of the 3-D rapid-prototyped macroporous HA-PELA scaffolds. Mandibular defects in rats have been used by other groups to test the healing potential of membranes and porous scaffolds with or without pre-loaded progenitor cells or therapeutics.[20–28] This defect model involves creating a 5-mm diameter through-and-through defect in the mandibular ramus using a trephine burr. Mandibular defects of this size do not heal without intervention and are typically filled with soft fibrous scar tissue. The critical-size mandibular defect model in rats can reasonably emulate relevant cranio-maxillofacial defects encountered clinically.

In a pilot study, 3-D HA-PELA scaffolds (5 mm diameter, 1.6 mm thick), with or without pre-loaded 1 μ g of rhBMP-2 or 100 ng of rhBMP-2/7, were implanted into 5-mm mandibular defects in male rats (~350 g weight) and monitored for up to 12 weeks by μ -CT. Bone ingrowth was compared to an empty defect control. End point histology was performed to further assess bone formation and immune response. An overview of the study procedure is shown in Figure 4.

Figure 4. Testing 3-D HA-PELA scaffolds in rat mandibular defects. (A) Study overview. (B) Surgical procedure.

Figure 4

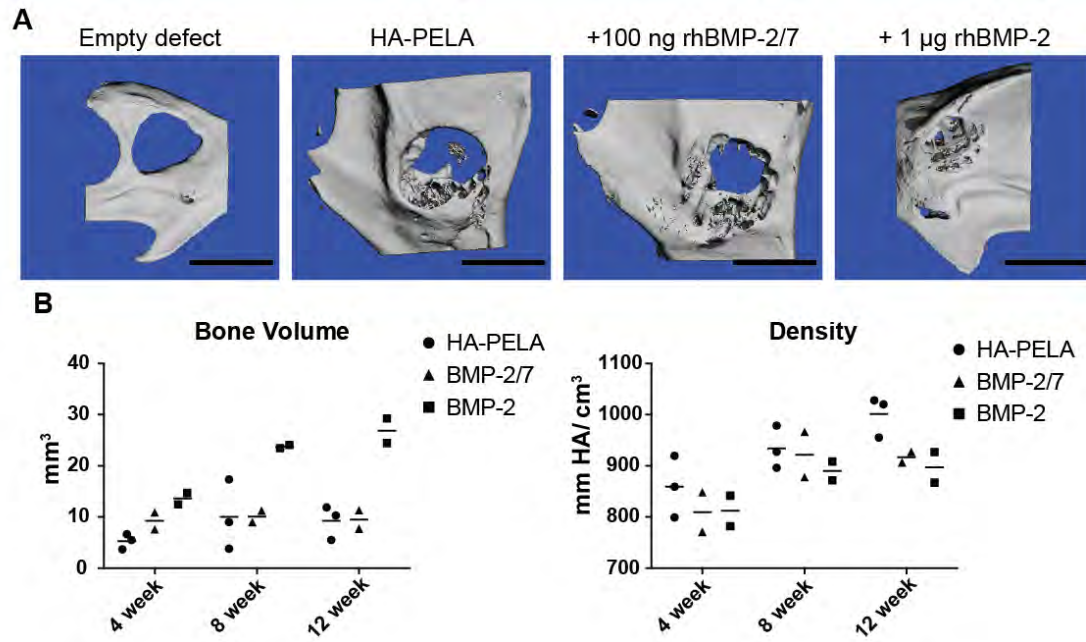


μ -CT results show that the empty control was not filled with new bone by 12 weeks, confirming the critical size nature of the 5-mm mandibular defect (Fig. 5A). Defects treated with HA-PELA alone and HA-PELA + 100-ng rhBMP-2/7 resulted in some bone ingrowth, primarily in the periphery of the defects, but was not completely filled by 12 weeks (Fig. 5A). rhBMP-2/7 has been shown to be more potent (up to 10-fold) than rhBMP-2 in terms of in vitro osteoinductivity.[29] rhBMP-2/7 may contribute to both the early and later stages of bone healing and has been successfully used by our lab to heal 5-mm rat femoral segmental defects in combination with HA-pHEMA in 400-ng loading dose. [30] Here, the limited healing observed with 100 ng of rhBMP-2/7 could be due to differences in healing between the mandibular defects and the femoral defects or due to inadequate loading dose of the protein. Defects treated with HA-PELA + 1- μ g rhBMP-2 were filled with bone by 12 weeks (Fig. 5A). Quantitative μ -CT analysis confirmed this result, with higher bone volume in the rhBMP-2 treated group than HA-PELA alone or HA-PELA + rhBMP-2/7 (Fig. 5B). There appeared to be no difference in bone density between groups, although the sample size is insufficient to draw statistical conclusions. This pilot study suggests that 3-D HA-PELA with 1 μ g of rhBMP-2 may be sufficient to heal critical size mandibular defects in rats. By comparison, Kowalczewski et al. used 5 μ g of rhBMP-2 in combination with a keratin-based scaffold to heal similar mandibular defects.[31] Similarly, DeConde et al. used rhBMP-2 doses ranging from 0.5 μ g to 15 μ g in a PLGA-based scaffold and found 5 μ g rhBMP-2 resulted in the highest percentage

(~70%) of defect fill, albeit in a different defect geometry (5 mm x 5 mm marginal defect).[32] Our preliminary healing results with a lower dose of rhBMP-2 provide further validation of the efficacy of HA-PELA in healing bone defects.

Figure 5. μ -CT analysis of HA-PELA treated mandibular defects. (A) 3-D reconstructions. (B) Quantitative analysis of bone volume and bone mineral density.

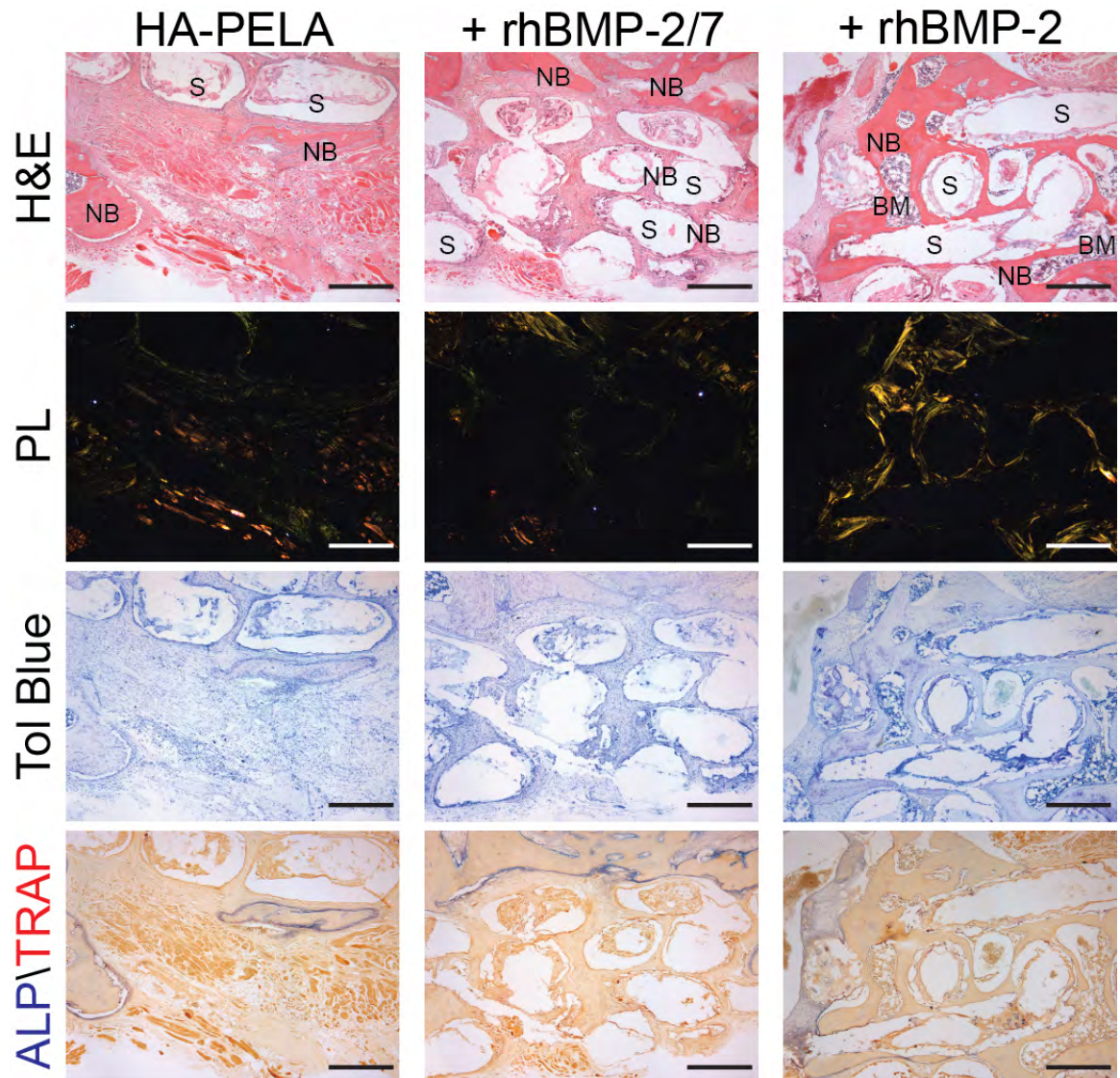
Figure 5



Histology shows bone ingrowth from the defect margins into the HA-PELA scaffolds. Robust and mature bone ingrowth was observed throughout the scaffold in the rhBMP-2 group (Fig. 6) as evidenced by the H&E staining showing dense and recanalized bone with strong birefringence under polarized light. Less mature bone formation was seen in the HA-PELA alone and the rhBMP-2/7 groups, but immature bone ingrowth could still be detected in the scaffold pores. Purple toluidine blue staining at areas of new bone formation indicates an endochondral ossification mechanism. Positive staining for alkaline phosphatase and tartrate resistant acid phosphate (TRAP) at the interface of new bone and HA-PELA scaffold indicates active bone remodeling and scaffold resorption. Minimal immune cell infiltration could be detected by H&E for all treatment groups, indicating minimal adverse local immune response to the HA-PELA scaffold or its degradation byproducts at 12 weeks. Overall, histology confirms the osteoconductivity and biocompatibility of 3-D HA-PELA scaffolds.

Figure 6. Histology of mandibular defects treated with 3-D HA-PELA scaffolds alone or loaded with rhBMP-2/7 or rhBMP-2. Bright field and polarized light (PL) micrographs of hematoxlyn & eosin (H&E), toluidine blue (Tol Blue), and Alkaline Phosphatase (ALP) / tartrate-resistant acid phosphatase (TRAP) stained sections. S = scaffold; NB = new bone; BM = bone marrow. Scale bars = 500 μ m

Figure 6



REFERENCES

- [1] Leferink AM, Hendrikson WJ, Rouwkema J, Karperien M, van Blitterswijk CA, Moroni L. Increased cell seeding efficiency in bioploted three-dimensional PEOT/PBT scaffolds. *J Tissue Eng Regen Med* 2013. doi: 10.1002/term.1842
- [2] Zhou Y, Chen F, Ho ST, Woodruff MA, Lim TM, Hutmacher DW. Combined marrow stromal cell-sheet techniques and high-strength biodegradable composite scaffolds for engineered functional bone grafts. *Biomaterials* 2007;28:814–24.
- [3] Temple JP, Hutton DL, Hung BP, Huri PY, Cook C a, Kondragunta R, et al. Engineering anatomically shaped vascularized bone grafts with hASCs and 3D-printed PCL scaffolds. *J Biomed Mater Res A* 2014:1–9.
- [4] Schantz J-T, Brandwood A, Hutmacher DW, Khor HL, Bittner K. Osteogenic differentiation of mesenchymal progenitor cells in computer designed fibrin-polymer-ceramic scaffolds manufactured by fused deposition modeling. *J Mater Sci Mater Med* 2005;16:807–19.
- [5] CLARK RAF. Fibrin and Wound Healing. *Ann N Y Acad Sci* 2006;936:355–67.

- [6] Guyette JP, Fakharzadeh M, Burford EJ, Tao Z-W, Pins GD, Rolle MW, et al. A novel suture-based method for efficient transplantation of stem cells. *J Biomed Mater Res A* 2013;101:809–18.
- [7] Cornwell KG, Pins GD. Discrete crosslinked fibrin microthread scaffolds for tissue regeneration. *J Biomed Mater Res A* 2007;82:104–12.
- [8] Ahmed TAE, Dare E V, Hincke M. Fibrin: a versatile scaffold for tissue engineering applications. *Tissue Eng Part B Rev* 2008;14:199–215.
- [9] Lind M, Larsen A, Clausen C, Osther K, Everland H. Cartilage repair with chondrocytes in fibrin hydrogel and MPEG polylactide scaffold: an in vivo study in goats. *Knee Surg Sports Traumatol Arthrosc* 2008;16:690–8.
- [10] Schantz J-T, Hutmacher DW, Lam CXF, Brinkmann M, Wong KM, Lim TC, et al. Repair of calvarial defects with customised tissue-engineered bone grafts II. Evaluation of cellular efficiency and efficacy in vivo. *Tissue Eng* 2003;9 Suppl 1:S127–39.
- [11] Endres M, Hutmacher DW, Salgado a J, Kaps C, Ringe J, Reis RL, et al. Osteogenic induction of human bone marrow-derived mesenchymal progenitor cells in novel synthetic polymer-hydrogel matrices. *Tissue Eng* 2003;9:689–702.

- [12] Xu J, Feng E, Song J. Bioorthogonally cross-linked hydrogel network with precisely controlled disintegration time over a broad range. *J Am Chem Soc* 2014;136:4105–8.
- [13] Lilja J. Alveolar bone grafting. *Indian J Plast Surg* 2009;42 Suppl:S110–5.
- [14] Schmitz JP, Hollinger JO. The critical size defect as an experimental model for craniomandibulofacial nonunions. *Clin Orthop Relat Res* 1986:299–308.
- [15] Neovius E, Engstrand T. Craniofacial reconstruction with bone and biomaterials: review over the last 11 years. *J Plast Reconstr Aesthet Surg* 2010;63:1615–23.
- [16] Kellman RM. Safe and dependable harvesting of large outer-table calvarial bone grafts. *Arch Otolaryngol - Head Neck Surg* 1994;120:856–60.
- [17] Zhang D, George OJ, Petersen KM, Jimenez-Vergara AC, Hahn MS, Grunlan M a. A bioactive “self-fitting” shape memory polymer scaffold with potential to treat cranio-maxillo facial bone defects. *Acta Biomater* 2014;10:4597–605.
- [18] Phillips JH, Rahn BA. Fixation effects on membranous and endochondral onlay bone-graft resorption. *Plast Reconstr Surg* 1988;82:872–7.

- [19] Aghaloo TL, Chaichanasakul T, Bezouglaia O, Kang B, Franco R, Dry SM, et al. Osteogenic potential of mandibular vs. long-bone marrow stromal cells. *J Dent Res* 2010;89:1293–8.
- [20] Park J, Ries J, Gelse K, Kloss F, von der Mark K, Wiltfang J, et al. Bone regeneration in critical size defects by cell-mediated BMP-2 gene transfer: a comparison of adenoviral vectors and liposomes. *Gene Ther* 2003;10:1089–98.
- [21] Schortinghuis J, Ruben JL, Meijer HJ., Bronckers ALJ., Raghoobar GM, Stegenga B. Microradiography to evaluate bone growth into a rat mandibular defect. *Arch Oral Biol* 2003;48:155–60.
- [22] Schliephake H, Weich H a, Dullin C, Gruber R, Frahse S. Mandibular bone repair by implantation of rhBMP-2 in a slow release carrier of polylactic acid--an experimental study in rats. *Biomaterials* 2008;29:103–10.
- [23] Gallego L, Junquera L, García E, García V, Alvarez-Viejo M, Costilla S, et al. Repair of rat mandibular bone defects by alveolar osteoblasts in a novel plasma-derived albumin scaffold. *Tissue Eng Part A* 2010;16:1179–87.
- [24] Arosarena O, Collins W. Comparison of BMP-2 and -4 for rat mandibular bone regeneration at various doses. *Orthod Craniofac Res* 2005;8:267–76.

- [25] Rai B, Ho KH, Lei Y, Si-Hoe K-M, Jeremy Teo C-M, Yacob K Bin, et al. Polycaprolactone-20% tricalcium phosphate scaffolds in combination with platelet-rich plasma for the treatment of critical-sized defects of the mandible: a pilot study. *J Oral Maxillofac Surg* 2007;65:2195–205.
- [26] Zellin G, Gritli-Linde A, Linde A. Healing of mandibular defects with different biodegradable and non-biodegradable membranes: an experimental study in rats. *Biomaterials* 1995;16:601–9.
- [27] Van Leeuwen a C, Huddleston Slater JJR, Gielkens PFM, de Jong JR, Grijpma DW, Bos RRM. Guided bone regeneration in rat mandibular defects using resorbable poly(trimethylene carbonate) barrier membranes. *Acta Biomater* 2011;8:1422–9.
- [28] Ren J, Ren T, Zhao P, Huang Y, Pan K. Repair of mandibular defects using MSCs-seeded biodegradable polyester porous scaffolds. *J Biomater Sci Polym Ed* 2007;18:505–17.
- [29] Zheng Y, Wu G, Zhao J, Wang L, Sun P, Gu Z. rhBMP2/7 heterodimer: an osteoblastogenesis inducer of not higher potency but lower effective concentration compared with rhBMP2 and rhBMP7 homodimers. *Tissue Eng Part A* 2010;16:879–87.
- [30] Filion TM, Li X, Mason-Savas A, Kreider JM, Goldstein SA, Ayers DC, et al. Elastomeric osteoconductive synthetic scaffolds with acquired

osteogenicity expedite the repair of critical femoral defects in rats. *Tissue Eng Part A* 2011;17:503–11.

[31] Kowalczewski CJ, Tombyln S, Wasnick DC, Hughes MR, Ellenburg MD, Callahan MF, et al. Reduction of ectopic bone growth in critically-sized rat mandible defects by delivery of rhBMP-2 from kerateine biomaterials. *Biomaterials* 2014;35:3220–8.

[32] DeConde AS, Sidell D, Lee M, Bezouglaia O, Low K, Elashoff D, et al. Bone morphogenetic protein-2-impregnated biomimetic scaffolds successfully induce bone healing in a marginal mandibular defect. *Laryngoscope* 2013;123:1149–55.

APPENDIX II: Stem cell labeling using polyethylenimine conjugated (α -NaYbF₄:Tm³⁺)/CaF₂ upconversion nanoparticles

This appendix has been adapted from:

Zhao L*, Kutikov A*, Shen J, Duan C, Song J, Han G. "Stem Cell Labeling using Polyethylenimine Conjugated (α -NaYbF₄:Tm³⁺)/CaF₂ Upconversion Nanoparticles" *Theranostics* 2013; 3(4):249-257. (*Equal contribution)

Preface

Tracking the fate of delivered cells is important for determining the mechanisms of cell-guided tissue repair and improving tissue engineering therapies. While GFP-labeling was used in this dissertation to track the MSCs, this approach has distinct disadvantages. These include strong tissue auto-fluorescence, down regulation of GFP expression, and poor tissue penetration requiring *ex vivo* imaging. This appendix describes some of our work on developing improved labeling approaches for MSCs, in collaboration with the laboratory of Dr. Gang Han.

Abstract

We report on a polyethylenimine (PEI) covalently conjugated (α -NaYbF₄:Tm³⁺)/CaF₂ upconversion nanoparticle (PEI-UCNP) and its use for labeling rat mesenchymal stem cells (rMSCs). The PEI-UCNPs absorb and emit near-infrared light, allowing for improved *in vivo* imaging depth over conventional probes. We found that such covalent surface *conjugation by PEI results in a much more stable PEI-UCNP suspension in PBS compared to conventional electrostatic layer by layer (LbL) self-assembling coating approach*. We systematically examined the effects of nanoparticle dose and exposure duration on rat mesenchymal stem cell (rMSC) cytotoxicity. The exocytosis of PEI-UCNPs from labeled rMSCs and the impact of PEI-UCNP uptake on rMSC differentiation was also investigated. Our data show that incubation of 100- μ g/mL PEI-UCNPs with rMSCs for 4 h led to efficient labeling of the MSCs, and such a level of PEI-UCNP exposure imposed little cytotoxicity to rMSCs (95% viability). However, extended incubation of PEI-UCNPs at the 100 μ g/mL dose for 24 hour resulted in some cytotoxicity to rMSCs (60% viability). PEI-UCNP labeled rMSCs also exhibited normal early proliferation, and the internalized PEI-UCNPs did not leak out to cause unintended labeling of adjacent cells during a 14-day transwell culture experiment. Finally, PEI-UCNP labeled rMSCs were able to undergo osteogenic and adipogenic differentiation upon *in vitro* induction, although the osteogenesis of labeled rMSCs appeared to be less potent than that of the

unlabeled rMSCs. Taken together, PEI-UCNPs are promising agents for stem cell labeling and tracking.

1. Introduction

Mesenchymal stem cells (MSCs) are multipotent cells that can differentiate into a number cell types. This technology holds great promise in a variety of life-threatening disease treatments such as diabetes,¹ cardiovascular disease,² spinal-cord injuries³ and cancers⁴. In order to facilitate their therapeutic use, the migration and differentiation of transplanted stem cells must be monitored over time with high spatial resolution. Optical imaging has emerged as a promising method for cell labeling due to its high sensitivity, cost-effectiveness, and rapid processing time. However, typical labeling agents such as organic dyes and fluorescent nanoparticles emit visible light with limited tissue penetration depth. To this end, many near infrared (NIR) emitting probes have been developed that take advantage of the elevated light penetration depth of NIR light. However, current NIR probes have drawbacks for *in vivo* tracking of stem cells. For example, synthetic NIR dyes are rapidly photobleached, making them ill suited for longitudinal study of stem cell fate. Common NIR quantum dots (e.g., CdTe, InAs, PbS) are composed of highly toxic elements, limiting their clinical applications.

Lanthanide-doped upconversion nanoparticles (UCNPs) are promising materials for stem cell tracking due to their unique optical properties. Unlike traditional organic-⁵⁻⁷ and protein-based materials⁸, metal complexes⁹⁻¹² or

semiconductor quantum dots^{13, 14}, these UCNPs generally have converse excitation and emission profiles: they are excited at NIR (980 nm), which is converted to a higher energy for emission at a visible or a shorter NIR wavelength. We have recently developed a novel biocompatible (α -NaYbF₄:Tm³⁺)/CaF₂ UCNP with enhanced NIR emission.¹⁵ We demonstrated that such core/shell UCNPs are ideal for high contrast and deep tissue bioimaging. For example, they are completely free of autofluorescence for *in vitro* cell imaging and exhibit an exceptionally high signal-to-noise-ratio *in vivo* (i.e., 310 for Balb-c mice). The combination of NIR excitation and emission of this UCNP allows for outstanding tissue penetration depth (>3.2 cm), and it is 6-8 orders of magnitude brighter than conventional fluorescence based imaging probes in two-photon processes¹⁶⁻²⁰, with minimal light scattering and background from the surrounding tissue²¹⁻²³. In addition, this nanoparticle is less toxic than quantum dots since they do not contain class I and class II toxic elements. The constituent ions of the shell of this UCNP, calcium and fluoride, are essentially endogenous elements in the living systems.

Proper surface modification of UCNPs is necessary to facilitate cellular uptake and subsequent applications for stem cell labeling. The intrinsic dynamic nature of cell surface antigen presentations on MSCs and the lack of unique cell surface markers or marker combinations for some animal MSCs (particularly mouse MSCs) have made an antibody-based UCNP surface modification and MSC targeting approach elusive. Surface modification of UCNPs with

polycationic macromolecules enabling non-specific endocytosis are facile and practical, and have been the most commonly used strategy for shuttling nanoparticles across cell membranes for drug delivery or cell-labeling applications. Herein, we report on the development of a polyethylenimine (PEI)-conjugated (α -NaYbF₄:Tm³⁺)/CaF₂ UCNP. We evaluated its stability, cytotoxicity, cell uptake, exocytosis, and impact on cell proliferation and differentiation in regard to the labeling of rat mesenchymal stem cells (rMSCs).

2. Materials and methods

2.1. Materials

Yb₂O₃ (99.9%), Tm₂O₃ (99.9%), CF₃COONa (99.9%), CF₃COOH, CaCO₃, 1-octadecene (90%), oleic acid (90%), diethylene glycol (99%), 1-Ethyl-3-(3-dimethylaminopropyl) carbodiimide hydrochloride (EDC·HCl), poly(acrylic acid) (PAA), N-hydroxysulfosuccinimide sodium salt (sulfo-NHS), NOBF₄ (97%) and branched polyethylenimine (PEI, Mw 25,000) were all purchased from Sigma-Aldrich and used without further purification. The trifluoroacetates of Yb and Tm were prepared as described²⁴.

2.2. Instrumentation

The size and the morphology of the core and core/shell nanocrystals were characterized by transmission electron microscopy (TEM) using a JEM-2010 microscope at an acceleration voltage of 200 KV. The powder x-ray diffraction (XRD) patterns were recorded by a Siemens D500 diffractometer using Cu K α

radiation ($\lambda = 0.15418$ nm). The 2θ angle of the XRD spectra was recorded at a scanning rate of $5^\circ/\text{minute}$. Upconversion photoluminescence (PL) spectra were recorded using a Fluorolog-3.11 Jobin Yvon spectrofluorimeter with a slit width defining a spectral resolution of 2 nm. The PL was excited at 975 nm using a fiber-coupled laser diode (Sheaumann, MA, USA) introduced to the sample chamber of the spectrofluorimeter. All upconversion PL spectra have been corrected for the spectral sensitivity of the system. Photographic images of upconverting nanocrystal colloids were taken with a digital camera (Canon Powershot SD800IS, Japan) without any filters.

2.3. Synthesis of PEI-Coated Core/Shell α -(NaYbF₄:0.5% Tm³⁺)/CaF₂ UCNPs

The hydrophobic oleic acid coated α -(NaYbF₄:0.5% Tm³⁺)/CaF₂ UCNPs were fabricated based on our previously reported approach¹⁵. The PEI modification on the UCNPs was carried out in a 3-step reaction (Scheme 1). In the first step, oleic acid ligands on the UCNP surface were removed using a nitrosonium tetrafluoroborate approach (NOBF₄).²⁵ During this reaction, 5 mL of oleic acid coated UCNP dispersion in hexane (~5 mg/mL) was mixed with a 5 mL dichloromethane solution of NOBF₄ (0.01 M) at room temperature. The resulting mixture was shaken gently, typically for 10 hours, until the precipitation of the UCNPs was observed. After centrifugation to remove the supernatant, the precipitated UCNPs were re-dispersed in dimethylformamide (DMF). In order to purify the UCNPs, toluene and hexane (1:1 v/v) were added to flocculate the UCNP dispersion. After centrifugation, DMF was added to re-disperse the

UCNPs, forming a stable colloidal dispersion. In the second step, 150 mg of PAA was added into a DMF dispersion of NOBF₄-treated UCNPs (5 mL, ~5 mg/mL) followed by vigorous stirring at 80 °C. After 30 minutes, the nanoparticles were precipitated by the addition of acetone and re-dispersed in water to form a stable dispersion. In the third step, the PAA-capped UCNPs were covalently grafted with branched PEI. 30 mg of PAA-capped UCNPs in 5 mL of DI water were activated by 1-Ethyl-3-(3-dimethylaminopropyl) carbodiimide hydrochloride (EDC·HCl, 50 mg) and sulfo-NHS (5 mg) in order to form the succinimidyl ester. PEI (20 mg) in PBS buffer (2 mL) was then added to the reaction. After 2 hours of incubation at room temperature, the PEI-conjugated UCNPs (PEI-UCNPs) were purified by centrifugation and re-dispersion in DI water (5 mL). The electrostatic layer-by-layer (LbL) self-assembled PEI coated UCNPs were synthesized as follows. PAA-capped UCNPs (30 mg) in 5 mL of DI water were mixed with PEI (20 mg) in a PBS buffer (2 mL). After 2 hours of incubation at room temperature, the PEI LbL assembled UCNPs were purified by centrifugation and re-dispersion in DI water (5 mL).

2.4. Isolation and culture of rat bone marrow stromal cells

All animal procedures were conducted in accordance with the principles and procedures approved by the University of Massachusetts Medical School Animal Care and Use Committee. Rat bone marrow cells were isolated from the long bones of a 4-week old male Charles River SASCO SD rat as previously described²⁶, and cultured in expansion medium (ascorbic acid-free α MEM

containing 20% FBS, 2% L-Glutamine, and 1% Penicillin-Streptomycin) at 37 °C and 5% CO₂. After removing non-adherent cells on day 4 of the culture, adherent rat bone marrow stromal cells enriched for MSCs (rMSCs) were cultured to reach 80% confluence before being passaged.

2.5. Cytotoxicity of PEI-UCNPs

Passage 1 rMSCs were seeded onto 96-well tissue culture plates (15,625/cm² or 5,000/well) and cultured for 24-h prior to the addition of PEI-UCNPs (0, 20, 50 and 100 µg/mL). Following 4 h or 24 h of incubation with PEI-UCNPs, the cells were washed 3 times with PBS to remove un-internalized PEI-UCNPs and fresh expansion medium was added. Cytotoxicity of 4 h or 24 h treatment with PEI-UCNPs was quantified by MTT assay (Roche) 24 h after the initial UCNP treatment. The effect of the 24 h UCNP exposure on rMSC proliferation was further examined by MTT 48 h after the removal of un-internalized UCNPs. Three replicates were used for each experimental condition. Absorbance of the MTT product was read on a Multiskan FC microplate photometer (Thermo Scientific) at 570 nm with a 690nm background correction.

2.6. Imaging of UCNP-labeled rMSCs

Passage 1 rMSCs were seeded onto glass-bottom dishes (MatTek Corp., 12,500/cm²) and cultured for 24 h prior to the addition of PEI-UCNPs (0, 50 or 100 µg/mL final concentration in medium). The rMSCs were exposed to the particles for 4 or 24 h before the un-internalized PEI-UCNPs were removed by

washing the cells 3 times with PBS. The cells were fixed by 3.7 v/v% methanol-free formaldehyde in PBS for 10 min and washed 3 times in PBS. Fixed cells were permeabilized with Triton X-100 (0.1% in PBS) for 5 min, washed with PBS, and then incubated in PBS containing 1% BSA for 30 min. Actin was stained with 2 units of Alexa Fluor 488-phalloidin (Invitrogen) in PBS containing 1% BSA for 20 min. Cell nuclei were stained with 300 nM of DAPI (Invitrogen) for 5 min. Cytoskeletal actin, UCNP uptake, and cell nuclei were visualized under a 2-photon microscope (Zeiss LSM 7 MP with W Plan-Apochromatic 20X objective) with 870-nm excitation for Alexa Fluor 488 phalloidin, 980-nm excitation for the UCNPs, and 690-nm excitation for DAPI, respectively.

2.7. PEI-UCNP exocytosis from rMSCs

A transwell system was used to study whether the internalized PEI-UCNPs were released from the rMSCs. The PEI-UCNP labeled rMSCs (4-h incubation with 100 $\mu\text{g}/\text{mL}$ particles) were cultured on the transwell insert (the upper compartment; 3.0 μm pore size, polyester membrane). Unlabeled rMSCs were cultured in the underlying plate well (the lower compartment). The same cell seeding density of 10,000 rMSCs/ cm^2 was applied for both top and bottom compartments. The labeled and unlabeled cells were co-cultured for up to 14 days prior to fixation, DAPI staining, and imaging as described above. To confirm that PEI-UCNPs can pass through the transwell membrane, PEI-UCNPs (100 $\mu\text{g}/\text{mL}$) were added to a cell-free control upper compartment and the rMSCs on the bottom compartment were imaged after 24 h.

2.8. Induced differentiations of PEI-UCNP labeled rMSCs

Passage 1 rMSCs (10,500 cells/cm²) were seeded onto a 12-well plate and cultured until they reached 70% confluence. rMSCs were labeled by 4-h incubation with PEI-UCNPs (100 µg/mL) followed by 3 washes with PBS. Osteogenic differentiation was induced by supplementing the expansion medium with 10-nM dexamethasone, 20-mM β-glycerol phosphate, and 50-µM L-ascorbic acid 2-phosphate. Adipogenic differentiation was induced by supplementing the expansion medium with 0.5-µM dexamethasone, 0.5-µM isobutylmethylxanthine, and 50-µM indomethacin. The rMSCs were differentiated for 14 days, with changes of differentiation medium twice a week, and fixed. Osteogenic differentiation was visualized by Alizarin Red S staining for mineral deposition. Adipogenic differentiation was visualized by staining lipid deposits with Oil Red O. MSCs without UCNPs labels were cultured, induced to differentiate, and stained in the same manner. Staining specificity was validated by negative Alizarin Red S staining of cells following adipogenic induction and negative Oil Red O staining of cells following osteogenic induction.

3. Results

3.1. Synthesis and characterization of PEI-UCNPs

PEI was coupled to the surface of the UCNPs by covalent conjugation with the PAA. The nanoparticles formed a clear, aggregate free solution in the PBS buffer. The PEI coating preserved the upconversion emissions in regard to both

visible and near infrared regions (Figure 1A). When excited with a 980nm NIR laser diode, we observed strong upconversion luminescence emitted from the nanoparticles in the PBS buffer with the naked eye (Figure 1B). TEM imaging showed that the PEI-UCNPs are monodispersed in size (Figure 1C). In contrast to the electrostatic LbL self-assembly approach, we found that covalently bound PEI resulted in significantly enhanced stability of the PEI-UCNPs. Dynamic light scattering measurement showed that the hydrodynamic nanoparticle size of this covalently bonded PEI-UCNP was almost identical before and after 24-h incubation in PBS (~ 91nm), while the size of LbL self-assembled PEI-UCNPs increased from ~100nm to ~1um in 5 hours (Figure 2A). Zeta potential measurement of the PEI-UCNPs confirmed the presence of a PEI surface coating with a positive potential of approximately +17.8 mV, which would be suitable for binding with negatively charged cell surfaces (Figure 2B).

3.2. PEI-UCNP cellular uptake and cytotoxicity

In order to determine the optimal time and nanoparticle concentration for stem cell labeling, rMSCs were treated with different concentrations of PEI-UCNPs (0, 20, 50, or 100 µg/ml) for 4 h and 24 h. After incubation, the cells were washed and imaged using a 2-photon microscope. The upconversion luminescence was observed in nearly all of the rMSCs, demonstrating that the stem cells were successfully labeled with the PEI-UCNPs. The level of PEI-UCNP uptake in individual cells was proportional to the nanoparticle treatment concentration and exposure time (Figure 3A). Co-staining for cytoskeletal actin

and nuclei further validated the localization of PEI-UCNP signal within the cytoplasm of rMSCs (Figure 3B).

We next examined the cytotoxicity of the nanoparticles at the aforementioned concentrations and time points. The MTT assay showed that nearly 95% of rMSCs were viable following a 4 h nanoparticle exposure at concentrations up to 100 $\mu\text{g}/\text{mL}$. There was no significant difference in cell viability between the PEI-UCNP labeled groups and unlabeled control ($p > 0.05$). When the exposure time was increased to 24 h, the cell viability significantly decreased compared to the unlabeled control at each concentration examined, with a 63% reduction at the treatment concentration of 100 $\mu\text{g}/\text{mL}$ (Figure 3C). There was no significant difference in toxicity between 50 $\mu\text{g}/\text{mL}$ and 100 $\mu\text{g}/\text{mL}$ doses at this exposure time. To investigate the impact of PEI-UCNP labeling on the proliferation capability of rMSCs, rMSCs were incubated with PEI-UCNPs at various concentrations for 24 h. After removal of un-internalized UCNPs, the cells were cultured for another 48 h before being subjected to MTT assay. The short-term proliferation of rMSCs was minimally impacted by the PEI-UCNP labeling. All groups exhibited significant increases in the number of viable cells, with 1.84-fold increase in viable cells for rMSCs treated with 100 $\mu\text{g}/\text{mL}$ of PEI-UCNPs after 48 h culture as compared to 1.79-fold increase for unlabeled rMSCs (Figure 3D).

3.3. Exocytosis of PEI-UCNPs from labeled rMSCs

One potential challenge for *in vivo* tracking of UCNP-labeled stem cells is the possibility that the uptaken nanoparticles could be exocytosed over time, leading to the unintended labeling of other surrounding cells. We investigated this issue using a transwell culture system²⁷ where rMSCs labeled with PEI-UCNPs (100 µg/mL, 4h) were cultured on the porous membrane in the upper compartment while the unlabeled rMSCs were cultured in the lower compartment (Figure 4A). PEI-UCNPs added to a cell-free upper compartment were able to quickly pass through the membrane and cause the labeling of rMSCs seeded in the lower compartment in 1 day (Figure 4B, control). The labeled and unlabeled cells were co-cultured for 14 days and the cells in the bottom compartment remained free of any PEI-UCNP signal throughout this culture period, supporting that there were no particles exocytosed from the labeled cells in the upper compartment (Figure 4D).

3.4. Differentiation of PEI-UCNP labeled rMSCs

The effect of PEI-UCNP labeling on the osteogenic and adipogenic differentiations of rMSCs were assessed. Passage 1 rMSCs labeled with PEI-UCNPs (100 µg/mL, 4 h) were cultured in osteogenic or adipogenic medium for 14 days and their differentiation potency was compared with that of unlabeled MSCs. Light microscopy shows that the PEI-UCNP labeled rMSCs were able to undergo osteogenic and adipogenic differentiation as supported by the positive Alizarin Red S (Figure 5A) and Oil Red O (Figure 5B) staining, respectively. The

intensity of Alizarin red S staining, however, was reduced for the PEI-UCNP labeled rMSCs compared to the unlabeled control (Figure 5A).

4. Discussion

The ability to label and track stem cells has far reaching applications in tissue engineering and regenerative medicine, where the fate of implanted stem cells remains unclear. Stem cell labeling with NIR probes has the potential to allow for the *in vivo* study of stem cell fate with greater tissue penetration depth and spatial resolution than conventional cell labeling methods. Herein, we report the application of a recently developed UCNP with NIR-excitation and NIR-emission to the labeling of rMSCs.

We compared two approaches of modifying the surface of the UCNPs with PEI, facilitating non-specific cellular uptake. In one approach, we used an LbL method that deposits PEI by electrostatic interactions around the nanoparticle surface. In a second approach, we covalently coupled the PEI to the UCNP surface through a PAA intermediate. The presence of a PEI coating was confirmed by zeta potential measurements that indicated a positive charge on the particle surface. We found that the covalently linked PEI resulted in increased particle stability, with no increase in hydrodynamic size over the course of a 24 h incubation in PBS. In contrast, the LbL assembled PEI resulted in rapid particle aggregation in PBS. Due to their increased stability, we chose the UCNPs with the covalently coupled PEI coating (PEI-UCNPs) for further cell-based analysis.

We used rMSCs as a model to determine the efficacy of PEI-UCNPs for stem cell labeling. MSCs are a multipotent cell that can differentiate into osteoblasts, chondrocytes, myocytes and adipocytes. They have been studied widely for musculoskeletal tissue engineering and have been used clinically. Tracking labeled MSCs *in vivo* is important for the validation and development of MSC-based therapeutic strategies. We show that the PEI-UCNP concentration and incubation-time can be optimized to achieve efficient rMSCs labeling with negligible cytotoxicity. Specifically, we showed that a 4 h incubation with 100 $\mu\text{g}/\text{mL}$ PEI-UCNPs effectively labeled rMSCs while maintaining ~95% cell viability. Although a longer exposure of 24 h did lead to increased cytotoxicity in a dose dependent manner, the cytotoxicity did appear to level off beyond a particle concentration of 50 $\mu\text{g}/\text{mL}$. Further, UCNP signals were localized to the rMSC cytoplasm and did not negatively impact the short-term (48 h) proliferation of MSCs.

Transwell coculture experiments showed that PEI-UCNP internalized in the rMSCs did not leak out via exocytosis during a 14-day period to cause unintended labeling of surrounding cells. This supports the feasibility of *in vivo* cell tracking over a couple of weeks without causing non-specific secondary labeling of other cells. Finally, we showed that PEI-UCNP labeled rMSCs were able to differentiate along the osteogenic and adipogenic lineages upon *in vitro* induction, suggesting that the PEI-UCNP labeling did not abolish these key functions of MSCs. Although the PEI-UCNP labeled rMSCs exhibited less potent

osteogenic differentiation than the unlabeled control, the potency of adipogenic differentiation was largely unaffected by PEI-UCNP labeling. It remains to be seen whether other lineage commitments and *in vivo* differentiation of MSCs is affected by the PEI-UCNP labeling. Finally, exploring even more cytocompatible surface coating strategies may further minimize the observed impact on the osteogenic differentiation potency of PEI-UCNP labeled rMSCs.

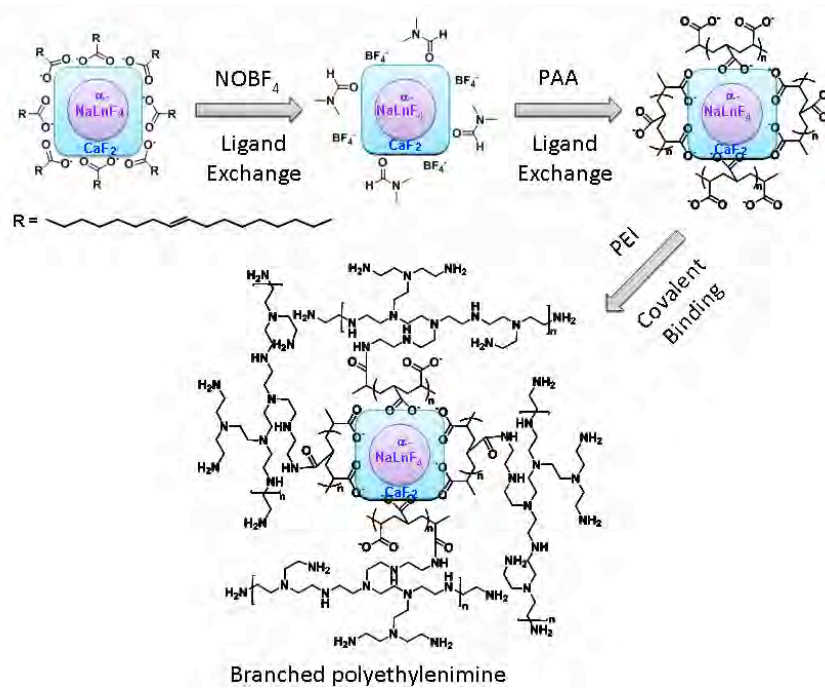
5. Conclusions

The NIR-excitation and NIR-emission of $\alpha\text{-NaYF}_4\text{:Yb}^{3+},\text{Tm}^{3+}/\text{CaF}_2$ UCNP allows for increased tissue penetration depth, facilitating *in vivo* imaging. We report the development of core/shell $\alpha\text{-NaYbF}_4\text{:Yb}^{3+},\text{Tm}^{3+}/\text{CaF}_2$ UCNP with a covalently coupled PEI coating (PEI-UCNPs) and their validation for stem cell labeling applications. We show that the covalently coupled PEI coating results in greater particle stability in PBS than UCNP coated with PEI using a layer-by-layer approach. The PEI-UCNPs show reasonable cytocompatibility at a concentration and exposure time adequate for efficient labeling of rMSCs. The cell viability remained above 95% after a 4 h PEI-UCNP exposure at 100 $\mu\text{g/mL}$. Further, the PEI-UCNP labeling did not impair short-term cell proliferation. Exocytosis of internalized PEI-UCNP from labeled cells was not observed during a 14-day culture period. Finally, PEI-UCNP labeled rMSCs were able to undergo osteogenic and adipogenic differentiations upon *in vitro* induction, although the potency of the former was reduced compared to unlabeled control.

Taken together, PEI-UCNPs have promising applications in cell labeling and *in vivo* tracking.

Acknowledgements

This research was supported by the University of Massachusetts Medical School and the Worcester Foundation Mel Cutler Award. L. Z. gratefully acknowledges support from the China Scholarship Council for the State Scholarship Fund.



Scheme 1. A surface modification scheme for PEI coated α -(NaYbF₄:0.5% Tm³⁺)@CaF₂ UCNPs.

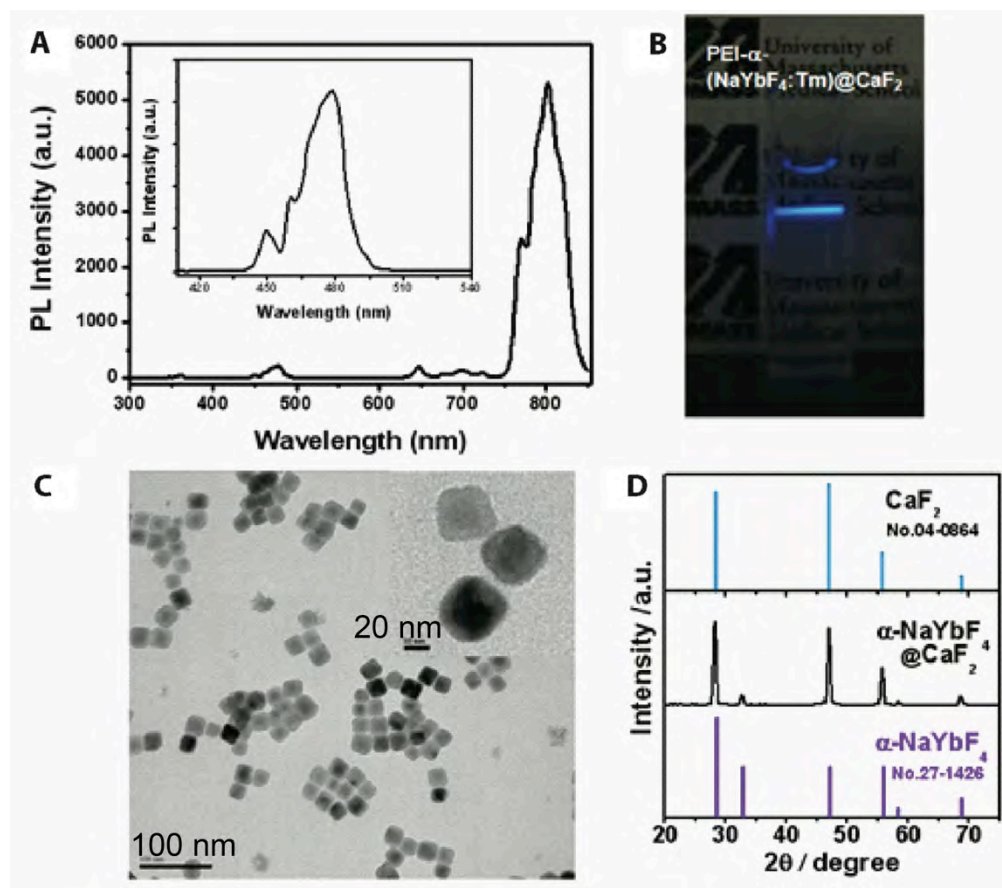


Figure 1. (A) The upconversion photoluminescence spectrum under laser excitation at 980 nm. (B) A photograph of PEI-UCNPs when excited by a NIR laser at 980 nm. (C) A TEM image of the NaYF₄:Yb³⁺,Tm³⁺/CaF₂ nanoparticles coated with 25kD PEI. (inset: High resolution TEM) (D) X-ray diffraction (XRD) patterns of α -NaYbF₄:Tm core and α -NaYF₄:Yb,Tm /CaF₂ core/shell UCNPs.

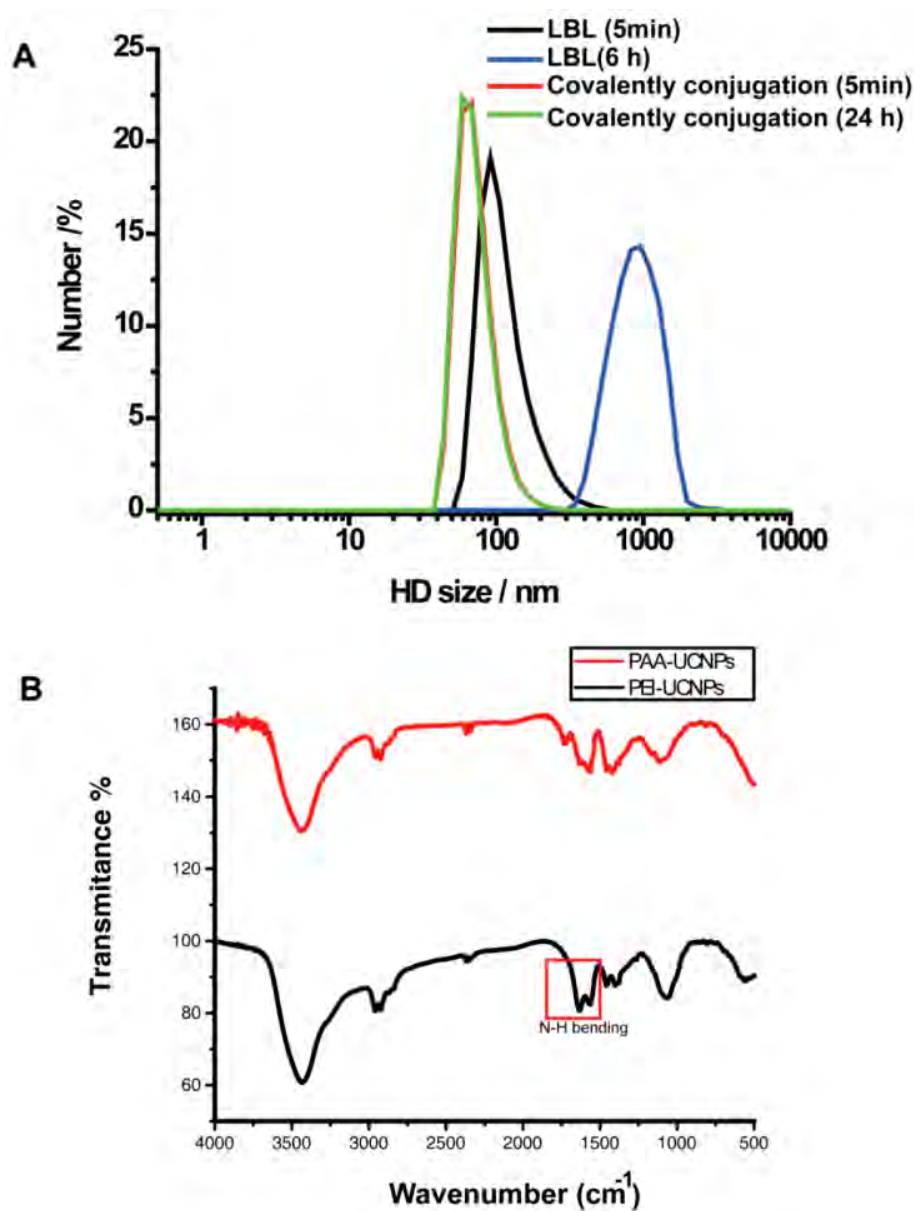


Figure 2. (A) The hydrodynamic (HD) size distributions of covalently conjugated and LbL self assembled PEI-UCNPs. (B) Plot of the zeta potential of covalently conjugated PEI-UCNPs

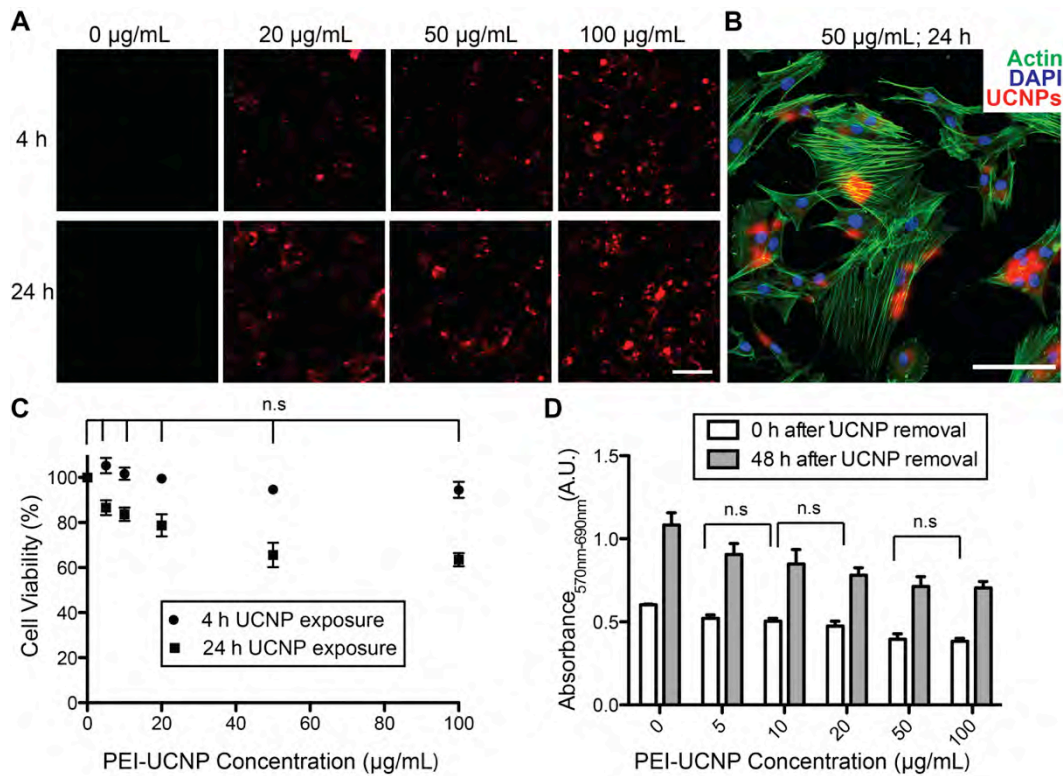


Figure 3. The uptake efficiency of PEI-UCNPs by rMSCs and the viability and proliferation of labeled rMSCs. (A) Two-photon microscopy images of rMSCs following 4-h and 24-h incubation with various concentrations of PEI-UCNPs. Scale bar = 50 µm (B) Co-localization of UCNP signal with rMSC actin and nuclei following incubation with 50 µg/mL UCNPs for 24 h. Scale bar = 50 µm (C) rMSC viability following 4 h and 24 h incubation with various concentrations of PEI-UCNPs. Percent viability is calculated relative to the MTT absorbance of unlabeled rMSCs. (D) The impact of PEI-UCNP labeling on rMSC proliferation as determined by MTT assay. Significance of statistical comparisons were determined by one-way ANOVA with Tukey post-hoc. All pairwise comparisons are significant ($p < 0.05$) unless denoted as n.s. ($p > 0.05$, (not significant)).

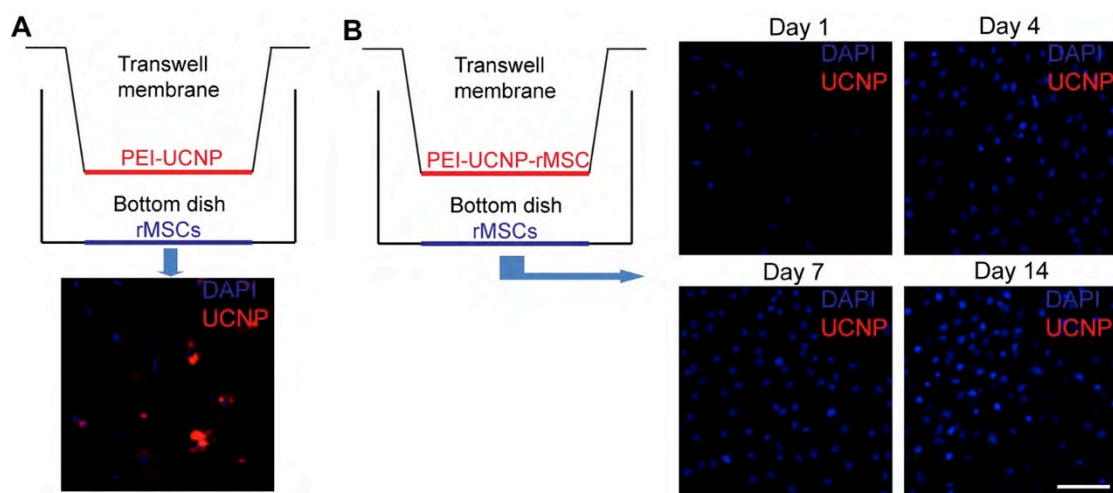


Figure 4. Exocytosis of PEI-UCNPs by labeled rMSCs. (A) Schematic of a control transwell setup containing PEI-UCNPs on the top well membrane and rMSCs on the bottom well, and the two-photon imaging of the bottom dish rMSCs. (B) Schematic of a transwell co-culture setup containing PEI-UCNP labeled rMSCs on top well membrane and unlabeled rMSCs on the bottom dish, and the two-photon imaging of the bottom dish rMSCs over a 14 day period. Cell nuclei were stained with DAPI. No UCNP fluorescence is visible in the bottom dish of the transwell plate. Scale bar = 50 μm .

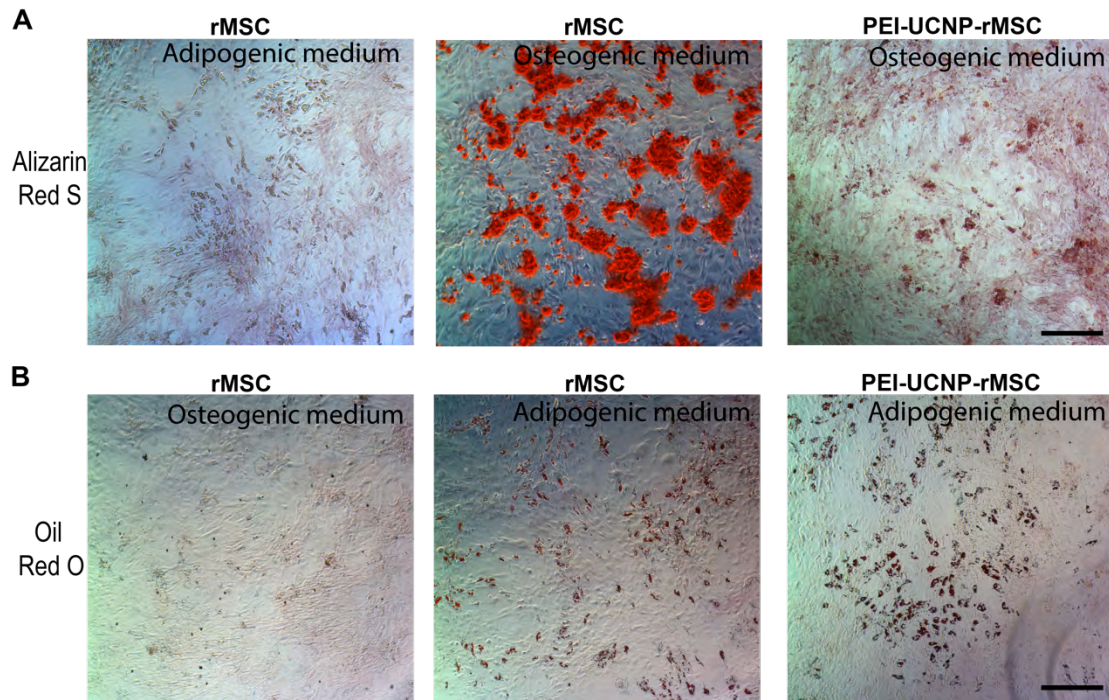


Figure 5. Osteogenic and adipogenic differentiation of PEI-UCNP labeled rMSCs. (A) Alizarin red S staining of unlabeled rMSCs after 14-day culture in adipogenic (negative staining control) and osteogenic medium (positive control), and labeled rMSCs after 14-day culture in osteogenic medium. Scale bar = 100 μ m. (B) Oil red O staining of unlabeled rMSCs after 14-day culture in osteogenic (negative staining control) and adipogenic medium (positive control), and labeled rMSCs after 14-day culture in adipogenic medium. Scale bar = 100 μ m.

References

1. Assady, S.; Maor, G.; Amit, M.; Itskovitz-Eldor, J.; Skorecki, K. L.; Tzukerman, M., Insulin production by human embryonic stem cells. *Diabetes* **2001**, *50* (8), 1691-1697.
2. Cao, F.; Lin, S.; Xie, X. Y.; Ray, P.; Patel, M.; Zhang, X. Z.; Drukker, M.; Dylla, S. J.; Connolly, A. J.; Chen, X. Y.; Weissman, I. L.; Gambhir, S. S.; Wu, J. C., In vivo visualization of embryonic stem cell survival, proliferation, and migration after cardiac delivery. *Circulation* **2006**, *113* (7), 1005-1014.
3. McDonald, J. W.; Liu, X. Z.; Qu, Y.; Liu, S.; Mickey, S. K.; Turetsky, D.; Gottlieb, D. I.; Choi, D. W., Transplanted embryonic stem cells survive, differentiate and promote recovery in injured rat spinal cord. *Nat Med* **1999**, *5* (12), 1410-1412.
4. Singh, S. K.; Hawkins, C.; Clarke, I. D.; Squire, J. A.; Bayani, J.; Hide, T.; Henkelman, R. M.; Cusimano, M. D.; Dirks, P. B., Identification of human brain tumour initiating cells. *Nature* **2004**, *432* (7015), 396-401.
5. Terai, T.; Nagano, T., Fluorescent probes for bioimaging applications. *Current Opinion in Chemical Biology* **2008**, *12* (5), 515-521.
6. Beija, M.; Afonso, C. A. M.; Martinho, J. M. G., Synthesis and applications of Rhodamine derivatives as fluorescent probes. *Chemical Society Reviews* **2009**, *38* (8), 2410-2433.
7. Zhang, M.; Yu, M. X.; Li, F. Y.; Zhu, M. W.; Li, M. Y.; Gao, Y. H.; Li, L.; Liu, Z. Q.; Zhang, J. P.; Zhang, D. Q.; Yi, T.; Huang, C. H., A highly selective fluorescence turn-on sensor for Cysteine/Homocysteine and its application in bioimaging. *Journal of the American Chemical Society* **2007**, *129* (34), 10322.
8. Giepmans, B. N. G.; Adams, S. R.; Ellisman, M. H.; Tsien, R. Y., Review - The fluorescent toolbox for assessing protein location and function. *Science* **2006**, *312* (5771), 217-224.
9. Zhao, L.; Qu, S. Y.; He, C.; Zhang, R.; Duan, C. Y., Face-driven octanuclear cerium(IV) luminescence polyhedra: synthesis and luminescent sensing natural saccharides. *Chemical Communications* **2011**, *47* (33), 9387-9389.
10. Zhao, Q.; Huang, C. H.; Li, F. Y., Phosphorescent heavy-metal complexes for bioimaging. *Chemical Society Reviews* **2011**, *40* (5), 2508-2524.

11. Lo, K. K. W.; Li, S. P. Y.; Zhang, K. Y., Development of luminescent iridium(III) polypyridine complexes as chemical and biological probes. *New Journal of Chemistry* **2011**, 35 (2), 265-287.
12. Eliseeva, S. V.; Bunzli, J. C. G., Lanthanide luminescence for functional materials and bio-sciences. *Chemical Society Reviews* **2010**, 39 (1), 189-227.
13. Michalet, X.; Pinaud, F. F.; Bentolila, L. A.; Tsay, J. M.; Doose, S.; Li, J. J.; Sundaresan, G.; Wu, A. M.; Gambhir, S. S.; Weiss, S., Quantum dots for live cells, in vivo imaging, and diagnostics. *Science* **2005**, 307 (5709), 538-544.
14. Wang, Q. B.; Liu, Y.; Ke, Y. G.; Yan, H., Quantum dot bioconjugation during core-shell synthesis. *Angewandte Chemie-International Edition* **2008**, 47 (2), 316-319.
15. Chen, G.; Shen, J.; Ohulchanskyy, T. Y.; Patel, N. J.; Kutikov, A.; Li, Z.; Song, J.; Pandey, R. K.; Agren, H.; Prasad, P. N.; Han, G., (alpha-NaYbF(4):Tm(3+))/CaF(2) Core/Shell Nanoparticles with Efficient Near-Infrared to Near-Infrared Upconversion for High-Contrast Deep Tissue Bioimaging. *ACS Nano* **2012**, 6 (9), 8280-7.
16. Wang, F.; Banerjee, D.; Liu, Y. S.; Chen, X. Y.; Liu, X. G., Upconversion nanoparticles in biological labeling, imaging, and therapy. *Analyst* **2010**, 135 (8), 1839-1854.
17. Mader, H. S.; Kele, P.; Saleh, S. M.; Wolfbeis, O. S., Upconverting luminescent nanoparticles for use in bioconjugation and bioimaging. *Current Opinion in Chemical Biology* **2010**, 14 (5), 582-596.
18. Chatterjee, D. K.; Gnanasammandhan, M. K.; Zhang, Y., Small Upconverting Fluorescent Nanoparticles for Biomedical Applications. *Small* **2010**, 6 (24), 2781-2795.
19. Zhou, J.; Liu, Z.; Li, F. Y., Upconversion nanophosphors for small-animal imaging. *Chemical Society Reviews* **2012**, 41 (3), 1323-1349.
20. Jie Shen, L. Z., Gang Han, Lanthanide-doped upconverting luminescent nanoparticle platforms for optical imaging-guided drug delivery and therapy *Adv Drug Deliver Rev* **2012**.
21. Frangioni, J. V., In vivo near-infrared fluorescence imaging. *Current Opinion in Chemical Biology* **2003**, 7 (5), 626-634.

22. Hilderbrand, S. A.; Weissleder, R., Near-infrared fluorescence: application to in vivo molecular imaging. *Current Opinion in Chemical Biology* **2010**, *14* (1), 71-79.
23. Gao, J. H.; Chen, X. Y.; Cheng, Z., Near-Infrared Quantum Dots as Optical Probes for Tumor Imaging. *Current Topics in Medicinal Chemistry* **2010**, *10* (12), 1147-1157.
24. Roberts, J. E., Lanthanum and Neodymium Salts of Trifluoroacetic Acid. *Journal of the American Chemical Society* **1961**, *83* (5), 2.
25. Dong, A. G.; Ye, X. C.; Chen, J.; Kang, Y. J.; Gordon, T.; Kikkawa, J. M.; Murray, C. B., A Generalized Ligand-Exchange Strategy Enabling Sequential Surface Functionalization of Colloidal Nanocrystals. *Journal of the American Chemical Society* **2011**, *133* (4), 998-1006.
26. Song, J.; Xu, J. W.; Filion, T.; Saiz, E.; Tomsia, A. P.; Lian, J. B.; Stein, G. S.; Ayers, D. C.; Bertozzi, C. R., Elastomeric high-mineral content hydrogel-hydroxyapatite composites for orthopedic applications. *J Biomed Mater Res A* **2009**, *89A* (4), 1098-1107.
27. Wang, C.; Cheng, L.; Xu, H.; Liu, Z., Towards whole-body imaging at the single cell level using ultra-sensitive stem cell labeling with oligo-arginine modified upconversion nanoparticles. *Biomaterials* **2012**, *33* (19), 4872-4881.

Appendix II: Publications completed during graduate education

Kutikov AB, Skelly J, Ayers DC, Song J. "Spiral-wrapped electrospun amphiphilic polymer-hydroxyapatite scaffold delivering MSCs or rhBMP-2 for the templated repair of long bone defects in rats" *Acta Biomaterialia* (submitted)

Kutikov AB, Reyer KA, Song J. "Shape memory performance of thermoplastic amphiphilic triblock copolymer poly(D,L-lactic acid-co-ethylene glycol-co-D,L-lactic acid) (PELA)/hydroxyapatite composites" *Macromolecular Chemistry and Physics* 2014. doi:10.1002/macp.201400340

Kutikov AB, Guirjala A, Song J. "Rapid prototyping amphiphilic polymer/hydroxyapatite composite scaffolds with hydration-induced self-fixation behavior" *Tissue Engineering Part C: Methods* 2014. doi:10.1089/ten.TEC.2014.0213

Kutikov AB, Song J. "An amphiphilic degradable polymer/hydroxyapatite composite with enhanced handling characteristics promotes osteogenic gene expression in bone marrow stromal cells" *Acta Biomaterialia* 2013; 9(9):8354-8364.

Zhao L*, **Kutikov A***, Shen J, Duan C, Song J, Han G. "Stem Cell Labeling using Polyethylenimine Conjugated (α -NaYbF₄:Tm³⁺)/CaF₂ Upconversion Nanoparticles" *Theranostics* (featured on cover) 2013; 3(4):249-257. (*Equal contribution)

Chen G, Shen J, Ohulchanskyy TY, Patel NJ, **Kutikov A**, Li Z, Song J, Pandey RK, Ågren H, Prasad PN, Han G. " $(\alpha$ -NaYbF₄:Tm³⁺)/CaF₂ Core/Shell Nanoparticles with Efficient Near-Infrared to Near-Infrared Upconversion for High-Contrast Deep Tissue Bioimaging" *ACS Nano* 2012; 6(9):8280-8287.

Filion TM, **Kutikov A**, Song J. "Chemically modified cellulose fibrous meshes for use as tissue engineering scaffolds" *Bioorganic & Medicinal Chemistry Letters* 2011; 21:5067-5070.